

CR 114745

AVAILABLE TO THE PUBLIC

(NASA-CR-114745) STUDY OF SPIN-SCAN
IMAGING FOR OUTER PLANETS MISSIONS
Final Technical Report (Santa Barbara
Research Center) 289 p HC \$17.50

N74-21801

Unclassified
CSCL 17B G3/07 37624

FINAL TECHNICAL REPORT

STUDY OF SPIN-SCAN IMAGING FOR OUTER PLANETS MISSIONS

Contract No. NAS2-7096

For - National Aeronautics and Space Administration
OAST Systems Studies Division
Ames Research Center
Moffett Field, California

By - Santa Barbara Research Center and
Lunar and Planetary Laboratory/University of Arizona



SANTA BARBARA RESEARCH CENTER

A Subsidiary of Hughes Aircraft Company

SBRC

SANTA BARBARA RESEARCH CENTER

A Subsidiary of Hughes Aircraft Company

75 COROMAR DRIVE • GOLETA, CALIFORNIA

FINAL TECHNICAL REPORT

STUDY OF SPIN-SCAN IMAGING FOR OUTER PLANETS MISSIONS

Contract No. NAS2-7096

For

National Aeronautics and Space Administration
OAST Systems Studies Division
Ames Research Center
Moffett Field, California

Original Draft Submitted
21 September 1973
Final Report Published
27 February 1974

Prepared by:

E. E. Russell
Member of Technical Staff
SBRC Systems Analysis

R. A. Chandos
Member of Technical Staff
SBRC Electronics

J. C. Kodak
Member of Technical Staff
SBRC Mechanics

S. F. Pellicori
Member of Technical Staff
SBRC Optics

M. G. Tomasko
Research Associate
Lunar and Planetary Laboratory
University of Arizona

Approved by: E. E. Russell
E. E. Russell, Study Manager

R. F. Hummer
R. F. Hummer, Manager
Electro-Optical Instrumentation

ACKNOWLEDGEMENTS

The authors wish to acknowledge the technical assistance of other members of the staff at SBRC during the course of this study. In addition, many people at the University of Arizona have contributed substantially to this report. We are grateful for Mr. N.D. Castillo's invaluable programming assistance throughout the study. Special recognition is also due Mr. C.E. KenKnight for his work on subsection 4.3, and Mr. L. Doose and Mr. A.E. Clements for developing many of the techniques of Section 8. The rectification programs of Section 8 were originally developed under the supervision of Dr. W. Swindell of the Optical Sciences Department of the University of Arizona for the Pioneer Jupiter Program. Finally, the assistance of Ames Research Center personnel and, in particular, of the technical monitor, Mr. L. Edsinger, is gratefully acknowledged.

CONTENTS

<u>Section</u>	<u>Page</u>
1 SUMMARY OF STUDY RESULTS	1-1
1.1 Scope of Study	1-1
1.2 System Modeling Methodology	1-3
1.3 Optimized Designs for Jupiter Orbiter Mission	1-4
1.4 Image Sequencing and Processing	1-6
1.5 Recommendations for Future Effort	1-6
2 INTRODUCTION TO SPIN-SCAN IMAGING	2-1
2.1 Prior History	2-1
2.2 Basic Concepts	2-2
2.3 Scope of Study Effort	2-4
3 IMAGER CONSTRAINTS	3-1
3.1 Science Imposed Constraints	3-1
3.1.1 Resolution	3-1
3.1.2 Signal-to-Noise Ratio	3-3
3.1.3 Modulation Transfer Function and Aliasing	3-8
3.1.4 Underlap	3-16
3.1.5 Scene Characteristics	3-20
3.1.6 Spectral Coverage	3-24
3.1.7 Spatial Coverage	3-26
3.1.8 Geometrical Accuracy	3-26
3.1.9 Quantization Accuracy and Dynamic Range	3-26
3.2 Spacecraft Imposed Constraints	3-28
3.3 Additional Constraints	3-29

CONTENTS (Continued)

<u>Section</u>	<u>Page</u>
4 DATA HANDLING AND RECONSTRUCTION	4-1
4.1 Data Handling, Storage, and Telemetry	4-1
4.2 Data Compaction	4-2
4.3 Image Reconstruction	4-12
4.3.1 Geometry of Spin-Scan Imaging.	4-13
4.3.2 Assignment of Intensities to Display Array.	4-22
4.3.3 Summary	4-35
5 IMAGER COMPONENTS	5-1
5.1 Detectors	5-1
5.1.1 Photoemissive Detectors.	5-1
5.1.2 Silicon Photodiode Array Detectors.	5-11
5.1.3 Other Candidate Detectors.	5-18
5.1.4 Detector Radiation Effects.	5-22
5.1.5 Signal-to-Noise (SNR) Equations.	5-37
5.2 Scan Mechanism	5-45
5.2.1 Image-Space Scanning.	5-45
5.2.2 Object-Space Scanning	5-46
5.3 Mechanics	5-48
5.3.1 Basic Design Approaches	5-48
5.3.2 Material Selection	5-49
5.4 Telescope Optics	5-50
5.4.1 Requirements for the Telescope	5-50
5.4.2 Image-Quality Analysis.	5-51
5.4.3 Restrictions on Fundamental Design Parameters	5-52
5.4.4 Defocus and Alignment Error Tolerances.	5-52
5.4.5 Selection of Radiation-Resistant Optical Materials	5-67

CONTENTS (Continued)

<u>Section</u>	<u>Page</u>
5 5.5 Electronics.....	5-72
(Cont) 5.5.1 Component Selection.....	5-72
5.5.2 Electronic Packaging	5-73
6 SYSTEM MODELING	6-1
6.1 Parametric Analysis	6-1
6.1.1 Summary of Constraints	6-1
6.1.2 Modeling Nomographs	6-4
6.2 Application to Jupiter	6-10
6.3 Application to Other Outer Planet Missions	6-17
6.3.1 Saturn/Uranus Mission: Uranus Encounter	6-18
6.3.2 Saturn/Uranus Mission: Saturn Encounter	6-23
7 POINT DESIGN FOR JUPITER ORBITER	7-1
7.1 System Design.....	7-1
7.1.1 Imager Point Design Assumptions.....	7-1
7.1.2 Functional Operation	7-5
7.2 Electronic Design	7-8
7.2.1 Preamplifiers	7-8
7.2.2 High-Voltage Supply	7-9
7.2.3 Analog Channel Electronics	7-10
7.2.4 Analog Processing	7-13
7.2.5 Data Handling	7-15
7.2.6 Logic Design.....	7-17
7.2.7 Telescope Control Electronics	7-18
7.2.8 Calibration Circuitry	7-20
7.2.9 Electronics Weight.....	7-22

CONTENTS (Continued)

<u>Section</u>		<u>Page</u>
7	7.3 Telescope Optical Designs	7-22
(Cont)	7.3.1 Point Designs 1 and 3	7-25
	7.3.2 Alternate Point Design 1	7-30
	7.3.3 Point Design 2	7-30
7.4	Mechanical Design	7-32
	7.4.1 Structural Configuration	7-32
	7.4.2 Thermal Effects	7-34
	7.4.3 Telescope Cross-Scan Drive Systems	7-36
	7.4.4 Weight	7-39
7.5	Calibration	7-46
	7.5.1 Inflight Radiometric Calibration	7-46
	7.5.2 Preflight Calibration	7-48
7.6	Minimum Weight OPM Imager Designs	7-50
8	IMAGE SEQUENCE PLAN FOR JUPITER ORBITER MISSION	8-1
8.1	Introduction to Orbit Geometry	8-1
8.2	Step Rate Selection	8-7
8.3	Plan for Orbit 1	8-9
	8.3.1 Jupiter Imaging	8-13
	8.3.2 Satellite Imaging	8-27
8.4	Overview for Six Orbits and Summary	8-38
9	REFERENCES	9-1

ILLUSTRATIONS

<u>Figure</u>	<u>Page</u>
3-1 MTF for Ideal and $\lambda/10$ Telescopes with ($\epsilon = 1/3$) and without ($\epsilon = 0$) Obscuration	3-6
3-2 MTF for 0.1-mr IFOV and $\lambda/10$ Telescope.....	3-7
3-3 Field of View Geometry for Spin-Scan OPM Imager	3-10
3-4 Illustration of Cross-Scan Aliasing	3-11
3-5 Illustration of Along-Scan Aliasing	3-12
3-6 Geometry with Spacecraft Spin Axis and Trajectory Both in Equatorial Plane of Planet.....	3-19
3-7 Rate of Change of Look Angle Versus Height Above Surface for Jupiter Orbit.....	3-21
3-8 Rate of Change of Look Angle Versus Height Above Surface for Saturn Flyby	3-22
3-9 Rate of Change of Look Angle Versus Height Above Surface for Polar Uranus Flyby	3-23
3-10 Geometric Albedos for Outer Planets.....	3-25
4-1 Reconstructed ATS-1 Imagery for Scene Area 1 with and without Data Compaction	4-9
4-2 Reconstructed ATS-1 Imagery for Scene Area 2 with and without Data Compaction	4-10
4-3 Motion of Spacecraft during Hypothetical Image.....	4-14
4-4 Unrectified Spin-Scan Images of Rotating and Translating Globe.....	4-15
4-5 Geometric Solution Procedure	4-18
4-6 Scan Map of Jupiter from Jupiter Orbiter for Conditions Indicated	4-21
4-7 Example Mapping of IPP Test Data onto Display Plane	4-23
4-8 Data of Figure 4-4 Displayed According to Scan Map of Figure 4-7	4-24
4-9 Possible Arrangement of Three General-Case Data Rolls in a Picture	4-26

ILLUSTRATIONS (Continued)

<u>Figure</u>	<u>Page</u>
4-10 Typical Scan Maps Consisting of Parallel Straight Lines in the Roll Direction	4-32
4-11 Form of the Spin-Scan Data	4-32
4-12 Possible Arrangement of Three Data Rolls in the Picture Plane	4-34
4-13 Rectified and Unrectified Spin-Scan Images of Translating Globe	4-36
5-1 Spectral Responsivities of Some Candidate Detectors	5-3
5-2 Detectivities of Candidate Infrared Detectors	5-20
5-3 GaAs PMT (RCA 31025J) Dark Current as a Function of Dynode Voltage for Various Radiation Dose Rates (^{60}Co Source)	5-27
5-4 GaAs PMT (RCA 31025J) Anode Current as a Function of Illumination at Various Radiation Dose Rates (^{60}Co Source)	5-28
5-5 GaAs PMT (RCA C31025J) Output Current as a Function of Time Before and After Exposure to 10^6 rads (Dark and Illuminated)	5-30
5-6 Channeltron Anode Current as a Function of Channel Potential when Exposed to a Radiation Environment	5-31
5-7 Three Object-Space Scan Methods	5-47
5-8 Relative Intensity at Central Diffraction Maximum Versus Obscuration Ratio	5-55
5-9 Point Spread Function with Obscuration Ratio as a Parameter	5-56
5-10 Normalized Point Spread Function with Obscuration Ratio as a Parameter	5-57
5-11 Relative Intensity at Center of Image Versus RMS Wavefront Aberration	5-58
5-12 Intensity at Center of Image Versus RMS Wavefront Aberration with Obscuration Ratio as a Parameter	5-59
5-13 Normalized Line Spread Function with Obscuration Ratio as a Parameter	5-62

ILLUSTRATIONS (Continued)

<u>Figure</u>	<u>Page</u>
5-14 Diffraction Limited MTF with Obscuration Ratio as a Parameter	5-63
5-15 Effect of Mirror Scatter on Radiometric Measure- ments.....	5-68
6-1 Imager Modeling Nomograph	6-5
6-2 Data Rate Modeling Nomograph	6-8
6-3 Nomograph Inserts.....	6-9
6-4 Parametric Modeling for OPM Imager Design 1 (Extended-Red, Digicon-Type Detector) at Jupiter	6-11
6-5 Parametric Modeling for OPM Imager Design 2 (GaAs PMT Detectors) at Jupiter	6-12
6-6 Parametric Modeling for OPM Imager Design 3 (Silicon Photodiode Detectors) at Jupiter	6-13
6-7 Telemetry Rate Modeling at Jupiter	6-14
6-8 Parametric Modeling for OPM Imager Design 1 (Extended-Red, Digicon-Type Detector) at Uranus	6-19
6-9 Telemetry Rate Modeling at Uranus	6-20
6-10 Parametric Modeling for OPM Imager Design 1 (Extended-Red, Digicon-Type Detector) at Saturn	6-24
7-1 Electronic Block Diagram of OPM Imager	7-11
7-2 Analog Processing for OPM Imager Designs	7-14
7-3 Telescope Control Logic for OPM Imager.....	7-19
7-4 Calibrator Sequence Logic for OPM Imager	7-21
7-5 Design Layouts for OPM Imager Point Designs 1 and 3	7-24
7-6 Design Layouts for OPM Imager Point Design 2 and Alternate Design 1	7-26
7-7 Spot Diagram of Telescope Design for OPM Imager Designs 1 and 3	7-27

ILLUSTRATIONS (Continued)

<u>Figure</u>	<u>Page</u>
7-8 Ray Trace of Telescope Design for OPM Imager Designs 1 and 3	7-28
7-9 Weight Versus Aperture Diameter for OPM Imager Design 1	7-42
7-10 Weight Versus Aperture Diameter for OPM Imager Design 2	7-43
7-11 Weight Versus Aperture Diameter for OPM Imager Design 3	7-44
7-12 Weight Versus Aperture Diameter for OPM Imager Alternate Design 1	7-45
7-13 Weight Versus Roll Rate for OPM Imager Design 1 (Extended-Red, Digicon-Type Detector)	7-51
7-14 Weight Versus Roll Rate for OPM Imager Design 2 (GaAs PMT Detectors)	7-51
7-15 Weight Versus Roll Rate for OPM Imager Design 3 (Silicon Array Detectors)	7-52
8-1 Possible Initial Insertion Orbit for Jupiter Orbiter Mission	8-2
8-2 Geometry of One Possible Orbit during Jupiter Mission	8-3
8-3 Geometry of Encounters with Ganymede during Six Successive Orbits	8-4
8-4 Geometry of Encounters with Jupiter during Six Successive Orbits	8-5
8-5 Geometry of Encounters with Europa during Six Successive Orbits	8-6
8-6 Stepping Rate Selection Chart for Imager	8-8
8-7 Look Angle (Degrees) Versus Time (Hours) for Orbit 1 and Part of Orbit 2	8-10
8-8 Roll Angle (Degrees) Versus Time (Hours) for Orbit 1 and Part of Orbit 2	8-11
8-9 Look Angle Versus Time on Expanded Scale Near Encounter	8-12

ILLUSTRATIONS (Continued)

<u>Figure</u>	<u>Page</u>
8-10 Look Angle Versus Time on Further Expanded Scale Near Periapsis	8-14
8-11a Scan Map of Jupiter for Conditions Indicated	8-15
8-11b Scan Map of Jupiter for Conditions Indicated	8-16
8-11c Scan Map of Jupiter for Conditions Indicated	8-17
8-11d Scan Map of Jupiter for Conditions Indicated	8-18
8-11e Scan Map of Jupiter for Conditions Indicated	8-19
8-11f Scan Map of Jupiter for Conditions Indicated	8-20
8-11g Scan Map of Jupiter for Conditions Indicated	8-21
8-12 Number of Scans at Given Resolution or Better	8-24
8-13 Number of Scans at Given Resolution or Better (Expanded Scale)	8-25
8-14 Imaging Sequence Plan for Ganymede	8-28
8-15 Imaging Sequence Plan for Europa	8-29
8-16a Scan Map of Ganymede for Conditions Indicated	8-30
8-16b Scan Map of Ganymede for Conditions Indicated	8-31
8-16c Scan Map of Ganymede for Conditions Indicated	8-32
8-16d Scan Map of Ganymede for Conditions Indicated	8-33
8-16e Scan Map of Ganymede for Conditions Indicated	8-34
8-16f Scan Map of Io for Conditions Indicated	8-35
8-16g Scan Map of Io for Conditions Indicated	8-36
8-16h Scan Map of Europa for Conditions Indicated	8-37
8-17 Statistical Analysis of Planned Images	8-39
8-18 Look Angle Versus Time for Orbits 2 and 3	8-40
8-19 Look Angle Versus Time for Orbits 3 and 4	8-41
8-20 Look Angle Versus Time for Orbits 4 and 5	8-42
8-21 Look Angle Versus Time for Orbits 5 and 6	8-43

T A B L E S

<u>Table</u>		<u>Page</u>
1-1	Scope of Spin-Scan Imaging Study	1-2
1-2	Comparison of OPM Imager Point Designs Optimized for Minimum Weight	1-4
4-1	Some Possible Data Compaction Techniques	4-4
4-2	Comparison of Results for Two Data Compaction Methods with ATS-1 Spin-Scan Cloud Camera Imagery as Input	4-8
5-1	Accumulated Dose Experiments on EMR Photo- multiplier Tubes (^{60}Co Source at Hughes Aircraft Company, Fullerton, May 1968)	5-26
5-2	Radiation Induced Degradation of Selected Optical Components	5-70
5-3	Transmission Loss Due to 142-MeV and 80-MeV Proton Irradiation	5-71
6-1	OPM Imager Point Design 1 (Extended-Red, Digicon-Type Detector) Signal-to-Noise Calculations	6-6
7-1	Spacecraft Characteristics Assumed for Spin-Scan Imager Point Design Analysis	7-2
7-2	Characteristics of Preliminary OPM Point Designs	7-4
7-3	OPM Imager Command List.	7-6
7-4	OPM Imager Electronics, Power/Weight/Size Comparison.	7-23
7-5	Telescope Design for OPM Imager Designs 1 and 3	7-29
7-6	Optical System Error Budget for 90% Energy Containment	7-29
7-7	Weight Summary for Preliminary OPM Imager Point Designs (20-cm Diameter Telescopes; 16 Detectors)	7-40
7-8	Comparison of OPM Imager Point Designs Optimized for Minimum Weight	7-52

Section 1

SUMMARY OF STUDY RESULTS

1.1 SCOPE OF STUDY

The areas included in this study are indicated in Table 1-1.

The constraints that must be imposed on the Outer Planets Missions (OPM) Imager design are obviously of critical importance and include those imposed by the desired scientific return, by the space-craft limitations, by the operating environment, and by the technological limitations. The imager-system modeling formed an important part of this study. In the system modeling analysis, the important parameters are defined, and a systematic means for trade-off analysis is developed and applied to a specific Jupiter orbiter mission.

Three promising point designs are detailed for values of the system variables established in the system modeling, and the important physical characteristics for each point design are parameterized. The engineering-type inputs so developed then permit point-design optimization.

Possible image-sequence plans for a Jupiter orbiter mission are discussed in detail. The discussion applies to a particular series of orbits that allow repeated near encounters with three of the Jovian satellites, although the approach can be readily extended to the development of image-sequence plans for other missions.

The data handling involved in the image processing is discussed, and it is shown that only minimal processing would be required for the majority of the images for a Jupiter orbiter mission. Where a small amount of distortion is present, a simple picture-point-assignment program sufficient to rectify the images is described. For those few

images subject to a significant amount of distortion, the more general methods developed to rectify the image data generated by the Pioneer 10 and 11 IPP instruments would be required and are outlined.

Table 1-1. Scope of Spin Scan Imaging Study

IMAGER CONSTRAINTS
SCIENTIFIC
SPACECRAFT-IMPOSED
ENVIRONMENTAL
IMAGER COMPONENT STUDY
DETECTORS
SCAN MECHANISMS
OPTICS
IMAGER SYSTEM MODELING
RESOLUTION (MTF, SAMPLING)
SCENE CHARACTERISTICS
SIGNAL-TO-NOISE RATIO MODELING
INCLUSION OF CONSTRAINTS
PRELIMINARY DESIGNS
IMAGER POINT DESIGNS
DETAIL PROMISING POINT DESIGNS
PARAMETERIZE IMPORTANT CHARACTERISTICS
OPTIMIZE ITERATED POINT DESIGNS
IMAGING SEQUENCE PLAN
JUPITER ORBITER IMAGING
SATELLITE IMAGING
IMAGING AT OTHER OUTER PLANETS
IMAGE PROCESSING
ALTERNATIVE METHODS
RECOMMENDED METHOD
SAMPLE IMAGERY

1.2 SYSTEM MODELING METHODOLOGY

A general system modeling methodology has been developed during the course of this study for analyzing spin-scan imaging systems. The process is an iterative one in which the mission, scene, spacecraft, and component characteristics, coupled with the scientific requirements, serve to determine the initial point-design values through the system modeling figure. The system modeling trade-off figure generated for each basic point design is used to vary such important system parameters as instantaneous field of view, telescope diameter, spectral bandwidth, and signal-to-noise ratio (SNR).

The initial point-design values determined may be further modified in a detailed point design by additional spacecraft constraints (e.g., maximum memory read-in rate) and operational considerations (e.g., minimization of command activity) not included in the trade-off figure. From the detailed point design, the important instrument characteristics are parameterized, e.g., the dependence of weight on telescope diameter and number of imager channels. The suitable combination of the system modeling figure with the parameterized point-design data permits the optimization of the point-design subject, e.g., to minimize instrument weight. If this procedure is followed for each point design under consideration, it is then possible to compare several point designs optimized on a consistent basis.

The interaction of bit rate, roll rate, sampling rate, number of detectors per spectral band, number of spectral bands, number of gray levels, samples per pixel, data compaction factor and line length can be combined to yield a telemetry rate modeling figure. This serves as a simple means to see the effect on the imagery as various instrument and spacecraft parameters are changed. While the implied requirement on the spacecraft memory capacity is not shown explicitly in this figure, it can be readily derived.

1.3 OPTIMIZED DESIGNS FOR JUPITER ORBITER MISSION

The primary constraints applicable to the optimization of specific OPM Imager Point Designs are sufficient resolution and signal-to-noise ratio, no underlap or significant aliasing, and operation within the range of possible spacecraft roll rates. The iterative process of optimization through the system modeling figure and parametric curves of the important instrument properties resulted in the point design characteristics shown in Table 1-2. Each point design was optimized individually subject to the constraint that weight was to be minimized. Implicit in the designs are assumptions regarding basic design philosophy. In general, high reliability, radiation resistance, and operational flexibility were emphasized.

Table 1-2. Comparison of OPM Imager Point Designs Optimized for Minimum Weight

POINT DESIGN	TELESCOPE DIAMETER (cm)	NUMBER OF DETECTORS	ROLL RATE (rpm)	WEIGHT (kg)
DESIGN 1 (DIGICON-TYPE DETECTOR)	15	32	5	8.2
DESIGN 2 (GaAs PHOTO-MULTIPLIERS)	16	12	13	9.5
DESIGN 3 (SILICON PHOTO-DIODE ARRAY)	14	18	9	7.3

(WEIGHT MINIMIZED FOR SNR ($\nu = 0$) = 100
AND IFOV = 0.1 mr)

THESE POINT DESIGNS PROVIDE:

1. 10 km RESOLUTION AT JUPITER
2. RADIOMETRIC QUALITY IMAGERY
3. FULL DISK IMAGES AT $10R_J$ (<50 kbps)
4. INSTRUMENT WEIGHT ~ 9 kg

Based on the results of this study, Point Design 1 is the preferred design. The primary reason for this selection is the predicted superior radiation resistance of this design relative to the other point designs. The point designs that use photoemissive detectors (Designs 1 and 2) have the advantage that the SNR would decrease only as the square root of a decrease of scene flux on the detector, e.g., due to a lower scene radiance or a narrower spectral bandwidth. In contrast, the SNR decrease with silicon array detectors (Design 3) would be directly proportional to a decrease in the scene flux on the detector (thermal or preamplifier noise limit assumed). The weight differences between the three designs are fairly small and the slight advantage indicated for Design 3 results since it has the lowest detector assembly weight. The simpler telescope drive system possible with Point Design 1 somewhat reduces this weight advantage relative to Design 1.

For both Designs 1 and 3 an increase in the number of channels could be accommodated with a very small increase in the detector assembly weight. (The main weight increase would be due to the additional electronics required.) However, since the available spacecraft telemetry rate fixes the number of bits that can be transmitted per roll, increasing the number of channels beyond the minimum required due to underlap considerations normally would not be desirable. This follows since fewer channels would reduce shading effects (responsivity variations across the array), simplify calibration, allow less costly optics, and permit lower read-in rates for data into the spacecraft memory (at a fixed roll rate).

1.4 IMAGE SEQUENCING AND PROCESSING

Possible image sequence plans were generated for a specific Jupiter orbiter mission that allows repeated near encounters with the three Jovian satellites, Io, Europa, and Ganymede. The image sequence plans were developed to be compatible with the characteristics of the OPM Imager Point Designs that were optimized for Jupiter. While the detailed sequencing was developed for a specific set of orbital characteristics, the general method can be readily extended to other missions.

Various methods of image processing are discussed with the view towards simplification of the data handling. It is shown that only minimal processing would be required for the majority of the images obtained during the example Jupiter orbiter mission. A simple picture-point-assignment program is described which is suitable to rectify images with a small amount of distortion. For images taken near periapsis and subject to a significant amount of distortion, software similar to that developed for the Pioneer 10 and 11 encounters would be required. These more general methods which require additional computer processing time are outlined for completeness.

1.5 RECOMMENDATIONS FOR FUTURE EFFORT

Four major recommendations seem appropriate based on the results of this study:

1. Modify and qualify a Digicon-type detector for spaceflight use.
2. Thoroughly radiation test both a Digicon-type detector and silicon solid-state array detectors including CCD arrays.
3. Closely monitor future CCD developments.
4. Similarly monitor Pioneer Imaging Photopolarimeter (IPP) software developments.

Other areas of importance that would benefit from additional work include:

1. Trade-off analysis relating to the selection of an optimal data compaction method with emphasis on outer planets missions imaging applications.
2. Selection of optimum sampling properties for an Outer Planets Mission Imager.
3. Application of the system modeling methodology to other types of missions, e.g., to cometary encounters.

Finally, it seems appropriate as regards the spacecraft to:

1. Study ways to increase the available telemetry rate since the quantity of the imagery is clearly bit rate dependent.
2. Evaluate possible means to reduce the wobble angle and improve roll reference repeatability should even greater resolution later be required.

Section 2

INTRODUCTION TO SPIN-SCAN IMAGING

2.1 PRIOR HISTORY

The first spin-scan imagers were the Spin-Scan Cloud Camera (single color) and the Multicolor Spin-Scan Cloud Camera (three colors) launched on ATS-I and ATS-III, respectively. (The single-color instrument failed in 1972 after more than five years of operation, while the three-color instrument is still operating six years after launch.) The spin-scan Imaging Photopolarimeter (IPP) instruments on Pioneer 10 and 11 are designed to take two-color imagery during the Jovian encounters. In addition to the imaging function, the IPP instruments are being used in a faint-light mode to take sky maps in both radiance and polarization and will be used in the photopolarimetry mode during the Jovian encounter to record the radiance and polarization of Jupiter. The Visible-IR Spin-Scan Radiometer (VISSR) is a multispectral instrument that will operate in both visible and infrared wavelengths. The VISSR will be launched in early 1974 and will operate on the Synchronous Meteorological Satellite (SMS).

It has been argued that the complex geometry entailed by many possible space missions would preclude the use of the spin-scan imaging approach. With modern-day computing facilities this is clearly not the case. In practice, the Pioneer 10 and 11 flyby missions, with the spin-scan IPP providing the imaging capability, are a severe departure from the ATS-I and -III spin-scan imagers used in synchronous orbit. While the Pioneer flyby geometry is indeed complex, the problems of image reconstruction have been solved, and the resultant software is extremely flexible. Thus, while the IPP flown on Pioneer 10 and 11 is a point scanner (single field of view), the software has been modified to accommodate multiple detectors, variable stepping rates, etc.

Diverse requirements, such as for orbiter and polar flyby missions, also are readily accommodated. A discussion of this is included in the later sections of this Technical Report.

2.2 BASIC CONCEPTS

The two fundamental types of spacecraft imaging instruments are scanning imagers and frame imagers. Scanning instruments are further subdivided into those flown on three-axis stabilized spacecraft and those on spin-stabilized spacecraft; instruments in the last category are referred to as spin-scan imagers. The fundamental nature of spin-scan instruments implies some basic advantages over the other two types of imagers.

With spin-scan imaging the angular rotation produced by a spinning spacecraft is used to provide one of the two relative angular motions required to scan a scene. As a consequence of the spacecraft roll, no physical motion of the imager in the roll (clock) angle direction is required, although it is often desirable that the angular sampling interval be electronically selectable. Scan motion in the orthogonal (cone angle) direction is normally required in a spin-scan imager unless either a single-swath image is sufficient or relative motion between the imager and scene provides the required scanning.

While the roll of a spinning spacecraft is essential for the operation of a spin-scan imager, it can often necessitate the use of elaborate image motion compensation with a frame imager. Finally, where the available telemetry rate is limited, the use of extensive, on-board memory storage or a very slow scan readout would be required for a frame camera. This latter approach can be particularly unattractive where operation in a high energy radiation environment is required. In contrast, a spin-scan imager can readily be designed to match the available telemetry rate with the on-board storage requirements being limited to that for data collected during one roll of the spacecraft.

A spin-scan imager with proper design can be considered to be a high resolution radiometer which utilizes the spacecraft roll to provide a portion of the scanning motion. This is a particularly attractive choice when high radiometric quality as opposed to cosmetic quality imaging is desired. This is true since high radiometric accuracy is more easily achievable with a spin-scan imager than with a frame imager. While the Multispectral Scanner (MSS) flown on the Earth Resources Technology Satellite (ERTS) is not a spin-scan imager, it is a scanning radiometer designed to compete directly with framing cameras. Return-beam-vidicon (RBV) cameras, one for each of three spectral bands, are also flown on the ERTS. The radiometric quality of the MSS imagery is certainly superior to that achievable with the RBV cameras, even with extensive calibration corrections. The shading across the image is the most serious contributor to the lower radiometric accuracy capability of such a frame camera. The geometric precision of the RBV imagery is probably somewhat better than that of the MSS, although the MSS imagery is now being used routinely for cartography, indicating the increased confidence of cartographers in these data. The spectral band-to-band registration of the MSS data is much better than one pixel for the MSS and better than that achievable with the three RBV cameras.

Where desirable to operate in several spectral bands and over a wide spectral range, the flexibility possible with an all-reflective spin-scan imager (radiometer) is especially significant. The Visible-IR Spin-Scan Radiometer (VISSR) is representative of these characteristics. Even for multispectral operation over the limited spectral range (for simultaneous imaging), the typical framing camera utilizes separate telescopes and cameras for each spectral band.

2.3 SCOPE OF STUDY EFFORT

The areas considered to be within the scope of this study are indicated in Table 1-1. The study results and recommendations for future effort towards satisfying anticipated outer planets missions imaging requirements also form an important part of the study. A brief summary of the principal areas studied and how they have been incorporated into this report follows.

The constraints that must be imposed on the OPM Imager design are obviously of critical importance. These constraints can be of a general nature; i. e., apply to all outer planets missions, and/or specific in that they apply to a particular mission, e. g., a Jupiter orbiter. The constraints can be broadly classified as being imposed by the desired scientific return, the spacecraft limitations, the operating environment, and the technological limitations. The first three constraint categories are reviewed in Section 3. The fourth category, technological limitations, is included in Section 5 where imager components are discussed.

The data handling and image reconstruction required for a spin-scan imager are discussed in Section 4. For the image reconstruction, it is shown that only minimal processing would be required for the majority of the images for a Jupiter orbiter mission. Where a small amount of distortion is present, a simple picture-point-assignment program sufficient to rectify the images is described. For those few images (near periapsis) subject to a significant amount of distortion, more general programs similar to those to be used during the Pioneer 10 and 11 encounters would be required. The methods developed to rectify the image data generated by the Pioneer 10 and 11 IPP instruments are also outlined.

The imager system modeling formed an important part of this study and is described in Section 6. This basically involved the development of a systematic means to parametrically model spin-scan imaging systems. In the system modeling analysis the important parameters are defined and a systematic means for trade-off analysis is developed. The detailed parametric analysis as applicable to a Jupiter orbiter mission is contained in subsection 6.2. In subsection 6.3, the system modeling methodology is applied to Uranus flyby and Saturn encounters.

In Section 7, three promising point designs are detailed for values of the system variables established in the system modeling. The important physical characteristics for each point design are then parameterized. The engineering-type inputs so developed then are optimized for minimum weight.

The image sequence plan for a Jupiter orbiter mission is discussed in some detail in Section 8. The plan developed applies to a particular series of orbits that allow repeated near encounters with three of the Jovian satellites. The image sequence planning using a specific set of orbital characteristics allows the various imaging options to be easily visualized. This approach can be readily extended to the development of image sequence plans for other missions.

Section 3

IMAGER CONSTRAINTS

3.1 SCIENCE IMPOSED CONSTRAINTS

Unlike the Moon and Mars, the outer planets have such thick atmospheres that solid surfaces are not expected to be observable; images of these planets will rather be of transient cloud features. This fact may be reflected in the imaging science of outer planet missions as an increased emphasis on the radiometric accuracy of the imager. In the sections that follow, the effect of some important scientific constraints on the instrument parameters is discussed.

3.1.1 Resolution

Significant dynamical features may be anticipated for these planets at least down to sizes comparable to the pressure scale heights near their cloud levels. For Jupiter, this scale is ~ 20 km; for the other outer planets, decreases in both temperature and surface gravity combine to yield comparable values. While still smaller structures probably exist, it may be hoped that resolution of features down to $1/2 - 1/4$ pressure scale height may allow studies of the principal forms of organized dynamical flow (from quiescent convective cells to the equivalent of thunderstorms), if not of the finest scale turbulence.

For studies of satellites with visible surfaces, better resolution is in general desirable, although images of the Jovian satellites at ~ 10 -km resolution would be nearly two orders of magnitude better than that available from Earth, and so of great interest. Images of satellites of the other outer planets at 10-km resolution would represent even larger improvements over ground-based capabilities. Lunar-like maria and moderate-sized craters could be observed if present. It may be fair to state, however, that if satellite images were the main objective of the instrument, much better resolution than 5 to 10 km would be desired.

A very common way to specify the resolution of an imaging system is to define it in terms of the spatial frequency at some specific level of the overall system MTF (modulation transfer function) curve. For example, if the point where the system MTF falls to 10% is designated as the "limiting" spatial frequency ν_L , then the resolution becomes

$$r = 1/(\nu_L) \quad (3-1)$$

With the above definition for resolution, the performance of two systems with the same "limiting" resolution can be decidedly different if the detailed shapes of the MTF curves differ significantly. In view of this, a number of definitions that attempt to account for such effects have been proposed. A useful definition due to Schade¹ is

$$r = \frac{1}{2\int [MTF(\nu)]^2 d\nu} \quad (3-2)$$

(Note that if the angular width of the field stop, α , were to completely determine the MTF, then $r = \alpha$, since the MTF (ν) = Fourier Transform of Rect (x/α) = Sinc ($\nu\alpha$) where Rect (x/α) = 1 for $|x/\alpha| \leq 1/2$; Rect (x/α) = 0 for $|x/\alpha| > 1/2$, and Sinc ($\nu\alpha$) = $\sin(\pi\nu\alpha)/(\pi\nu\alpha)$.)

Additional definitions which are sometimes used for resolution have been reviewed by Sendall.² However, either equation (3-1) or (3-2) seems adequate to describe the potential resolution of an imaging system. For a detailed systems analysis, the latter expression probably is a better quantitative measure of instrument resolution.

It is important to recognize that the effective resolution of an image reconstructed from the telemetered instrument output is dependent on parameters other than those included in the above equations. Such factors as the scene characteristics, sampling effects, scan overlap/underlap, instrument SNR, and image processing/reconstruction have an effect on the resultant image "quality." These and other related factors will be discussed in the subsections that follow.

The ultimate use of the data is also of critical importance. For example, the requirements for obtaining a cosmetically pleasing picture are much less severe than for a radiometric-quality reconstruction. The parametric study and point design for a spin-scan OPM Imager have emphasized radiometric quality instruments. This was done for two basic reasons: 1) spin-scan imagers as a class are particularly suitable for such an application by reason of their simplicity, stability, and relative ease of calibration compared to frame imagers, and 2) the increased scientific return seems to warrant such performance.

Since the satellites may not be the principal objective of these outer planet missions, one may be inclined to trade some resolution for increased SNR once sufficient resolution is achieved to allow study of atmospheric dynamics. For this study the surface resolution was specified as 100 to 300 km for full-disk pictures of Jupiter. This is about one order of magnitude better than that obtainable from Earth-based telescopes. Near encounter with Jupiter, and at the satellites, a surface resolution of 10 to 15 km was specified.

3.1.2 Signal-to-Noise Ratio (SNR)

A very desirable feature of an outer planet imager would be to have an SNR adequate for radiometric analysis of the images, in addition to qualitative detectability of features to some limiting characteristic size. Since all imaging systems progressively attenuate the components of viewed scenes of increasing spatial frequency, the SNR will not be a single number but will vary for scene components of different spatial frequency. The modulation transfer function (MTF) gives the amplitude of a spatial frequency component in the image expressed as a fraction of the total amplitude with which that spatial frequency component appeared in the original scene. If the noise may be assumed to be independent of spatial frequency (often the case) the SNR (ν) at spatial frequency ν is given by

$$\text{SNR}(\nu) = \text{SNR}(\nu = 0) \text{MTF}(\nu) S(\nu) \quad (3-3)$$

where $\text{SNR}(\nu = 0)$ is the SNR at zero spatial frequency, $\text{MTF}(\nu)$ is the overall system MTF at spatial frequency ν , and $S(\nu)$ is the amplitude of the scene component of spatial frequency ν relative to the amplitude of the $\nu = 0$ component.

The form of acceptable $\text{SNR}(\nu)$ curves will certainly vary depending on the details of particular imaging experiments, but some general desirable features can be discussed. Two quantities of particular importance are: 1) the SNR at zero spatial frequency, and 2) the spatial frequency, ν_c , at which some minimum acceptable SNR is desired for an assumed scene contrast and radiance.

If it is assumed that an SNR of 3 in the image is acceptable for qualitative detectability of scene components at ν_c which have an amplitude of 30% of the "flat field" ($\nu = 0$) component, and if the MTF is as low as 10% at this point, then the $\text{SNR}(\nu = 0)$ must be on the order of 100 which is adequate for radiometric studies. An additional decrease in the signal and SNR results from the scattering phase law at large phase angles. If the radiance of the scene is reduced by a factor, k , at some phase angle, then for a photon-noise-limited sensor, the SNR will decrease by a factor of \sqrt{k} . For a detector-noise-limited sensor the SNR will decrease by the full factor of k . (See subsection 5.1.6 for a discussion of SNR behavior for the candidate detectors.) If it is assumed that the planet is Lambertian, then the signals from an area with a 60° sun-zenith angle will be reduced by cosine (60°) or a factor of 2 from those for a region with a 0° sun-zenith angle. Thus, the SNR would decrease by either $\sqrt{2}$ or 2, depending on the limiting noise mechanism. Because of the importance of views at large phase angle for these planets, it seems undesirable to reduce $\text{SNR}(\nu = 0)$ much below 100.

The second parameter, the value of ν at which the MTF reaches some small value ($\sim 10\%$), is determined by the desire to resolve features with sizes on the order of a scale height in the atmosphere at the minimum range from the planet.

This leads to $\nu_c \approx 10$ cycles/mrad for the class of outer planet missions being considered in this study. To minimize aliasing, the sampling frequency should be greater than or equal to $2\nu_c$ (one sample every 0.05 mrad).

The system response at any frequency results from the MTF of the optics, detectors (IFOV), and image motion (including effect of electronics). A 10-cm diameter ideal telescope has response out to 200 cycles/mrad. Practical telescopes of this size can have good response out to 100 cycles/mrad (see also subsection 5.4), approximately 10 times the required ν_c . The MTF of an ideal telescope with no obscuration ($\epsilon = 0$) and with one-third of the aperture obscured ($\epsilon = 1/3$) is given in Figure 3-1. Also shown are the corresponding MTF curves when a wavefront error of $\lambda/10$ is assumed for the telescope.

If motion along the trajectory is less than 0.3 mrad/sec (typical maximum for Jupiter orbiter point design), then for pixel integration times of less than 0.05 sec, the smear from line to line will be negligible. It will be shown that the smear along the roll will have to be matched to the desired resolution to allow sufficient integration time for each pixel to have the required SNR and still be small enough to achieve the desired resolution. Indeed, for spin-scan systems, the size of the IFOV will be the factor limiting the resolution. For a rectangular IFOV, the MTF in either the scan or the cross-scan direction will be

$$\text{Sinc } (\nu\alpha) = \sin(\pi\nu\alpha)/(\pi\nu\alpha) \quad (3-4)$$

which has its first zero at $\nu = 1/\alpha$ where α is the IFOV width in the corresponding direction. (See Figures 3-1 and 3-2.) This means that

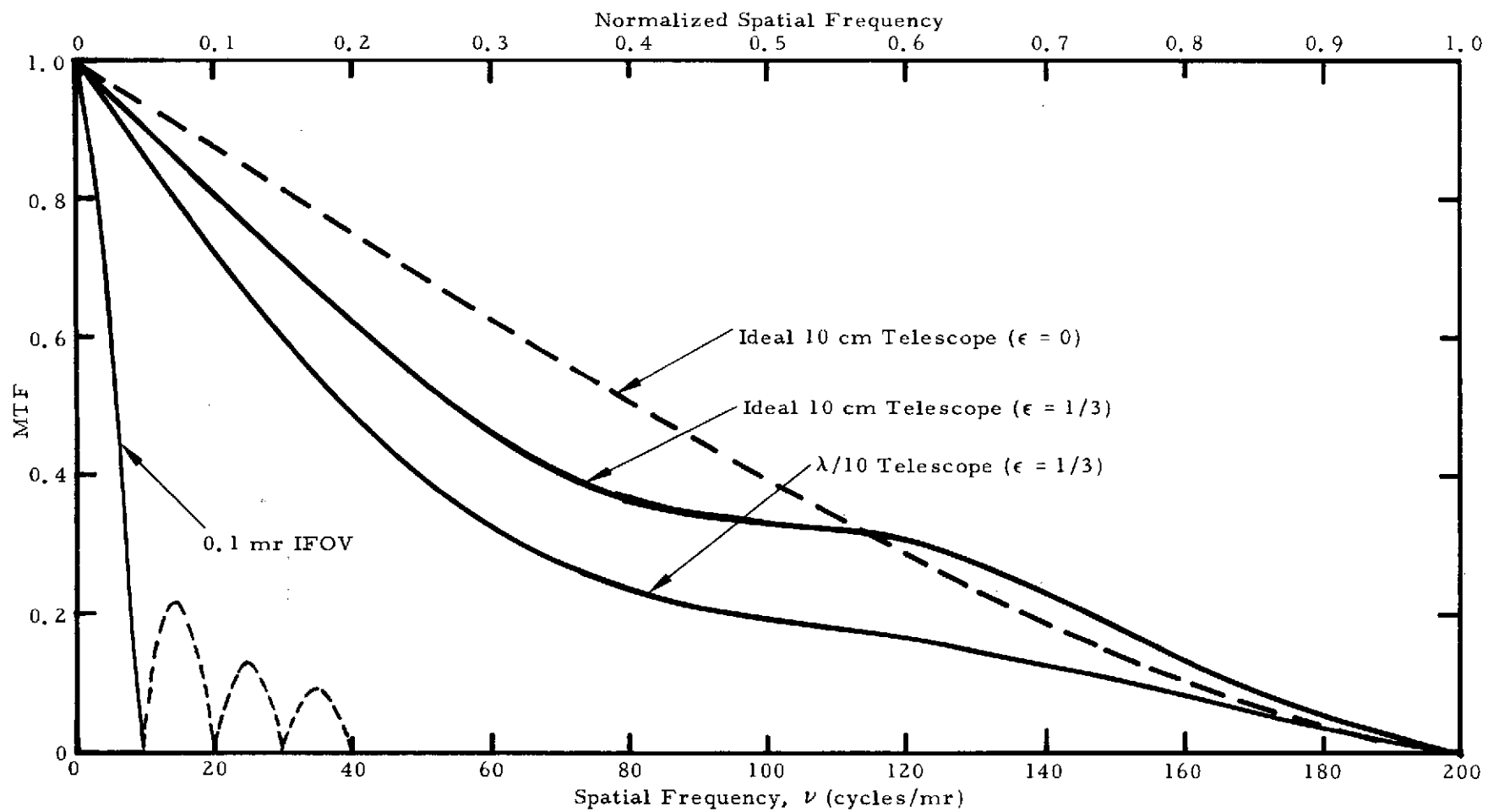


Figure 3-1. MTF for Ideal and $\lambda/10$ Telescopes with ($\epsilon = 1/3$) and without ($\epsilon = 0$) Obscuration

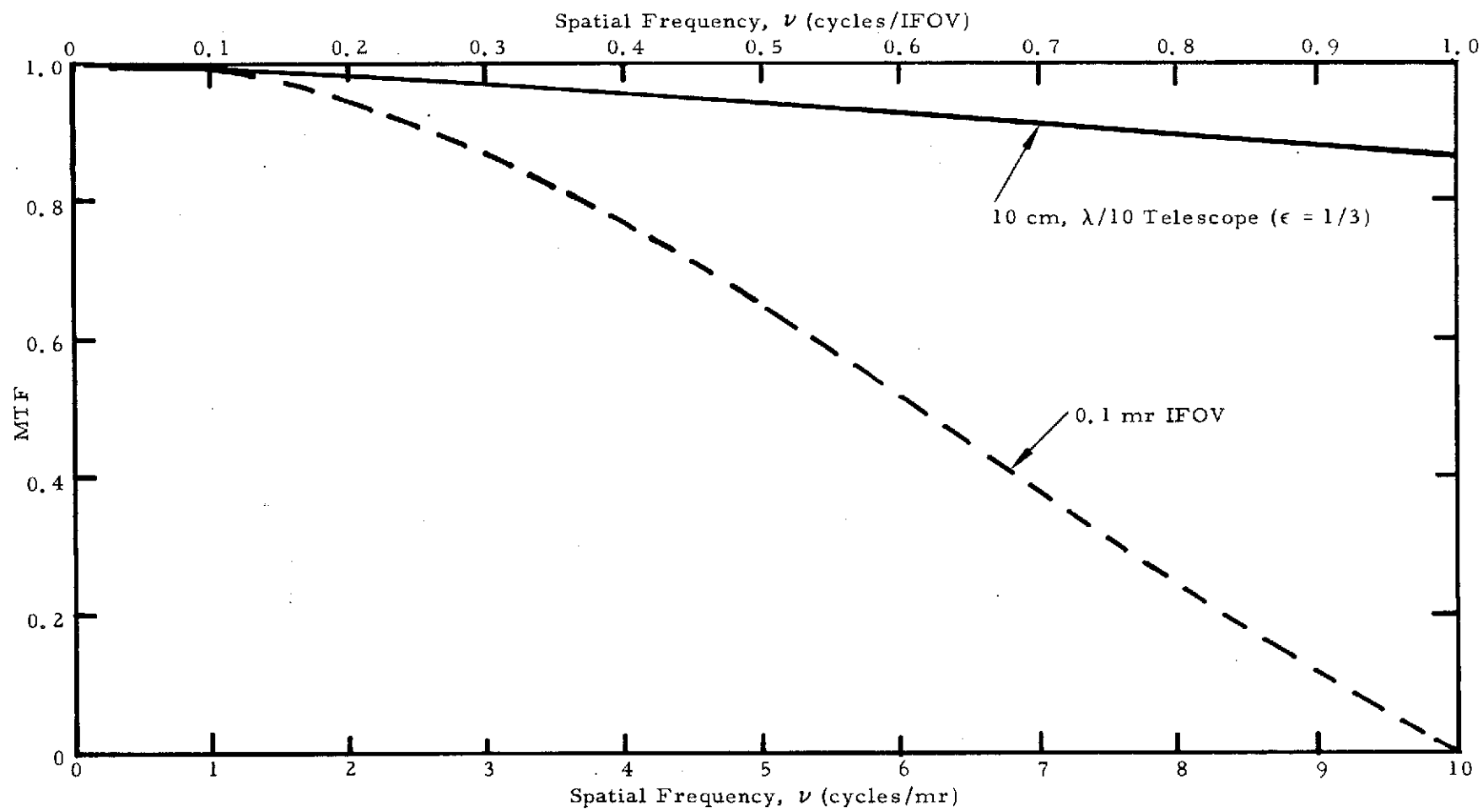


Figure 3-2. MTF for 0.1-mr IFOV and $\lambda/10$ Telescope

to achieve response to signals at 10 cycles/mrad, the IFOV must be no more than 0.1 mrad. Actually, for a total MTF of more than 10% at 10 cycles/mrad, an IFOV less than 0.08 - 0.09 mrad would be required, but 0.1 mrad was adopted for purposes of parametric scaling.

3.1.3 Modulation Transfer Function and Aliasing

The spatial frequencies present in the original scene are modified by the modulation transfer function (MTF) of the imager. In the along-scan direction these spatial frequencies translate into temporal frequencies. These are used to specify the bandwidth of the electronics. In the cross-scan direction, the spatial frequency components are determined by detector spacing, overlap, and shape. These effects must be taken into account when designing the instrument.

As stated previously, problems can result unless the sampling frequency exceeds ν_c , the effective band limit of the system. According to the sampling theorem, scene components at frequencies greater than the Nyquist frequency ν_N ($= 1/2$ cycle/sample) will be indistinguishable from scene components an equal interval below ν_N . Thus, when ν_N is less than ν_c , higher frequency components of the scene are mixed or "folded" with the lower frequency scene components. This effect is called "aliasing," and the folded, high frequency components are the alias components. When ν_N is greater than or equal to ν_c , no frequencies above ν_N are passed by the system and no mixing occurs. To achieve satisfactory fidelity in the imagery, it is necessary that no appreciable mixing of spatial frequencies occurs in the final images.

While the safest way to do this is to choose ν_N greater than or equal to ν_c , i.e., to have a spatial overlap of at least 50% between the IFOV samples (of width α or $1/\nu_c$), in most scenes the amplitude of scene components rapidly decreases with increasing spatial frequency. In these cases an overlap between samples of less than 50% might be acceptable. While the optimum amount of overlap between samples

has not been studied in detail, the optimum overlap in the cross-scan direction is expected to be between one quarter and one half the cross-scan width of the IFOV.

To fully explain the aliasing constraint, it is necessary to review the effects of detector geometry on spatial frequency. Then, since the modulation transfer function (MTF) of an imaging system is closely related to the effective resolution, as previously indicated by equations (3-1) and (3-2), it is appropriate to show how the MTF will vary as the parameters for a line-scan imager are changed.

In Figure 3-3 a portion of a focal-plane detector array is shown which indicates the basic parameters for a line-scan imager with multi-spectral capability. The detector elements are shown as rectangular elements with angular subtenses of $\alpha_{||}$ and α_{\perp} in the along-scan (roll) and cross-scan directions, respectively. The angular separation of "adjacent" detectors in the scan and cross-scan directions are $\beta_{||}$ and β_{\perp} , respectively. The angular separation between equivalent detectors in adjacent spectral bands is denoted by γ . The angular separations $\beta_{||}$ and γ are not of fundamental significance since they are equivalent to a time delay between samples. However, to facilitate the image reconstruction and avoid interpolation, it is desirable that at the nominal roll rate

$$\beta_{||} = m_1 t_s = \gamma/m_2 \quad (3-5)$$

where t_s = time period between successive samples of a given detector output and m_1 and m_2 are integers. (That is, with m_1 and m_2 integers, the detectors are sampled at equivalent points in each pixel.)

In Figures 3-4 and 3-5, the MTFs are shown for the cross-scan and scan directions, respectively. It has been assumed that the IFOV aspect ratio is selected to approximately equalize the "effective resolution" in the two directions; for example, by making the overall MTFs equal to some preselected spatial frequency, $1/r$ (MTF = 0.20 at $1/r$ in the figures).

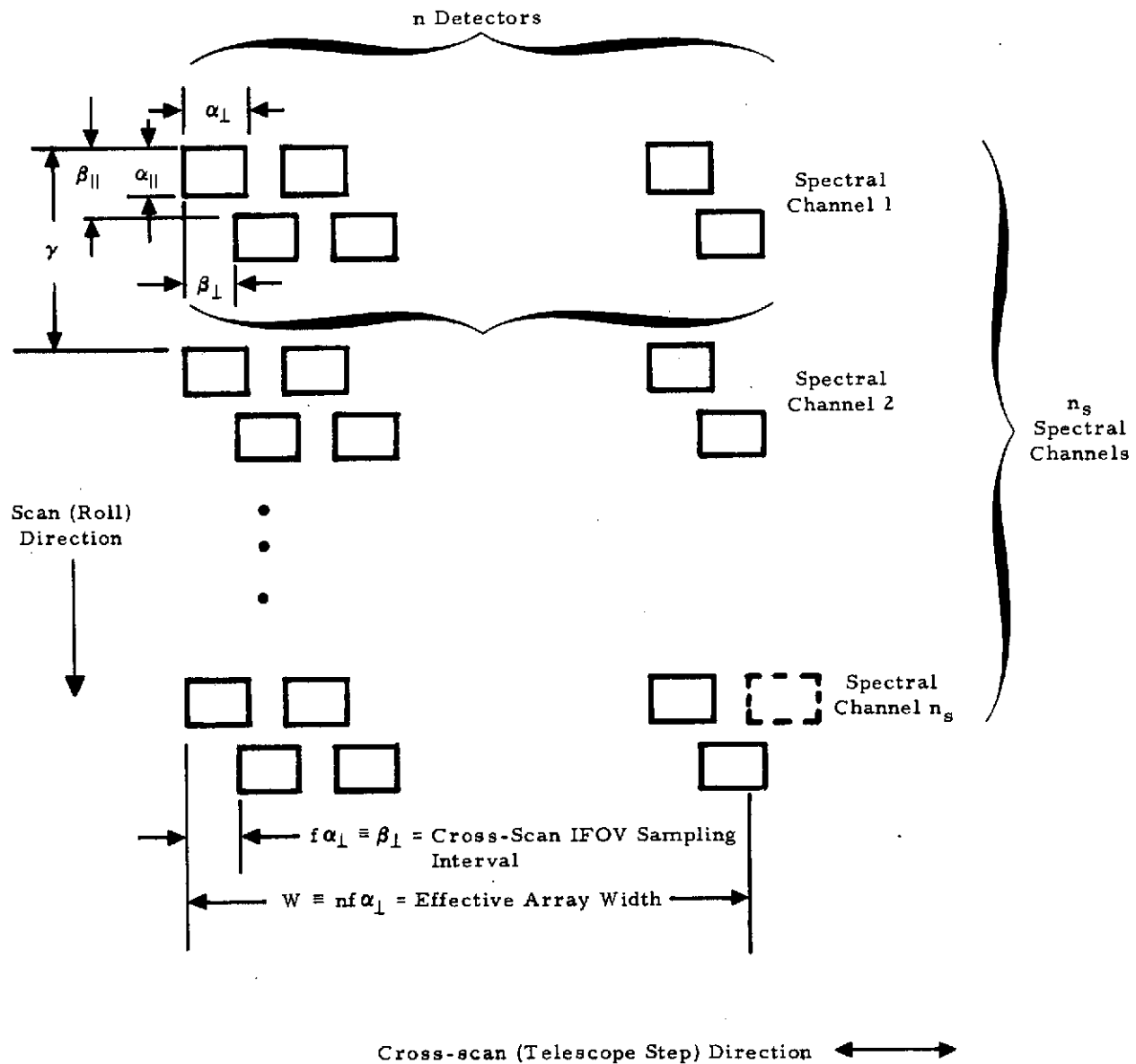


Figure 3-3. Field of View Geometry for Spin-Scan OPM Imager

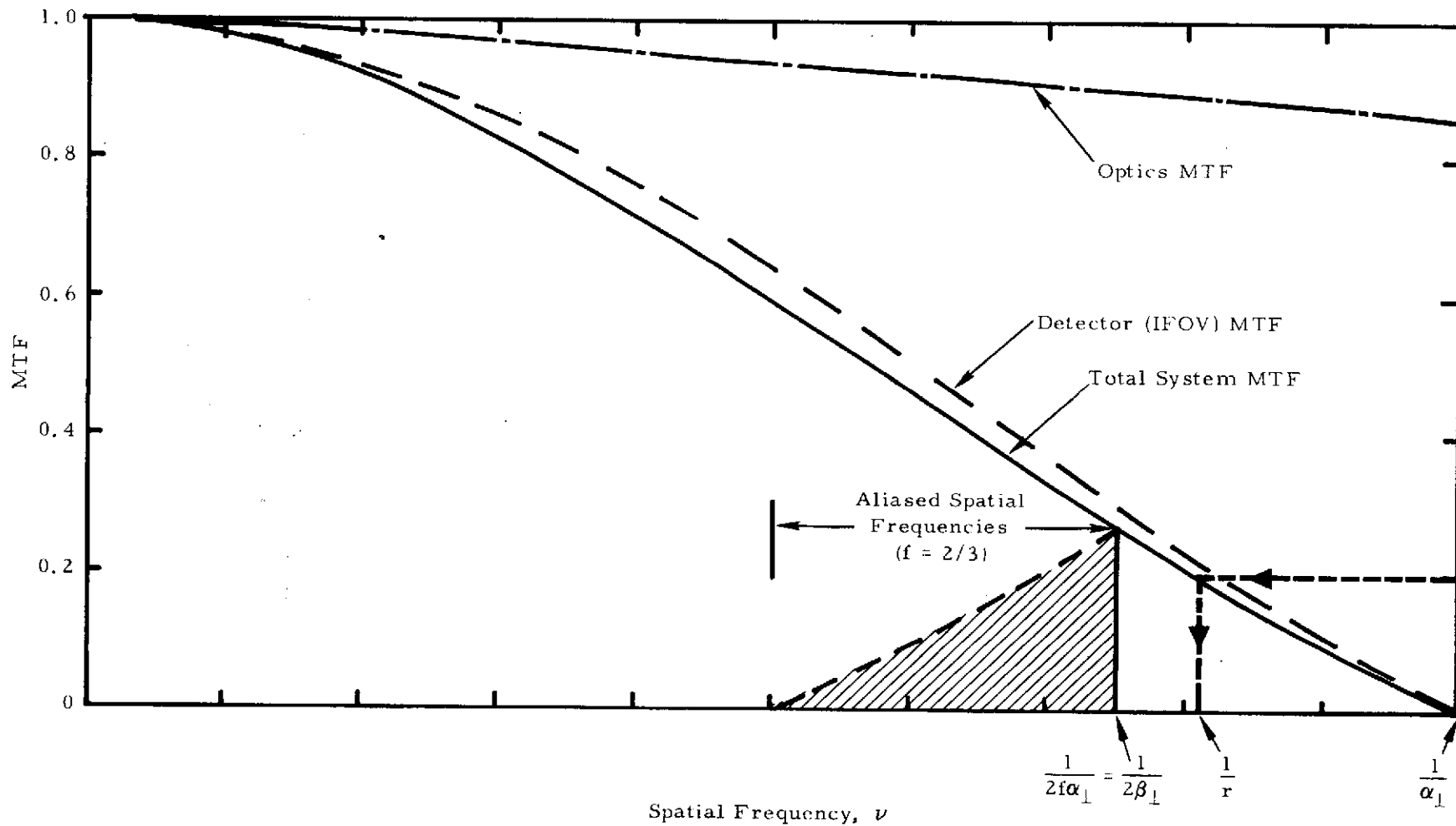


Figure 3-4. Illustration of Cross-Scan Aliasing

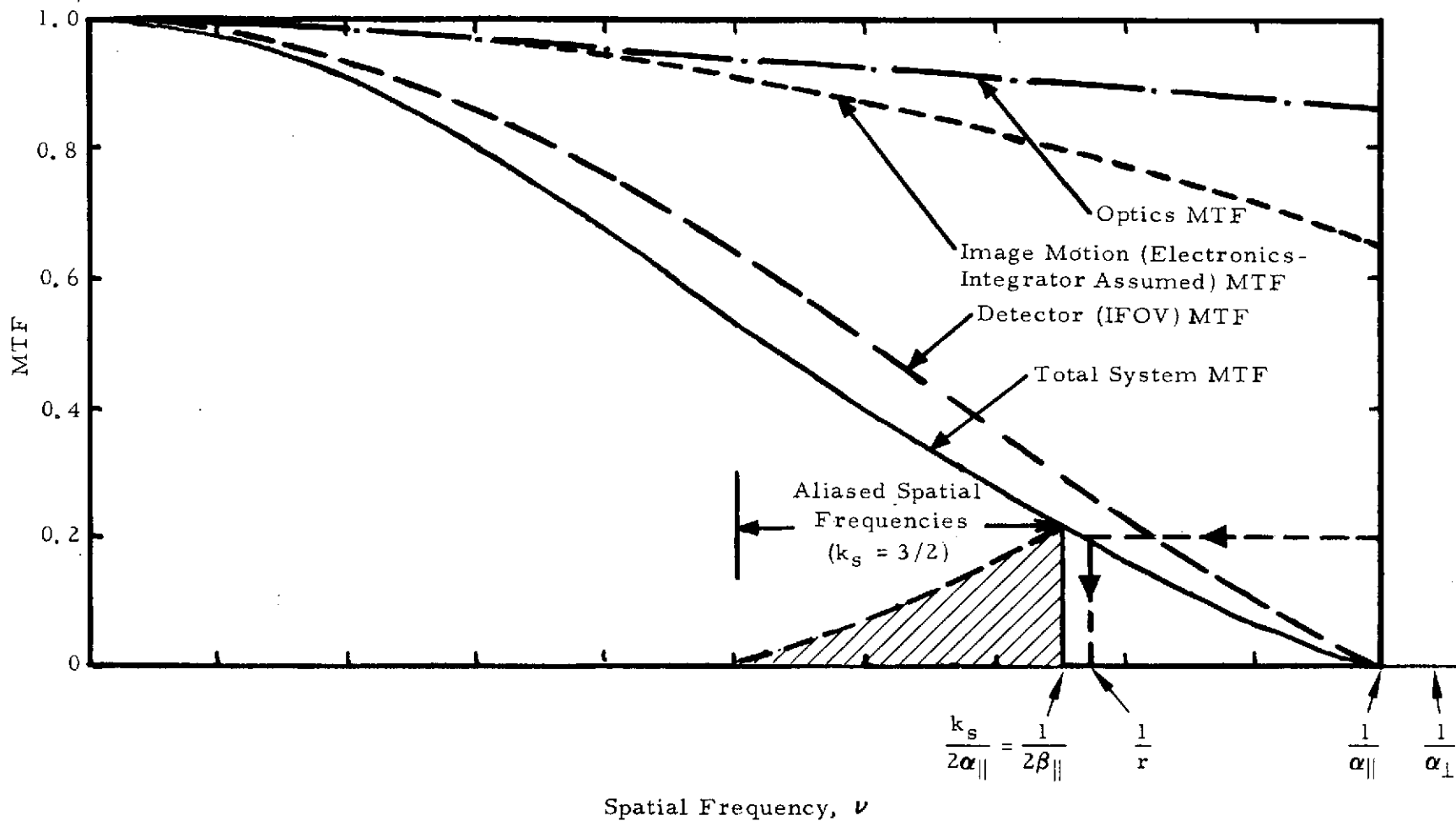


Figure 3-5. Illustration of Along-Scan Aliasing

The overall MTF in the cross-scan direction is the product of the optics and detector MTFs. The spatial frequency, $1/(2\beta_{\perp})$, corresponding to the cross-scan sampling interval, β_{\perp} , is indicated with a vertical line. If it is assumed that the system is bandlimited at $1/\alpha_{\perp}$, i.e., at the first zero of the MTF curve, then the highlighted area corresponds to "aliased" components that would be present in the video output for a scene with a constant power spectrum. (If the system cannot be considered to be bandlimited at $1/\alpha$, then additional alias components might be present due to the high frequency lobes.) In actual practice, the usual scene would not have a constant power spectrum. The power spectrum of a typical scene falls off approximately as the reciprocal of the spatial frequency. Thus, the observed aliasing when imaging a "typical" scene will be less than that indicated in the figure. It should be noted that the cross-scan overlap parameter, $f = \beta_{\perp}/\alpha_{\perp}$ has been chosen to illustrate rather than minimize a potential aliasing problem.

As can be seen from the figures, the MTF of the optics (MTF_o) has a relatively minor effect on the overall system MTF. For the purpose of most of the system modeling, the parametric effects of MTF_o on the overall system MTF can be ignored insofar as scaling about reasonable design points is concerned. The MTF in the cross-scan direction determined by the IFOV, and therefore by the detector shape (assumed rectangular), is denoted by MTF_d and given by

$$MTF_d = \sin(\pi\nu\alpha_{\perp})/(\pi\nu\alpha_{\perp}) \quad (3-6)$$

The angular dimension, α_{\perp} , of an individual detector is given by

$$\alpha_{\perp} = W_{d,\perp}/f \quad (3-7)$$

where $W_{d,\perp}$ is the cross-scan detector width and where f is the effective focal length of the telescope.

The overall MTF in the scan direction is the product of the optics, detector field-of-view and image-motion MTFs. The along-scan field-of-view or detector MTF is given by equation (3-6) with

$$\alpha_{\parallel} = W_{d,\parallel}/f \quad (3-8)$$

replacing α_{\perp} . The MTF resulting from the linear image motion is dependent on the low pass filtering introduced by the electronics. If the low pass filtering is in the form of an integrator, then the MTF is given by

$$MTF_{im} = \sin(\pi\nu\alpha_{\parallel}/k_s)/(\pi\nu\alpha_{\parallel}/k_s) \quad (3-9)$$

where k_s , is the ratio of the IFOV dwell time to the signal integration time. (The integration could be accomplished with the so-called photon-integration mode where the photoelectrons are effectively stored in the detector and periodically read out, or by integrating the preamplified detector outputs.) In the usual case, the sampling interval would be approximately α_{\parallel}/k_s ; hence, the along-scan recovered spatial frequency is $k_s/2\alpha_{\parallel}$. The value of k_s used in Figure 3-5 is chosen to accentuate the along-scan aliasing in a manner similar to that used for the cross-scan direction.

To prevent aliasing in the scan direction, it is necessary to choose a sample rate at a minimum of twice highest spatial frequency present. If the first zero of the sinc function defined by equation (3-6) (with α_{\parallel} replacing α_{\perp}), i. e., $\nu = 1/\alpha_{\parallel}$, can be considered to be the band limit, then two samples per dwell time, τ_d , would be required. If an integrator serves as the low-pass filter (or the photon-integration mode is used with the solid-state array detectors), an integration time satisfying

$$t_{integration} \lesssim \tau_d/2 \quad (3-10)$$

should be chosen to avoid aliasing. It is then reasonable to choose $t_{integration}$ equal to $\tau_d/2$ for an imager application. Noting that this

implies $k_s = 2$ in the photon-integration mode (when viewing normal to the spin axis), it will be assumed that $k_s = 2$ is appropriate for each of the OPM Imager variants considered insofar as bit-rate considerations are concerned. When the cone angle is other than 90° , then the effective number of samples per pixel, $k_{s, \text{eff}}$, is

$$k_{s, \text{eff}} = k_s / |\sin \theta| \quad (3-11)$$

where θ is the cone angle (referenced to the spin axis). It is because of this effective increase in the sampling rate when the imager views near the spin axis that a commandable or automatic low-sample-rate function is recommended (see subsection 7.2.5).

It is convenient to relate the effective noise bandpass, Δf_n , to the IFOV dwell time, τ_d , by

$$\Delta f_n = \frac{k_f}{\tau_d} = \frac{2\pi k_f \Omega}{\alpha} \quad (3-12)$$

where k_f is a constant dependent on the particular low-pass filtering used, Ω is the roll rate, and α is the IFOV. With an integrator providing the low-pass filtering,

$$\Delta f_n = (2 t_{\text{integration}})^{-1} \quad (3-13)$$

For the choice of $t_{\text{integration}}$ equal to $\tau_d/2$ as suggested above, k_f is equal to 1. To be able to compare various point designs on an equivalent basis if different low-pass filtering is used, k_f equal to 1 is used for all system modeling calculations.

While the detector IFOVs are shown in Figure 3-3 as being rectangular, other shapes may be more appropriate. This will be especially true if the sampling in either direction is insufficient, thereby producing aliasing. Katzberg, et al.³ have discussed the use of various IFOV shapes and their effect on reducing aliasing when the sampling is insufficient. This approach is of particular interest for limited telemetry rate situations (such as may occur for missions to

the outer planets). However, it must be recognized that the alternative of sufficient sampling (in both the scan and cross-scan directions) is preferable in terms of recovery of the high spatial frequencies of the scene with maximum SNRs. Since radiometric accuracy is a strong point of spin-scan imagers (versus frame cameras) and the high spatial frequency features of a scene are often of the most scientific interest, a trade-off which compromises either of these must be weighed carefully.

3.1.4 Underlap

It is necessary that the instrument be able to step sufficiently rapidly to prevent gaps between image segments generated on successive spacecraft rolls. This is required even at the closest range to the planet as this will generally be the only time the terminator will be visible at high resolution. Due to the wide range in the rate-of-change of the look angle encountered during a typical mission, it is essential that some selectability of the angular step size be incorporated into the design. The number of selectable step sizes desirable for given mission and instrument characteristics can be determined from a parametric analysis.

To prevent gaps between image segments generated on consecutive spacecraft rolls, the net scan rate over the target should be less than or equal to the width, W , of the image segments generated each roll divided by the roll period. The net scan rate is the rate of change of the look angle, ϕ , from the spin axis to a point on the target minus the instrument step rate,

$$\left| \frac{d\phi}{dt} \right| - A \frac{W}{P} \leq \frac{W}{P} \quad (3-14)$$

for no underlap, where up to A steps of the n detector array of total angular length, W , are made in a roll of period P .

Usually $A = 1$ and $W = fn\alpha$ where $0.5 < f < 1$, and where n is the number of detectors of IFOV, α , in each spectral channel compromising the images. For some trajectories, $|d\phi/dt|$ can become so large that gaps occur between image segments obtained on successive rolls unless $A > 1$ or $\frac{n\alpha}{P}$ is larger than otherwise required. Allowing $A > 1$ means stepping more than one detector array width of the instrument per roll and, in addition, it means that only small variations in $d\phi/dt$ can occur during an image if gaps between image segments are to be avoided (unless A is continually adjusted). For most applications, A can be limited to 3 or less and usually $A = 1$. Large $\frac{n\alpha}{P}$ can also eliminate gaps between image segments, but only at the price of a large number of detectors, lower angular resolution, or lower SNR. That is, the number of detectors (of the same angular size) could be increased, the size of the detectors could be increased (lower angular resolution), or the roll period P could be decreased (with a consequent decrease in the SNR). It should be noted that an arbitrary increase in the number of detectors is not desirable where imager weight is an important consideration. This follows since the weight increases in the electronics and in the detector assembly, to a greater or lesser extent depending on the detector type, may force system changes, e.g., a smaller telescope aperture, to stay within weight limits.

If the spacecraft spin axis is perpendicular to the plane of the trajectory around the planet, the look angle to a given point on the planet will not change at all from roll to roll and there will be no "underlap" problem. In the system modeling and point designs that follow, it is assumed (as for Pioneer 10 and 11) that the spacecraft spin axis will be earth pointing and within a few degrees of the plane of the trajectory. Under these circumstances, the requirement that no gaps exist between adjacent scans of the planet can impose definite instrument design constraints.

Considering only motions which influence spacing of surface scans, and assuming the spin axis to be in the plane of the trajectory, the rate of change of the look angle to a point on the surface of a planet will depend on the component of planet rotational velocity in the plane of the trajectory and on the true anomaly rate at the particular point in the trajectory. Since the desire for satellite encounters will argue for trajectories near the equatorial plane of the planet, this case has been considered in some detail.

For the somewhat idealized but illustrative conditions of the spacecraft spin axis and the trajectory both in the equatorial plane of the planet, the magnitude of the rate of change of the look angle, $d\phi/dt$, for viewing the surface element on the equator is given by

$$\left| \frac{d\phi}{dt} \right| = \left| \frac{R\dot{\theta} - \omega_p r_p}{R - r_p} \right| \quad (3-15)$$

where R is the range of the spacecraft from the center, r_p is the planetary radius, $\dot{\theta}$ is the true anomaly rate for the trajectory, and ω_p is the angular velocity of rotation of the planet (see Figure 3-6). Here it has been assumed that the spacecraft orbits the planet in the same sense as the planet rotates.

For two body central force problems, $\dot{\theta}$ is proportional to $1/R^2$ with the constant of proportionality for elliptical orbits being related to the semi-major axis, a , and the eccentricity, ϵ , of the ellipse along with the mass, M , and the gravitational constant, G , by

$$C_E = \sqrt{a(1-\epsilon^2) MG} \quad (3-16)$$

Thus for elliptical orbits,

$$\dot{\theta} = C_E / R^2 \quad (3-17)$$

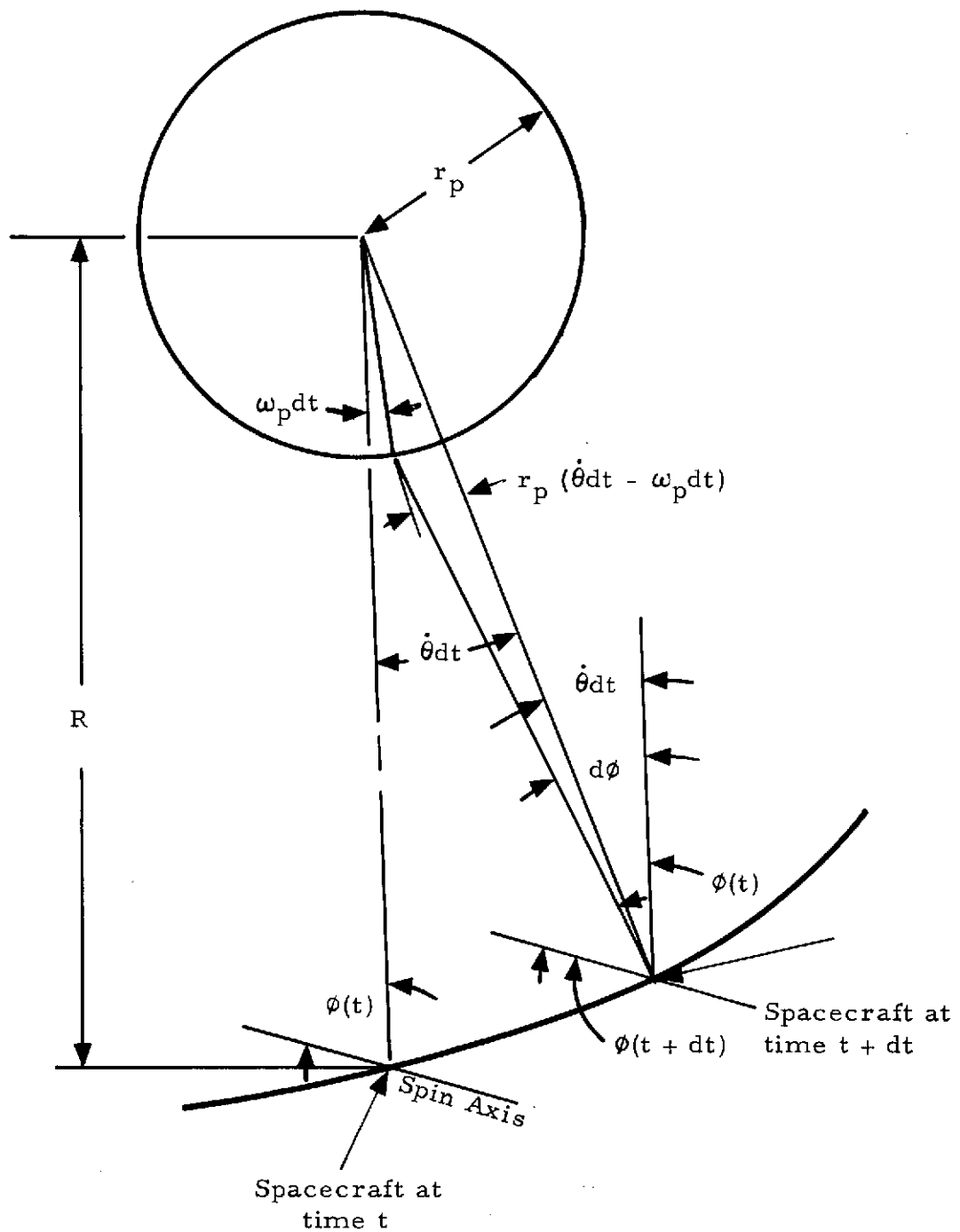


Figure 3-6. Geometry with Spacecraft Spin Axis and Trajectory Both in Equatorial Plane of Planet

For hyperbolic orbits, C_E of equation (3-17) is replaced by C_H where

$$C_H = \frac{\sqrt{\epsilon^2 - 1}}{\epsilon - 1} V_\infty R_{\min} \quad (3-18)$$

and R_{\min} is the minimum range to the center of planet for the trajectory.

The expression for the rate of change of look angle for either elliptical or hyperbolic orbits in the equatorial plane of a planet then becomes

$$\left| \frac{d\phi}{dt} \right| = \left| \frac{C - R \omega_p r_p}{R(R - r_p)} \right| \quad (3-19)$$

where $C = C_E$ or C_H for elliptical or hyperbolic orbits respectively.

Figures 3-7, 3-8, and 3-9 show $\left| \frac{d\phi}{dt} \right|$ versus height above the planetary surface ($R/r_p - 1$) for some typical equatorial Jupiter and Saturn trajectories and for a polar Uranus flyby. Note the existence of a range $R = C/\omega_p$ where the spacecraft true anomaly rate cancels the planetary rotation rate to make $d\phi/dt = 0$ (except for the polar flyby).

3.1.5 Scene Characteristics

The basic function of an imager is to recover the spatial variations of the scene so that the scene features can be accurately reproduced. The spatial power spectrum of a scene often varies with wavelength and for this reason multispectral imaging is often desirable. In the visible and near infrared portion of the spectrum, the scene radiance for the outer planets of interest in this study is determined by the incident solar irradiance and the scene reflectance. The spectral radiance, $N(\lambda)$, for a solar illuminated, Lambertian object can be calculated from

$$N(\lambda) = p(\lambda) H_\odot(\lambda) \cos \theta (\pi d^2)^{-1}$$

$$\approx \frac{p(\lambda) H_{\odot, \text{total}} N(\lambda)_{\text{bb}}(T=6000^\circ\text{K}) \cos \theta}{\pi d^2 N_{\text{total, bb}}(T=6000^\circ\text{K})} \quad (3-20)$$

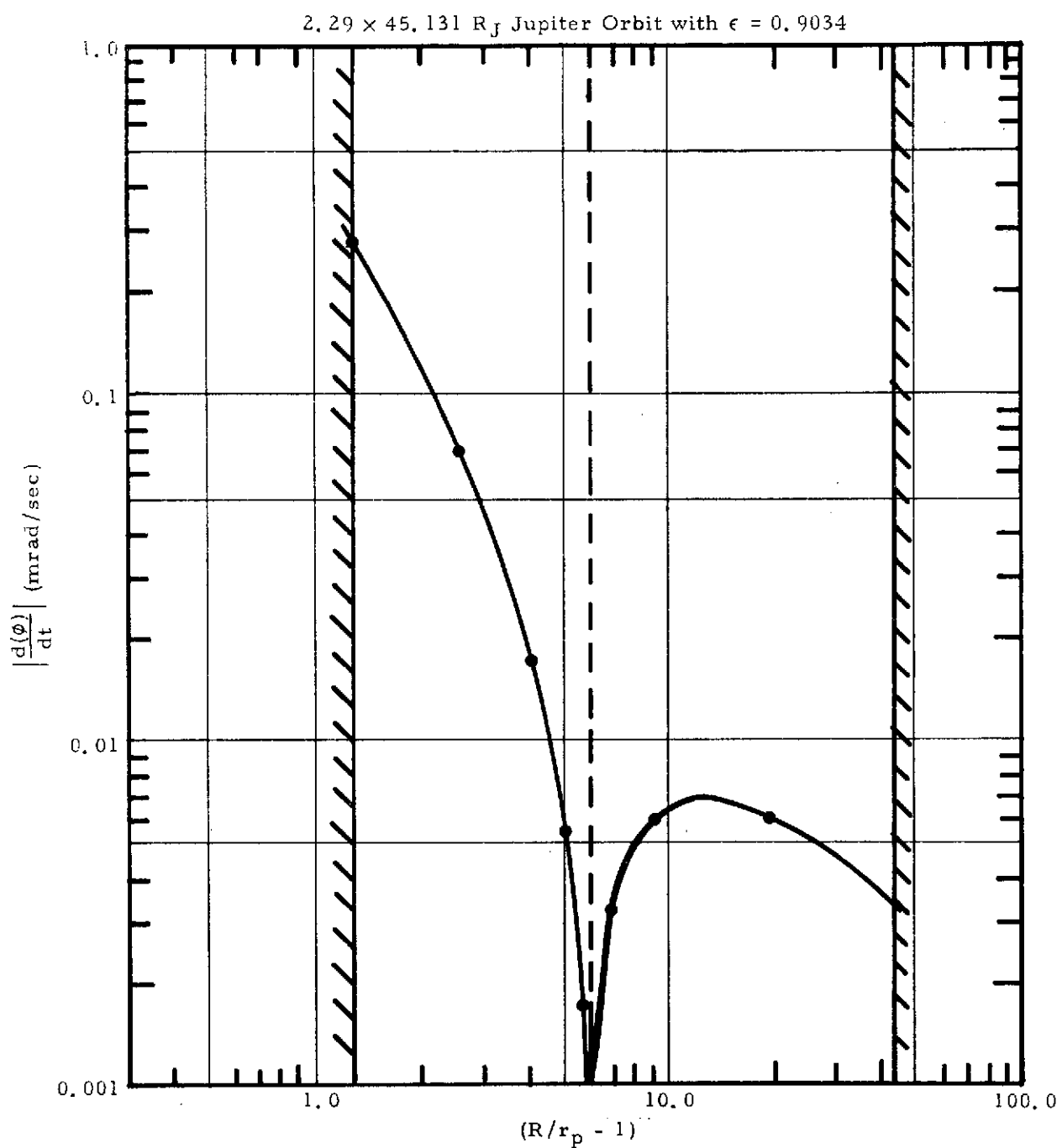


Figure 3-7. Rate of Change of Look Angle Versus Height Above Surface for Jupiter Orbit

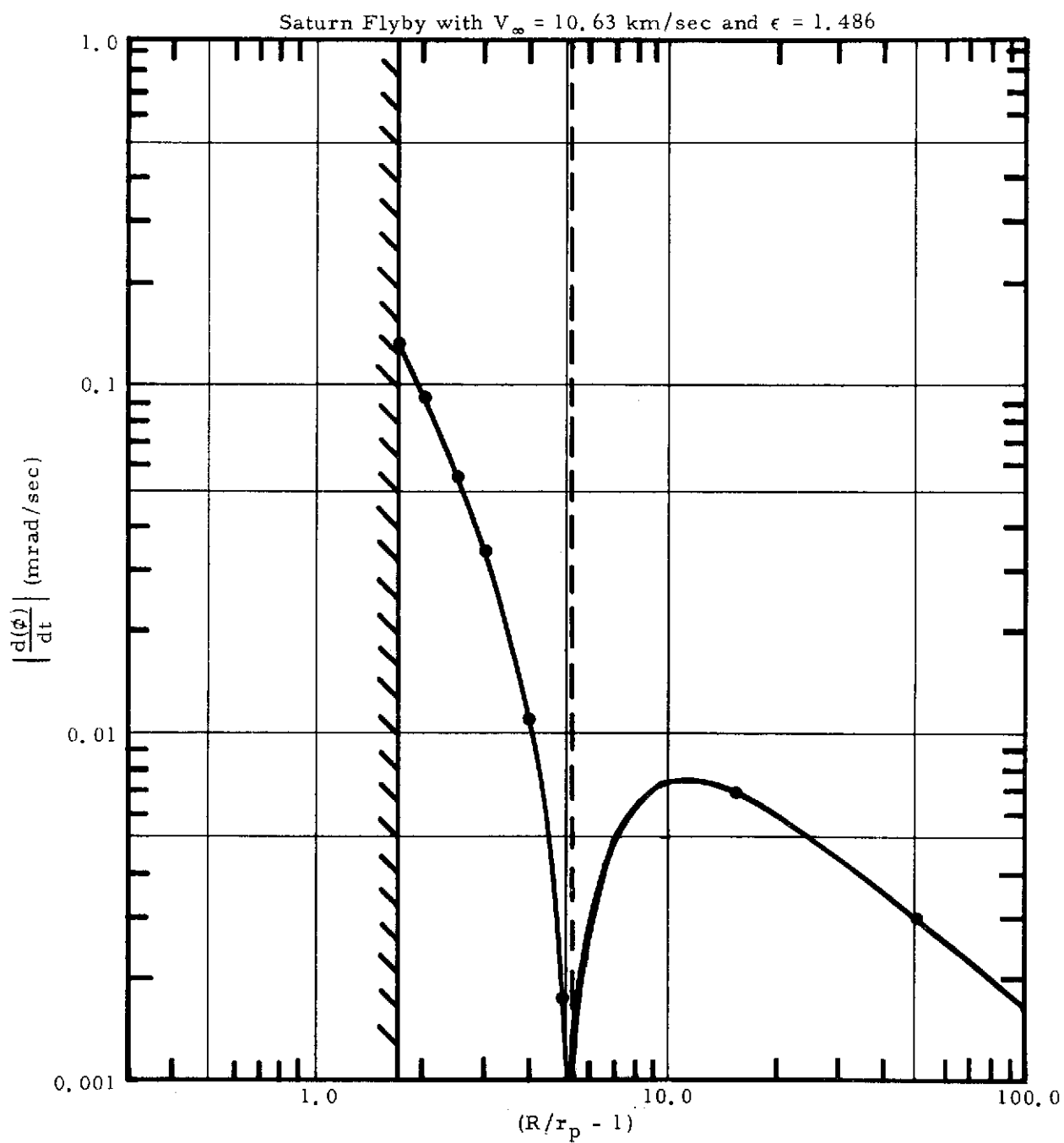


Figure 3-8. Rate of Change of Look Angle Versus Height Above Surface for Saturn Flyby

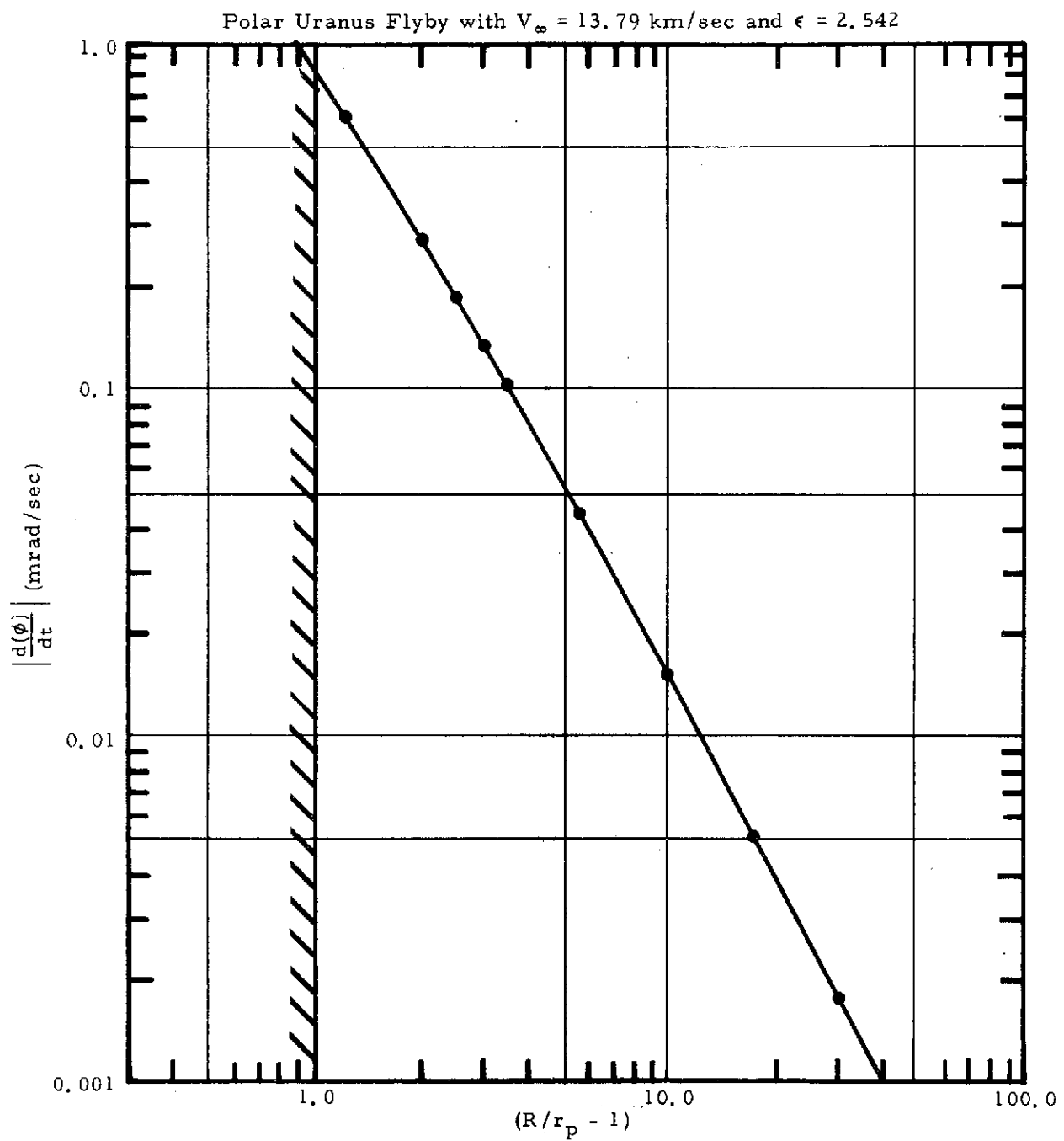


Figure 3-9. Rate of Change of Look Angle Versus Height Above Surface for Polar Uranus Flyby

where

$p(\lambda)$ = geometric albedo at wavelength, λ

$H_{\odot}(\lambda)$ = spectral irradiance of sun at earth
($\text{W cm}^{-2} \text{nm}^{-1}$)

d = sun-object distance (AU)

$H_{\odot, \text{total}}$ = integrated irradiance of sun at earth =
 0.14 W cm^{-2}

$N(\lambda)_{\text{bb}}(T=6000^{\circ}\text{K})$ = blackbody spectral radiance for $T = 6000^{\circ}\text{K}$

$N_{\text{total, bb}}(T=6000^{\circ}\text{K})$ = integrated blackbody spectral radiance for
 $T = 6000^{\circ}\text{K}$

θ = sun-zenith angle

The second line of equation (3-20) assumes that the spectral distribution of the solar flux approximates that of a 6000°K blackbody.

In Figure 3-10 measured values of the geometric albedo $p(\lambda)$ are given for four of the outer planets.⁴ Unfortunately, albedo data are not available for all the planets for the entire spectral range over which the OPM Imager point designs can operate. In such cases, the available albedo data have been extrapolated as indicated by the dashed lines in the figure. The spectral radiances calculated as indicated in the equation (3-10) form the basis for estimating the performance of various imager configurations.

3.1.6 Spectral Coverage

The comments with respect to SNR and resolution apply to broad-band images. If the achievable SNR values permit, one or two narrower spectral bands could be substituted for or added to the wide band. It is probable that the SNR and resolution requirements should take precedence over spectral coverage. However, this is an area where trade-offs should be dictated by the ultimate users. The effect of changes in spectral coverage of the sensors is included in the parametric modeling section.

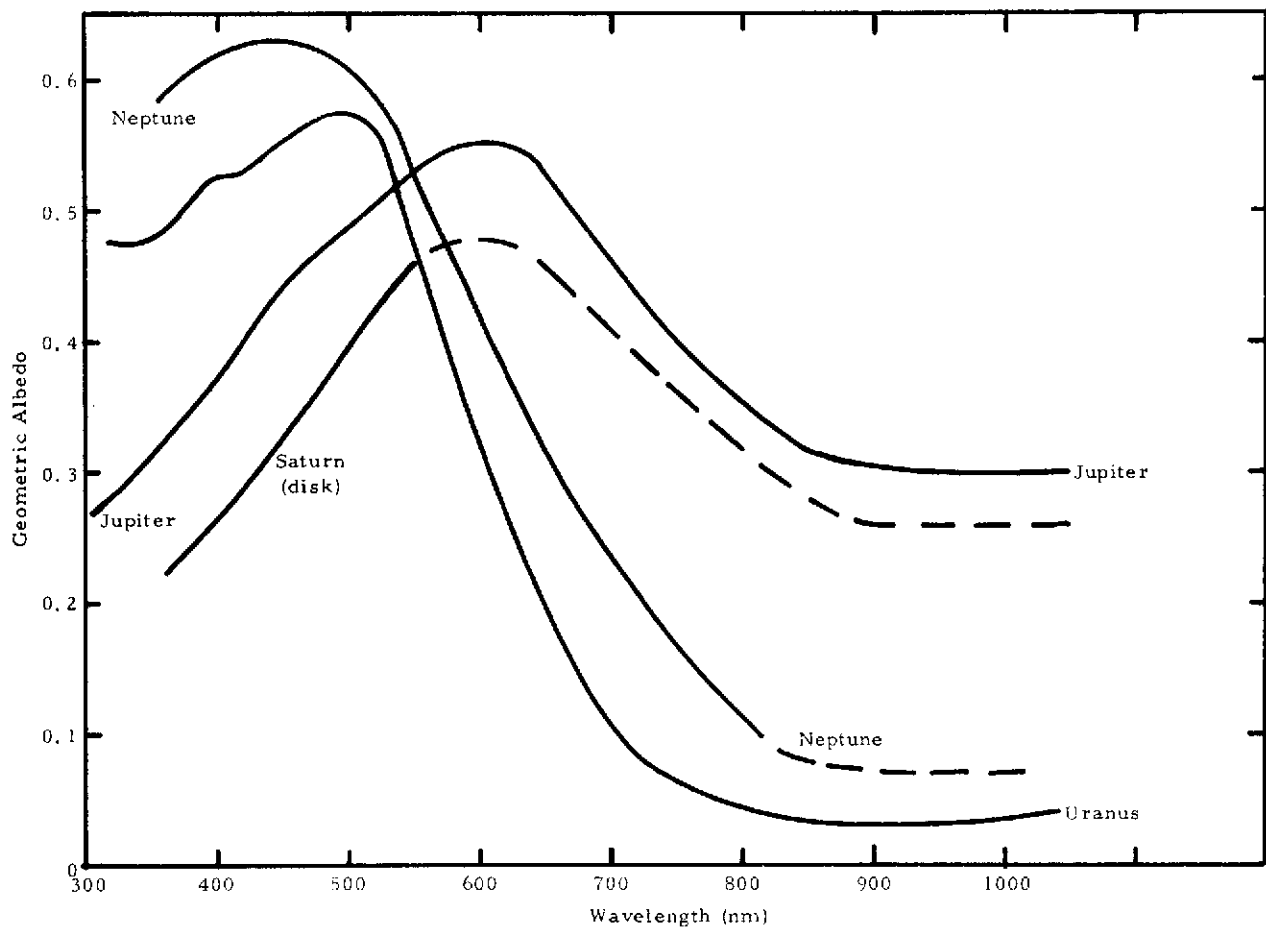


Figure 3-10. Geometric Albedos for Outer Planets

3.1.7 Spatial Coverage

Because of the open format of spin-scan images and the duration of the orbiter mission, spatial coverage is not considered a problem for that mission. For flybys, it is appropriate to require a fair fraction of the planet ($\approx 10\text{-}20\%$) to be covered at the highest resolution, with full disk images at a resolution perhaps 10 times lower.

3.1.8 Geometrical Accuracy

A geometrical accuracy of ~ 1 pixel in the location of the pixels on the final image is necessary for maximum scientific return. This requires extensive data handling, but does not present fundamental difficulties. For long-duration missions such as the Jupiter orbiter where vast quantities of data are obtained, the ability to rectify any image to 1-pixel accuracy would be required, but in practice a scheme that rectifies 1000×1000 pixel images to ≈ 50 -pixel accuracy might be used for the selection of a relatively small fraction of the data which would then be rectified to 1-pixel accuracy. Thus, the cost of rectification can be much less with this approach than if rectification of all images to 1-pixel accuracy were required.

3.1.9 Quantization Accuracy and Dynamic Range

The dynamic range of the instrument consists of the factor of 2^b gray levels for b bit per sample quantization plus some factor that can be provided by changes in the "gain" of the system. The imager SNR desired clearly affects the number of gray levels. If the value of b is too large, then a portion of the telemetry is "wasted," since the quantization interval is small compared to the system noise. If the value of b is chosen too small then quantization noise, which is proportional to the quantization interval, dominates and the system performance capability is impaired. If the OPM Imager is designed to provide a SNR ($\nu = 0$) ≈ 100 as suggested in subsection 3.1.2, it might seem that $b = 6$ or 7 would be adequate to encode the image data. However, if the gain is not quite matched to the scene or if the responsivity

across the detector array varies significantly, then such a choice could prove to be ill-advised. The choice of $b = 7$ or 8 thus seems more appropriate, and $b = 8$ is assumed for the point designs.

Once the number of gray levels is chosen, the total gain change factor can be derived from the range of illumination over which the instrument is to operate so that quantization noise does not dominate other sources of noise. For shot-noise-limited detectors imaging a planet which scatters like a Lambert surface, the SNR decreases as the solar-zenith angle, θ , of the viewed portion of the planet increases according to

$$\text{SNR}(\theta) = \frac{S_o \cos \theta}{\sqrt{N_Q^2 + S_o \cos \theta}} \quad (3-21)$$

where S_o is the signal received at the subsolar point and N_Q is the quantization noise. The quantization noise can be decreased by a factor F if the gain of the instrument boosts the signal by a factor F as the terminator is approached (θ is increased). That is, as the terminator is approached, F should be increased so that N_Q does not dominate in the total noise, N , given by

$$N = \sqrt{\frac{N_Q^2}{F^2} + S_o \cos \theta} \quad (3-22)$$

This will be the case if

$$F = \left(\frac{1}{\cos \theta} \right)^{1/2} \quad (3-23)$$

indicating how the largest solar-zenith angle at which observations are to be made, dictates the dynamic range of the instrument to be provided by "gain steps."

For the Jupiter imager point design, a pixel subtends about 10 km at closest approach, presumably enabling one to image to within 10 km of the geometrical terminator. This corresponds to the rather extreme

value of $\theta = 89.922$ and implies $F = 85$. This factor of 85 could be covered by 11 gain steps each of a factor of 1.5. The total required dynamic range of the instrument having 256 gray levels and $F = 85$ would formally be 2.2×10^4 . Note that if the SNR were 100 at zero spatial frequency at the subsolar point, it would be 1.2 at zero spatial frequency when imaging a point 10 km from the geometrical terminator of a Lambert sphere of Jupiter's radius. Even with no gain boosting capability at all, however, quantization noise alone would not reduce the SNR ($\nu = 0$) to 1/100 of the subsolar value until $\theta = 89.4^\circ$ (approximately 700 km from the Jovian terminator). Thus, while dynamic ranges of up to 10^4 might be useful if available, a dynamic range on the order of 1000 would probably be adequate for many applications.

3.2 SPACECRAFT IMPOSED CONSTRAINTS

The constraints discussed in this subsection are those imposed by the spacecraft. These are often the limiting constraints for imagers designed for planetary missions. For a spin-scan OPM Imager the telemetry rate, instrument weight, and roll rate range are of critical importance in the design and therefore are emphasized in this study.

The effective telemetry rate available for imaging is one of the most important constraints on the OPM Imager. A very fundamental consideration must be resolved where the telemetry rate is indeed limited. That is, is it more desirable in a given time interval, and with a given spatial resolution, to transmit data equivalent to a greater number of pixels of lower "quality" or fewer pixels of higher "quality"? The measure of quality referred to here is radiometric accuracy of the telemetered data; i. e., the number of gray levels and the accuracy with which the gray levels can be related to the scene radiance. If the answer to this question is that high radiometric accuracy is an important consideration, then the spin-scan imaging is a particularly attractive approach.

For this study the available telemetry rate at Jupiter was specified to lie between 2 and 83 kbps depending on the spacecraft equipment. Of course, for missions to the other outer planets the available telemetry rate decreases as the square of the communication distance.

Once such system characteristics as the number of gray levels, allowable aliasing, data compaction factor, total number of detector channels, and spacecraft roll rate are defined, the actual telemetry rate available determines the line or swath length. Similarly, since the spacecraft memory basically serves as a buffer store for data taken during each roll, i.e., provides "line stretching," the required memory capacity for the imaging function therefore is equal to the telemetry rate times the roll period. The desirable or required maximum read-in rate to the spacecraft memory can be accommodated through the multi-processor approach discussed in subsection 7.2.

The roll rate has been restricted to a range of 2 to 30 rpm for the purposes of this study. A related quantity is the spacecraft wobble angle which, if excessive, can lead to noncorrectable distortions in the imagery. A wobble angle that is on the order of 15% or less of the nominal IFOV of each detector is sufficiently small that the effect on the imaging can be ignored. An equivalent angular tolerance on the roll index pulse repeatability would also be required. Weight, power, and number of commands are all imager variables to be minimized. The study guidelines for the maximum allowable weight for the OPM Imager is 18 kg (40 lbs).

3.3 ADDITIONAL CONSTRAINTS

The high energy radiation environment to which an OPM Imager could expect to be exposed is one of the most important constraints on instrument design. For an outer planets mission involving a close passage by Jupiter, the Jovian trapped radiation belts would probably form the major hazard. If, as is probable, RTGs (radioisotope

thermoelectric generators) are used to provide spacecraft power for missions to the outer planets, they would constitute an additional radiation hazard. A discussion of available radiation effects data is included in subsection 5.1.5 (detectors), subsection 5.4.5 (optics), and subsection 5.5.1 (electronics).

Lifetime effects are important for multiyear missions to the outer planets. Tests designed to stress system components to simulate lifetime effects may be required in lieu of preflight opportunity to actually simulate mission life for reliability purposes. The launch vibrational environment and anticipated thermal environment places limits on detailed instrument design, although the ability to satisfy such requirements is well within the state of the art. Contamination prior to and during spaceflight is an ever present possibility and is a strong constraint on optical system testing and calibration. Only if instrument cleanliness is demanded during all phases of preflight and launch phase operations can radiometric calibration accuracy be maintained.

Section 4

DATA HANDLING AND RECONSTRUCTION

An analog signal is generated by each detector throughout the roll of the spacecraft. This is sampled and digitized during the scan sector containing the area to be imaged. Each sample is likewise recorded in a buffer storage unit, and, during the balance of the roll, these data are transmitted to Earth stations for recording. The received data are processed to recover the original image. This section discusses the data handling aboard the spacecraft; alternative methods of improving the telemetry capability through data compaction, and, finally, the image reconstruction procedure.

4.1 DATA HANDLING, STORAGE, AND TELEMETRY

The rate at which digital data are collected from each detector is given by

$$B_d = 2\pi b k_s \Omega / \alpha \text{ bps} \quad (4-1)$$

where b is the number of bits per sample, k_s is the number of samples per pixel along the scan, Ω is the spacecraft roll rate (revolutions per unit time), and α is the along-scan IFOV. The total rate into the buffer storage during the active scan period is, for n detectors in each of n_s spectral bands,

$$B_s = n n_s B_d \text{ bps} \quad (4-2)$$

The time required to scan L pixels is $\alpha L / 2\pi \Omega$. The buffer must therefore be sized to store a total of

$$C = L n n_s b k_s \text{ bits} \quad (4-3)$$

The average telemetry rate during the roll period required to transmit this amount of data is

$$B = C\Omega \quad (4-4)$$

which must be less than or equal to $B_{s/c}$, the spacecraft telemetry rate available for imagery data.

Normally the scan period is a negligible portion of each roll. This has been assumed in the above equations for the telemetry rate. For long scans, however, simultaneous storage and telemetry of the data would be feasible.

Equation (4-4) for the telemetry rate represents the effective rate remaining after housekeeping data for spacecraft condition, indexing for image reconstruction, and data from other non-imaging scientific instruments are accounted for. It is clear that, without long-term storage aboard the spacecraft, the total data return is fixed by the telemetry rate during encounter. Thus, it is of critical importance to enhance the telemetry rate or, as discussed in the next subsection, to lower the data load by compaction procedures.

4.2 DATA COMPACTION

Various data compaction techniques provide a means to increase the effective information transmission rate without a corresponding increase in the basic telemetry rate (bit rate for digitally encoded data). The use of such techniques is especially desirable for image data from space missions where high data rate requirements can adversely affect the mission payload because of the consequent power and weight increases in the telemetry system. For this reason, data compaction techniques which reduce redundancy in telemetered image data are particularly attractive for outer planets missions.

In Table 4-1 are summarized some possible data compaction techniques along with a brief description and summary of the relative advantages/disadvantages. It is assumed that N-bit quantization and hence 2^N gray levels are required. The first four data compaction methods have been discussed extensively in the literature. Additional combinations are also possible, e.g., adaptive differential pulse code modulation (DPCM) with or without tapered quantization. In addition, periodic updating (i.e., transmitting the undifferenced signal periodically with N-bit precision) is desirable in practice to reduce the effect of transmission errors on the decoded signals. Similarly, automatic updating is useful to improve fidelity by transmitting a full N-bit word following a sample that cannot be accurately encoded by the data compaction process.

In many situations the cosmetic quality of the reconstructed imagery is the major criterion for judging the suitability of a given data compaction method. In such instances, significant distortion of the original data usually can be tolerated. In addition, where cosmetic aspects are the main concern, the amount of aliasing that can be tolerated is also greater. In such a case, the achievable data compaction factor can be much higher than where high fidelity is required.

The data compaction factor, C_{DC} , for a given data compaction method can be defined as the ratio of the total number of bits required to transmit a given image without data compaction to that required with the use of data compaction. For the first four techniques listed in Table 4-1 (which are all forms of DPCM), the data compaction factor is independent of the redundancy in the image data. The fidelity of the reconstructed data is, of course, strongly dependent both on the redundancy of the data and on the data compaction method. For M-bit DPCM with basic N-bit words and periodic updates every Jth sample, the data compaction factor is given by

Table 4-1. Some Possible Data Compaction Techniques

NAME	DESCRIPTION	ADVANTAGES / DISADVANTAGES
DELTA MODULATION (ALSO CALLED 1-BIT DPCM)	BASICALLY THE DIFFERENCE BETWEEN THE $(i+1)$ -th SAMPLE AND i -th SAMPLE IS ENCODED WITH A TWO-LEVEL (1-BIT) QUANTIZER.	DATA COMPACTION FACTOR HIGH. WITH RAPIDLY VARYING SIGNALS, ENCODER MAY NOT BE ABLE TO KEEP UP WITH CHANGES LEADING TO SLOPE OVERLOAD NOISE. IN UNIFORM REGIONS, LIMIT CYCLING LEADS TO CHECKERBOARD PATTERN.*
ADAPTIVE DELTA MODULATION (VARIABLE SLOPE DMI)	STEP SIZE IS VARIED DEPENDENT ON PAST HISTORY OF INPUT.	DATA COMPACTION FACTOR HIGH. ENCODED SIGNAL AMPLITUDE PRECISION MAY BE POOR WHERE LARGE SLOPES ARE ENCOUNTERED AND ALSO PRECEDING AND FOLLOWING SUCH REGIONS.
DIFFERENTIAL PULSE CODE MODULATION (DPCM) WITH EQUALLY SPACED LEVELS	SIMILAR TO DELTA MODULATION EXCEPT 2^M EQUALLY SPACED LEVELS ARE ENCODED WITH AN M-BIT DPCM SYSTEM.	LOWER DATA COMPACTION FACTOR THAN DELTA MODULATION. LIMIT CYCLING CAN STILL OCCUR, BUT, BY CHOOSING ONE LEVEL AT ZERO DIFFERENCE, IT IS EQUIVALENT TO THAT WITHOUT DATA COMPACTION. SLOPE OVERLOAD ERROR IS REDUCED COMPARED TO DM AND IS DEPENDENT ON NUMBER OF ENCODER LEVELS AS WELL AS SCENE CHARACTERISTICS.
DPCM WITH TAPERED QUANTIZATION	SAME AS DPCM EXCEPT 2^M LEVELS HAVE VARIABLE SPACING (USUALLY SPACING IS CHOSEN TO INCREASE AS DIFFERENCE SIGNAL LEVEL INCREASES).	DATA COMPACTION FACTOR IS SAME AS DPCM WITHOUT TAPERED QUANTIZATION. LARGE AMPLITUDE CHANGES CAN BE FOLLOWED MORE FAITHFULLY AT EXPENSE OF SOMEWHAT POORER REPRODUCTION OF INTERMEDIATE AMPLITUDE CHANGES.
DPCM (2^M EQUALLY SPACED LEVELS) WITH RANGE EXPANSION	SAME AS DPCM EXCEPT WHEN MINIMUM OR MAXIMUM LEVEL IS REACHED OR EXCEEDED, AN ADDITIONAL N-M BITS ARE USED TO EXTEND QUANTIZATION RANGE.	DATA COMPACTION FACTOR SOMewhat REDUCED OVER STRAIGHT DPCM. EXACT REPRODUCTION (COMPARED TO N-BIT QUANTIZER) OVER RANGE OF $\pm [2^{(M-1)} + 2^{(N-M)} - 1]$ FROM PRECEDING SIGNAL LEVEL. WHERE THE DIFFERENCE SIGNAL EQUALLED OR EXCEEDED FULL RANGE, THE NEXT SIGNAL COULD BE ENCODED TO THE FULL RANGE OF THE N-BIT QUANTIZER.
DPCM (WITH EQUALLY SPACED LEVELS) WITH RANGE EXPANSION TO FULL QUANTIZATION	SAME AS ABOVE EXCEPT WHEN MINIMUM OR MAXIMUM LEVEL OF DPCM IS REACHED OR EXCEEDED, A FULL N-BIT WORD REPRESENTING EITHER THE DIFFERENCE OR ORIGINAL SIGNAL IS GENERATED.	THE DATA COMPACTION FACTOR IS SOMEWHAT REDUCED AND, UNDER UNUSUAL CIRCUMSTANCES, MAY EVEN BE LESS THAN 1.0. OUTPUT DATA RATE WILL EXCEED THAT FROM NORMAL N-BIT QUANTIZER OVER SHORT TIME INTERVALS. EXACT CORRESPONDENCE TO N-BIT QUANTIZER IS MAINTAINED, ALTHOUGH TELEMETRY ERRORS ARE OF GREATER CONSEQUENCE.

*THIS EFFECT IS MINIMIZED WHEN SYSTEM NOISE IS SUFFICIENTLY LARGE THAT THE GRANULARITY IS RANDOMIZED.

- NOTES: 1. ADDITIONAL SCHEMES ARE OF COURSE POSSIBLE, E.G., DPCM WITH TAPERED QUANTIZATION AND/OR ADAPTIVE ASPECTS, BUT THOSE DESCRIBED SERVE TO ILLUSTRATE THE GENERAL APPROACHES.
2. PERIODIC UPDATING, I.E., TRANSMITTING THE UNDIFFERENCED SIGNAL WITH N-BIT PRECISION, IS DESIRABLE IN ACTUAL PRACTICE TO REDUCE THE EXTENT OF TRANSMISSION ERRORS ON THE DECODED SIGNALS.

$$C_{DC} = \frac{N}{M + (N - M) \frac{1}{J}} \quad (4-5)$$

With M-bit DPCM, if provision is made for automatic updating, i.e., using the basic N-bit word length when the differential signal is at or beyond the limits of the DPCM range, then

$$C_{DC} = \frac{N}{M + (N - M) (\frac{1}{J} + \frac{1}{K})} \quad (4-6)$$

where, on the average of once every Kth sample, an additional full N-bit word is transmitted due to automatic updates. The M-bit words representing differential signals at or beyond the differential range provide an automatic "barker" code to indicate the N-bit character of the next data word. It is apparent that as $M \rightarrow N$ the data compaction factor will decrease, unless the resultant increase in K is enough to offset this decrease.

The next method given in Table 4-1 is designated as DPCM with range expansion. In contrast to M-bit DPCM with automatic updating, additional $N - M$ bits are used to extend the quantization range when the differential signal is at or beyond the nominal DPCM range limits. For equally spaced quantization levels the total range (number of levels), ΔS , that can be accurately encoded for M-bit DPCM is

$$\Delta S = 2^M \quad (4-7)$$

For M-bit DPCM with range expansion, this range is increased to

$$\Delta S = 2^M + 2^{(N - M + 1)} - 2 \quad (4-8)$$

Thus, two adjacent signals with a contrast (maximum signal/minimum signal) can be accurately encoded if the contrast is equal to or less than $S/(S - \Delta S/2)$ where S is the larger of the two adjacent signals and where a symmetrical differential range about the previous sample is

assumed. With the latter method, if $N = 8$ and $M = 3$ with S equal to half scale, then a contrast of about 1.4 or less between adjacent samples could be accurately encoded.

The data compaction factor applicable to DPCM with range expansion when both periodic and automatic updates are used is given by

$$C_{DC} = \frac{N}{M + (N - M) \left(\frac{1}{J} + \frac{1}{K'} + \frac{1}{K''} \right)} \quad (4-9)$$

The above equation applies where a periodic update occurs every J th sample, a range expansion (to a total of N bits) occurs on the average of once every K' samples, and an automatic update (differential signal at or beyond the limits of the expanded DPCM range) occurs on the average of once every K'' samples.

The final method shown in the table has range expansion to full quantization. That is, a full N -bit word is generated when the differential signal is at or beyond the nominal DPCM range limits. The data compaction factor in this case is given by

$$C_{DC} = \frac{N}{M \left(1 + \frac{1}{K} \right) + (N - M) \left(\frac{1}{J} + \frac{1}{K} \right)} \quad (4-10)$$

where the range expansion occurs on the average of once every K samples. This method exactly reproduces the PCM data where the telemetry error rate is zero. The data compaction factor for this method is lower than that for DPCM with range expansion unless

$$(N - M) \left(\frac{1}{K'} + \frac{1}{K''} \right) > (N - M) \frac{1}{K} + \frac{M}{K} \quad (4-11)$$

which usually would not be the case. Indeed, the data compaction factor could be less than 1.0 under unusual circumstances where most of the differential signals exceed the nominal DPCM range. This method does not seem attractive for the OPM Imager application, however, since the maximum instantaneous data rate is significantly higher by a factor of $(N + M)/N$ than that for any of the other methods shown.

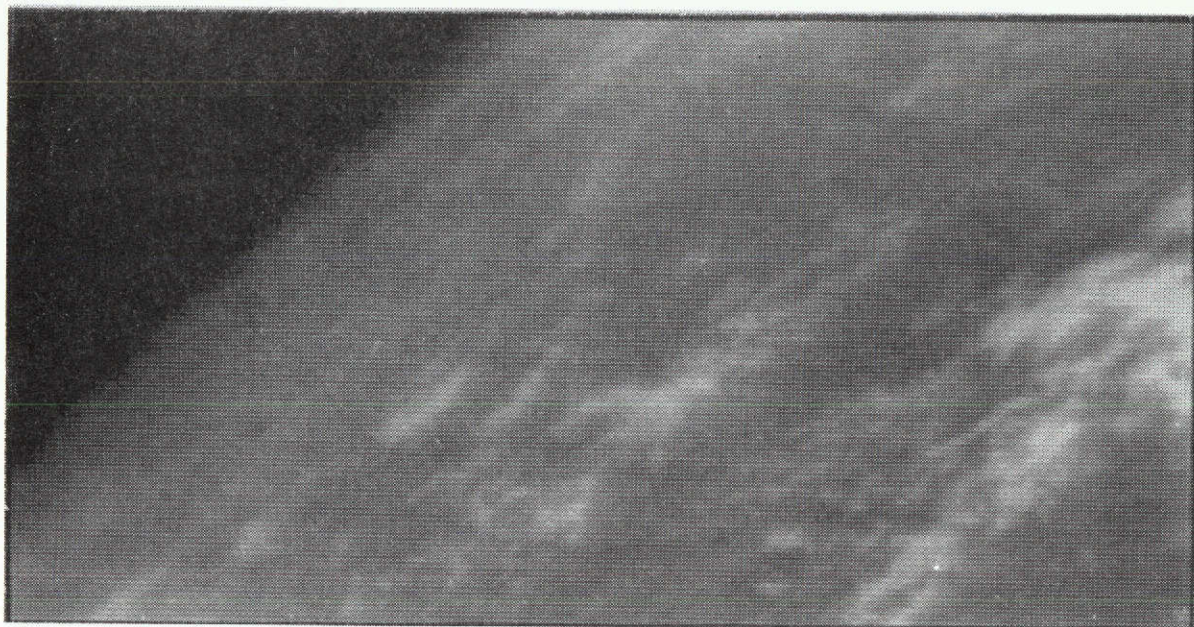
In Table 4-2 is given a comparison of the results for two data compaction methods applied to image data obtained with the ATS-1 Spin-Scan Cloud Camera. Three separate scene areas were selected for evaluation. Scene area 1 is representative of the limb region with a small amount of cloud cover. Scene area 2 was selected as having significant high frequency modulation produced by a "patchy" cloud cover. Scene area 3 is representative of a fairly cloudy region (about 80% cloud coverage) and hence a fairly high albedo.

Scene area 1 image reconstructions from the original PCM data ($N = 6$) and from the output of a computer-modeled DPCM data compaction with $N = 6$, $J = 50$, and $M = 2$ is shown in Figure 4-1. The DPCM image shown has the "worst" fidelity but the highest data compaction factor of the four data compaction methods applied to scene area 1. However, the percentage of samples in error is only 2%, and the difference between the images is negligible from a cosmetic viewpoint.

Figure 4-2 shows similar reconstructions for scene area 2. In this case, 13% of the samples with the $M = 2$ DPCM are in error, and it is relatively easy to note differences between the reconstructions with and without data compaction. In spite of such differences, the overall cosmetic appearance is very similar. It is interesting to note that $C_{DC} = 1.77$ with 13% of samples in error for the $M = 2$ DPCM, and $C_{DC} = 1.83$ with 2% of the samples in error for the $M = 3$ DPCM case. This higher error rate results since for scene area 2 DPCM with $M = 2$ is not adequate to keep the error rate down sufficiently, and thus many more automatic updates are required than for the $M = 3$ case. These additional required updates more than compensate for the nominal difference in data compaction factor between the $M = 2$ and $M = 3$ cases.

Table 4-2. Comparison of Results for Two Data Compaction Methods with ATS-1 Spin-Scan Cloud Camera Imagery as Input

	DATA COMPACTION METHOD	N	M	FRACTION OF SAMPLES WITH ERROR	DATA COMPACTION FACTOR C_{DC}
SCENE AREA 1 - LIMB REGION WITH SMALL AMOUNT OF CLOUD COVER	DPCM WITH AUTO-MATIC AND PERIODIC UPDATES	6	2	1.8×10^{-2}	2.15
	DPCM WITH RANGE EXPANSION AND WITH AUTOMATIC AND PERIODIC UPDATES	6	3	1.5×10^{-4}	1.95
	DPCM WITH RANGE EXPANSION AND WITH AUTOMATIC AND PERIODIC UPDATES	6	2	0	2.03
	DPCM WITH RANGE EXPANSION AND WITH AUTOMATIC AND PERIODIC UPDATES	6	3	0	1.95
SCENE AREA 2 - "PATCHY" CLOUD COVER WITH ABOUT 50% CLOUDS	DPCM WITH AUTO-MATIC AND PERIODIC UPDATES	6	2	0.13	1.77
	DPCM WITH RANGE EXPANSION AND WITH AUTOMATIC AND PERIODIC UPDATES	6	3	0.02	1.83
	DPCM WITH RANGE EXPANSION AND WITH AUTOMATIC AND PERIODIC UPDATES	6	2	0	1.44
	DPCM WITH RANGE EXPANSION AND WITH AUTOMATIC AND PERIODIC UPDATES	6	3	0	1.81
SCENE AREA 3 - "DENSE" CLOUD COVER WITH ABOUT 80% CLOUDS	DPCM WITH AUTO-MATIC AND PERIODIC UPDATES	6	2	0.050	1.95
	DPCM WITH RANGE EXPANSION AND WITH AUTOMATIC AND PERIODIC UPDATES	6	3	0.001	1.93
	DPCM WITH RANGE EXPANSION AND WITH AUTOMATIC AND PERIODIC UPDATES	6	2	0	1.71
	DPCM WITH RANGE EXPANSION AND WITH AUTOMATIC AND PERIODIC UPDATES	6	3	0	1.93
NOTES: 1) N = FULL RANGE ENCODED (PCM BITS PER SAMPLE) AND M = DIFFERENTIAL RANGE ENCODED (BITS) 2) AN UPDATE INTERVAL EVERY 50 SAMPLES USED IN EACH CASE					



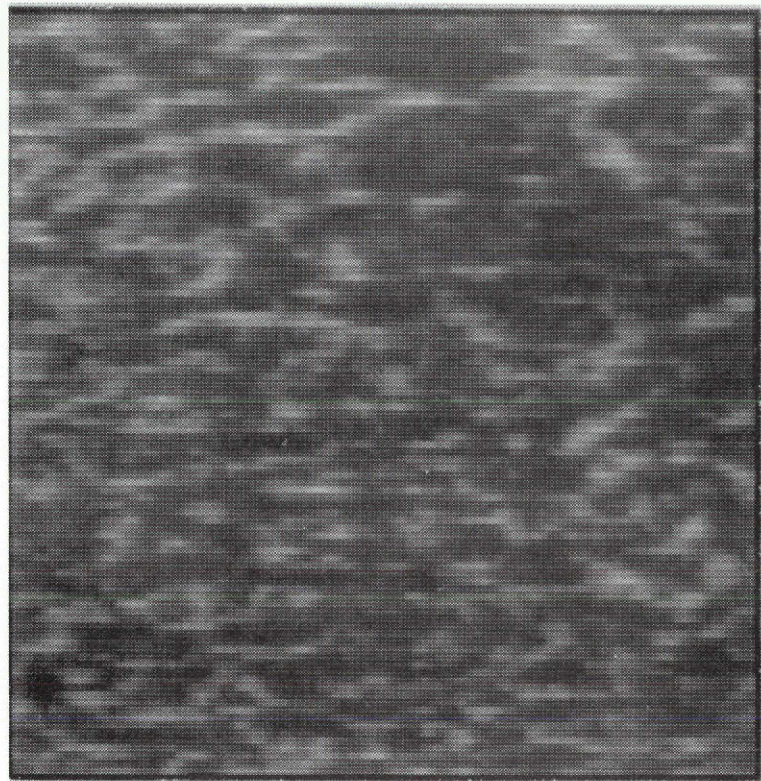
Area 1 - Original



Area 1 - N = 6, J = 50, M = 2

Figure 4-1. Reconstructed ATS-1 Imagery for Scene Area 1
with and without Data Compaction

Area 2 - Original



Area 2 -
 $N = 6, J = 50, M = 2$

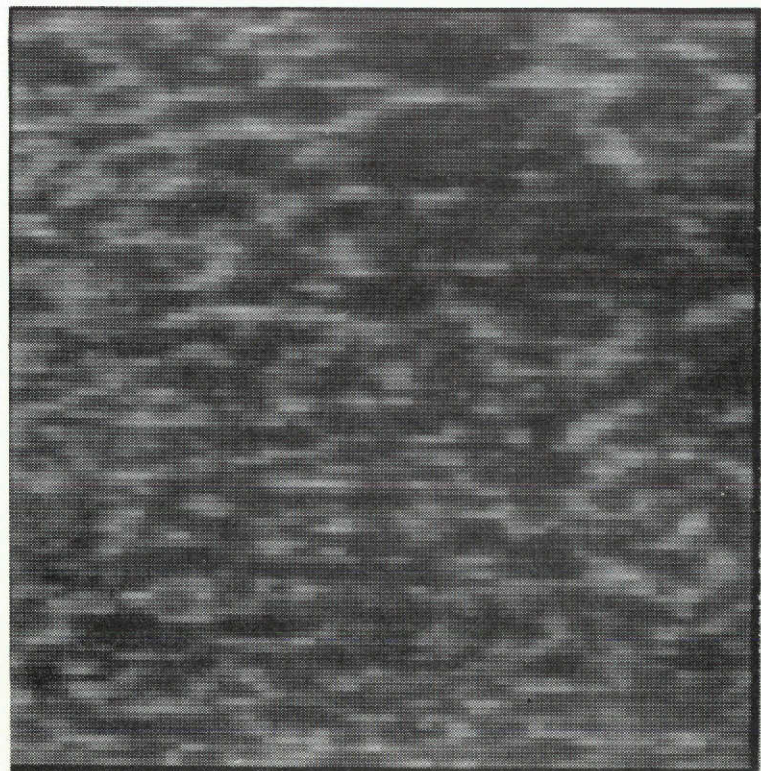


Figure 4-2. Reconstructed ATS-1 Imagery for Scene 2
with and without Data Compaction

As is apparent from Table 4-2, scene area 3 is intermediate between scene areas 1 and 2 both in regards to error characteristics and achieved data compaction factor. The difference between reconstructed images with and without data compaction is negligible for scene area 3 from a cosmetic viewpoint. For these reasons, scene area 3 reproductions have not been included.

The choice of $M = 3$ for DPCM with both automatic and periodic updates should yield satisfactory performance. This choice is assumed for the OPM Imager point designs, and is a compromise as has been demonstrated. The DPCM with range expansion would provide better fidelity, although it is significantly more difficult to mechanize. For the anticipated scene characteristics, an encoding system with $N = 8$ (see subsection 3.1.9), $M = 3$, and $J = 32$ or 64 should provide reasonably high fidelity and a data compaction factor equal to approximately two.

Other data compaction techniques are obviously possible, and some such choices have not been discussed here at all. However, it was felt that the recommended choice should be relatively simple and conservative so as not to significantly reduce system reliability. Beyond straightforward data compaction in the along-scan direction, utilization of the cross-scan redundancy and the probable correlation between different spectral bands might permit further increases in the data compaction factor. However, such potential gains are probably not worth the added complexity and probable impact on system reliability for precursor-type missions.

4.3 IMAGE RECONSTRUCTION

The instrument is presumed to be sweeping out many lines of image data, possibly in more than one spectral channel, on the small portion of each spacecraft revolution when it is pointing toward the target. The measured intensities are buffered to the spacecraft memory, and the rest of the spacecraft revolution is used to transmit all the intensities obtained on the roll, along with housekeeping data. The lines of image data generated during the roll can be multiplexed in any fashion before transmission and stored on the ground into separate arrays for each spectral channel. Each array would contain image intensities arranged according to the spacecraft roll on which the data were obtained and according to the roll sector within the roll. For a given spectral channel, data obtained by different detectors on the same roll would be ordered according to detector number. At the end of this sorting process, the image segments generated each spacecraft revolution would be stored next to each other in the order in which they were obtained, and one such array would exist for each spectral channel.

At this point, the housekeeping data are used to solve for the location of each data pixel in the final displayed image. This depends on the projection chosen for the final display as described in subsection 4.3.1. While the geometry problem must be solved many times for some distribution of points in the picture, it is straightforward and is described below. Subsection 4.3.2 describes the assignment of the intensity data to the image display array. For all but the images obtained at the closest range, the regularities in the scan geometry can be used to speed the assignment. Example data are presented for the frequently occurring case where scan lines map to straight parallel lines in the final image. For the images obtained at very close range, a more general form of image-point assignment is required, which is also outlined. Programs which accomplish this assignment at

reasonable cost for the general case are currently in the final stages of checkout at the University of Arizona for use with the IPP instrument aboard Pioneers 10 and 11.

After the picture display array has been filled in with intensity values, a tape containing the rectified image can be displayed on a film scanner to produce a hard-copy photograph.

The procedure for a Jupiter orbiter mission would probably be to simply sort and immediately display the geometrically unrectified images first. The distortion present in most (perhaps 2/3) of the images would be negligible for most purposes. The images obtained at slightly closer range (all the remaining images except for perhaps the last 20) could be rectified using the simple picture-point-assignment program described in subsection 4.3.2. The last few images would be rectified using more general programs similar to those used for the IPP before display; these are also outlined in subsection 4.3.2.

4.3.1 Geometry of Spin-Scan Imaging

The geometric condition under which the data are collected determines where the data pixels should be placed in the image display array. Figure 4-3 illustrates the motion of a spacecraft during a hypothetical image. The image extends from t_{start} to t_{end} . During the time in which the image is made, the instantaneous appearance of the planet changes; it changes its apparent angular diameter and direction in inertial space, and it rotates about its axis. The simplest method of data display assigns a column of image display pixels to each roll of data for each detector. Because of the varying geometry, such a display may have little resemblance to the actual appearance of the object at any time during the image. For example, Figure 4-4 shows such a display of a rotating and translating globe obtained by the Jupiter Pioneer Imaging Photopolarimeter (IPP) during laboratory tests.

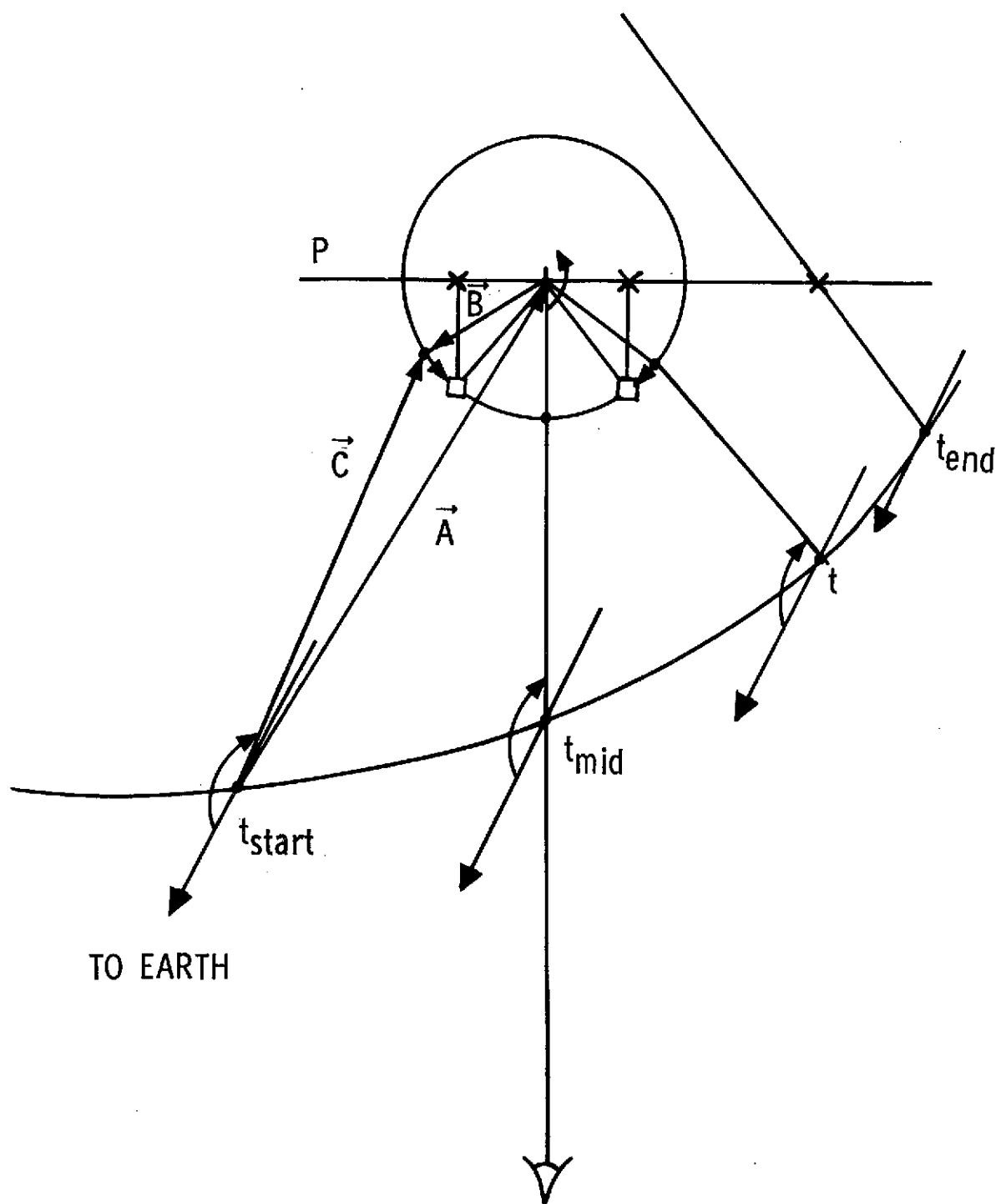


Figure 4-3. Motion of Spacecraft during Hypothetical Image

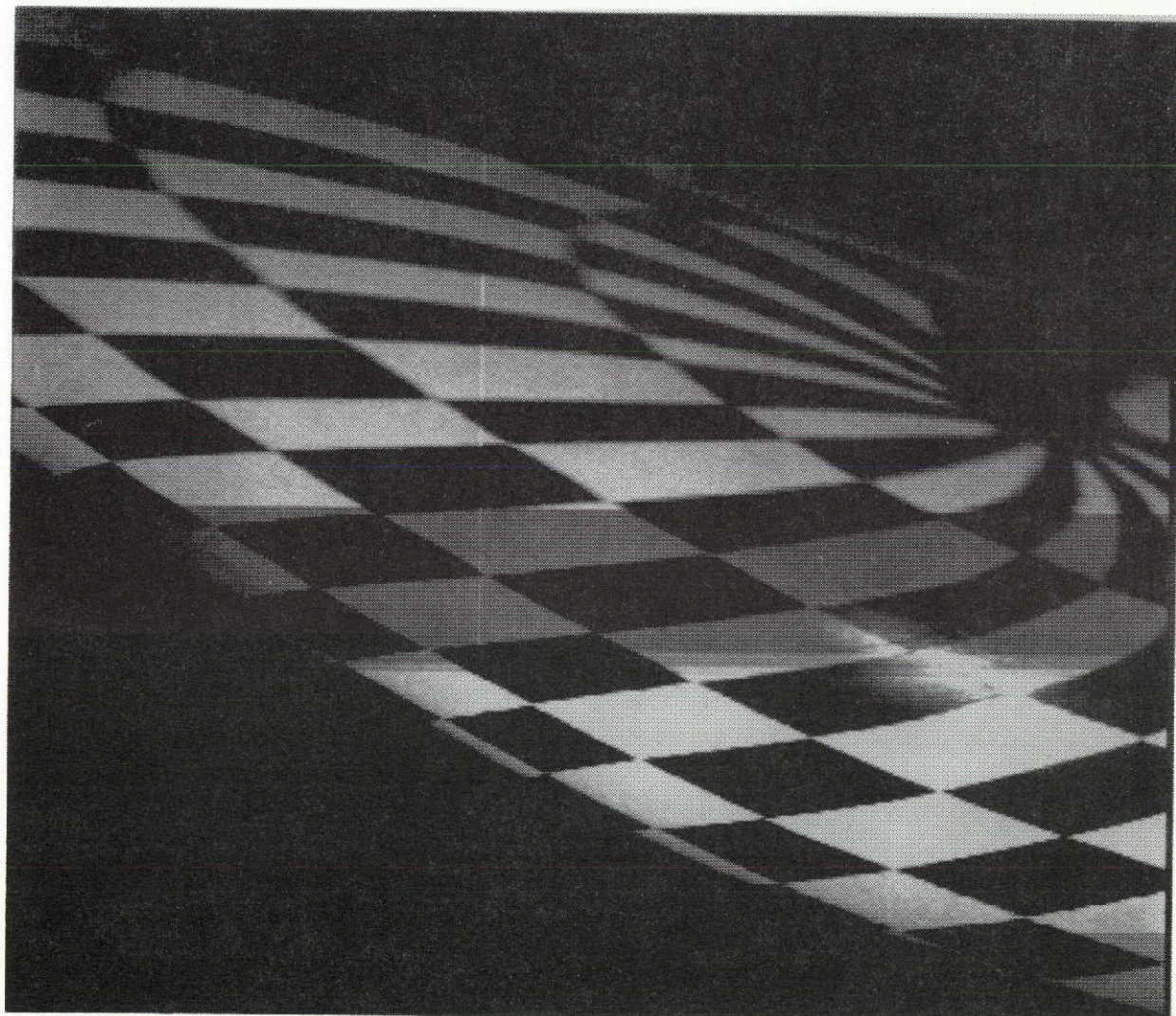


Figure 4-4. Unrectified Spin-Scan Images of Rotating and Translating Globe

It is desirable to display the data in a more familiar format. Figure 4-3 shows a projection scheme for displaying the spin-scan imaging data to resemble a snapshot taken from long range at the mid-time of the image. \underline{P} is a plane perpendicular to the spacecraft trajectory and to the spacecraft-planet line at the midtime of the image. The line-of-sight of the telescope is traced from the spacecraft until it strikes either the planet or the plane, \underline{P} . If the line-of-sight first strikes the plane, \underline{P} , the coordinates (X, Y), of the intersection in the plane, \underline{P} , are computed. If the line-of-sight first strikes the planet, a perpendicular is dropped from the point of intersection onto the plane, \underline{P} . The coordinates, (X, Y), in the plane, \underline{P} , are again computed. The (X, Y) coordinates indicate the position at which each data point is to be displayed in the final image.

Other types of projections are also possible. For a Mercator projection, the points of intersection of the line-of-sight with the planet would be expressed in terms of planetocentric latitude and longitude. The display coordinates would be:

$$\begin{aligned} X &= \text{Longitude} \\ Y &= \sin(\text{Latitude}) \end{aligned}$$

All such projections have the limitation that all of the rolls of data were not obtained simultaneously. It is necessary to select a standard time for projection and to attempt to reproduce the appearance of the object at that time. For example, as explained below, the rotation of an object during the image can be removed by displaying each data pixel not at its observed position, but at its position at the standard time.

Images during which the viewing geometry changes considerably cannot be well-restored to a snapshot-type projection. For example, consider two features on the planet at equal distance from the terminator when the first one is scanned at time t_1 . By the time the second feature is scanned at time t_2 , it may have rotated into the dark side of

the planet. If so, the terminator of such a rectified picture would appear distorted. Both the relative position and lighting conditions over the planet's surface cannot be salvaged in a display projection.

Solution for Location of Data Pixels in Display Array

Figure 4-5 shows the steps which must be taken in determining where in the image display plane the data pixels are to be displayed. The first objective is the determination of the intersection of the instrument line-of-sight and the surface of the object. It is necessary to have a priori knowledge of the size, shape, rotation axis, and rotation rate of the planet as well as accurate spacecraft trajectory and instrument pointing direction (look and roll angle) data for this purpose. The planet is assumed to be a spheroid of oblateness, ϵ , and

$$\epsilon = 1 - \frac{R_p}{R_e} \quad (4-12)$$

where

R_p = Polar radius

R_e = Equatorial radius

Define a cartesian coordinate system centered at the center of the planet in which \hat{e}_x , \hat{e}_y , and \hat{e}_z are unit vectors pointing in the following direction:

\hat{e}_z points toward the north pole,

\hat{e}_x lies in the equatorial plane and points as closely as possible to the direction of the vernal equinox of the planet, and

\hat{e}_y forms a right-handed system with X and Z.

Let $B_x \hat{e}_x + B_y \hat{e}_y + B_z \hat{e}_z$ be a vector from the center to the surface of the planet at the point where the surface is intersected by the line-of-sight of the instrument. Since the end of the vector lies on the surface of the planet, it follows that

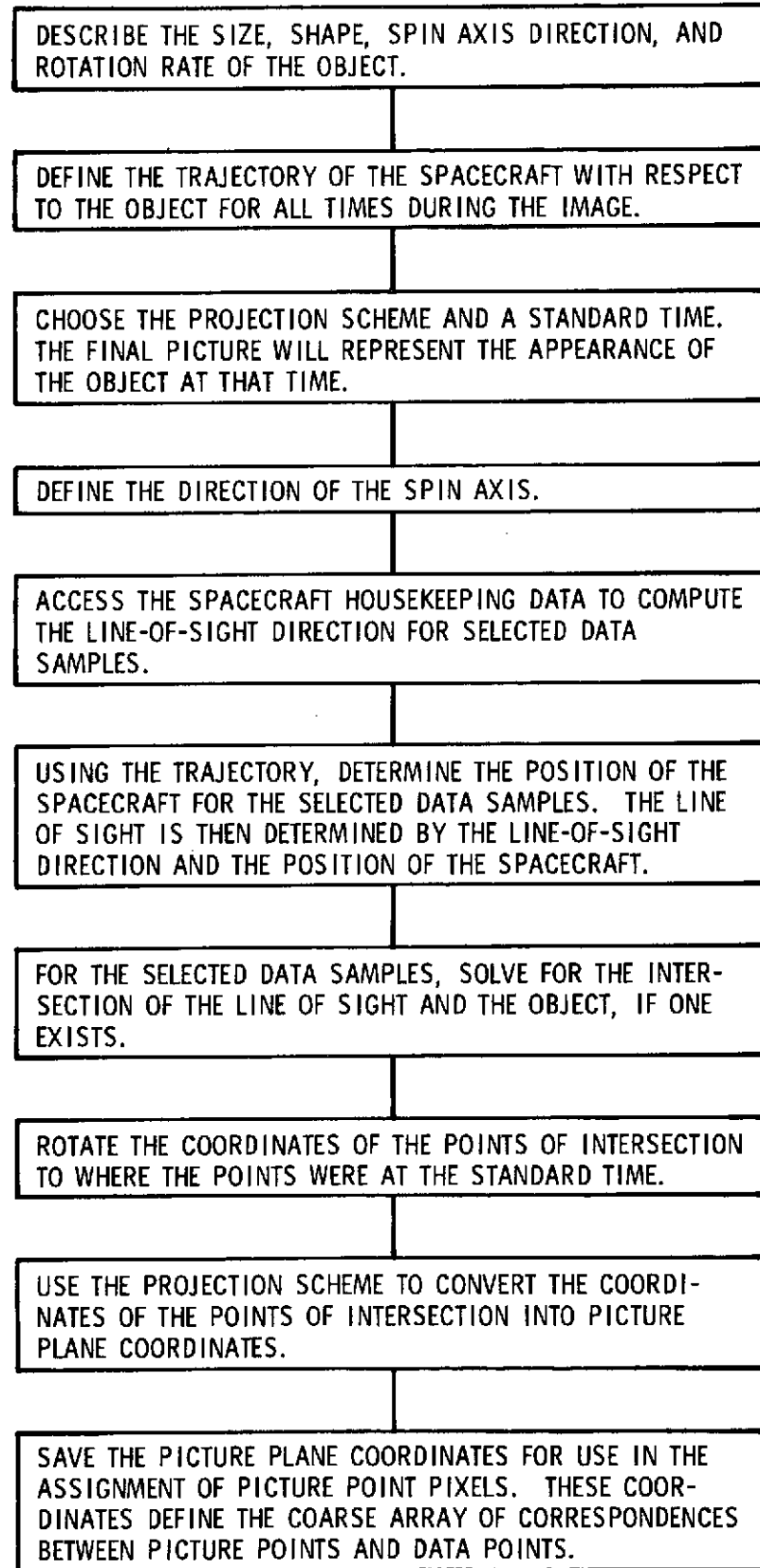


Figure 4-5. Geometric Solution Procedure

$$B_x^2 + B_y^2 + \frac{B_z^2}{(1 - \epsilon)^2} = R_e^2 \quad (4-13)$$

giving one relation between the three unknown components of vector \vec{B} .

Let \vec{A} be the vector from the spacecraft to the center of the planet. This vector is presumed known from trajectory data and, while usually given in terrestrial Aries-ecliptic coordinates, is easily transformed to the planetocentric coordinate system using the known direction of the planetary spin axis and the definitions of the two coordinate systems.

Let \vec{C} be a vector along the direction of sight of the telescope on the spacecraft. The direction of this vector is known in the spacecraft frame from encoders giving look angle to the spacecraft spin axis and roll angle obtained from a roll reference pulse provided, for example, by a star sensor. With the known direction of the spacecraft spin axis, the vector along the line-of-sight of the telescope can be transformed to Aries-ecliptic and then to planetocentric coordinates.

While the direction of vector \vec{C} is known, the distance along this vector to the intersection with the surface of the planet is not yet known. If this distance is called r , vector \vec{C} can be expressed as $r(c_x \hat{e}_x + c_y \hat{e}_y + c_z \hat{e}_z)$ where \vec{c} is the known unit vector pointing in the direction of the telescope line of sight expressed in planetocentric coordinates.

From the definition of vectors \vec{A} (from the spacecraft to the center of the planet), \vec{B} (from the center of the planet to the surface intersection with the telescope line-of-sight), and \vec{C} (along the line-of-sight from the spacecraft to the surface of the planet), we have the vector relation $\vec{A} + \vec{B} = \vec{C}$ or

$$A_x + B_x = r c_x \quad (4-14)$$

$$A_y + B_y = r c_y \quad (4-15)$$

and

$$A_z + B_z = r c_z \quad (4-16)$$

These three equations, along with equation (4-13), give four equations in the four unknowns r , B_x , B_y , and B_z which are easily solved for the location of the viewed element on the surface of the planet. Due to the quadratic nature of equation (4-13), two solutions are generally found corresponding to the two intersections of the line-of-sight with the planet. The point of intersection nearest to the spacecraft is, of course, the one seen by the instrument. This solution is repeated for some coarse network of data points with their associated look and roll angles as determined from spacecraft housekeeping data.

These points of intersection must next be derotated to their position at some standard time t_0 . If the planetary rotation rate is $\dot{\theta}$ and the point is sampled at time t , let

$$\theta = \dot{\theta} (t_0 - t) \quad (4-17)$$

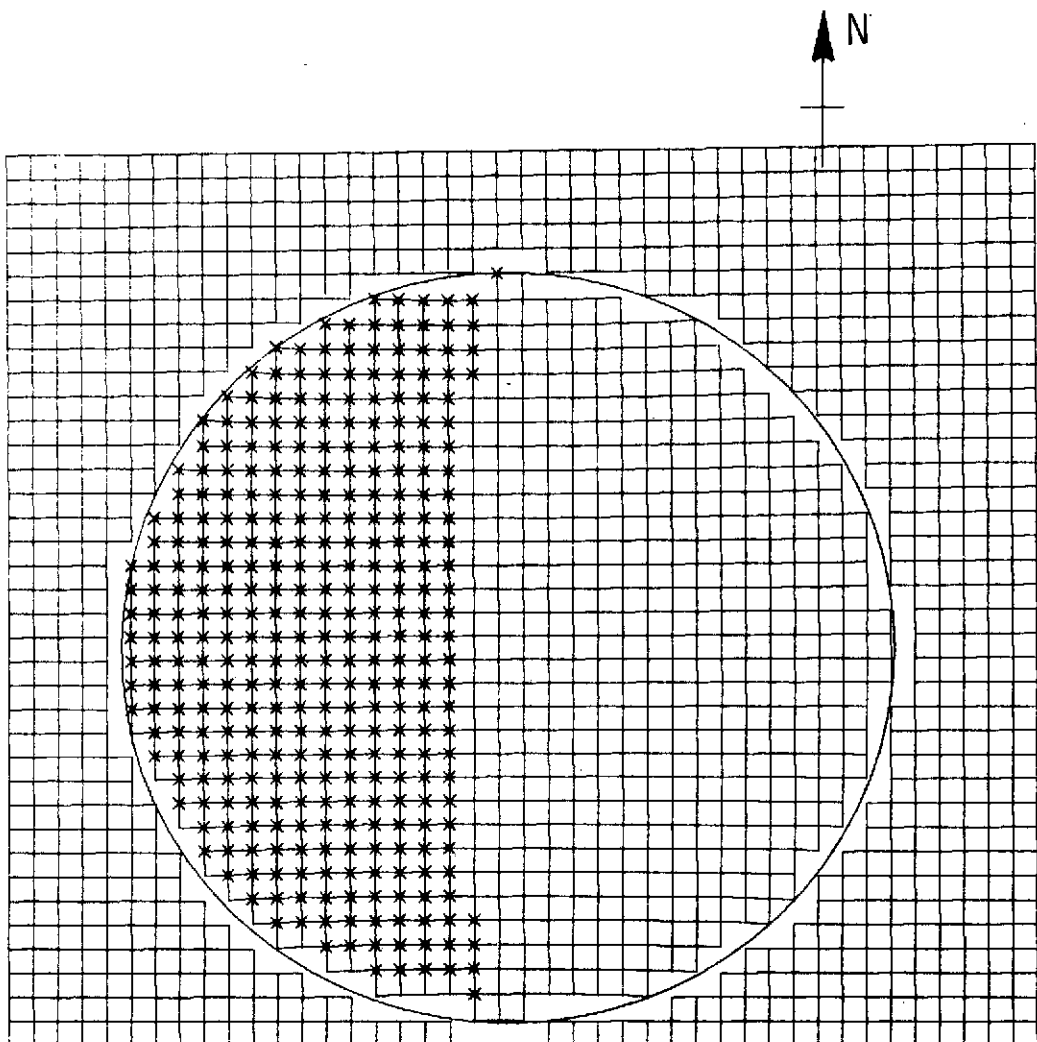
Then

$$\left. \begin{aligned} x_o &= B_x \cos \theta - B_y \sin \theta \\ y_o &= B_x \sin \theta + B_y \cos \theta \\ z_o &= B_z \end{aligned} \right\} \quad (4-18)$$

are the derotated coordinates of the point of intersection, (B_x, B_y, B_z) .

The points, (x_o, y_o, z_o) , are then projected onto the plane, \underline{P} , according to the type of map projection the user wishes to use. The final resulting coordinates, (x, y) , indicate the position in the final picture at which a given data pixel is to be displayed.

An example of the geometry of data taken on a planet is displayed in Figure 4-6 in the form of a scan map. This figure is the same as Figure 8-11a, and is explained more fully in Section 8. The plane of the paper corresponds to plane, \underline{P} , in Figure 4-3. Lines connect the



JUPITER ORBIT NO. 1 START TIME 244.15 END TIME 244.29 HRS.
CLOSEST APPROACH 39.50 RJ SAMPLE RATE 1 FORWARD STEPPING
S/C ROTATION 10.00 RPM EVERY 2TH LOOK AND 16TH ROLL POINT SHOWN
STARTING LOOK ANGLE 98.50 DEG STARTING ROLL ANGLE -1.40 DEG
NO. DETECTORS PER CHANNEL 8 NO. POINTS PER ROLL 600
IMAGE FIELD OF VIEW IN THE ROLL 0.10 AND LOOK DIRECTION 0.10 MRAD

Figure 4-6. Scan Map of Jupiter from Jupiter Orbiter for Conditions Indicated

data pixel coordinates (x, y) as they are mapped onto the plane, P . Only every n th data pixel along a roll and every m th roll are displayed. A roll corresponds to a nearly vertical line. The scan map displays how the data pixels are to be positioned to produce a rectified image.

Linear interpolation for the coordinates of intermediate data pixels between every n th pixel can be used to reduce the computer expense of solving the four simultaneous equations a large number of times. The number of data pixel coordinates which must be solved for the linear interpolation depends on the regularity of the scan map. The more regular the scan map, the fewer sets of simultaneous equations need be solved. In general, the cost to rectify an image depends on the regularity of the scan map.

4.3.2 Assignment of Intensities to the Display Array

Conceptual Approach for General Case

Figure 4-7 illustrates how the rolls of IPP test data which are simply displayed one roll per column in Figure 4-4 should be mapped onto the display plane to look like an instantaneous view of the target globe as seen from the "spacecraft" position midway through the data taking. In this general case, where significant rotation and translation of the target relative to the spacecraft occur during the image, the scan lines are curved in addition to being discontinuous at the edge of the planet. Successive scan lines are not separated by exactly one pixel width, causing overlap or underlap. Given knowledge of where each data pixel maps onto the picture display plane, a correspondence between picture display pixels and data pixels must be established so that picture pixels can be assigned appropriate intensities. Figure 4-8 shows the data of Figure 4-4 displayed according to the scan map of Figure 4-7. While the periphery of the image is treated only crudely in this early version of the Pioneer pixel assignment program, the program succeeds in displaying the data in a "snapshot" type display.

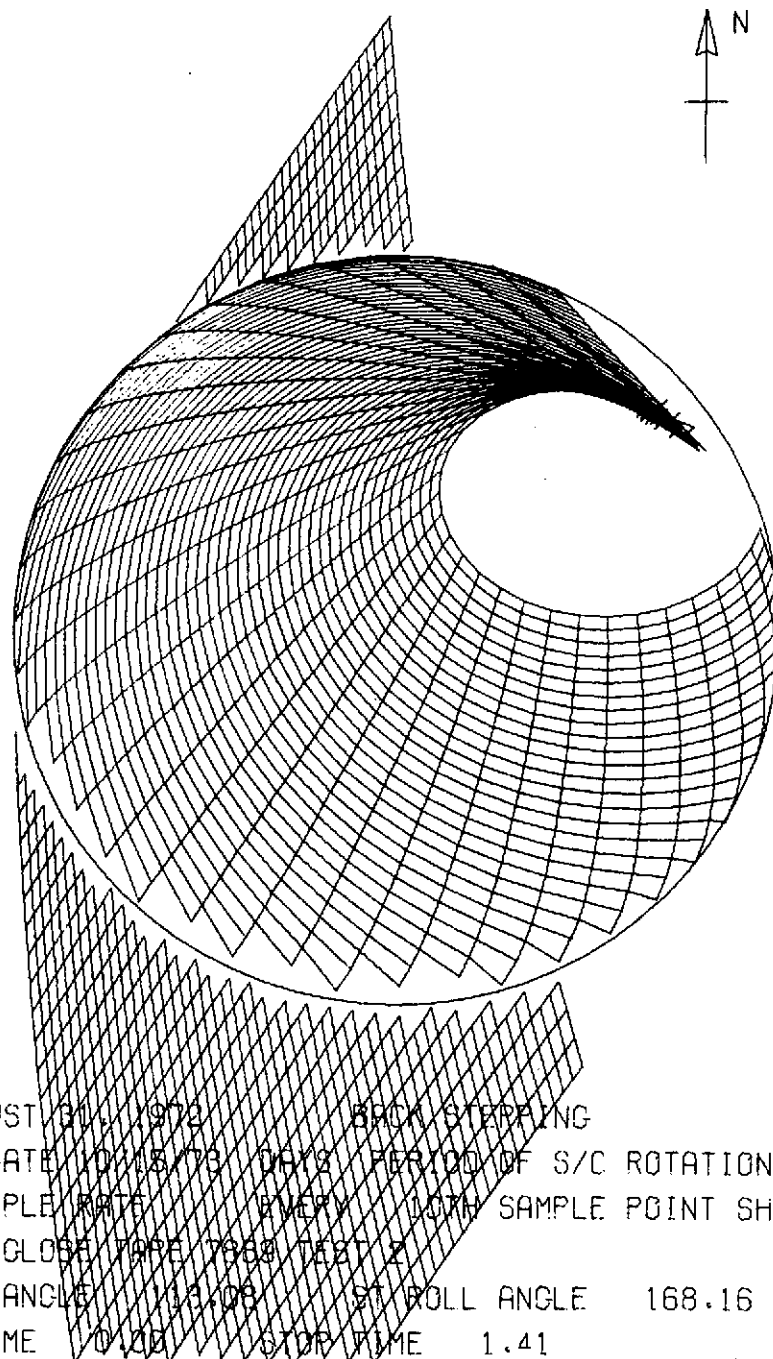


Figure 4-7. Example of Mapping of IPP Test Data onto Display Plane

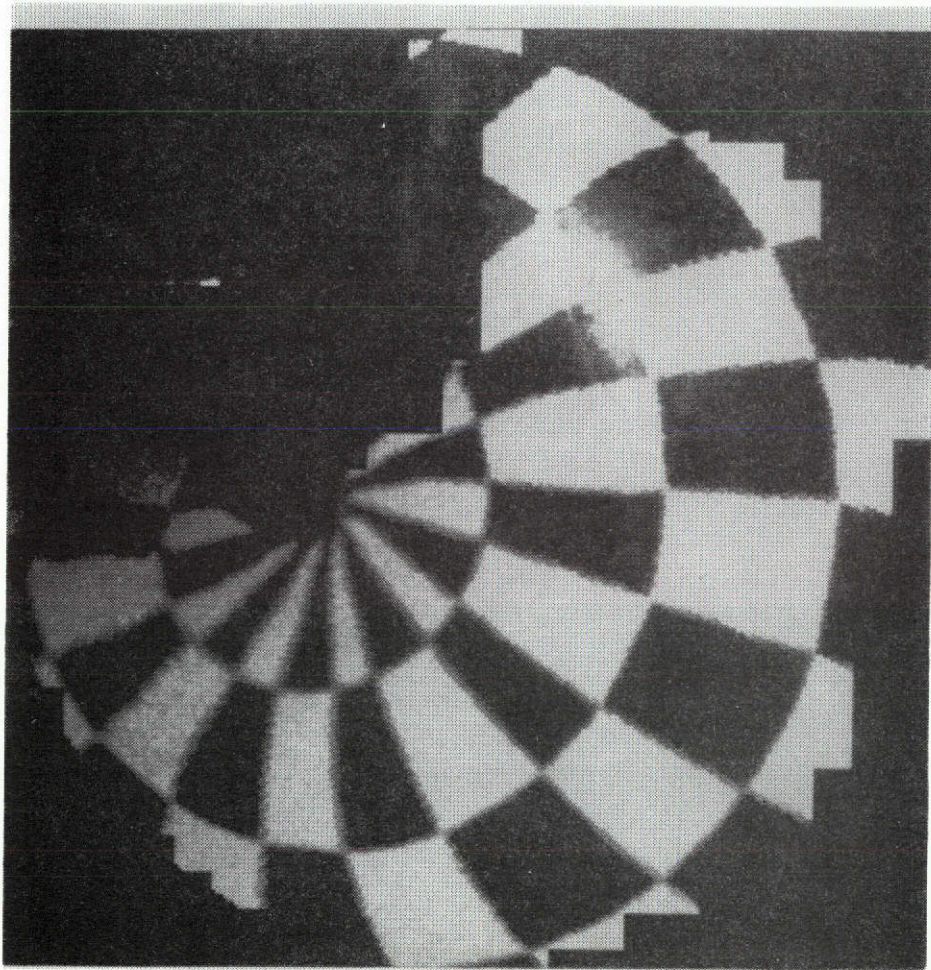


Figure 4-8. Data of Figure 4-4 Displayed According to Scan Map of Figure 4-7

Note that the bulk of the spin-scan images produced on a planetary flyby or orbiter mission will not have the severe geometrical distortion now being considered (see Figure 4-6 and the scan maps of Section 8 for the geometry of typical Jupiter orbiter images). An efficient technique is outlined for assigning intensities to the display arrays of images having more regular geometry later in this subsection after consideration of the general case.

The objective of the following discussion is to outline in some detail methods to be used in a computer program for assigning intensities to the display array when the "roll directions" in picture display space are continuous curves of arbitrary shape (a roll direction curve may even loop back to intersect itself), and the lengths, locations and shapes of these curves can change from roll to roll (generally, but not necessarily, with some degree of regularity in the changes). Also, the sizes of data pixels in picture space change not only from roll to roll, but also from point to point within an individual roll.

To aid the visualization of the situations and procedures which will be discussed, the specific case is referred to in Figure 4-9. In this hypothetical arrangement of three data rolls in picture space, the conditions of overlap, underlap and variations of curvature and pixel size have been exaggerated over what would be encountered in most real situations for purposes of clarity in illustration.

Input and Initialization. - The spin-scan data are assumed to be supplied as N rolls, each roll consisting of intensities for every pixel in a block N_R pixels wide by M_R pixels long (in Figure 4-9, N is 3, N_R is 4, and M_R is 12). We also require as input picture space coordinates, (x', y') (on any Cartesian system) of points equally spaced along each of the N roll-direction curves. These points are marked with crosses in Figure 4-9. These points should be as closely spaced along the roll curves as is required to ensure that the use of linear interpolation results in only negligibly small errors.

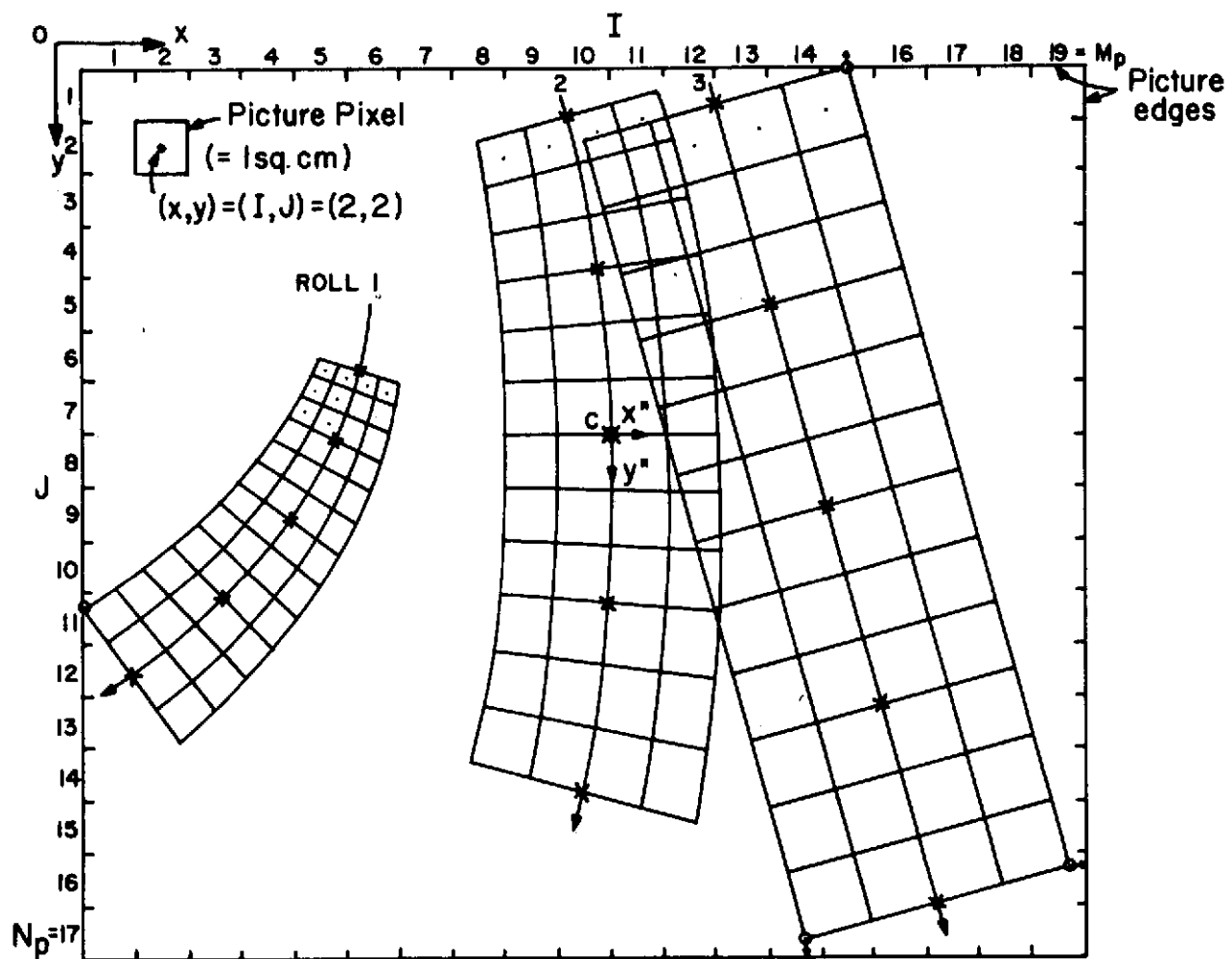


Figure 4-9. Possible Arrangement of Three General-Case Data Rolls in a Picture

The first step in initialization is conversion of input (x', y') to the (x, y) coordinates used in constructing the picture. This is done using a two-step method involving rotation, rescaling, and translation of the input coordinate system proceeding as follows. First, one of the data rolls which is extended to lie near the middle of the final picture and which is judged to have intermediate pixel sizes and curvature (e.g., roll No. 2 of Figure 4-9) is selected. The (x', y') coordinates of points near the midpoint of this roll (marked "C" in Figure 4-9) are used to calculate a coordinate rotation angle and rescaling factor leading to the (x'', y'') system which has: 1) its origin at point C, 2) the positive y'' axis tangent to the roll curve at C and pointing toward the end of the roll, with the positive x'' axis in the same relation to it as in the (x, y) system, and 3) a scale such that the unit length (width of a picture pixel) is the same as the width of a data pixel near point C. The aim of this first transformation is to make picture pixels and data pixels conform as closely as possible in size and orientation, hopefully over the entire picture, but certainly near the picture center where the object of interest is presumably located.

The second step in the coordinate transformation is the simple translation of the (x'', y'') system into the (x, y) system in such a way that all spin-scan data occur at $x \geq 0.5$ and $y \geq 0.5$. To do this, the (x'', y'') coordinates of the roll curve points are searched to find the maximum and minimum values of x'' and y'' (corresponding to the circled dots in Figure 4-9). From the minimum values found are derived integer values Δx and Δy needed to translate the origin (integers are required to preserve the coincidence of data and picture pixels at point C). When the translation is accomplished, the whole coordinate transformation process is completed. The end result is that the input (x', y') coordinates of points equally spaced along the roll curves have been converted to the corresponding (x, y) coordinates. These are available for use in the picture-making procedures to follow.

The final step of initialization is to use the maximum values of x'' and y'' found above to determine the dimensions the pictures must have to accommodate all the data within its boundaries. Integer Δx and Δy values are again derived which locate the lower right-hand corner of the picture with respect to the point C. These are then used to compute N_p and M_p , the dimensions of the picture (in picture pixel widths) in the x and y directions, respectively.

Assignment of Roll Data Intensities to Matching Picture Pixels.-

In the interests of minimizing computer time and core requirements, it is felt that it is important to process the data rolls one at a time in sequence. In this way, only a single roll need be stored in core at one time, and it is not necessary to undertake any costly back-and-forth searches of input tapes or disk files to locate a particular piece of needed data. For similar reasons, it is highly desirable that only picture pixel columns that can be assigned from the current roll of data be in working core. As soon as a picture column is assigned as completely as allowed by the data, it is removed to disk or tape storage. Likewise, blank columns are not brought into core until it is found that they can be at least partially assigned data from the current roll.

The steps followed in the processing of each individual roll are as follows:

1. The (x, y) coordinates of points along the roll curve are used to compute a table containing (x, y) locations of the centers of each and every data pixel of the roll (N_R M_R of them) together with the sizes of the pixels (relative to the unit picture pixel size).
2. The maximum and minimum x values from this table are used to determine which picture columns can be filled using data from the current roll. For example, only columns 1 through 6 of Figure 4-9 can be filled with data from roll No. 1; only columns 8 through 12 are considered in the case of roll No. 2; and only columns 10 through 19 in the case of roll No. 3. Picture columns not needed for the current roll are removed to disk or tape files for storage. They may be returned to core if needed in the processing of a later data roll.

3. The assignment of data intensities to picture pixels proceeds as follows. First, the (x, y)-size table of step 1 is used to examine the data roll pixel by pixel. The first step in the examination of the data pixel is to relate it to a specific picture pixel. Because of the way the (x, y) system was set up, simply rounding the (x, y) coordinates of a data pixel to the nearest integers yields the coordinates of the picture pixel within which the center of the data pixel lies. In the next step, the size of the data pixel comes into play, giving rise to three possible cases (since the picture pixels are of unit area):
 - a. If the size of the data pixel is near unity (between roughly 0.8 and 1.2), it will nearly always be the only one whose center lies within the corresponding picture pixel. In this case, it is not necessary to search further for a better match of data and picture pixel. If the particular picture pixel has not previously been assigned, it is given the intensity of the data pixel being considered, while in the rare cases where it has been previously assigned, its intensity is left unchanged. From this simple assignment procedure it follows that, in cases where the data pixel size is approximately the same throughout all the data, the picture-making process can go quite rapidly.
 - b. If the data pixel area is very much less than 1.0 (as, for instance, near the start of roll No. 1 of Figure 4-9), then more than one data pixel may have its center within some picture pixel. On this account, the procedure used for small data pixels is:
 - 1) Data pixels of the roll are considered one at a time. For each data pixel, x and y are rounded to yield the corresponding picture pixel.
 - 2) If this picture pixel is still unassigned, step 1) is repeated for all data pixels surrounding the one of concern (within some radius depending on its size) to see if any of these map into the same picture pixel. Those that do are noted for comparison; they are all candidates for assignment to the particular picture pixel.
 - 3) The candidates are examined to decide what intensity should be assigned to the picture pixel. The simplest way to do this is to determine which of the candidate data pixels has its center nearest the picture pixel's center and to assign the intensity of

this candidate. Another (slower) method would be to compute a weighted average of all the candidate intensities and to assign this to the picture pixel.

- c. If the data pixel area is much greater than 1.0, the centers of several picture pixels may lie within the boundaries of the same data pixel (e.g., roll No. 3 of Figure 4-9). In this case, all such picture pixels should be assigned the intensity of the data pixel; hence the procedure for large data pixels is:
 - 1) Data pixels are taken one at a time, and each is mapped into the picture pixel whose center is nearest to the center of the data pixel being considered. If this pixel is still unassigned, it is given the intensity value of the data pixel, while if previously assigned, it is left unchanged.
 - 2) Picture pixels immediately surrounding the nearest one are examined in turn. In each case, the distance between picture and data pixel centers is computed, and if this distance is less than half the size of the data pixel, the picture pixel is assigned the intensity value of the data pixel.

The application of the procedures described assigns all of the data intensities (except possibly some small-pixel cases) to picture elements with positional accuracy and resolution better than a pixel width for all parts of the picture. When the assignment of a roll has been finished, the procedure is restarted at step 1 and the processing of the next roll begins, continuing until all of the rolls have been used up and the entire picture is complete.

Because the coverage of the data is seldom complete due to underlap and other causes, not all of the pixels of the final picture will be assigned from the data, and some parts of the picture will necessarily be left "blank." The "blank" means that before the assignment starts, all picture pixels are set to some intensity value which is clearly distinguishable from all possible data intensities, and after assignment is finished, all pixels left with this intensity value are considered blank. Note that once a blank pixel is assigned an intensity, it

is never subsequently reassigned. This means that if overlap coverage of the data occurs (as between roll No. 2 and roll No. 3 of Figure 4-9), the first-processed data are used in the picture-making, and the later duplication is ignored.

Special Case Where Roll Directions are Parallel
Straight Lines in the Display Array

This subsection describes a rapid method of assigning intensities to the picture display array elements for the rather common special case where the scan map (the map indicating the location of the data points in the picture display array) is made up of nearly parallel straight lines along the direction of spacecraft roll. Two typical scan maps are shown in Figure 4-10. No restrictions are made with regard to the start or end points of the spin-scan rolls except that these are known and are such that all the roll directions are straight and parallel. Any degree of overlap and/or underlap between successive rolls of data is permitted, and the rolls may be any number (including one) of detectors (pixels) wide.

Input Variables and Form of the Spin-Scan Data. - As shown in Figure 4-11, the spin-scan data consist of N identical rolls, each N_R pixels wide and M_R pixels long. These pixels are assumed to be squares, each having its own particular intensity value and each identified by roll number J_R and I_R . The start and end points of each roll are indicated by circled dots labelled S and E. The line SE is the roll direction. It is assumed that $(x'_S, y'_S)_i$ and $(x'_E, y'_E)_i$ are provided as input for all rolls, $1 \leq i \leq N$, where (x', y') are picture-space coordinates on any Cartesian system (any origin, any orientation of axes, and any units). These start- and end-point coordinates are generated by the solution of the equations of subsection 4.3.1.

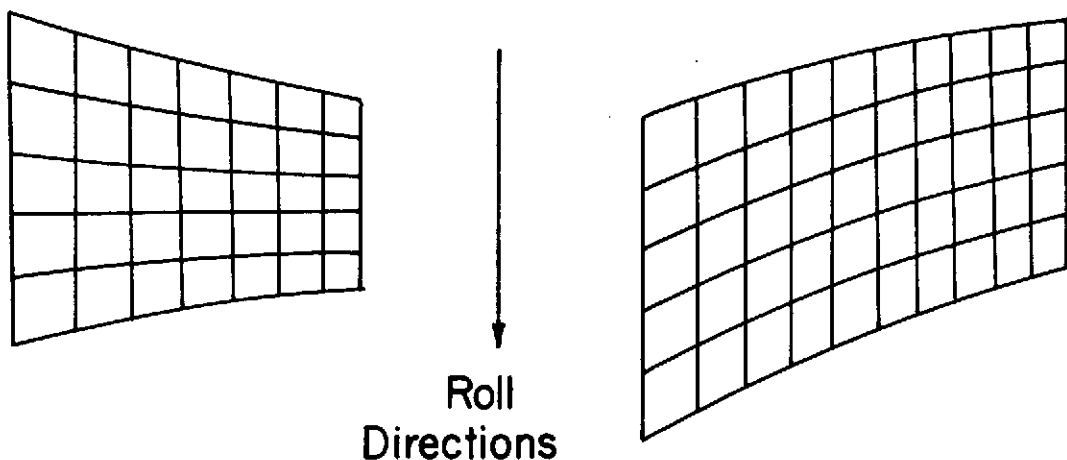


Figure 4-10. Typical Scan Maps Consisting of Parallel Straight Lines in the Roll Direction

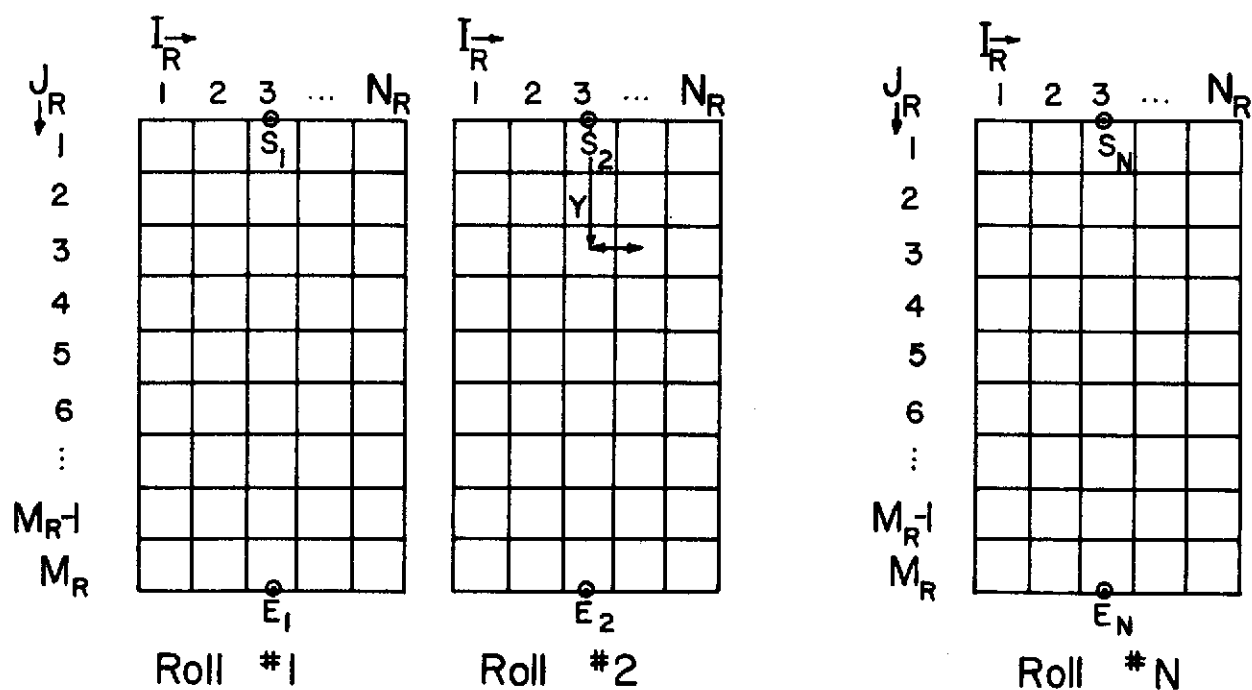


Figure 4-11. Form of the Spin-Scan Data

It is necessary to locate the center of any roll data pixel, (J_R, I_R) , within a roll relative to the start-point of that roll (S_i). To do this, the (x, y) system of coordinates shown in Figure 4-11 is used. The origin is the start-point of the roll, $+x$ is the direction of increasing I_R , $+y$ is the direction of increasing J_R , and the (x, y) of the (J_R, I_R) pixel are given by

$$\begin{aligned} x(I_R) &= \left[\frac{1}{2} - (N_R - 1) + (I_R - 1) \right] w \\ y(J_R) &= (J_R - \frac{1}{2}) w \end{aligned} \quad (4-19)$$

where w is the size of the data pixel, and $1 \leq I_R \leq M_R$, $1 \leq J_R \leq N_R$.

Arrangement of Roll data in Picture. - Figure 4-12 shows a possible arrangement of three rolls of data in the picture plane and indicates how data pixel intensities can be related to picture pixels. Note that the apparent size of a data pixel as projected on the picture plane changes from roll to roll as the spacecraft approaches or recedes from the object pictured. Each point in the picture plane is located by its (x, y) coordinates. The origin of this system lies just outside the upper left-hand corner of the picture, and the units are such that the center of the (I, J) picture pixel is at $x = I$, $y = J$.

The general approach to picture construction followed is to use each roll of data in turn to fill as many columns of picture pixels as possible before proceeding on to the next roll. The first roll of data is adopted as the left edge and upper left-hand corner of the picture. Roll No. 1 data pixels correspond one-for-one with picture pixels; hence the first roll sets the standards to which subsequent rolls are referred (e.g., roll No. 1 pixel size = $w_1 = 1.0$).

For succeeding rolls, the procedure is to compare x for the center of the current picture column (to be filled) with x -values for the centers of the N_R data pixel columns of the roll to determine if one of them corresponds. If this comparison indicates a correspondence does exist in the x -direction, then a y -direction assignment table,

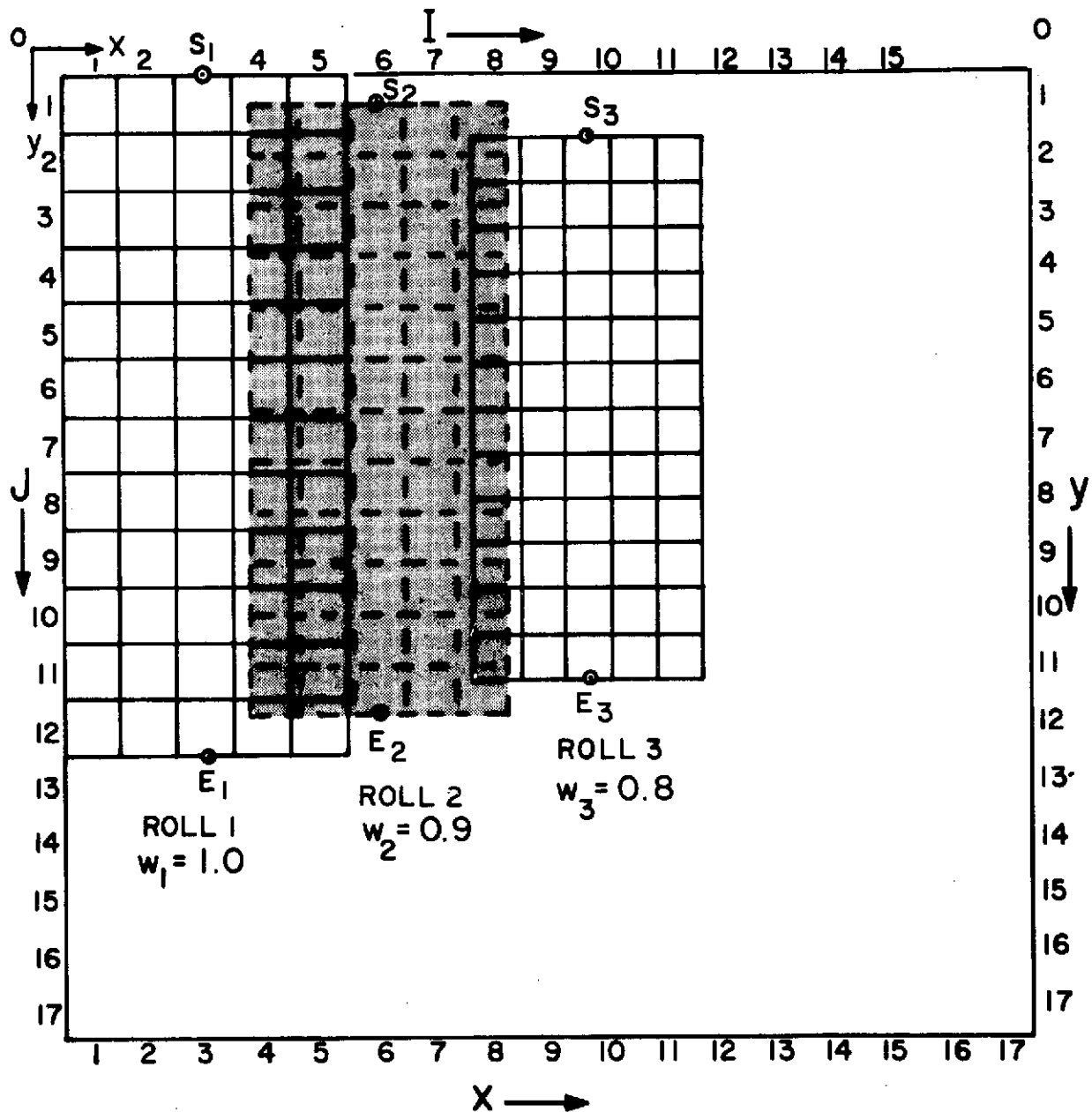


Figure 4-12. Possible Arrangement of Three Data Rolls in the Picture Plane

which indicates which data-column pixel corresponds to which picture-column pixel, and which can be used in assigning any of the data columns of the roll, is derived. Finally, this table is used in assigning intensities to all picture pixels corresponding to data pixels from the current roll, before going on to the next roll to repeat the procedure.

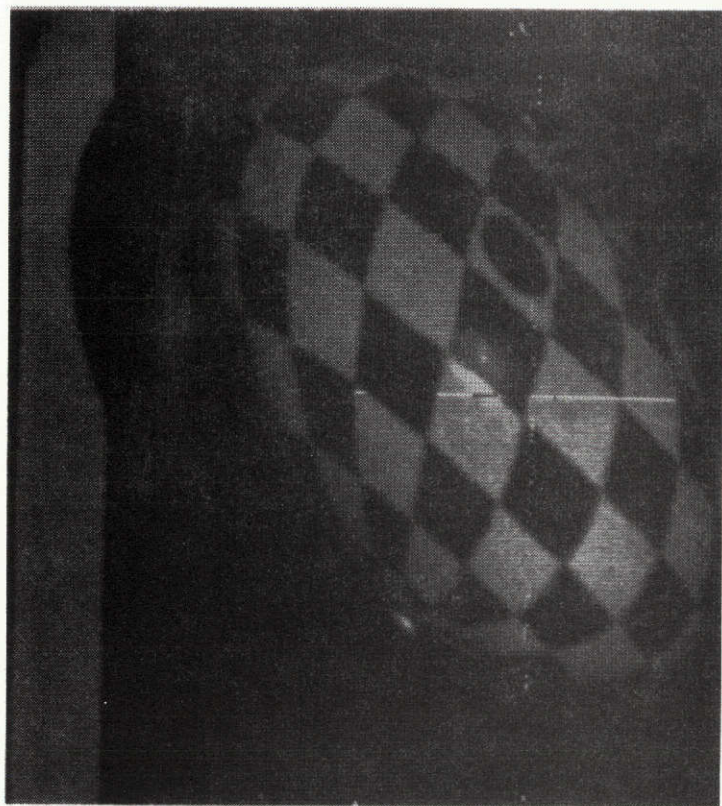
Figure 4-13 shows an image of a translating globe obtained by the Jupiter Pioneer IPP instrument during laboratory tests. The upper image is the data simply displayed roll by roll as it was taken. Some instrument stepping anomalies are apparent in the upper half of the globe image. Also, a simple corrector lens was used to modify the IPP (designed to focus at infinity) for the close-range test. Insufficient depth of field was provided by this arrangement to keep all parts of the globe in good focus during the test. Nevertheless, the distortion produced by the translation during the image is apparent.

The bottom half of Figure 4-13 shows the same image displayed after application of the simple rectification procedure outlined above. In addition to the stepping anomalies present in the original data, the rectification procedure has introduced a 1-pixel jitter, which is apparent in the gray strip along the left side of the frame as well as in the boundaries of the light and dark segments of the globe. This effect could have been easily reduced by making the display pixels smaller than the data pixels. In any case, the simple assignment procedure performs exactly as expected in compensating for the distortion introduced by motion during the image.

4.3.3 Summary

In summary, both problems of determining where to locate the data in the display array (treated in subsection 4.3.1) and actually assigning intensity values to pixels in the display array (treated in subsection 4.3.2) have been solved for display of IPP image data. Since the geometry problem need only be solved for a coarse net of data points, it proceeds rapidly and inexpensively on the computer. The

Translating globe,
unrectified



Translating globe,
rectified

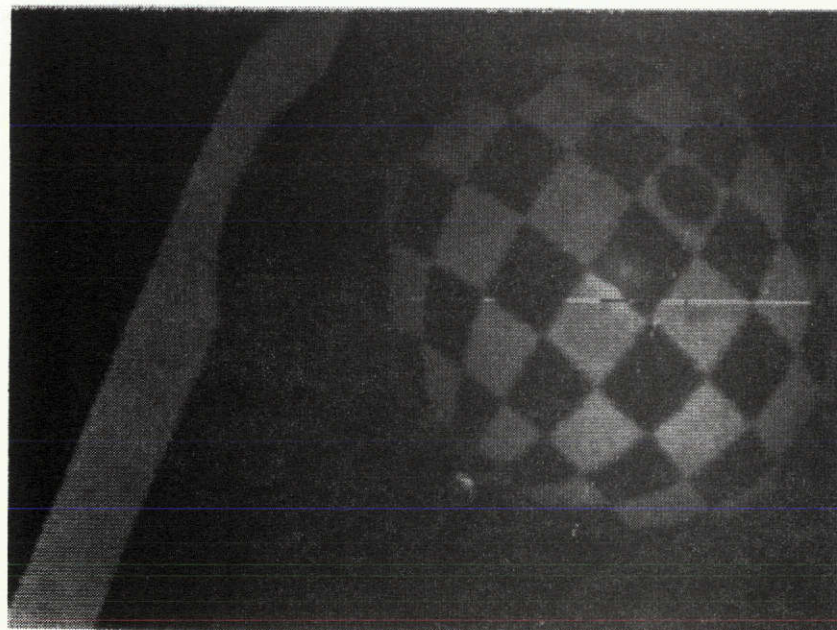


Figure 4-13. Rectified and Unrectified Spin-Scan Images of
Translating Globe

cost of assigning intensities to the elements of the display array depends in general on the regularity of the "scan map" geometry. However, for the vast majority of images expected even on a long duration mission such as the Jupiter Orbiter mission, the data points simply map to nearly straight parallel lines of various length and spacing. For this case, special techniques have been developed to accomplish the assignment of intensities to display elements very efficiently and inexpensively. (The cost is determined by input-output charges on our computer.) Even for the most general geometry, existing techniques accomplish the assignment at modest cost. Further, these programs are still in a state of optimization, and it is recommended that the continued development of the IPP programs be monitored for expected improvements. In total, even the vast quantity of image data expected from orbiter-type missions as described in Section 8 could be rectified and displayed at not unreasonable cost.

Section 5

IMAGER COMPONENTS

5.1 DETECTORS

In the subsections that follow, the properties of the various candidate detectors for use on the spin-scan OPM Imager will be discussed. The approach taken will be to emphasize those aspects which are important for the OPM Imager and to briefly review or even omit those which are of little or no consequence to this goal.

The detector types have been divided into three broad categories: photoemissive-type detectors, silicon photodiodes, and other candidate detectors. Due to weight and power limitations anticipated for the OPM Imager, the candidate detectors will probably be limited to ones selected from either the first or second categories. However, since the scope of future requirements could well demand greater spectral coverage, especially in the infrared, the inclusion of this additional category is felt to be appropriate.

5.1.1 Photoemissive Detectors

The distinguishing feature of photoemissive detectors is the photoemissive surface, or photocathode, where incident photons of sufficient energy liberate free electrons into the surrounding vacuum. The efficiency of this process is the most important characteristic of a photocathode. The fraction of the incident photons that produce photoelectrons is called the quantum efficiency and is usually expressed as a percentage. A corresponding quantity called the photocathode responsivity gives the photocathode current per unit of incident flux.

The photocathode responsivity (or quantum efficiency) is dependent on the photocathode composition and processing as well as on the wavelength of the incident flux. It is expected that, for the OPM Imager, the number of spectral bands will be limited to no more than three and

quite possibly to either a single wide spectral band or two fairly broad spectral bands. If a single spectral band is acceptable, then it is obvious that a detector with wide spectral coverage can give better signal-to-noise performance than one with more limited coverage when the other properties are similar. Thus, for the OPM Imager, detectors with wide spectral coverage coupled with high absolute responsivity are to be preferred. One situation where this may not be optimum is where it is possible to select a detector with a high responsivity over a limited spectral range of interest and low responsivity at other wavelengths, e.g., the use of a bialkali photocathode over the 0.35- to 0.5- μ m spectral region. However, if all channels are packaged in a single envelope (such as with Design 1, Section 6) then the use of more than one photocathode is not practical.

In Figure 5-1, the absolute spectral responsivity is shown for several types of photocathodes possibly appropriate for use in the OPM Imager. The characteristics of the extended-red, multialkali-type photocathode (variously designated as ERMA, S-25, etc. by different manufacturers) can be varied to optimize the spectral responsivity for a specific application. For example, by increasing the photocathode thickness, the red response can be increased at the expense of the blue response. As indicated in the figure, the use of prism enhancement⁵ is particularly useful at longer wavelengths with the extended red photocathodes. The three opaque photocathodes (GaAs, GaAsP, and GaInAs) included in the figure are relatively recent developments. With the possible exception of the already highly-developed, opaque GaAs photocathode, improved responsivities and extended spectral ranges for the negative-electron-affinity, semiconductor-type photocathodes are probable. The further development of semi-transparent, semiconductor-type photocathodes such as the GaAs photocathode used in the RCA C33105 image tube would offer improved performance for some possible configurations of the OPM Imager.

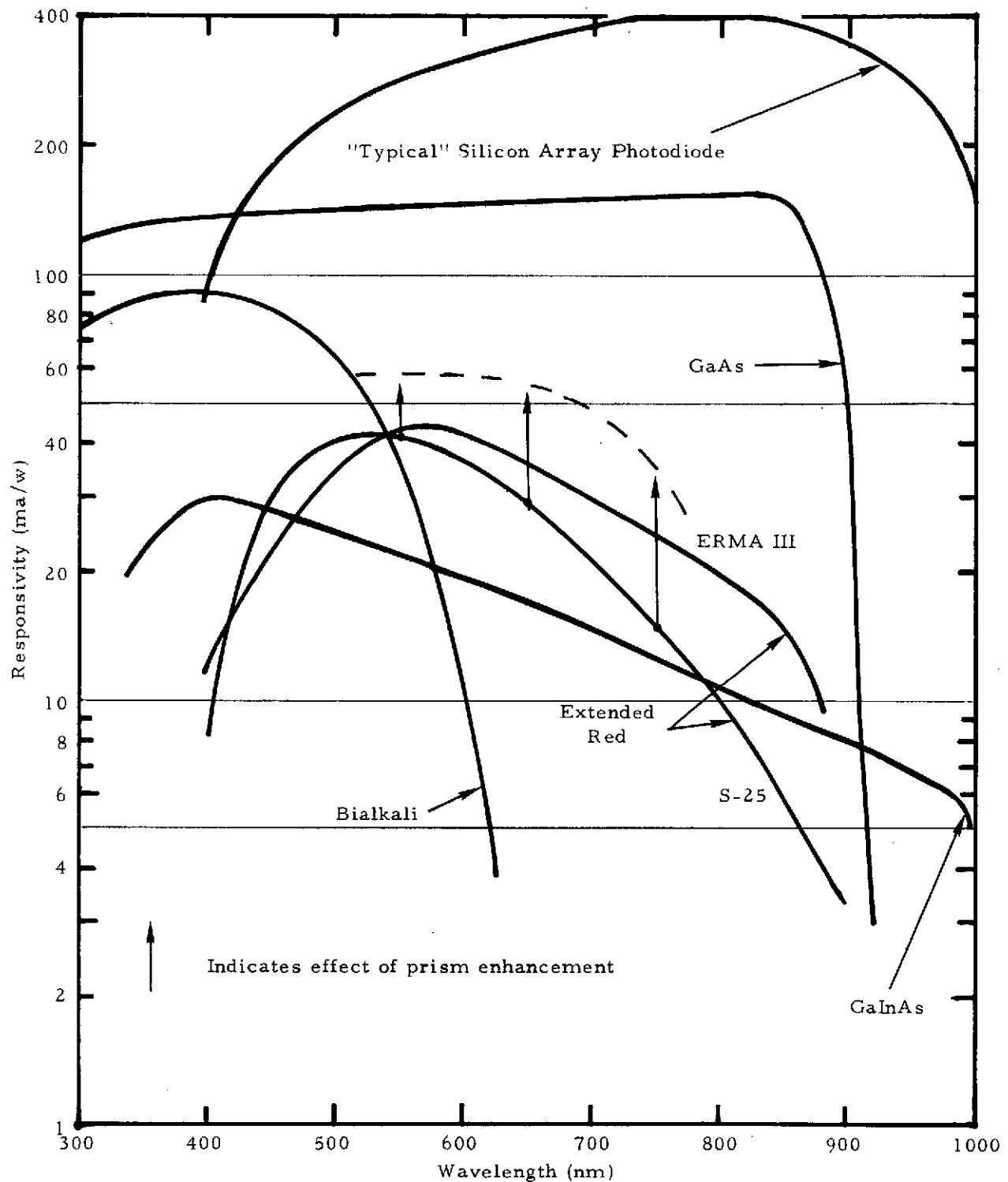


Figure 5-1. Spectral Responsivities of Some Candidate Detectors

In summary, it is apparent that the GaAs photocathode offers the best combination of high responsivity and extended spectral coverage where an opaque photocathode can be used. In applications where a semi-transparent photocathode is required, the extended-red, multi-alkali photocathode with prism enhancement (where possible) is the present practical choice, although this choice may be superseded as noted above. In the subsections that follow, the detailed characteristics of various candidate photoemissive-type detectors are discussed.

Photomultiplier Detectors

The combination of a photocathode followed by a series of secondary-emitting electrodes (dynodes) is commonly called a photomultiplier tube (PMT). The series of dynodes functions as a very low-noise electron multiplier yielding a charge or current gain at the output anode which is the product of the gain of the individual dynode stages.

For the previous reasons, a GaAs photocathode is to be preferred over other possible photoemissive materials for the OPM Imager. Measurements on a GaAs PMT were performed by SBRC as a portion of another study⁶ and some of the results are of importance for the OPM Imager. An RCA C31025J PMT was selected as the best off-the-shelf detector for the photometer-polarimeter of interest in that study. An extensive series of tests was run on this detector to assure suitability for such an application.

Many of the tests performed in the above evaluation are of only minor interest for the OPM Imager. Such tests as the polarimetric spectral responsivity, angular responsivity, and contour responsivity fall in this category and need not be discussed here. The measured responsivity, both in absolute magnitude and in spectral shape, differed somewhat from that shown in Figure 5-1. This is not surprising in view of probable processing differences. The linearity, differential current gain, and dark current as a function of high voltage were

entirely within the performance requirements that would be demanded for the OPM Imager. The anode current as a function of time from initial turn-on was also monitored. The radiation test results are discussed separately in a later subsection. While additional qualification testing obviously would be required before this detector could be used on an OPM Imager, these initial tests indicate basic suitability.

Image Dissectors

An image dissector is basically a photomultiplier in which the photocathode area sampled is electronically selectable. This is accomplished in the following manner. Photoelectrons emitted from the photocathode are accelerated and focused onto a plane containing an aperture which defines a small area on the photocathode. This small area can be scanned across the photocathode by means of deflection coils or plates. The photoelectrons passed by the aperture impinge on an electron multiplier which provides a low-noise electron gain.

For use in the OPM Imager, an image dissector could be used to provide successive cross-scan sampling of the scene with a high-speed retrace. This is analogous to TV usage, except that the "raster scan" is provided by the roll of the spacecraft. Used in this fashion, the image dissector operation is equivalent to an array of PMT detectors, except that the dwell time for a given IFOV is less than that for the PMT array by a factor nearly equal to the number of array detectors, n . In this situation, the SNR would be reduced by a factor of approximately \sqrt{n} as a consequence of the sequential sampling of the image dissector. The trade-offs of such parameters as weight, power, complexity, and reliability between such alternative systems obviously would depend on the detailed mission requirements. However, since the use of a Digicon-type detector provides the multichannel capability of an array and the small photocathode area sampling of the image dissector, an image dissector is not felt to be an optimum choice for the OPM Imager.

application. Another consideration is photocathode loading (flux per unit of photocathode area), which would be less by a factor of n for the same SNR performance if an equivalent Digicon-type detector replaces an image dissector.

Channeltron-Type Detectors

A Channeltron⁷ Photon Counter Tube is basically a PMT which used a channel multiplier to provide the electron gain. The high-gain narrow-pulse height distribution and low dark count rate make this detector especially useful for photon counting applications. Other attractive features are that it is a low-power, compact, and relatively radiation-resistant device. Dual channel versions of this tube (BX784) were developed for use on the Pioneer 10 and 11 IPP instrument because of such advantages. These detectors were used in the analog mode in the IPP due to the high flux levels required for adequate precision in the photopolarimetry mode.

The main disadvantage of this type of detector is the limited output current capability ($\sim 10^{-7}$ A) due to the use of the continuous channel multiplier. Another disadvantage is the apparent finite lifetime characteristics^{8,9} of channel multipliers. SBRC's experience indicates that the responsivity of the channel photomultiplier will be degraded in excess of 50% after approximately one coulomb of charge has passed through the channel, independent of charge rate. This conclusion is based on very few samples, however. It has recently been reported¹⁰ that two Pioneer 10 and 11 experimenters who have used large numbers of channel multipliers have found that not all channel multipliers tend to exhibit such finite lifetime characteristics. Their experience in testing hundreds of devices indicated that about half of the units tested were not depleted after 10^{12} to 10^{14} counts. Moreover, those devices which did withstand the 10^{14} counts have continued to function indefinitely.



Another device of the same family is the multi-anode photomultiplier described by Catchpole and Johnson.¹¹ In one version of this device, photoelectrons released from the photocathode are imaged using proximity focusing onto a microchannel plate (a compact array of channel multipliers). These channel multipliers provide the electron gain and the channel outputs collected by corresponding matrices of anodes. The use of a Chevron Microchannel Plate⁷ in this device allows large electron gains ($\sim 10^7$) to be achieved without significant ion feedback which could damage the photocathode. The maximum output current of the tube is limited to $\sim 10^{-7}$ A/cm² by the resistance characteristics of the microchannel plate, which correspondingly limits the individual anode currents. The anode current limitation and the possible finite channel lifetime are the most serious drawbacks of these devices for use on the OPM Imager.

Digicon-Type Detectors

The Digicon^{12, 13} is a relatively recent development that has been shown to offer great promise for astronomical applications. The commercially available Digicon (manufactured by Electronic Vision Corporation) is basically a magnetically-focused image intensifier in which the phosphor screen is replaced by an array of individually-connected, reversed-biased planar silicon diodes. Careful tube construction has resulted in measured dark noise performance approaching that expected due to the dark current of the photocathode itself. Since there is a one-to-one correspondence between the diode array and the photocathode planes, the equivalent dark current per channel (as defined by each diode) is lower than normally could be achieved with an equivalent array of PMT detectors. For astronomical applications, pulse counting techniques are used to read the channel outputs.

The acceleration voltage used in the Digicon to produce the electron-multiplication gain is typically 20 kv, yielding a gain of nearly 6000. The magnetic field used for focusing is provided either with a permanent

magnet array or with a solenoid. While detailed MTF measurements of the Digicon have not been performed, it is estimated that a limiting resolution (\sim 5 to 10% modulation) of \sim 70 to 80 lp/mm is currently being achieved.¹⁴

Certain characteristics of the commercially available Digicons are not optimum for the OPM Imager. These include the method of electron focusing and deflection, the choice of faceplate and substrate materials, the diode-array geometry, the high-voltage supply design, and the method of signal processing. Future developments in other areas are possible and would yield increased performance. These items will be discussed in the paragraphs which follow.

The use of magnetic focusing (in which the magnetic field is superimposed on the electric field used to accelerate the photoelectrons) has the advantage that high resolutions can be obtained with a flat photocathode over a relatively wide image plane. However, such an approach yields a larger and heavier tube than either proximity or electrostatic focusing. If a solenoid is used to produce the required magnetic field instead of permanent magnets, then the instrument power consumption is significantly increased. For the OPM Imager, the more limited FOV coverage and/or decreased resolution are of less importance than the increased power and/or weight.

With proximity focusing the transverse distance traveled by electrons emitted from the photocathode would be kept small by the short distance and the large electric field between the photocathode and diode array. The resolution with proximity focusing over the image field required for the OPM Imager (less than \sim 1 mm) is approximately a factor of two less (\sim 20 to 30 lp/mm) than that which can be achieved with electrostatic focusing. The weight and size for these two approaches are similar.

The fact that it is not practical to design an electrostatically focused lens for good extended field coverage with a flat photocathode is of little consequence for the OPM Imager because of the limited coverage required. Similarly, while the resolution expected (~ 40 to 50 lp/mm) is less than with magnetic focusing, it is quite adequate for the OPM Imager application. Finally, the desirable electrostatic deflection capability would be difficult to incorporate if proximity focusing were used. Thus, the use of electrostatic focusing for a "modified" Digicon-type detector suitable for the OPM Imager is indicated.

For operation in the trapped radiation belts expected at Jupiter and possibly at other outer planets, it is desirable that the detector faceplate and substrate materials be changed. The use of high-purity fused silica for the faceplate and selected MgF_2 for the photocathode substrate would be appropriate choices. The thickness of the elements should also be reduced to minimize the effect of Cerenkov radiation under operating conditions. The incorporation of these changes into a modified Digicon should pose no significant problems.

It is apparent that the diode array geometry must be modified as discussed in subsection 3.1.3 to optimize it for use in the OPM Imager. This is a straightforward modification and will not cause difficulty.

The high-voltage design should be changed to reduce power consumption, improve stability over the anticipated temperature range, and minimize the possibility of dielectric breakdown in space. While suitable precautions are essential, no fundamental problems are anticipated.

Since the typical IFOV dwell time is very short, e.g., ~ 0.1 msec at a spacecraft roll rate of 10 rpm for $\alpha = 0.1$ mr, pulse-counting techniques are not practical for the SNR performance (~ 100) assumed

to be required for the OPM Imager. (With the above assumptions, counting rates in excess of 10^8 counts/sec would be required.) Analog signal processing is therefore necessary and is described in subsection 7.2.

The widest spectral coverage presently available with a Digicon-type detector is obtained with a multialkali (extended-red) photocathode. For the OPM Imager application the spectral coverage and high responsivity afforded by a GaAs photocathode would offer a substantial improvement in performance. However, the present Digicon design is inherently restricted to being used with semi-transparent photocathodes. Semi-transparent GaAs photocathodes are being manufactured¹⁵ and improvements can be expected in the future.

The highest cathode responsivity (over the 0.4- to 0.9- μm spectral range) is obtainable with reflective-type (opaque) GaAs photocathodes. Thus, a modification incorporating a reflective photocathode while retaining the other features of a Digicon-type detector would be a significant improvement. An electron lens recently described¹⁶ is one approach that could be used to achieve this. In this electron lens the optical axis is separated from the electron-optical axis through the use of uniform electric and magnetic fields oriented to an angle θ with respect to each other. For $\theta = 15^\circ$ a limiting resolution of 50 lp/mm is obtained versus 70 lp/mm at $\theta = 0^\circ$. This lens used with a GaAs photocathode and coupled to a diode array should result in a detector with the desired properties.

A modified Digicon-type detector can provide near photoelectron-noise-limited, multichannel performance at low flux levels in a relatively light-weight, low-power package. Obviously, such a detector could prove useful for outer planets imaging applications and should certainly be developed further and space qualified.

5.1.2 Silicon Photodiode Array Detectors

For the purpose of discussing the various types of silicon solid-state detectors, this subsection will be broken down to five different array concepts. The first uses discrete silicon photodiode detectors to sense the scene flux optically relayed from the telescope image plane. The second uses an array in which each photodiode has an individual preamplifier and processing circuitry associated with it. The third approach consists of a self-scanned photodiode array in which a scanning circuit shifts the signal off the chip by accessing each array location sequentially. The fourth approach uses a phototransistor array in which both sensing and amplification are provided with the phototransistor array elements, and the outputs are sequentially shifted out. The fifth approach makes use of a CCD (charge-coupled device) imaging array in which photoexcited minority carriers are read out by multiple charge transfers through an array of induced junctions to the output.

The advantages of various array approaches using silicon detectors include small physical size (and hence low weight) and low-power requirements. Thus, the use of large numbers of detecting elements is practical for imaging applications. The much lower voltages required for the solid-state arrays in comparison to those for photoemissive detectors is an additional plus factor. Also, compared to most photoemissive-type detectors, the solid-state array detectors are much less affected by the presence of external magnetic fields.

Discrete Silicon Photodiode Detectors

This approach basically involves the use of a means of defining an array of individual FOVs and then relaying the flux incident on each FOV onto a discrete silicon photodiode. The output of each detector would then be amplified, low-pass filtered (or integrated), multiplexed, and digitized. The processed digital outputs would then be stored in the spacecraft memory prior to telemetry of the sampled imagery.

An array of fiber optics located in the focal plane is used in both the MSS/ERTS and VISSR/SMS instruments to provide the separation referred to above. Each fiber is then re-imaged onto a discrete photodiode detector. With this approach, individual detectors and preamplifiers can be selected and optimized with respect to responsivity, gain, noise characteristics, etc. However, unless the number of channels is relatively small, there would be a significant weight and complexity increase as compared to approaches using monolithic silicon array structures. In addition, there would be a reduction in overall system optical transmittance with the use of fiber optics. Finally, there would be a greater susceptibility of the imager to high-energy radiation effects with this approach because of the fiber optics. In summary, the disadvantages of the discrete silicon photodiode approach outweigh the advantages, and, hence, this approach was not analyzed further for use in the OPM Imager.

Silicon Photodiode Array With
Individual Readouts

With this approach, the output of each array detector would be individually processed in the manner described above for the discrete photodiode detectors. This approach lends itself to optimization of the array responsivity so that uniformity of the channel outputs to within a few percent can be achieved for a constant scene radiance over a relatively wide range of operating conditions. This, then, would significantly reduce the possibility of striping in the reconstructed imagery and/or reduce the required number of gray levels. Striping is a very noticeable defect in reconstructed imagery. Its prevention for an array with poor uniformity would require either a reduced gain (with consequent increase in the quantization noise in the other channels) or an increased number of gray levels (with a corresponding increase in the required telemetry rate).

The disadvantage of this approach with separate channel processing is that there is some increase in weight, power, and complexity compared to the alternative self-scanned or charge-coupled silicon photodiode arrays. However, for the relatively small number of channels envisioned for the OPM Imager (<100), the increased uniformity of the channel outputs, reduced electronic cross talk, and potentially better radiometric calibration accuracy are important advantages. For these reasons, this approach was selected as the preferred solid-state array approach for the OPM Imager, and it was analyzed in detail as Point Design 3. The spectral responsivity of a typical array photodiode has been included in Figure 5-1.

Self-Scanned Silicon Photodiode Array

The self-scanned photodiode array approach involves the periodic sampling of each array photodiode in a predetermined scan sequence. Some commercial self-scanned arrays sample the photodiode outputs directly, which permits the use of a single output amplifier. Since this approach yields reduced signal-to-noise performance, due to loading of the sampled output by the array switches and output bus, this would be a poor choice for the OPM Imager. Another approach has a pre-amplifier associated with each photodiode as is done, for instance, in the Westinghouse self-scanned photodiode arrays. In general, this results in an improved signal-to-noise performance.

In self-scanned arrays, the "noise" is often considered to consist of a random or "true" noise and pattern or coherent noise. The latter noise is position-dependent (varies across the array) and results from the coupling of external electrical transients associated with the scanning process into the signal channel. The pattern-noise component consists of both a fixed-offset component, which varies spatially across the array, but not temporally for a given set of operating conditions, and a random component. The fixed-offset component, in particular, is amenable to calibration and/or subtraction. For a typical high-quality

self-scanned array (Westinghouse), a noise equivalent signal (NES) of approximately 1 microjoule/m² with no incident scene flux can be expected.¹⁷ For an irradiance ($\sim 600 \text{ mw/m}^2$) that yields an output of about 60% of full scale, with dark offset subtracted, the NES is approximately doubled. The dark offset is typically 20% to 30% of full scale output. The above applies to an array with an active area of 0.7×0.9 mil, operated with an integration time of 1 msec and a 6000°K source bandlimited to 400 to 800 nm. Linearity is reasonably good for these arrays, and with thorough calibration is probably adequate for radiometric applications.

Silicon Phototransistor Array

The silicon phototransistor array approach is in many respects similar to that with a self-scanned array where a preamplifier is associated with each photodiode. One such phototransistor array (TRW) consists of an array of 195 phototransistor elements each with 0.7×0.9 mil active area and a center-to-center separation of 0.6 mil. A preamplifier is associated with each array phototransistor.

In operation, the base-collector capacitance of each phototransistor of the array is charged prior to the sensing interval and discharged during the exposure interval. The discharge is proportional to the absorbed energy. The readout of the 195 preamplified outputs of the TRW array consists of the serial readout within groups of 39 followed by the parallel readout of the five groups of 39.

The performance of the TRW array is comparable to that achieved with the Westinghouse self-scanned array under similar operating conditions. For the TRW array,¹⁸ the dark-noise level or noise equivalent signal (NES) is 1.2 microjoules/m² ($1.2 \times 10^{-3} \text{ w/m}^2$ for an integration time of 1 msec). This corresponds to an equivalent electron noise of approximately 800 electrons (rms). The linearity and dynamic range (10^3) for these arrays is comparable to that achievable with high-quality

self-scanned arrays. The overall responsivity variation at full scale output is 2/1 (three sigma value), suggesting that array selection would be essential if telemetry bandwidth and/or quantization noise are to be minimized.

The primary disadvantages to the use of phototransistor arrays are the stringent thermal environment requirements necessary for suitable phototransistor array operation. Because the responsivity across the array is a strong function of temperature by virtue of the phototransistor gain, it is essential that gradients across the array be both minimized and held constant irrespective of temperature changes external to the detector assembly. The alternative to active temperature control of the detector assembly for radiometric quality imagery would be an extensive calibration program that might, depending on the adequacy of the spaceflight simulation, still prove to be inadequate. As a result of the above considerations, the use of a phototransistor array seems less desirable for use on the OPM Imager than alternative silicon photodiode array approaches.

Silicon Charge-Coupled Device Arrays

The charge-coupled device (CCD) imaging array technology is an area of extremely rapid development. The discussion in this subsection will be limited to CCD arrays in which the sensing, storage, and transfer all occur on a monolithic silicon structure. Thus, the electronic readout mode (see subsection 5.1.3) will not be discussed here.

The CCD function consists of moving minority charge packets stored in potential wells formed under closely-spaced electrodes. The application of a multiphase clock provides the means to translate the potential minimum, and thereby produce the required unidirectional charge transfer. This can be achieved in several ways. In the so-called three-phase operation, the three drive lines, ϕ_1 , ϕ_2 , and ϕ_3 are connected in cyclic fashion to the sensing array electrodes. The cyclic

application of three voltage levels, V_1 , V_2 , and V_3 , where $V_1 > V_2 > V_3$ in the sequential set

$$\left. \begin{array}{l} \phi_1 = V_2, \phi_2 = V_3, \phi_3 = V_3; \\ \phi_1 = V_2, \phi_2 = V_1, \phi_3 = V_3; \\ \phi_1 = V_3, \phi_2 = V_1, \phi_3 = V_3; \text{ and} \\ \phi_1 = V_3, \phi_2 = V_2, \phi_3 = V_3, \text{ etc.}, \end{array} \right\} \quad (5-1)$$

provides unidirectional charge transfer by one electrode spacing. Four-phase operation can be achieved by the use of two-level metalization in the CCD structure. In a four-phase CCD, the scan direction is determined by the clock sequencing. In contrast, with two-phase operation, the charge transfer direction is determined by a built-in, potential-well asymmetry. This asymmetry can be achieved either with two-level metalization structures by using different oxide thicknesses or with a single metalization plus an ion-implanted barrier.

For practical application of a CCD in an OPM Imager, a single CCD shift register and output circuit would not be adequate. The limitation would be the significant image smearing that would occur when the CCD is being read out while also sensing the scene flux. Thus, a somewhat more complicated configuration in which the sensor array outputs are gated into a CCD transport array (or one transport array on each side of the sensing array for convenient chip organization) would normally be preferred.

In any charge-transfer device the charge transfer efficiency is a key factor in characterizing the device. The transfer inefficiency per transfer, ϵ , is the fractional signal charge left behind at each transfer. This results in a transfer of charge into successive charge packets. With n transfers, the overall transfer inefficiency product $n\epsilon$ results in a change of the frequency response of the system. An $n\epsilon$ product of 0.1 is considered necessary if the maximum bandwidth capabilities

of the device are to be achieved in an analog application.¹⁹ Transfer inefficiencies with $\epsilon < 10^{-4}$ have been reported. Such performance should be quite adequate for an OPM Imager application.

Blooming is a more serious problem with CCDs than with self-scanned arrays, since a scene highlight will merely saturate the affected diode(s) in the case of a self-scanned array. While blooming, or lateral spreading of charge, with CCDs can be reduced or eliminated with an overflow drain, this would complicate the geometry somewhat. However, should a CCD ultimately prove suitable for use on an OPM Imager, such a drain, or its equivalent to divert excess minority carriers when the potential well is filled, should certainly be required.

The absolute responsivity of CCDs is typically on the order of a factor of two lower than that of other silicon arrays. This results because the scene flux is incident on the front of the CCD. Thus, the flux must either pass through gaps between metal electrodes or through polysilicon electrodes. The responsivity loss due to the polysilicon is especially pronounced at the shorter wavelengths. It is possible to avoid such losses by thinning the chip so that illumination from the back surface can be used.

To achieve improved noise and transfer efficiency, it is desirable that the potential well minima not be at the silicon/silicon-diode interface, but rather within the bulk material. The advantages of the buried-channel versus the surface-channel CCD accrue because the charge is stored and transferred in the bulk silicon away from the surface-state traps. One disadvantage of the buried-channel CCD is that the charge capacity is more limited than that of an "equivalent" surface-channel CCD.

Typical CCD array SNR performance is comparable to that achievable with other types of silicon arrays. For the best devices built to date, an equivalent electron noise on the order of 150 electrons (rms) is claimed (Fairchild data).

Some of the potential advantages unique to CCDs offer great promise. The so-called time-delayed integration method can be used to increase the SNR by summing signal charge in the along-scan direction. With this approach the number of photodiodes would be increased by stacking detectors along the roll scan direction. It is then possible, by appropriately matching the sampling rate to the roll rate, to accumulate a signal charge n times larger from a given IFOV (for a factor of n more detectors). Since the charge summing occurs before preamplification, the SNR improvement will be nearly proportional to n , assuming amplifier noise dominates, unless the signal is high enough that photon noise becomes significant. In this latter case, the improvement would approach a \sqrt{n} dependence. It is apparent that further developments in CCD technology will make such sensing arrays strong candidates for possible OPM Imager use. For the purpose of this study, a more established silicon-array approach was selected for the solid-state point-design approach (OPM Imager Point Design 3). However, it is strongly recommended that future CCD developments be actively monitored, since further progress in this area will undoubtedly occur.

5.1.3 Other Candidate Detectors

In this subsection, the characteristics of candidate detectors for an OPM Imager with extended spectral capability are reviewed. In the ultraviolet spectral region, photomultipliers with solar-blind photocathodes or channel-multiplier detectors (open channel) are usually used. Thus, detectors suitable for the ultraviolet are similar to those used for visible and near-infrared applications, although pulse-counting techniques are more generally applicable in the ultraviolet. Because of this close similarity with detectors already described, the remaining portion of this text will be restricted to detectors suitable for operation in the infrared.

For extension of multispectral coverage into the infrared, either thermal or quantum detectors can be considered. Space-qualified thermal detectors include thermistor-bolometer, thermopile, and pyroelectric detectors. The detectivity obtainable with thermal detectors is, in general, lower than that obtainable with quantum detectors. However, as opposed to many quantum detectors, thermal detectors do not require cooling to cryogenic temperatures. The spectral responsivity of thermal detectors is very nearly constant, i.e., "gray" over an extended spectral interval. This latter feature is particularly useful in a wide spectral bandpass radiometer, since interpretation of results is simplified.

It is anticipated that the scientific requirements for an OPM Imager would dictate that for the infrared channel(s), the IFOV(s) be equal to a small multiple of that for the visible/near-infrared spectral band(s). This, coupled with the probable desire to limit the spectral bandwidth of the infrared channel(s) to improve the interpretation of the results, would probably lead to the selection of quantum detectors for a multispectral OPM Imager. For this reason, the characteristics of various quantum detectors will be discussed in some detail.

In Figure 5-2, the spectral detectivity (expressed in terms of the normalized detectivity, D^*) of a number of candidate quantum detectors is shown. Also shown (dashed lines) are the theoretical limits for ideal background-limited photoconductive and photovoltaic detectors operated with a 2π -steradian field of view for a 295°K background temperature. Cold shielding and cold spectral filtering can be used to reduce the background flux incident on the detector and thereby increase achievable D^* .

Detectors which require cooling to less than about 77°K (LN_2) have not been included in the figure since passive radiative cooling would probably not be practical to achieve significantly lower temperatures. In addition, the requirements imposed on radiation cooler

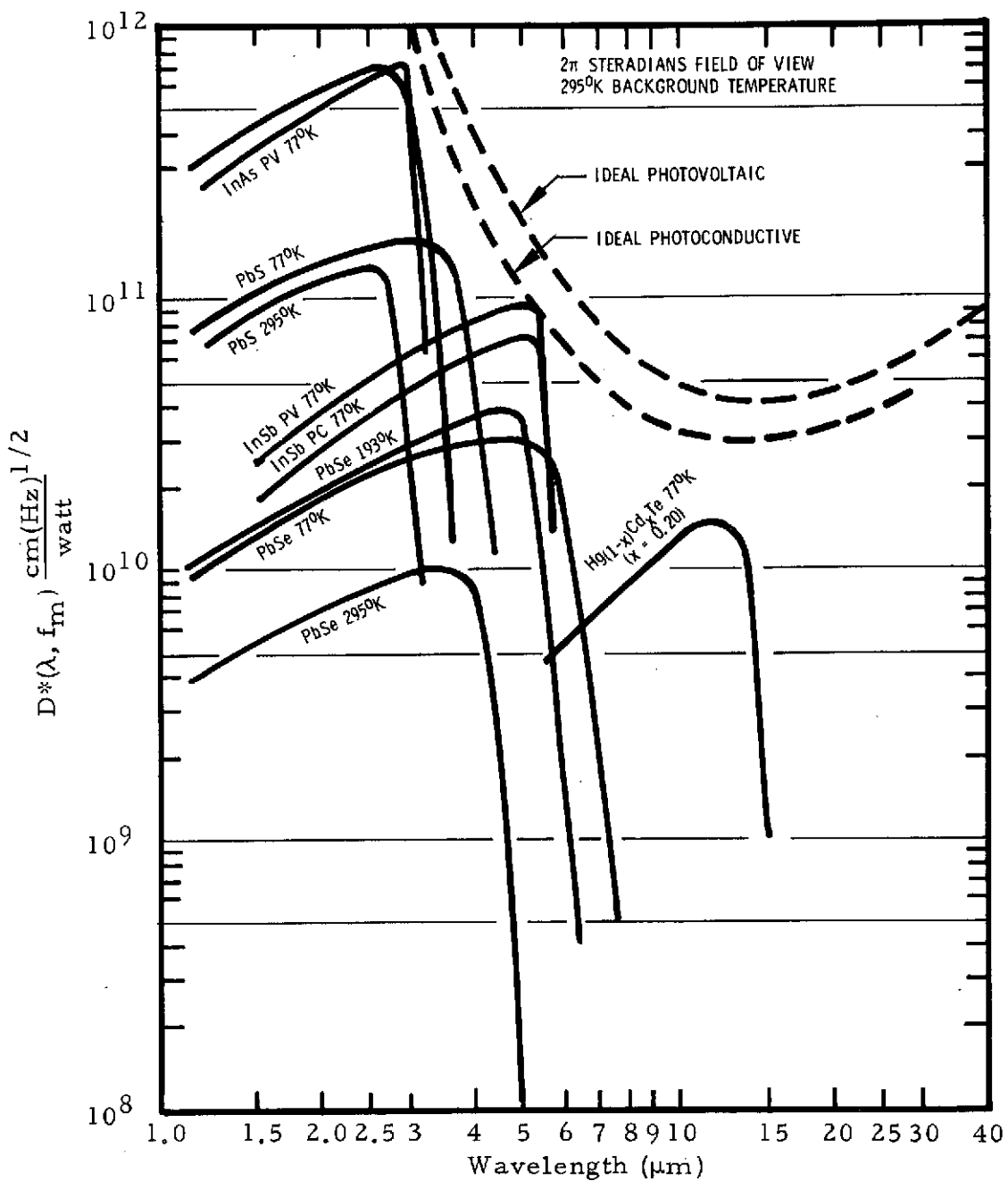


Figure 5-2. Detectivities of Candidate Infrared Detectors

design with a spinning spacecraft (spin axis assumed to be in plane of the orbit) can be expected to be rather severe for flyby and orbiter missions because of the changing geometry. A spin-stabilized spacecraft with spin axis oriented perpendicular to the ecliptic would significantly relax the constraints on the radiation cooler design. With the exception of the effect due to changing spacecraft-planet distance, most of the potential radiation cooler problems have already been solved with the VISSR instrument for the latter spin axis orientation. (The VISSR will be flown on the spin-stabilized SMS spacecraft and operate in earth-synchronous orbit.)

As indicated in Figure 5-2, the spectral response of quantum detectors is limited to wavelengths less than about 5 μm for operation near 300°K. In addition to the room temperature PbS and PbSe detectors shown, Ge and Si-Ge alloy photodiodes are possible candidates for operation at wavelengths on the order of 1.5 μm or less.

For operation in the region between the silicon photodiode cutoff near 1 μm and about 5.5 μm , photovoltaic InSb is probably the best detector choice. The peak D^* for photovoltaic InSb remains essentially constant for detector temperatures up to about 110°K and decreases by less than a factor of three for operation at 150°K. A well-developed array technology and good linearity at low signal levels are additional plus factors.

At longer wavelengths, HgCdTe would probably be the recommended choice for operation between the InSb cutoff to near 20 μm . By varying the proportions of Hg and Cd, the long-wavelength cutoff is widely selectable, thus making this material extremely useful. The suitability of this detector for use in the 8- to 13- μm water vapor window has led to a well-developed technology for the production of HgCdTe detector arrays. HgCdTe detectors are used for the VISSR/SMS and for the fifth band of the MSS/ERTS instruments. In each case, the proper

operating temperature ($\sim 100^{\circ}\text{K}$) is achieved through radiative cooling. PbSnTe is another candidate material for long-wavelength detectors. However, the more highly developed, space-qualified HgCdTe detectors presently would be the recommended choice.

It is appropriate to mention how CCDs may prove useful in combination with certain infrared detectors. A CCD can be used to replace the multiplexer of an infrared system when the array detectors (operating in the charge integration mode) are dumped into a CCD and clocked out. This is the so-called electronic readout mode and has particular promise for use with InSb or short-wavelength cutoff HgCdTe arrays. The signal-to-noise increase achievable through the use of time-delayed integration can similarly be obtained through the coupling of an along-scan detector array with silicon CCDs.

5.1.4 Detector Radiation Effects

In this subsection, the important characteristics of the various detectors will be compared as they relate to operation in a high-energy radiation environment. Obviously, the detectors are only one part of the radiation effects problem; however, since low-level signals are involved, it is often the most important aspect of the total system radiation susceptibility. Both permanent damage and interference during operation are of importance, and these effects could be evaluated from a known or modeled environment. While much effort has gone into generating realistic models of the Jovian radiation belts in particular,²⁰ it was felt that basing detailed point designs on such a model was inappropriate, both because of the effort required and because of the probable lack of detailed validity of the conclusions. This is true since a substantial improvement of our knowledge of these radiation belts should be available from the Pioneer 10 and 11 Missions. Thus, a more general approach to the radiation effects problem was taken with the expectation that data will be available in the future to define such instrument details as the required radiation shielding.

In the point designs described in Section 6, precautions were taken in both the optics and electronics to minimize the effect of high-energy radiation. For example, the telescope is an all-reflective design, and in each of the four point designs, the total transmissive optical path length is minimized. An all-reflective design is possible since wide field coverage is not essential, as the total number of channels required for the spin-scan OPM Imager is relatively small. In the design of the electronics, provision has been made to subtract any dc signal offsets produced by high-energy radiation. In this manner, the dynamic range of the telemetered data can be maintained with some degradation in the imager SNR as the primary remaining effect. It is anticipated that the detector and/or low-level preamplifiers will provide the main limit to operation in planetary radiation belts.

Radiation Effects - PMT-Type Detectors

Photomultiplier-type detectors have received the most extensive radiation testing of any of the candidate detectors for the spin-scan OPM Imager. The primary conclusions drawn from such testing will be summarized first, followed by discussion of some specific results relevant to the OPM Imager.

For PMT-type detectors, the "signal" produced by the high-energy radiation (including charged particles) originates predominately from the photocathode/window combination rather than from the electron-multiplier structure. Much of the apparent permanent reduction of photocathode responsivity caused by large accumulated radiation dosage is attributable to radiation darkening of the tube window. At high dose rates, the tube dark current can be expected to increase markedly, perhaps orders of magnitude, with a consequent decrease of detector dynamic range. Where adequate dynamic range remains, this radiation signal can often be "subtracted out" with little adverse effect on sensor performance.

Radiation shielding is possible and has been used to reduce the effects of the Van Allen belts for earth orbiting instruments.²¹ For the very high-energy electrons and protons expected in the Jovian belt, it would be difficult to provide sufficient shielding (due to weight limitation) to assure that the primary particle flux is reduced to negligible levels. Even if this could be achieved, the energy loss that appears as Cerenkov radiation, luminescence, bremsstrahlung, and secondary electrons could cause interference. The reduction of the transmissive optical elements to a minimum can significantly reduce these first two sources of radiation signals. Similarly, the coupling of the source of the interference photon flux to the photocathode has been shown by Young²² to be an important consideration and is automatically reduced in some side-window PMTs.

Radiation testing^{21, 23} using 2.5-MeV electrons produced with a Van de Graaff accelerator was used to simulate the inner Van Allen belt, and thereby account for the high dark current observed on the OGO-2 Main Body Airglow Photometer. As discussed in Reference 21, added shielding of aluminum and tungsten with this instrument, coupled with an orbit not exceeding 925 km, resulted in a background current reduction of more than two orders of magnitude on OGO-4. The PMT used in both cases was an EMR 541E-05M (S-20, sapphire window). The marked difference in radiation background current (nearly five orders of magnitude) between that instrument on OGO-2 and a horizon scanner on the same spacecraft also is discussed. The horizon scanner was similar except: 1) the PMT was an EMR 641E of the side-window type with Corning 7056 glass as the window, and 2) the opaque trialkali photocathode was decoupled from the entrance window and additionally shielded with aluminum and tungsten.

A rather complete series of radiation tests on several EMR photomultiplier tubes has been reported by Wey.²⁴ The PMTs tested were EMR 541A-01-14, 541A-05-14, 541E-01-14, and 541E-05-14.

(The A and E designations denote S-11 and S-20 type photocathodes, respectively; the 01 and 05 designations denote 7056 glass and sapphire windows, respectively.) In the tests, both accumulated dose and radiation rate effects were evaluated with ^{60}Co sources.

In the accumulated dose tests the detectors were alternately irradiated and checked for responsivity and dark current at dose levels of 10^4 , 10^5 , and 10^6 rads. These data are given in Table 5-1, which is taken directly from Wey's report. A sizable increase in dark current is seen to occur after each radiation dose. The dark current tended to decrease with time following exposure and was within an order of magnitude of the original value two or three days after the tests. The greater responsivity decrease in tubes with 7056 glass was probably due to the greater radiation darkening of that window material compared to that of sapphire. In the radiation rate measurements, the dose rate was varied over a factor of more than 20 and showed the expected increase of the radiation signal proportional to the dose rate. The results also confirmed the results of other investigations that tubes with sapphire faceplates are significantly more radiation rate sensitive than other faceplate materials due to luminescence.

The radiation testing of an RCA C31025J (GaAs photocathode, sapphire window) previously mentioned was accomplished with ^{60}Co sources. Two types of measurements were made with the tube active in the radiation environment: dark current was measured as a function of high voltage while subjected to dose rates from approximately 10 rad (Si)/hour to approximately 40 rad/hour; and, secondly, the anode current was measured as a function of illumination level while subjected to the same radiation doses, but at two different high-voltage (gain) settings. Graphs of the resultant data are shown in Figures 5-3 and 5-4, respectively. The dark current and anode current resulting at a fixed illumination level is shown as a function of time before and after subjecting the tube (inactive) to a 7000-Curie cobalt-60 source, yielding

Table 5-1. Accumulated Dose Experiments on EMR Photomultiplier Tubes (^{60}Co Source
at Hughes Aircraft Company, Fullerton, May 1968)

TUBE TYPE →		541E-01-14 (S-20, 7056 GLASS)		541E-05-14 (S-20, SAPPHIRE)		541A-01-14 (S-11, 7056 GLASS)		541A-05-14 (S-11, SAPPHIRE)	
DATE	DOSE	LIGHT*	DARK	LIGHT*	DARK	LIGHT*	DARK	LIGHT*	DARK
5/6/68	NEGLIGIBLE (BASELINE)	1.35×10^{-8}	1.3×10^{-11}	3.75×10^{-8}	---	4.1×10^{-8}	---	6.4×10^{-8}	1×10^{-10}
5/6/68	AFTER 10^4 RADS	1.35×10^{-8}	8.0×10^{-10}	3.3×10^{-8}	1.1×10^{-9}	4.4×10^{-8}	6.2×10^{-10}	6.0×10^{-8}	6.2×10^{-10}
5/6/68	AFTER 10^5 RADS	1.55×10^{-8}	4.4×10^{-9}	3.6×10^{-8}	1.1×10^{-8}	4.4×10^{-8}	4.8×10^{-9}	6.2×10^{-8}	2.3×10^{-9}
5/6/68	AFTER 10^6 RADS	1.55×10^{-8}	5.7×10^{-9}	3.5×10^{-8}	4.0×10^{-8}	3.3×10^{-8}	5×10^{-9}	6.1×10^{-8}	4.4×10^{-9}
5/13/68	RETEST	1.05×10^{-8}	9.0×10^{-11}	3.2×10^{-8}	1.9×10^{-10}	2.75×10^{-8}	1.2×10^{-11}	6.35×10^{-8}	6.0×10^{-11}

*USING GALLIUM PHOSPHIDE LIGHT SOURCE AT 100 MILLIAMPS AND 1000 VOLTS ACROSS THE PHOTOMULTIPLIER.

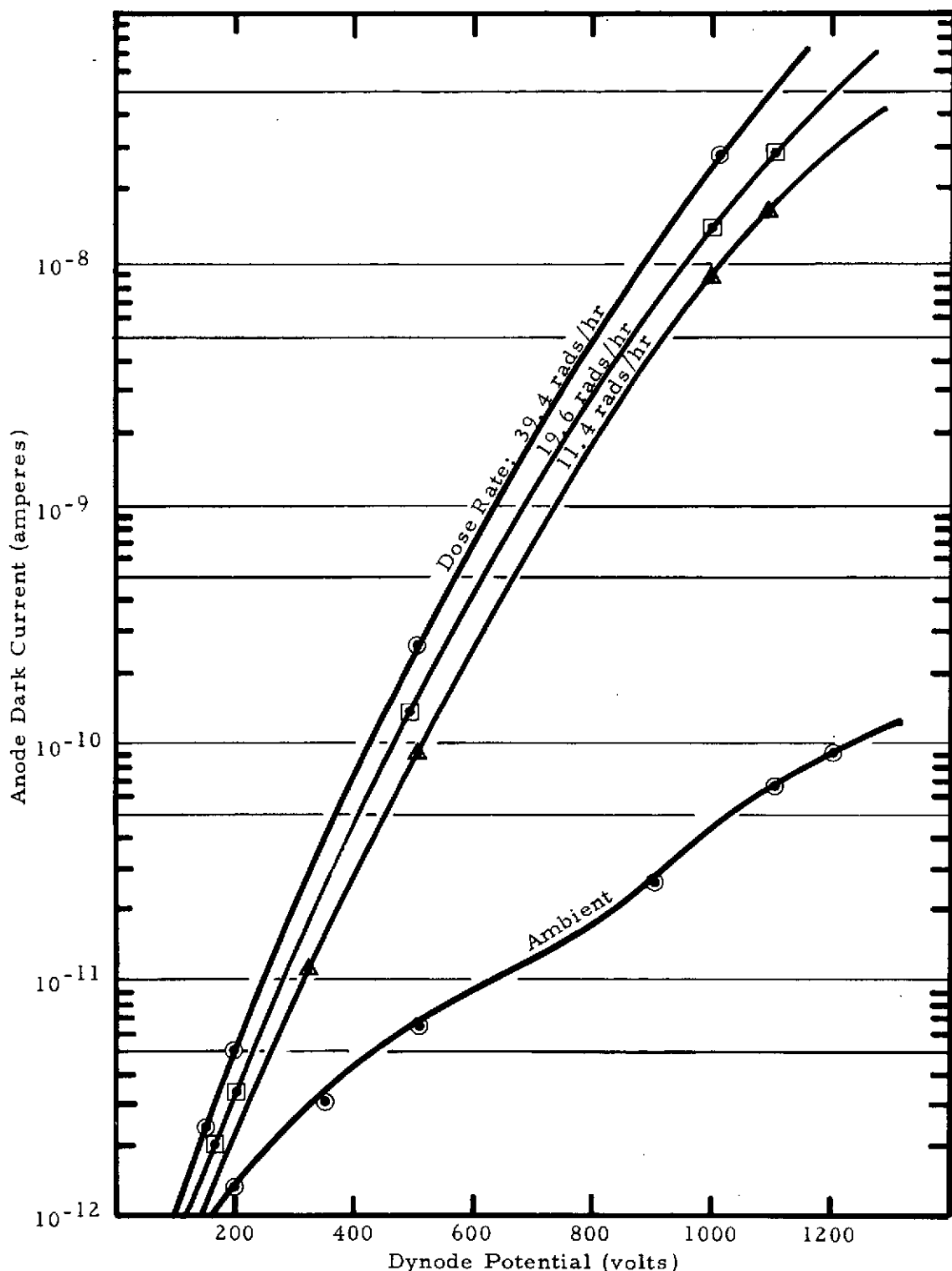


Figure 5-3. GaAs PMT (RCA 31025J) Dark Current as a Function of Dynode Voltage for Various Radiation Dose Rates (^{60}Co Source)

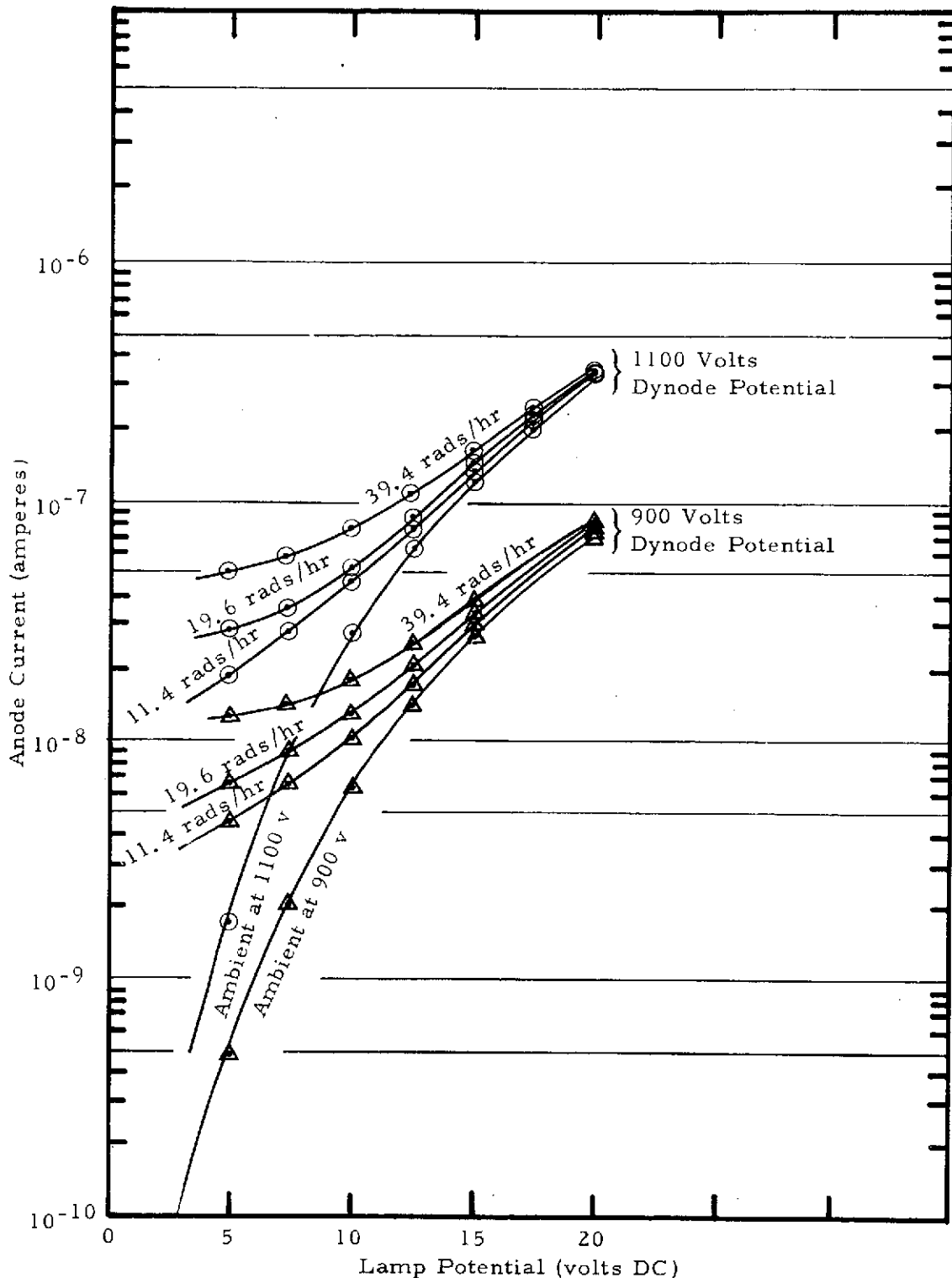


Figure 5-4. GaAs PMT (RCA 31025J) Anode Current as a Function of Illumination at Various Radiation Dose Rates (^{60}Co Source)

a cumulative dose of 10^6 rads in 70 minutes (see Figure 5-5). Post-exposure dark current was excessively elevated due to the combined radiation effects; however, much of this is probably attributable to the sapphire window. The tube responsivity degraded approximately 12%, and the dark current increased in excess of an order of magnitude permanently.

Radiation Effects - Image Dissectors

An image dissector can be expected to have properties in a high-energy radiation environment similar to those observed with a PMT-type detector of similar geometry. The main difference is that the effective photocathode area, i. e., portion of photocathode sampled at any given time, is much smaller than for an "equivalent" PMT. Thus, the radiation induced signal current that originates from the photocathode should be less than that for the equivalent PMT by a factor approximating the ratio of the effective photocathode areas. Wolff²⁵ found, for an OGO-1 experiment that used an image dissector tube, that radiation noise was proportional to the effective cathode area and, therefore, concluded that most of the noise originated in the optical elements and photocathode rather than in the dynode structure or in the subsequent electronics. Permanent damage effects in an image dissector should be similar to that observed in an equivalent PMT with the same photocathode material.

Radiation Effects - Channeltron-Type Detectors

Figure 5-6 shows typical dark-current values at several radiation dose rates for a BX-784 Dual Channeltron^R developed for the Pioneer 10 and 11 IPP instrument.²⁶ As the rate approaches 10^3 rads/hr of Cobalt-60 exposure (primarily 2-MeV gamma rays and 1- to 1-1/2-MeV Compton secondary electrons), the dynamic range between the dark value of the anode current and the maximum usable channel current of 2×10^{-7} A is increasingly restricted. To isolate the major source of the radiation induced dark current, a BX-786 tube with one

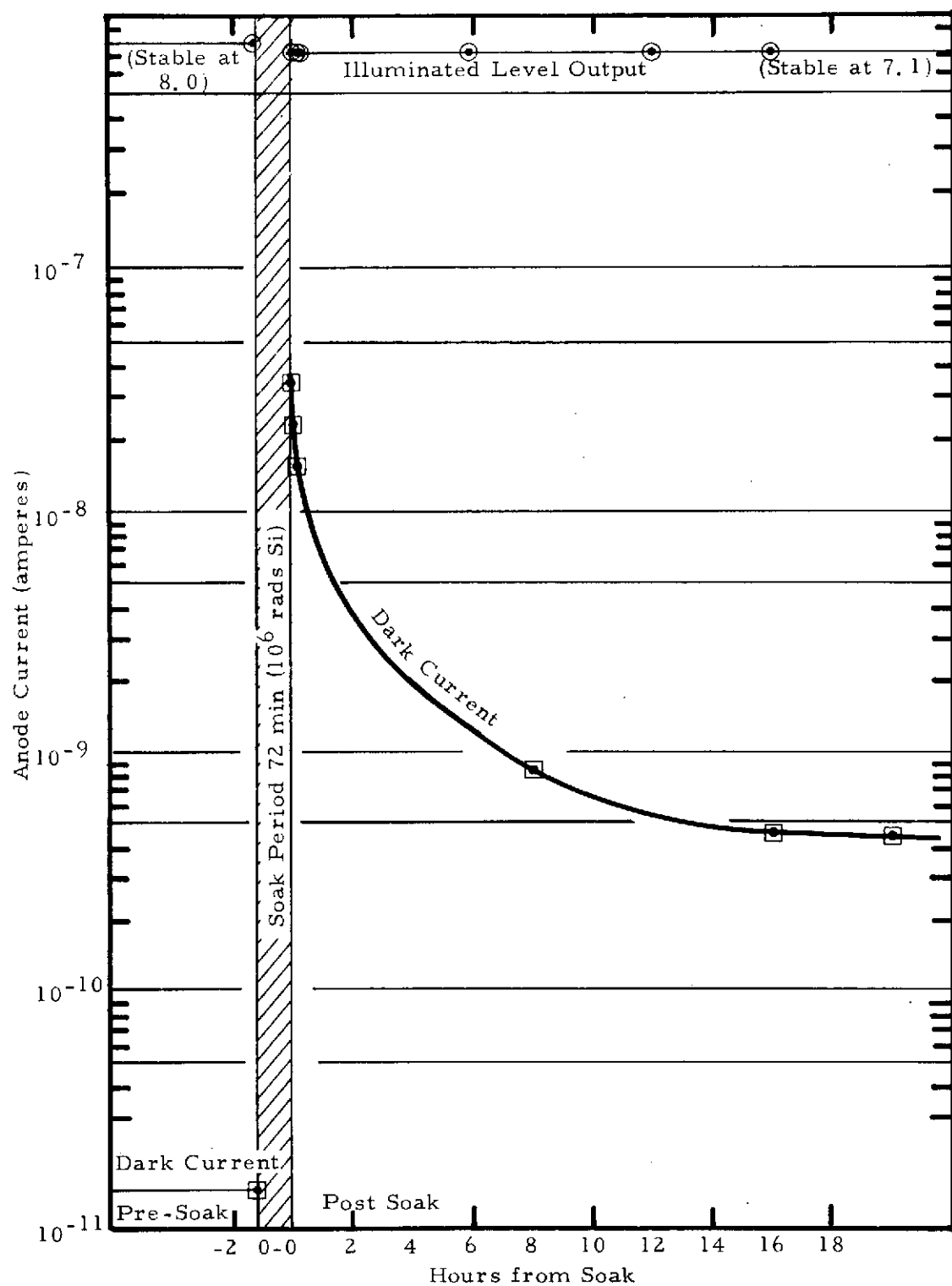


Figure 5-5. GaAs PMT (RCA C31025J) Output Current as a Function of Time Before and After Exposure to 10^6 rads (Dark and Illuminated)

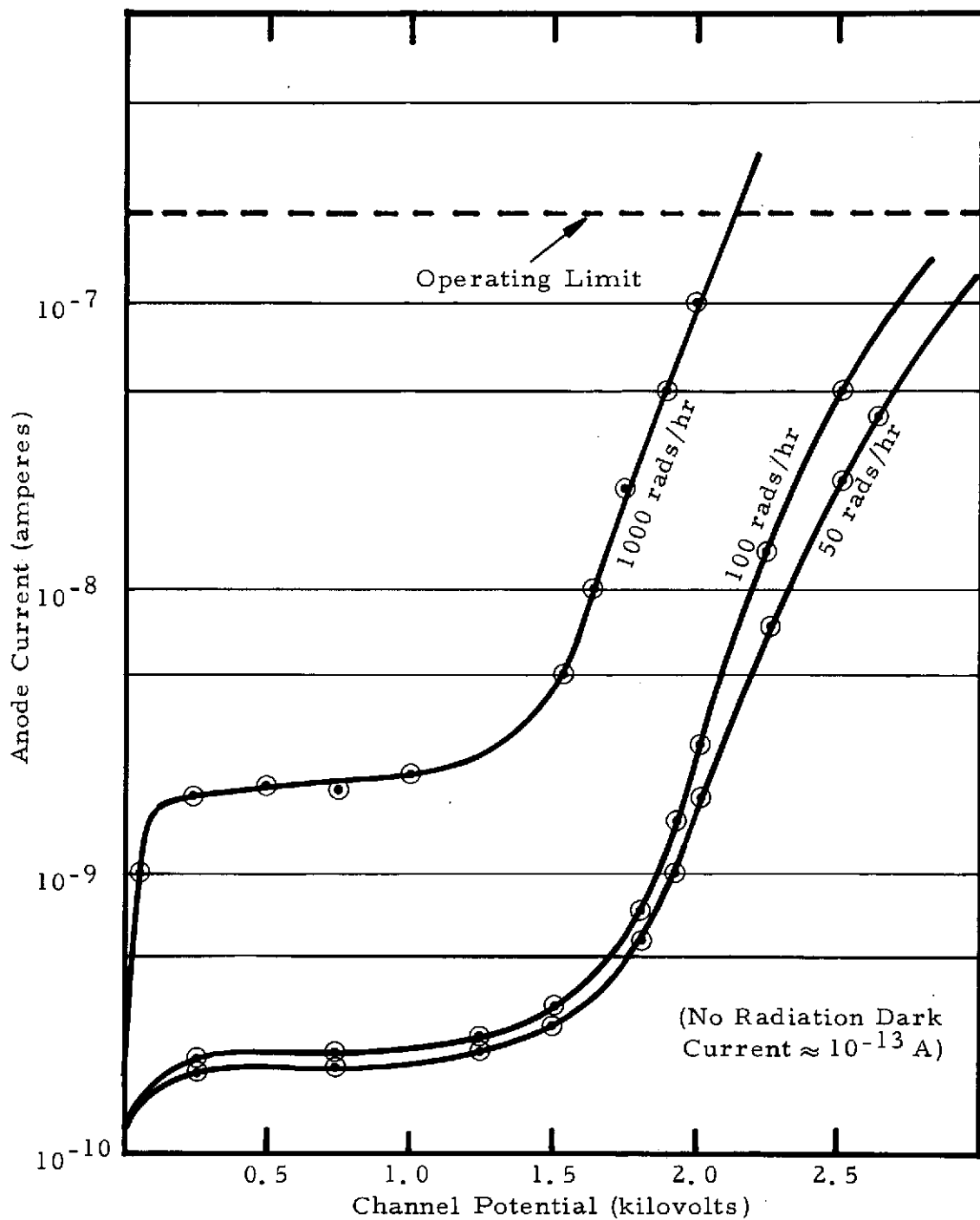


Figure 5-6. Channeltron Anode Current as a Function of Channel Potential when Exposed to a Radiation Environment

complete channel and with one channel minus the photocathode was tested in a radiation environment of 10^3 rads/hr. In this test the output of the "blind" channel was a direct result of radiation detection by the channel multiplier. The difference between the "blind" and complete channels, therefore, represents the sum of the Cerenkov emission, phosphorescence, and radiation induced photocathode outputs. It was observed that the channel multiplier contributed about half the dark current under such conditions, in contrast to the results for PMT and image dissector sensors where the electron gain stages yield a smaller relative contribution.

A detection system that uses a channel plate array coupled with a photoemissive surface to yield a multi-anode photomultiplier is also of interest, but has not been radiation tested to our knowledge. Since the effective photocathode area for each channel will be much smaller than that for the 0.25-cm diameter photocathode of the BX-784 used on Pioneer 10 and 11, the radiation induced photocathode current should be correspondingly lower. However, a corresponding reduction in the channel multiplier diameter will restrict both the maximum usable output current and the radiation induced channel multiplier currents approximately proportionately. Thus, it may be necessary, in such a case, to provide an additional stage of amplification, for instance, with an electron-bombarded diode array within the tube. While such an approach is feasible, it seems more complex and hence less desirable than the use of a Digicon-type detector.

Radiation Effects - Digicon-Type Detectors

A modified, Digicon-type detector offers great promise with regard to operation in a high-energy radiation environment. To illustrate the potential advantage of this detector, the relevant parameters will be compared to other candidate photoemissive and solid-state detectors.

The basic detection process for a PMT, image dissector, Channeltron (including channel photo arrays), and Digicon detectors are similar. That is, flux incident on a photocathode produces electrons which, in turn, are accelerated and produce an electron gain upon impact. This electron gain can be achieved by several means, such as a series of discrete dynodes, a channel multiplier, a silicon diode, etc. With the solid-state photodetectors considered for use on the OPM Imager, the absorption of a photon produces an electron-hole pair, and subsequent amplification of this signal yields the desired high-level output.

When a Digicon detector is used for imaging, only a small area of the photocathode is imaged onto the corresponding diode. Thus, the effective photocathode area per channel is small compared to that normally used for an equivalent system using PMT detectors. If the same type of photocathode were used with each of these detectors, the ratio of the high-energy induced photocathode currents could be expected to be proportional to the ratio of the corresponding photocathode areas producing these currents. Thus, a system using a Digicon-type detector should be less sensitive to radiation induced photocathode signals than a similar system using PMT detectors. An image dissector would have the same relative advantage as the Digicon in this respect, although it would be at a disadvantage due to SNR considerations compared to a system based on either PMT or Digicon-type detectors.

The radiation induced signals in diodes serving as high-gain multipliers in a Digicon should be relatively unimportant in comparison to those resulting from electrons emitted at the photocathode. This follows since the latter signals are greater by the diode gain due to the accelerating potential. The area of a diode also is small compared to the area of the first dynode of a PMT detector (the other dynodes are of much less importance), thus yielding another potential advantage in

favor of the Digicon approach. For a Channeltron or channel plate array, the potential advantage due to geometry is less, but still may be significant.

As compared to a photodiode array, the Digicon-type detector has a potential gain in radiation susceptibility of this same factor of the diode gain for primary signals generated in the respective diodes. For the Digicon, the radiation induced signals from the photocathode also contribute to the radiation induced signal and would reduce this advantage. It is probable that the array diodes in the Digicon could be optimized better with regard to the undesired effects caused by high-energy radiation than could an array of photodiodes which has severe restrictions imposed by the need for high responsivity, very low dark current, etc.

While it is apparent that the Digicon detector seems suitable for use in a radiation environment, it is also true that there is a paucity of empirical data to support this contention. Obviously, an experimental evaluation of a Digicon (preferably the modified Digicon recommended as being most suitable for use in the OPM Imager) is needed to evaluate properly these characteristics. It is recommended that such a study be undertaken.

Radiation Effects - Silicon Detectors

Radiation effects data on silicon detectors are much less readily available than those for photoemissive detectors and are more difficult to interpret. The problem here is that many of the most recent detector configurations, such as the self-scanned MOS and CCD arrays, have not been radiation tested. While general statements often are made about the radiation susceptibility of such devices, for instance, that arrays using MOS structures will have a useful fluence range similar to other MOS devices, such an approach cannot be trusted in designing imaging systems where a severe radiation environment is expected. A quote from the NASA Space Materials Handbook²⁷ seems apropos:

"The complexities which broaden the scope of the problem of radiation vulnerability and circumvention result from: 1) multiplicity in degradation modes, and corresponding multiplicity in tolerance levels, 2) possible interaction between modes, 3) dependence on secondary environments, 4) damage to circuits or degradation of system performance by transient effects, 5) dependence on nonradiation ambients such as temperature, pressure, mechanical stress, and electrical stress, 6) wide variations in radiation tolerance of devices of similar electrical characteristics fabricated by different manufacturers or even by the same manufacturer, 7) very rapid developments and changes in electronic device technology and application, and 8) proximal or interface effects related to configuration rather than basic transducer properties."

In the case of the several alternative self-scanned and CCD arrays currently available and potentially suitable for the OPM Imager and other spaceflight usage, points 1, 2, 6, and 7 are particularly pertinent.

With the above reservations duly noted, the results of some radiation effects tests on silicon detectors will be given. An EG&G SGD-100A silicon photodiode exposed to a $2 \times 10^{12} \text{ n/cm}^2$ fluence²⁸ was found to be unaffected in responsivity (to the $\pm 5\%$ measurement accuracy) and to have a dark-current increase of one order of magnitude. A set of measurements by Martz and Neilsen²⁹ on the effect of gamma and 6-MeV electron irradiation on RCA silicon photodiodes produced the following results. The noise was increased by over two orders of magnitude for a $3.5 \times 10^5 \text{ r/hr}$ gamma flux, and, for electron doses less than about $2 \times 10^{14} \text{ e/cm}^2$, no permanent reduction of signal nor noise increase was observed. Following the maximum dose of 10^{16} e/cm^2 , the measured SNR decreased nearly 50% with more than 30% resulting from signal decrease.

In contrast to other candidate arrays, some radiation data are available on the TRW phototransistor arrays. For these arrays³⁰ the phototransistor current gain was found to be unchanged for 10^3 rads and to be reduced by 10% after 10^5 rads of gamma irradiation using a ^{60}Co source. With 1-MeV neutron irradiation, the current gain was reduced by 20% and by 75% after 10^{13} and 10^{14}n/cm^2 , respectively.

It is recommended that various candidate silicon arrays be radiation tested both actively and for dose effects. This recommendation is based both on the paucity of such data and the probable necessity for such data for future mission planning, especially for outer planet missions. It is expected that this will be an important consideration in the selection of the optimum detector for such missions.

Radiation Effects - Other Candidate Detectors

Since there was no significant effort in this study to incorporate other than visible and near-infrared detectors in the OPM Imager design, the effect of high-energy radiation on other candidate detectors is only briefly reviewed. The data by Parker,³¹ which included results of proton irradiation on several types of infrared detectors, are probably the most useful. In those tests, HgCdTe, PbS, and thermopile detectors were exposed to a fluence of $\sim 10^{13} \text{ p/cm}^2$ of $\sim 140\text{-MeV}$ photons with no permanent effects observed. An EMR channel multiplier (EMR-648F) suitable for UV usage was exposed (unpowered) to similar fluences with no damage. A PbS detector was actively monitored at a flux of $\sim 10^8 \text{ p-cm}^{-2} \text{ sec}^{-1}$ with no interference observed.

As a part of a previously mentioned study, PbS detectors (from several manufacturers) and SBRC PbS detectors were irradiated with a range of gamma, electron, and neutron fluences.

The resistance and noise variation and SNR degradation for the PbS detectors following gamma irradiation (^{60}Co source) varied widely both by manufacturer and by type. The best PbS detectors from a

radiation standpoint showed a negligible effect on SNR up to a 70-megaroentgen dose. Coated PbSe detectors showed similar radiation resistance to that exhibited by the best PbS detectors, while the uncoated detectors underwent orders of magnitude changes of all parameters. The PbS and PbSe detectors were also exposed to a 6-MeV pulsed electron beam from a linear accelerator. The behavior here was similar to that under gamma irradiation with degradation in the SNR starting at about 10^{14} e/cm^2 . Only PbS detectors were tested with neutrons. Up to fluences of $5 \times 10^{12} \text{ n/cm}^2$ (a relatively low dose), there was no measurable change in detector parameters.

Much additional information is available on radiation effects in infrared detectors. However, since weight limitations may well preclude the addition of infrared channels to an OPM Imager, it seems inappropriate to discuss this area in more depth. Should the need for such channels arise, it is probable that sufficient data are available to adequately evaluate this aspect of the radiation effects problem.

5.1.5 Signal-to-Noise (SNR) Equations

A knowledge of the SNRs achievable with various candidate detectors is essential for trade-off analyses in the selection of the optimum detector for a given requirement. In the paragraphs which follow, SNR expressions are given for various candidate detectors.

SNR Equations – Photoemissive-Type Detectors

The signal current from the photocathode can be expressed by

$$i_s = A\omega \int N(\lambda)R_d(\lambda)T_o(\lambda)d\lambda \quad (5-2)$$

where $N(\lambda)$ is the spectral radiance of the scene [see equation (3-20), subsection 3.1.5], $R_d(\lambda)$ is the cathode responsivity at wavelength, λ , $T_o(\lambda)$ is the optical transmittance at wavelength, λ , A is the clear area of the entrance aperture, and ω is the IFOV solid angle. With proper instrument design of the OPM Imager, the dominant noise source will

be shot noise of the photoelectrons. The rms signal shot noise, i_n , referred to the photocathode is given by

$$i_n = (2e k_d i_s \Delta f_n)^{1/2} \quad (5-3)$$

where e is the electron charge, k_d is a noise factor to account for added noise in subsequent electron multiplication, and Δf_n is the effective noise bandwidth.

For a PMT detector the noise factor, k_d , is given to good approximation by

$$k_d = \sigma / (\sigma - 1) \quad (5-4)$$

where the gain per stage, σ , is a constant. For this system modeling, a value of $k_d = 1.3$ was used for the PMT detectors which corresponds to a value of σ between 4 and 5. If a very high-gain secondary-electron emitter is used for the first dynode, then the noise factor can be made to approach unity. GaP activated with cesium has been shown,^{32, 33} to produce gains of 30 or more as compared to gains of 4 to 6 obtained with conventional dynode materials. For detectors which use channel multipliers, k_d values on the order of 1.3 can be expected. The electron-focusing stage of a Digicon detector typically has an electron gain greater than 1000 and, thus, $k_d = 1.0$ is appropriate for such detectors.

For much of the parametric modeling, it is convenient to set $\omega = \alpha^2$, i.e., to assume the IFOV is square. Finally, the clear area of the entrance aperture is related to the area obscuration factor, ϵ^2 , and aperture diameter, D , by

$$A = \pi D^2 (1 - \epsilon^2) / 4 \quad (5-5)$$

Combining equations (5-2), (5-3), and (5-5) yields the peak signal to rms noise at zero spatial frequency, SNR ($\nu = 0$), given by

$$\text{SNR } (\nu = 0) = \frac{i_s}{i_n} = \left[\frac{\alpha^{3/2} D}{\Omega^{1/2}} \right] \left[\frac{(1 - \epsilon^2) \int N(\lambda) R_d(\lambda) T_o(\lambda) d\lambda}{16 e k_d k_f} \right]^{1/2}$$

$$= K \alpha^{3/2} D (k_N / \Omega)^{1/2} \quad (5-6)$$

Here K is a constant dependent on the instrument characteristics and reference scene conditions given by

$$K = \left[(1 - \epsilon^2) \int_{400 \text{ nm}}^{900 \text{ nm}} N_0^\circ(\lambda) R_d(\lambda) T_o(\lambda) d\lambda / 16 e k_d k_f \right]^{1/2} \quad (5-7)$$

In the above equation, $N_0^\circ(\lambda)$ is the spectral radiance of the object of interest (assumed Lambertian) at 0° sun-zenith angle. The scaling factor, k_N , is defined by

$$k_N = \frac{\int_{\text{Selected Spectral Bandpass of Imager}} N(\lambda) R_d(\lambda) T_o(\lambda) d\lambda}{\int_{400 \text{ nm}}^{900 \text{ nm}} N_0^\circ(\lambda) R_d(\lambda) T_o(\lambda) d\lambda} \quad (5-8)$$

where $N(\lambda)$ is the actual spectral radiance of the area viewed by the imager.

SNR Equations – Silicon Array Detectors

For silicon photodiodes, the signal current is given by equation (5-2) applicable to the photoemissive detectors. The rms noise current, i_n , however, is made up of several components and may be expressed by

$$i_n = (i_{ns}^2 + i_{nd}^2 + i_{np}^2 + i_{nt}^2)^{1/2} \quad (5-9)$$

where

$$i_{ns} = (2e i_s \Delta f_n)^{1/2} = \text{signal shot-current noise}$$

$$i_{nd} = (2e i_{dark} \Delta f_n)^{1/2} = \text{dark-current noise}$$

$$i_{np} = \text{preamplifier equivalent noise current}$$

$i_{nt} = (4kT\Delta f_n/R_f)^{1/2}$ = thermal noise current of the feedback resistance, R_f , where k is the Boltzmann constant and T is the temperature

The signal current, i_s , is given by equation (5-2). The signal shot-noise expression excludes the factor, k_d , as the noise due to subsequent amplification is shown explicitly here, in contrast to photo-emissive-type detector case [equation (5-3)]. The dark-current noise, i_{nd} , would normally be negligible for the OPM Image application, except possibly due to high-energy radiation effects.

In the frequency range of most interest for the OPM Imager, when using silicon array detectors, i.e., up to 10 kHz, an input noise current for the preamplifier of

$$\bar{i}_n \approx 1 \times 10^{-15} \text{ A Hz}^{-1/2} \quad (5-10)$$

is achievable. The corresponding noise voltage is

$$\bar{e}_n = e_o(1 + f_o/f)^{1/2} \quad (5-11)$$

where e_o and f_o are approximately equal to $3 \times 10^{-9} \text{ V Hz}^{-1/2}$ and 10 Hz, respectively, with the current equivalent to \bar{e}_n being given by \bar{e}_n/R_f . The equivalent current due to e_n is boosted at 6 db/octave due to the feedback above the frequency

$$f_i = (2\pi R_f C_{in})^{-1} \quad (5-12)$$

For the geometry envisioned in the detector-preamplifier assembly, capacitances of $C_{in} = 10 \text{ pF}$ and $C_f = 0.1 \text{ pF}$ for the preamplifier input and feedback resistor are reasonable. The intersection of the \bar{i}_n and current equivalent \bar{e}_n curves thus occurs at

$$f_i = \bar{i}/(\bar{e}_n 2\pi C_{in}) \quad (5-13)$$

or 5.3 kHz for the stated values. If the i_n and the current equivalent to e_n are uncorrelated, then the total noise is the root sum square value of the components. Significant correlation can be expected, however,

and for the worst case with totally correlated components, the pre-amplifier equivalent current noise is given by

$$i_{np} = \sqrt{[i_n + (e_n/R_f)_{\text{Closed Loop}}]^2 df}^{1/2} \quad (5-14)$$

The required system response -3 db frequency is dependent on the roll rate and IFOV. As the noise current, i_{nt} , decreases as the feedback resistance is increased, it is usually desirable to increase R_f until another noise component dominates within practical limits for R_f . The feedback resistance and capacitance product affects the overall system response and leads to a signal (and noise) fall-off with a -3 db point at

$$f_2 = (2\pi R_f C_f)^{-1} \quad (5-15)$$

The product of the noise filter and $R_f C_f$ responses yields the overall system frequency response. The noise filter constants and R_f can be chosen consistent with the required overall system -3 db frequency.

If a two-section RC noise filter with each section having a -3 db point at f_2 is specified, then the overall system response (-18 db/octave roll-off) will have a -3 db point at

$$f_3 \text{ db} = f_2 / 1.96 \quad (5-16)$$

That is, each individual component of the system response will have a -3 db frequency at $1.96f_3$ db.

For the system modeling calculations, $k_f = 1$ [see equation (3-12)] was selected. (It should be noted that a somewhat smaller value of k_f , while causing some attenuation of the higher spatial frequencies in the along-scan direction, could reasonably have been made and this would give better SNR performance.) With the selected system response (equivalent to a triple RC roll-off)

$$\Delta f_n = 1.15f_3 \text{ db} \quad (5-17)$$

and for a consistent design, it follows from equations (3-12), (5-15), (5-16), and (5-17) that

$$R_f = 0.0149\alpha/(C_f\Omega) \quad (5-18)$$

As an example, with $\alpha = 0.1 \text{ mr}$, $\Omega = 5 \text{ rpm}$ (0.0833 rps), and $C_f = 0.1 \text{ pF}$, $R_f = 178 \text{ M}\Omega$ and $\Delta f_n = 5.2 \text{ kHz}$, $i_{nt} = 7 \times 10^{-13} \text{ A}$, $i_{np} = 1 \times 10^{-13} \text{ A}$, and $i_{nd} = 3 \times 10^{-13} \text{ A}$ with the additional assumptions of $T = 300^\circ\text{K}$, $C_{in} = 0.1 \text{ pF}$, and $i_{dark} = 50 \text{ pA}$.

The signal-to-noise ratio (peak signal-to-rms noise) at zero spatial frequency SNR ($\nu = 0$) is calculated from the ratio of i_s/i_n by combining equations (5-2) and (5-9). If thermal noise can be considered to dominate, then since

$$\left. \begin{aligned} i_{nt} &= (4kT\Delta f_n/R_f)^{1/2} = \text{constant}(T, C_f, k_f) \times \Omega/\alpha \text{ and} \\ i_s &= \text{constant} \times D^2\alpha^2k_N \end{aligned} \right\} \quad (5-19)$$

it follows that

$$\text{SNR} \propto \frac{D^2\alpha^3k_N}{\Omega} \quad (5-20)$$

With preamplifier or dark noise dominating, the corresponding SNR dependence is

$$\text{SNR} \propto \frac{D^2\alpha^{5/2}k_N}{\Omega^{1/2}} \quad (5-21)$$

Finally, if the signal shot noise were to dominate

$$\text{SNR} \propto \frac{D\alpha^{3/2}k_N^{1/2}}{\Omega^{1/2}} \quad (5-22)$$

which has the same dependence indicated for photoemissive detectors in equation (5-6). In those cases where the thermal noise still dominates and it is therefore desirable to increase the value of R_f to a larger value than indicated in equation (5-18), the addition of a high-frequency boost circuit following the current mode amplifier can be appropriate to further improve SNR performance.

For solid-state array detectors used in the photon-integration mode of operation, it is often more convenient to express the relative quantities in terms of charge. The signal charge accumulated during integration time, T_{int} , is given by

$$n_s = i_s T_{int} / e \quad (5-23)$$

where i_s is given by equation (5-2). The rms electron noise, n_n , can be expressed as

$$n_n = (n_s + n_o)^{1/2} \quad (5-24)$$

where n_o is a noise term which is nearly independent of signal level. This term represents the combined noise associated with the detector readout (sampling) and preamplifiers. The ratio n_s/n_n is then SNR ($\nu = 0$).

SNR Equations – Other Candidate Detectors

The signal-to-noise analysis for the infrared detectors of possible interest for a multispectral OPM Imager is similar to that described in the previous subsection for the silicon array detectors. The signal power P_s incident on the detector is equal to

$$P_s = A \omega \int N(\lambda) R(\lambda)_{d, rel} T_o(\lambda) d\lambda \quad (5-25)$$

where $R(\lambda)_{d, rel}$ is the relative spectral response of the detector and the other quantities are as previously described. The noise equivalent power, NEP, of an infrared detector is related to the specific detectivity, D^* , by

$$NEP = (A_d \Delta f_n)^{1/2} / D^* \quad (5-26)$$

where A_d is the detector area. A_d can be related to the IFOV, α , and effective focal length, f , of the optics by

$$A_d = \omega f^2 = \alpha^2 f^2 \quad (5-27)$$

where the second equality assumes a square IFOV.

The limiting noise mechanism in an intrinsic infrared detector is the statistical fluctuation in the carrier concentration due to the random arrival of photons from the thermal background surrounding the detector. The detectivity of such background limited photoconductors is given by

$$D_{BLIP}^* = \frac{\lambda}{2hc} \left(\frac{\eta}{Q_B} \right)^{1/2} \quad (5-28)$$

where

λ = wavelength in μm

$h = 6.6 \times 10^{-34}$ watt sec²

$c = 3 \times 10^{10}$ cm sec⁻¹

η = quantum efficiency (carriers/photon)

Q_B = background photon flux density in photons $\text{cm}^{-2} \text{sec}^{-1}$

Where appropriate, a further reduction in background flux density can be achieved with: 1) a cold filter to define the desired spectral bandpass; 2) a cooled geometric shield to reduce the detector field of view to the minimum necessary to receive the scene flux; and 3) cool optics to reduce thermal emission.

It is often true that for a particular set of system requirements other noise mechanisms will limit system performance. In infrared detectors, the "1/f" noise usually dominates at low frequencies and thus may be the most important effect for low-frequency video systems. Preamplifier and thermal noise often dominate, and an approach similar to that described in the subsection describing silicon array detectors can be used to optimize the preamplifier and thermal noise components. In any case, with the appropriate value for D^* substituted into equation (5-26),

$$\text{SNR } (\nu = 0) = P_s / \text{NEP} \quad (5-29)$$

where P_s is obtained from equation (5-25). For infrared usage, such derived quantities as the noise equivalent radiance and noise equivalent temperature difference are often used instead of the signal-to-noise ratio at a given scene radiance.

5.2 SCAN MECHANISM

With a spin-scan imager, the scan motion is produced by a combination of two orthogonal angular motions. The roll of the spacecraft produces the scan in the roll, or clock-angle, direction and requires no supplemental motion within the instrument. The orthogonal scan (cross-scan) motion in the cone-angle direction must be produced by the imager unless a single-swath image is sufficient or the relative motion between the imager and scene provides the required scanning. In the paragraphs that follow, the various means to provide the required cross-scan motion are discussed.

5.2.1 Image-Space Scanning

Image-space scanning can be thought of as an angular motion produced by an operation(s) that occurs in the image plane of the telescope. This could be accomplished by a physical displacement of the field defining aperture(s) to yield a corresponding displacement of the sampled area(s) in the object plane. Another method is the use of an acousto-optical deflector between the entrance aperture and image plane to deviate the scene flux. Such an approach would normally require significant added complexity and produce spectral dispersion in the output. Finally, image scanning by deflection of photoelectrons emitted from a photocathode with electric or magnetic fields, as in an image dissector tube, is an attractive approach for relatively limited scanning.

It is apparent that the primary advantage of image-space scanning is that it can often be accomplished with little or no mechanical displacement. If the required angular coverage is limited, then image-space scanning is an attractive approach. However, for the OPM Imager a very large angular range ($\sim 120^\circ$) is needed. Image-space scanning is not adequate to achieve such coverage. Thus, some form of object-space scanning must be used for the OPM Imager as the prime scan technique.

5.2.2 Object-Space Scanning

Object-space scanning is considered to include scan motion produced by changing the direction of the incident flux prior to reaching the telescope entrance aperture. Typically, a mechanical motion of an optical element (refractive or reflective) is utilized. A rotation of the entire telescope and field stop assembly is considered to fall within the scope of the definition.

Three basic methods for achieving object-space scanning are illustrated and defined in Figure 5-7. The telescope is represented by a lens in the figure for convenience. No approach using refractive (transmissive) elements to produce the scanning is shown since: 1) the angular coverage is too limited for the required application; and 2) the additional problems due to high-energy particles that would result are not warranted. Several of the more important advantages and disadvantages of each method are indicated in the figure.

For the OPM Imager, the very large angular range needed ($\sim 120^\circ$ or $\pm 60^\circ$) would dictate for Method A (as shown in Figure 5-7) both a very large scan mirror and large distance from the secondary mirror to the scan-mirror pivot point. The required size is excessive and is the primary reason this method is not recommended for the OPM Imager.

Method B produces a rotation of the projection of the field-of-view array into the object (scene) plane. For a relatively small angular coverage, this would not be of serious concern. However, for the OPM Imager, this defect is considered sufficiently important to reject this approach. Both Methods A and B require the use of a scan mirror. This alone is a rather serious disadvantage since, in each case, the scan mirror would be relatively unprotected from possible micrometeorite scouring. In addition, wavefront deformations caused by the scan mirror would affect the image quality of the optics.

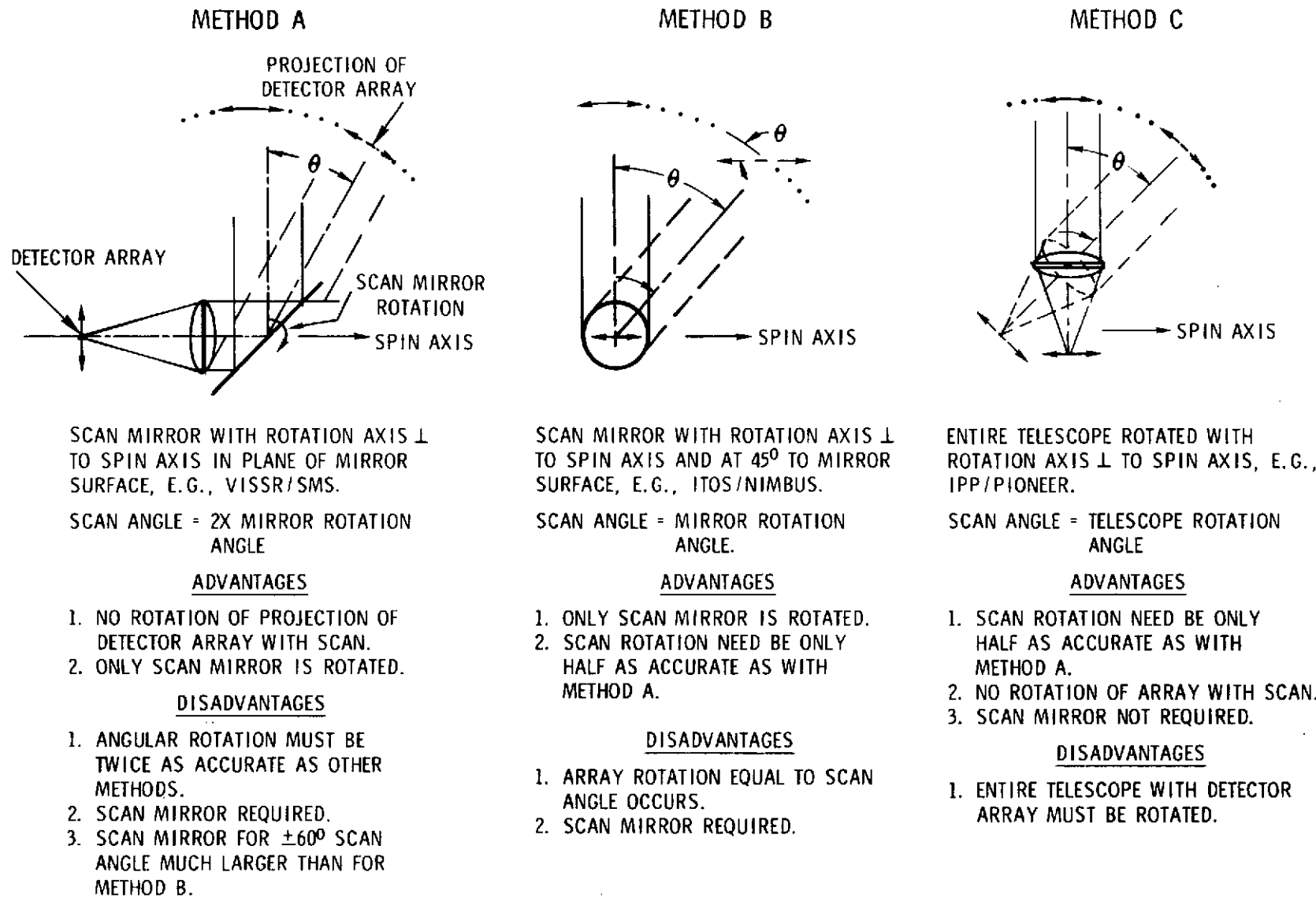


Figure 5-7. Three Object-Space Scan Methods

Method C involves rotation of the entire telescope assembly. However, if a lightweight detector assembly such as the modified Digicon or a photodiode array is used, this is not a serious defect. With a reasonable number of PMT detectors, this approach is still to be preferred.

5.3 MECHANICS

Many possible designs were considered before arriving at the final four that are described in detail in this subsection. For the critical scan mechanism, the use of rotating scan mirrors, fixed scan mirrors with rotating telescopes, and the proposed scanning telescope without scan mirror was considered in detail. The chosen concepts were selected because of minimum system weight, higher reliability, and improved maintainability, as well as the system advantages described in subsection 5.2.

5.3.1 Basic Design Approaches

Design 1 utilizes a single, electrostatically focused, "Digicon-type" detector. Another configuration, Alternate Design 1, is similar to Design 1 except that two Digicon-type detectors are utilized, each detector optimized for a different spectral region. In Design 2, a folding mirror reflects the optical image onto a group of photomultiplier tubes via fiber optics. Design 3 uses elements common to Designs 1 and 2. In this case, the modified Digicon detector is replaced by a solid-state array located at the image plane. There is no "trim" capability for the telescope stepping (as is possible by electrostatic deflection with the modified Digicon detector approach), so the scan drive mechanism is the same as for Design 2.

5.3.2 Material Section

Selection of materials requires definition of design goals and constraints. For purposes of this study, the primary concern was the minimizing of weight. In addition, thermal gradients, thermal defocusing, and the use of magnetic materials were minimized.

Beryllium has been selected for fabrication of the primary optics for the reasons stated in the subsection on telescope materials. To minimize thermal defocusing, it is advantageous to interface the primary and secondary mirrors with a material having the same thermal expansion coefficient as the mirrors. Beryllium would therefore be a likely choice. Beryllium also exhibits low density, high stiffness, and good thermal conductivity. If a material is used that does not have the same expansion as the primary/secondary optics, it would be necessary to refocus the detectors as a function of temperature, resulting in a significant weight increase.

In addition to beryllium, titanium will be used in areas where high strength is a requirement. Titanium has an expansion coefficient very close to beryllium, a precision elastic limit (PEL) considerably greater than beryllium, and like beryllium, is essentially non-magnetic. The use of non-magnetic materials is considered a requirement because of the probability of the spacecraft utilizing a magnetometer.

Extensive use of beryllium was required in the design of the hardware for the Pioneer Imaging Photopolarimeter (IPP), the Pioneer Infrared Radiometer (IRR) experiments, and the Visible Infrared Spin-Scan Radiometer/Synchronous Meterological Satellite (VISSR/SMS). The IPP and the IRR instruments also required high radiation resistance and very low magnetic signature.

5.4 TELESCOPE OPTICS

The functional and performance requirements for the telescope optics are defined in this subsection. In addition, the image quality is analyzed as influenced by focus and decenter error tolerances, by diffraction and wavefront distortion resulting from geometrical aberration and figure error, and by beryllium thermo-mechanical and surface polish properties. This analysis is used to optimize the image quality consistent with the performance requirements. Finally, degradation of transmitting materials by high-energy radiation is considered. The results of radiation testing of various optical materials are presented.

5.4.1 Requirements for the Telescope

The basic assumed requirements for the telescope are listed below:

1. Instantaneous FOV for each element of the array shall be approximately 0.10 mr.
2. Total corrected field: 1-mr diameter.
3. Effective focal length: $3.0 \leq EFL < 3.5$.
4. Aperture: 20-cm (8-inch) diameter.
5. Obscuration ratio (defined as the ratio of the secondary diameter to the diameter of the primary): $0.30 < \epsilon < 0.45$.
6. The Seidal aberrations shall be minimum over the full field using aspheric sags equal to zero, i. e., the mirrors may be conic or non-conic surfaces with no higher order aspheric figuring.
7. The conjugates of the primary and secondary mirrors and of the system shall have minimum dependence (within the weight constraint) on such parameters as temperature changes, secondary mirror tilt, and decentering.
8. The primary mirror focal ratio shall be as small as possible within the constraint imposed by the state-of-the-art manufacture of light-weight hyperboloidal beryllium mirrors.
9. The sky and internally scattered light from near-field bright sources shall be effectively minimized within the constraints of weight and volume.

5.4.2 Image-Quality Analysis

While the requirements for the telescope do not necessitate diffraction-limited performance, certain minimum image-quality criteria must nevertheless be obeyed. These criteria specify the optical quality anticipated for imaging points and extended objects. Furthermore, they are useful in ex-post-facto image processing.

A common quality criterion is the Modulation Transfer Function (MTF). This may be derived from the point spread function, which is the three-dimensional response of the optics to a point source and implies a value of rms wavefront error. The MTF can also be derived from the line-spread function (LSF), which is a more useful descriptor for extended-object imaging. The Strehl ratio³⁴ is a performance descriptor which relates the decrease in energy contained in the core of an image of a point source diffraction figure due to aberration, central obscuration, or rms wavefront errors. In addition, image blur due to motion can be included. Since an extended object such as a region on the disk of a planet is obviously a complex scene, the underlap/overlap and sampling considerations previously discussed determine the detailed placement of the detectors in the focal plane for efficient spatial coverage with minimum crosstalk.

Both the MTF and Strehl ratio performance criteria will be used to define the central obscuration diameter and the manufacture, alignment, and thermal distortion tolerances within the restrictions imposed by the minimum weight and volume limits. For additional related background material, the reader is referred to the excellent studies for the NASA Large Space Telescope by the Perkin-Elmer Corporation³⁵ and Itek Corporation.^{36, 37}

5.4.3 Restrictions on Fundamental Design Parameters

The telescope aperture is dictated by the minimum SNR required in each pixel for typical planetary radiance and contrast conditions. For the preliminary design, a nominal 20-cm (8-inch) primary diameter system is evaluated.

Since minimizing the weight of the optical system will be the ultimate goal, it is important to determine the functional dependence of the weight on the system parameters. The succeeding discussion will show that minimum system effective focal length (EFL) results in the minimum weight, and that minimum central obscuration ratio, ϵ , leads to maximum encircled energy density in the point source diffraction figure. The value of ϵ therefore directly influences the Strehl ratio and the MTF. Both of these design parameters (EFL and ϵ) are directly influenced by the primary focal ratio, N_p . The fabrication state-of-the-art for beryllium light-weight mirrors limits N_p to be greater than 1.5. An N_p of 1.8 has been chosen for this discussion.

5.4.4 Defocus and Alignment Error Tolerances

Offner (see Appendix A of reference 35) discusses some of the properties of a two-mirror system. The tolerances on the tilt, decentration, and separation of the two mirrors of a Cassegrain telescope can be reduced to the tolerances on the departure from coincidence of the foci of the mirrors if the angle between the axes of the mirrors is small. In the case of the Ritchey-Chretien, the two foci do not coincide, so the tolerances are expressed in terms of the nominal separation of the foci. The following definitions are used:

N = system focal ratio

N_p = primary mirror focal ratio

m = magnification of secondary, $m = N/N_p$

W_t = optical path difference (OPD) departure
from closest sphere

A longitudinal separation of the foci of the primary and secondary mirrors (δX_t) results in spherical aberration at an off-axis image position. The δX_t corresponding to the maximum wavefront aberration, W_t , i.e., OPD departure from the closest sphere, is given approximately by

$$\delta X_t \simeq \frac{512 N^4}{m^2(m^2 - 1)} W_t \quad (5-30)$$

The tolerance on the lateral separation of the foci (which produces coma) of the two mirrors, Y_t , is related to the tolerance on the resultant wave aberration, W_t , by the expression

$$Y_t \simeq \frac{64 N^3}{m(m^2 - 1)} W_t \quad (5-31)$$

This expression and the preceding one are correct for a system having the back focal distance equal to the mirror separation.

Thus, for $OPD_{max} = \lambda/4$, $N = 3.0$, $\lambda = 0.55 \mu m$

$$\left. \begin{array}{l} \delta X_t \simeq 0.78 \text{ mm (0.031 inch) and} \\ Y_t \simeq 0.06 \text{ mm (0.0024 inch)} \end{array} \right\} \quad (5-32)$$

Obscuration Effects

Note that the $\lambda/4$ wavefront tolerance is the classical Rayleigh criterion for diffraction limited performance. This is used as a reference basis for the discussion.

A $\lambda/4$ wavefront departure due to spherical aberration would result in a decrease of 20% in the normalized intensity (Strehl ratio) at the diffraction focus. For an unobscured aperture, the radius of the first dark ring in the diffraction pattern defines a circle which contains 84% of the energy in the image, or 84% of the maximum intensity in the absence of aberrations (Strehl definition, i.e., Strehl ratio of 1.0). As the obscuration ratio, ϵ , increases, more energy is diffracted into

the outer rings and the central maximum decreases and thus, the Strehl ratio decreases. The following relationship describes the relative intensity, I_ϵ , at the center of the image:

$$I_\epsilon = I_0 (1 - \epsilon^2)^2 \quad (5-33)$$

I_0 is the central density produced by an unobscured aperture, and I_ϵ is plotted in Figure 5-8. Figures 5-9 and 5-10 show the profile of an image of a point produced by a 20-cm diameter telescope system for 0.55- μm wavelength and three different obscuration ratios. In Figure 5-10, the curves are normalized to 1.0 at the center of the image. Note that as ϵ is increased from 0.35 to 0.45, the intensity at the central peak drops by 20% and the energy in the outer rings increases. It is obvious from these results that diffraction effects alone are not the major concern with regard to a field size of 0.10 mrad.

Wavefront Aberration

The relationship³⁴ between rms wavefront aberration, $\Delta\phi$ (for a reference sphere centered on the diffraction focus), and peak intensity is the Marechal criterion expressed as

$$I_W \approx 1 - (2 \pi / \lambda)^2 (\Delta\phi)^2 \quad (5-34)$$

This is valid only for small aberrations and is plotted in Figure 5-11. Notice the large sensitivity to rms wavefront errors.

The Perkin-Elmer LST report³⁵ considers a modified Strehl ratio comprised of the product of the above two equations, $I = I_\epsilon I_W$, as a figure of merit. This product is shown in Figure 5-12 and references the image quality of the imager telescope to that produced by a telescope of the same aperture but having neither obscuration nor aberration. Although this merit criterion is excessively severe for the resolution sought with this imager, it provides an indication of the wavefront error budget (due to geometrical aberrations, figuring error, tilts, and decentration) tolerable for typical obscuration ratios, ϵ .

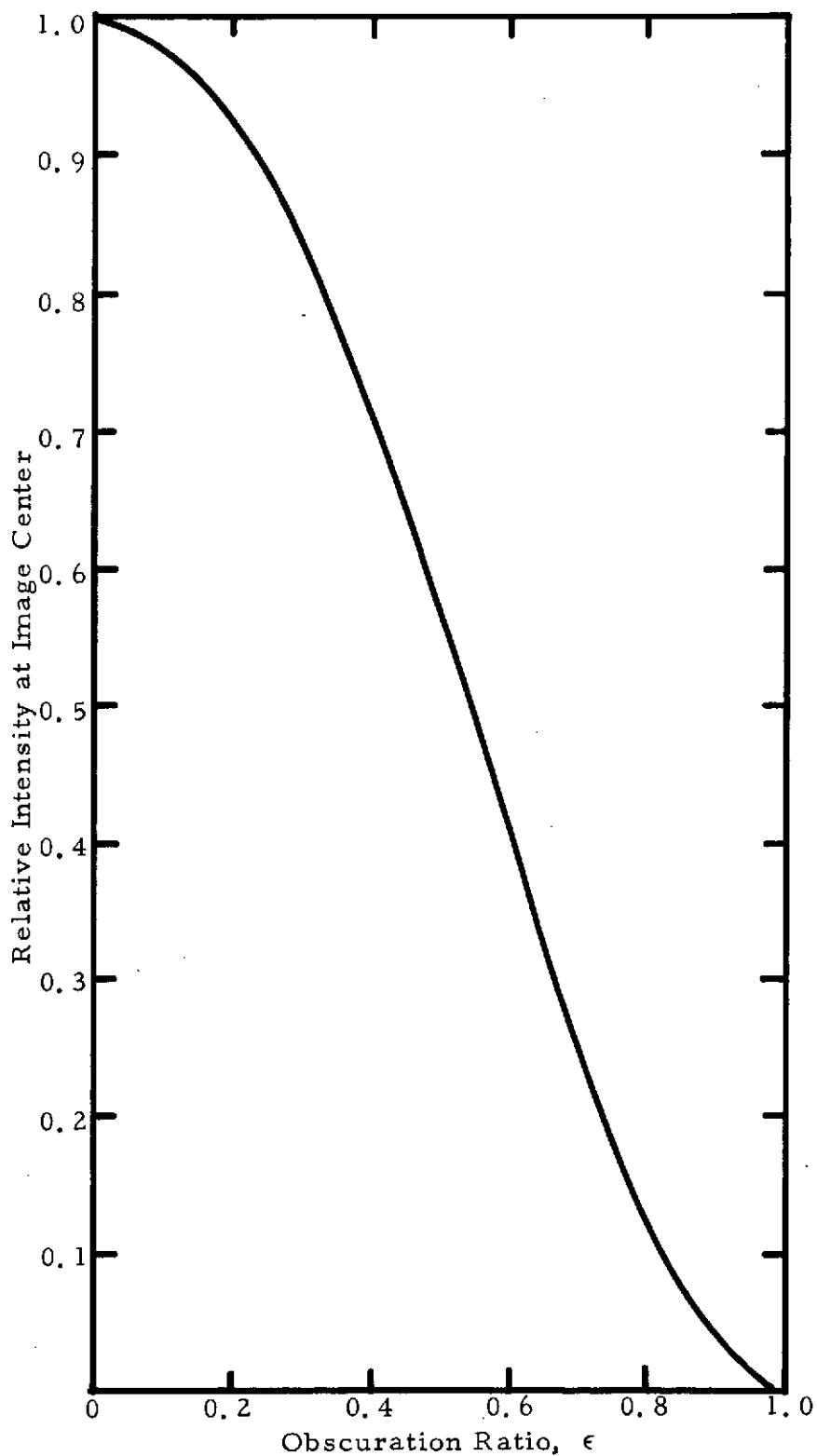
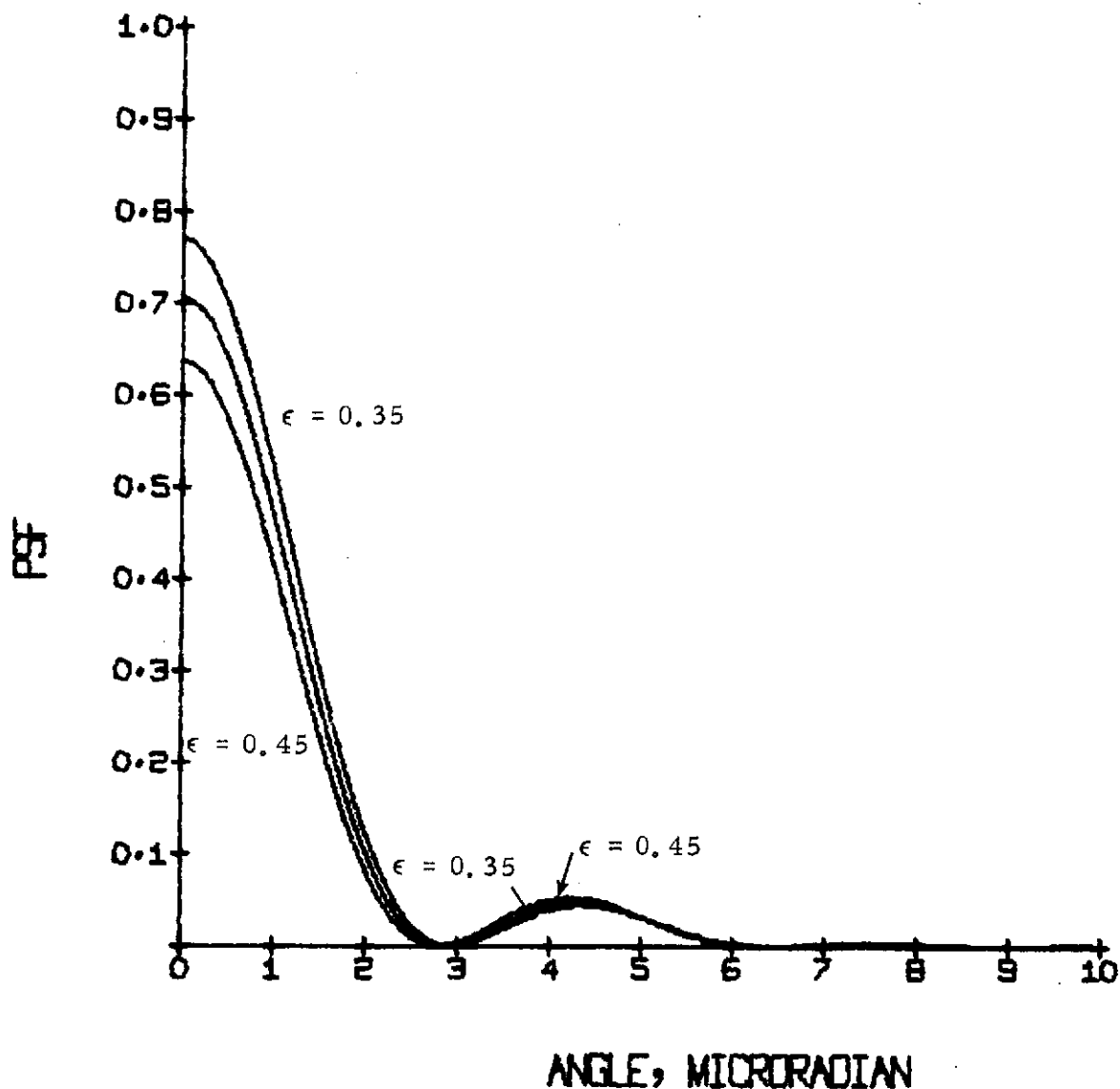
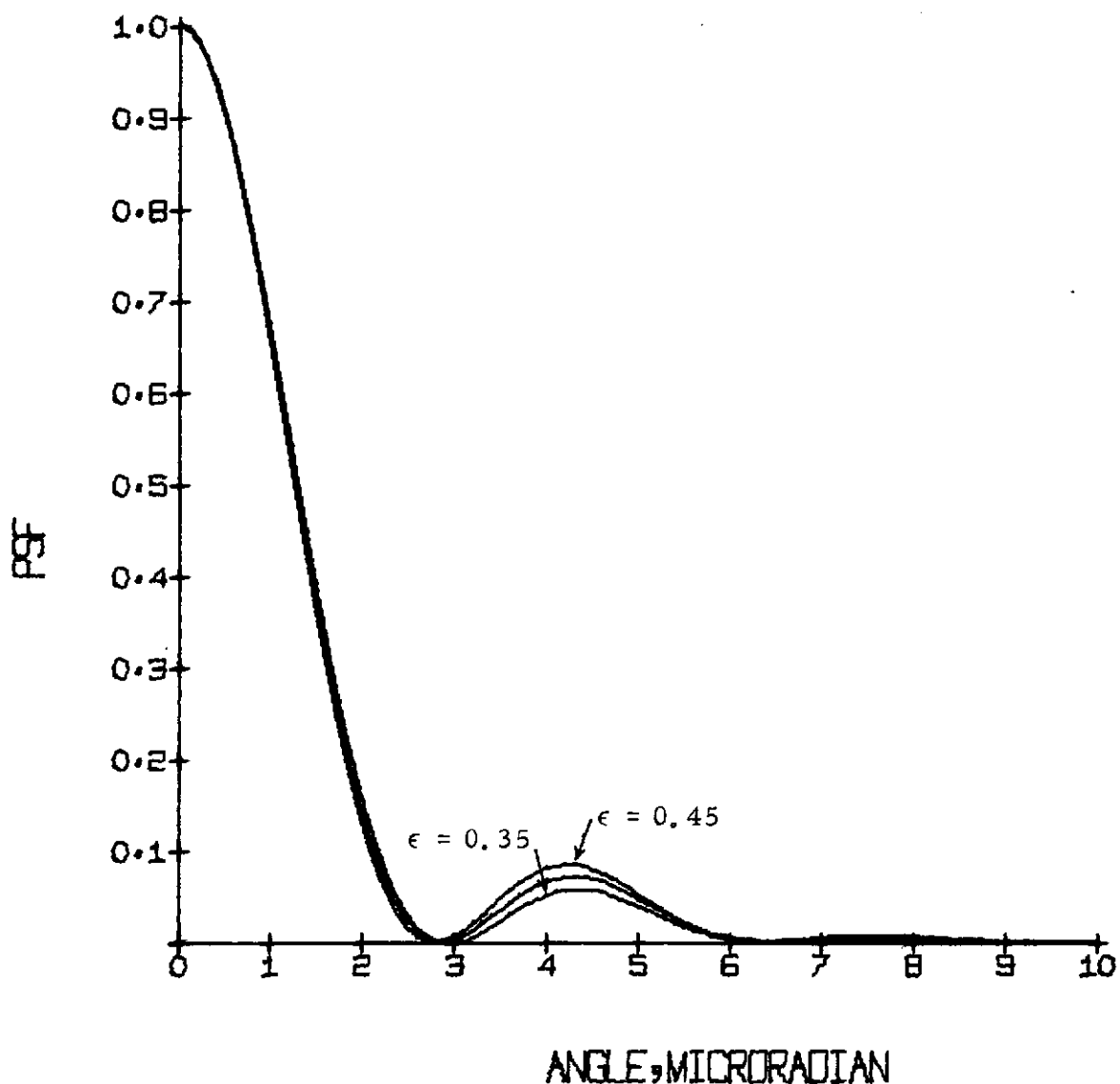


Figure 5-8. Relative Intensity at Central Diffraction Maximum Versus Obscuration Ratio



ANGLE, MICRORADIAN
DIFFRACTION LIMIT PSF
 $E=0.35, 0.40, 0.45$

Figure 5-9. Point Spread Function with Obscuration Ratio as a Parameter



DIFFRACTION LIMIT PSF
 $\epsilon = 0.35, 0.40$ AND 0.45

Figure 5-10. Normalized Point Spread Function with Obscuration Ratio as a Parameter

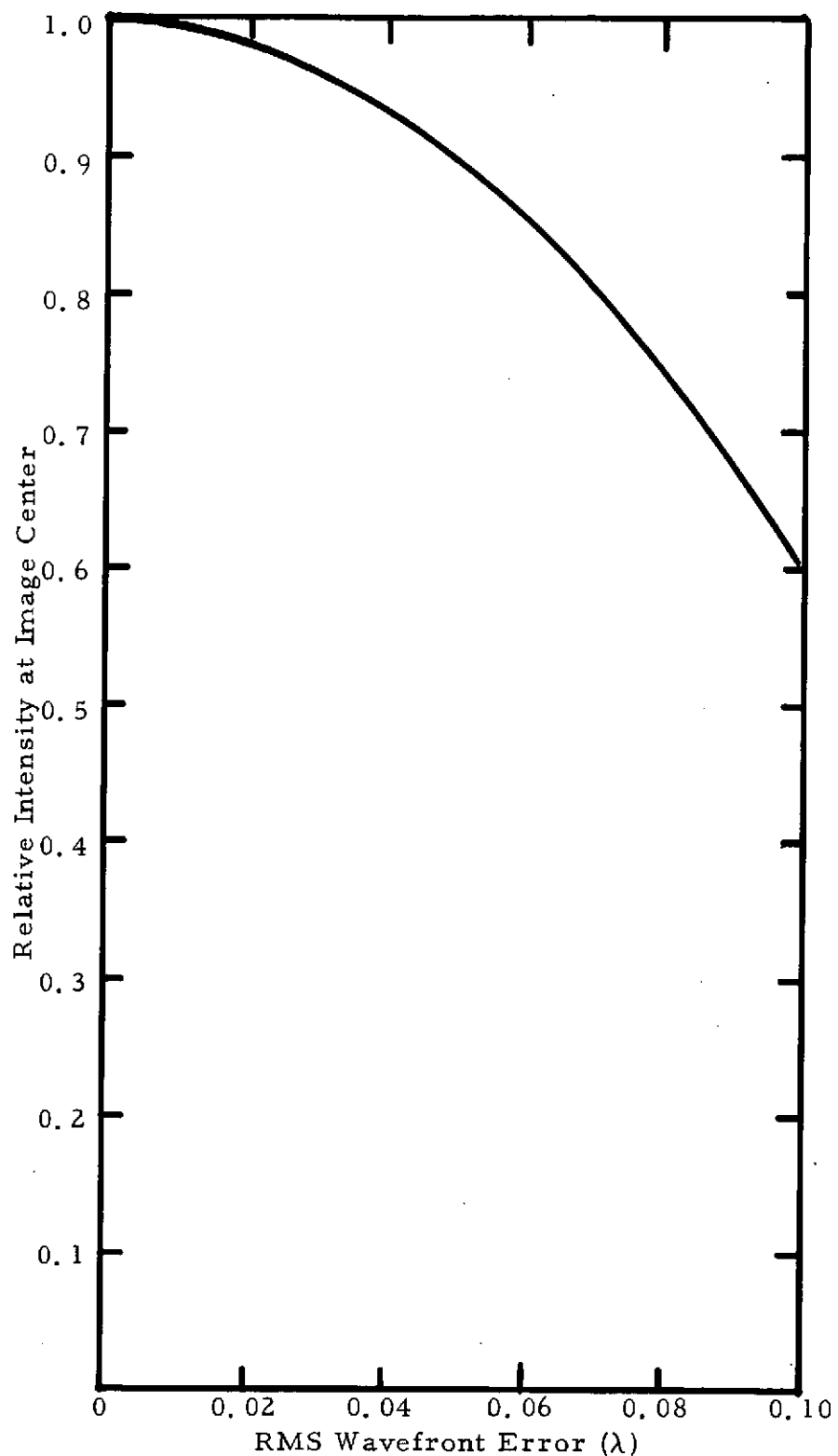


Figure 5-11. Relative Intensity at Center of Image Versus
RMS Wavefront Aberration

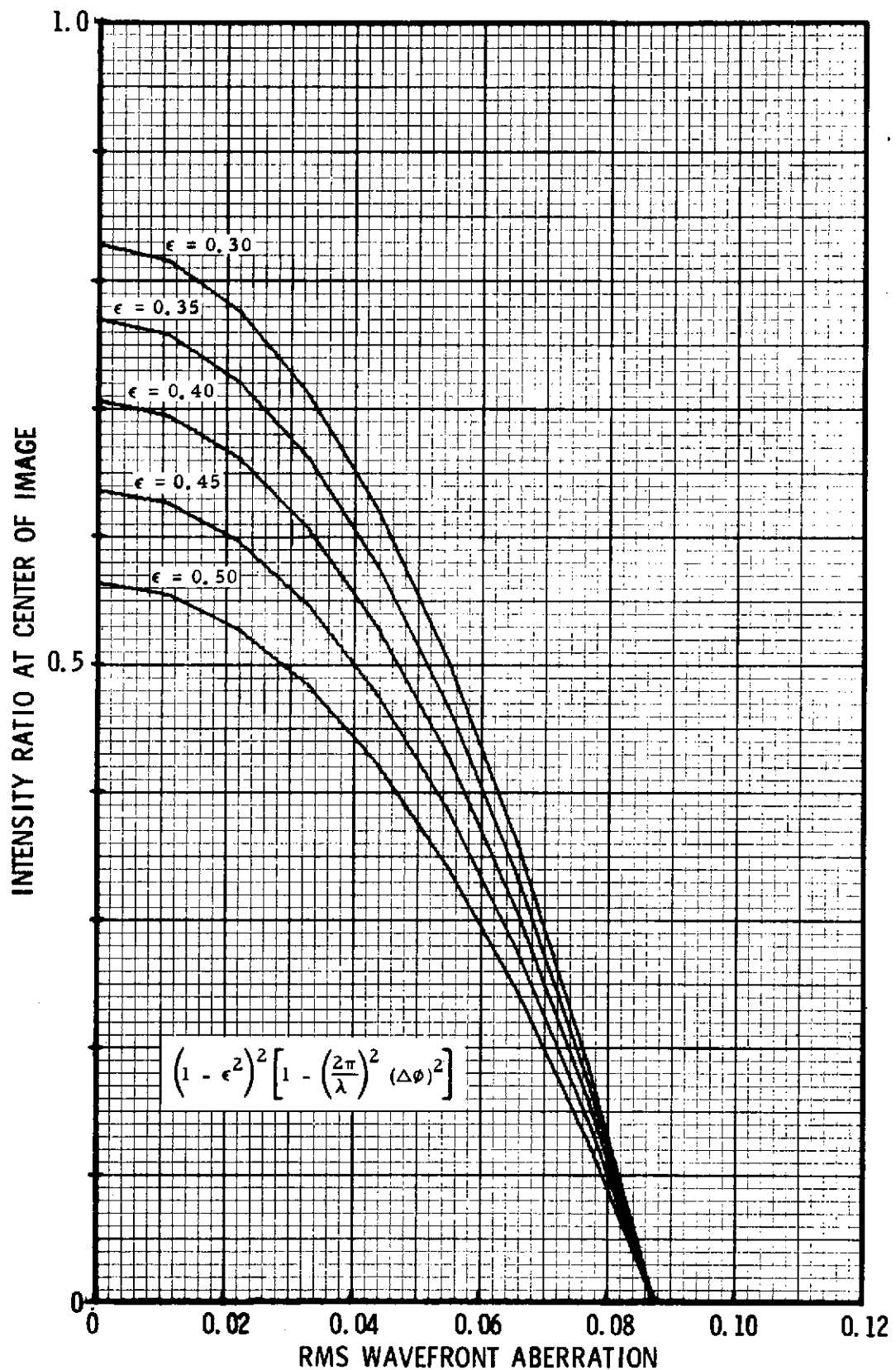


Figure 5-12. Intensity at Center of Image Versus RMS Wavefront Aberration with Obscuration Ratio as a Parameter

A modified Strehl ratio, S , of 0.80 is considered necessary for diffraction limited performance. This implies $\epsilon_{\max} = 0.325$, since $\epsilon_{\max}^2 = 1 - \sqrt{S}$. The weight and size constraints imposed on a planetary imager imply a baffled obscuration ratio ranging from 0.35 to 0.45. Reducing ϵ to 0.35 would require an additional 5-inch length on the telescope baffle, holding the other telescope parameters constant. From Figure 5-12 the influence of the rms wavefront aberration on the central intensity as ϵ is varied is apparent. For an unaberrated system, the increase in ϵ from 0.325 to 0.375 results in a decrease of only $\sim 8\%$ in the central intensity. Thus, a value $\epsilon \approx 0.375$ seems to be a reasonable compromise between weight, baffling effectiveness, and point-spread distribution.

Figures of Merit for Extended Object Imagery

The Strehl ratio criterion describes the point-spread characteristic of an optical system. When extended objects are the major concern, as they are for the planetary imager, the line-spread function (LSF) from which the Modulation Transfer Function (MTF) is derived is more directly applicable. An analogous figure of merit is the slope of the edge response. The relationships between the various figures of merit are described mathematically below.

The image of an edge, $e(x)$, obtained through a system having a line-spread function, $l(x)$, is

$$e(x) = l(x) * s(x) \quad (5-35)$$

where

$$s(x) = \text{step function} = \begin{cases} 1, & x > 0 \\ 0, & x \leq 0 \end{cases} \quad (5-36)$$

and $*$ denotes convolution.

The line-spread function is, in terms of the point-spread function, $p(x)$,

$$l(x) = \int_{-\infty}^{\infty} p(x, y) dy \quad (5-37)$$

Thus

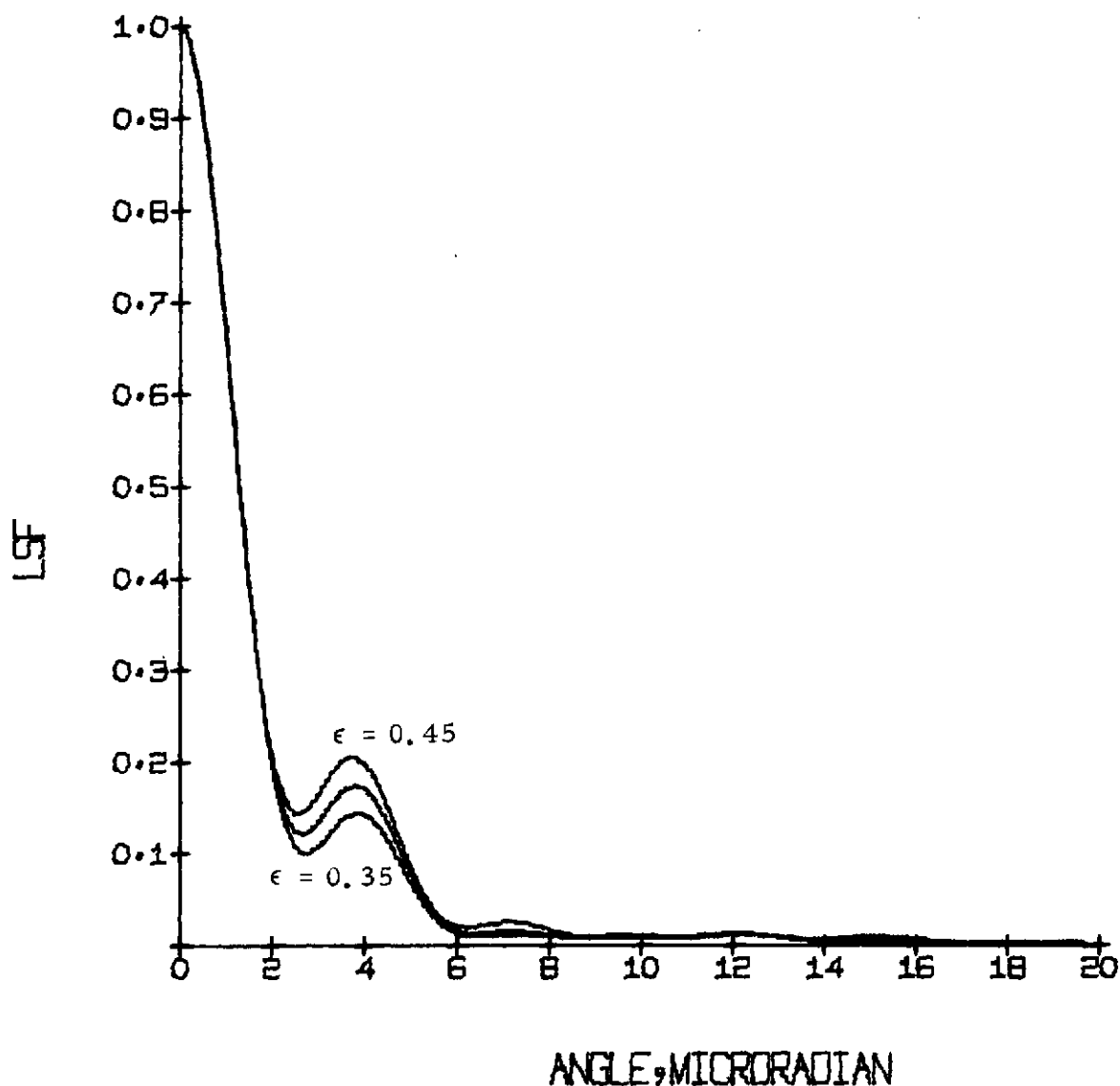
$$e(x) = \int_0^{\infty} \int_{-\infty}^{\infty} p(x - u, y) dy du \quad (5-38)$$

It can be shown that the relative edge response is analogous to the Strehl ratio for the LSF; in other words, it describes the peak intensity of the line-spread function (LSF).

Figure 5-13 presents the normalized LSF as a function of obscuration, ϵ , for the expected range of baffled ϵ and a 20-cm aperture. At 1.2 times the IFOV (100- μ r nominal IFOV plus angular spread shown in Figure 5-13), in the absence of aberrations and mirror scatter, the crosstalk between channels will be much less than 1%. The LSF can be transformed into the MTF, which is a useful engineering term and is also indicative of the rms wavefront error tolerance. The aberration-free (diffraction limited) MTF is shown in Figure 5-14. The diffraction blur for 25% modulation corresponds to 2 μ rad in object space. The central obscuration is responsible for depressing the MTF at low spatial frequencies. The low frequencies are of the greatest concern for imaging continuous objects, and the depression of the MTF means that energy is transferred to the outer portions of the image. When we consider the spatial frequency limit imposed by the geometrical field stop, namely

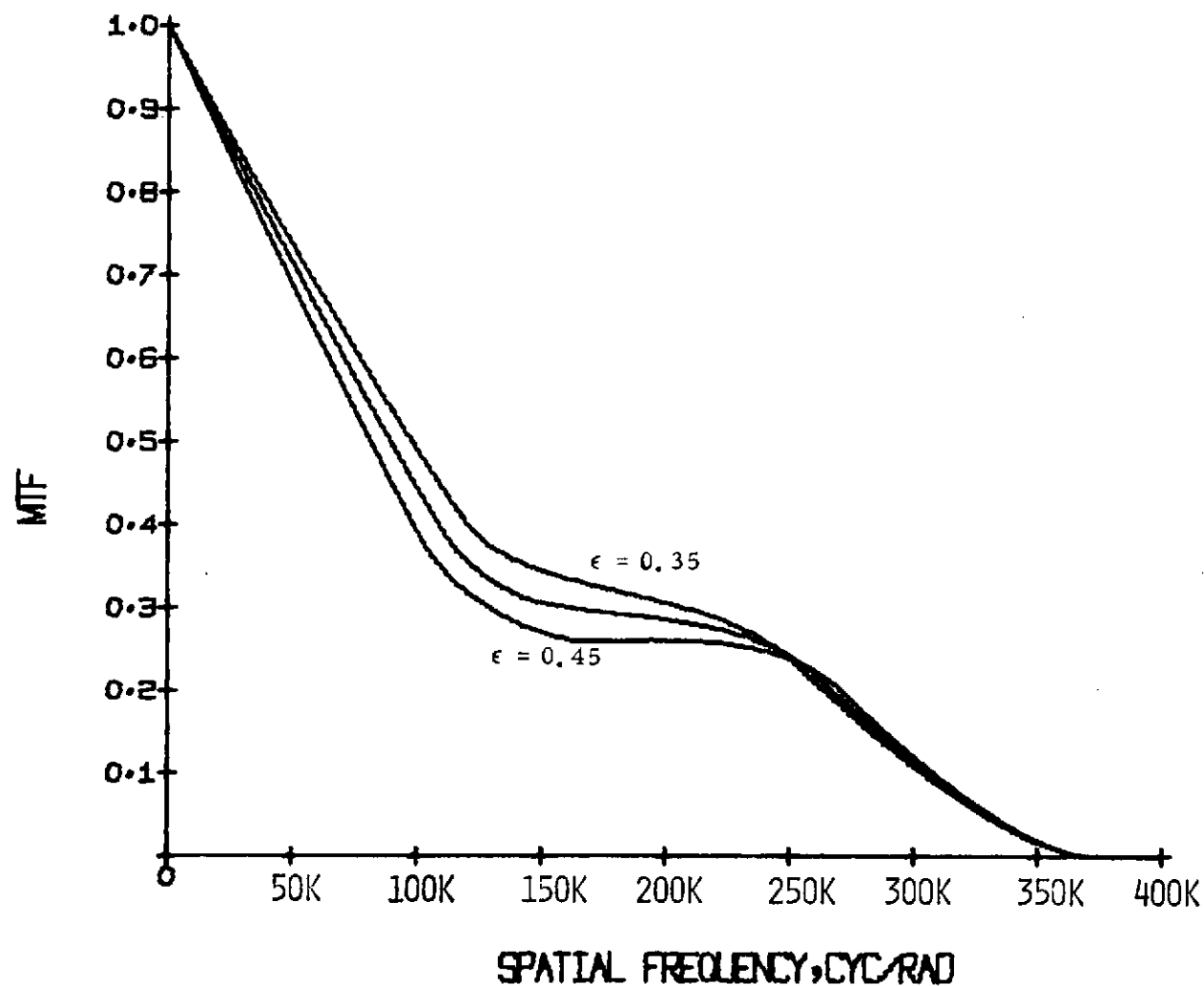
$$\nu_L = \frac{1}{2 \cdot \text{IFOV}} = \frac{1}{2 \times 0.1 \times 10^{-3} \text{ rad}} = 2000 \text{ cycles/rad} \quad (5-39)$$

we conclude that diffraction effects alone are not nearly as important as wavefront errors due to geometrical aberrations, figuring error, decentration, and defocusing.



DIFFRACTION LIMIT LSF
E=0.35, 0.40 AND 0.45

Figure 5-13. Normalized Line Spread Function with Obscuration Ratio as a Parameter



DIFFRACTION LIMIT MTF $E=0.35, 0.40 \text{ AND } 0.45$

Figure 5-14. Diffraction Limited MTF with Obscuration Ratio as a Parameter

A computer design showing image quality as influenced by geometrical aberrations is given in subsection 7.3 (Telescope Optical Designs). In that subsection, a system error budget combining aberrations, decenter and defocus tolerances, diffraction, and manufacturing error is presented.

Influence of Beryllium Properties on Image Quality

For the purposes of minimizing weight, thermal gradients, and thermal defocusing, the use of beryllium optics is preferred over fused silica. The manufacturing state of the art for stable precision beryllium optics is highly developed. As an example, the VISSR/SMS optical system (26- by 16-inch scan mirror, 16-inch diameter primary, and 4-inch secondary) is a high-resolution ($26\text{-}\mu\text{rad IFOV}$), all beryllium system.

The VISSR image quality specification which includes degradation due to mounting stresses, manufacturing tolerances, and diffraction was very closely achieved in practice.

There are several beryllium characteristics that can affect the final spatial resolution. These include material anisotropic thermal expansion coefficients, thermal gradients, residual stresses, Kanigen plating stresses, and mirror surface scattering. These factors are discussed in the following paragraphs.

Uniaxial pressing of the beryllium crystallites during consolidation results in a difference in expansion coefficient depending on direction. The difference can range up to 7%. Due to this anisotropy, the optical figure will be a function of temperature. The image degradation θ_D (field angle) due to a temperature difference ΔT , is given by

$$\theta_D = \frac{(\alpha_R - \alpha_L)\Delta T}{(f/\#)} \quad (5-40)$$

and the surface deformation ΔX under the same conditions is

$$\Delta X = \frac{\theta_D D}{16} \quad (5-41)$$

where $f/\# = 1.8$, f = focal length = 24 in., D = diameter = 8 in., and $\alpha_R - \alpha_L = 0.07 \times 11.3 \times 10^{-6}$. With $\Delta T = 10^\circ\text{C}$, these expressions yield

$$\left. \begin{aligned} \theta_D &= \frac{0.07 \times 11.3 \times 10^{-6} \times 10}{1.8} = 4.4 \times 10^{-6} \text{ rad, and} \\ \Delta X &= \frac{4.4 \times 10^{-6} \times 8}{16} = 2.2 \times 10^{-6} = \lambda/10 \end{aligned} \right\} \quad (5-42)$$

These distortions are completely negligible for a 100- μrad IFOV.

Thermal gradients have not been calculated, but by analogy with the VISSR, the largest gradient for any element is expected to be $< 0.05^\circ\text{C}$. This is expected to have negligible influence on image quality. Obviously, a detailed thermal analysis would be required prior to construction of an actual imager. In any event, the thermal sources and sinks must be distributed in such a manner to limit the thermal gradients to a tolerable level.

The dimensional stability of beryllium mirrors is a function of metallurgical instability, relaxation of residual stresses, and plastic deformation. The residual stresses can be caused by machining, heat treatment, and thermal expansion anisotropy. They can be minimized by special machining procedures, heat treatments, and chemical etching prior to Kanigen plating. These processes have been perfected and are detailed in an SBRC process specification which was evolved for the VISSR mirrors.

Plastic deformation is the result of applied stresses in excess of the precision elastic limit (PEL). The PEL is defined as the stress at which 1 microinch/inch of plastic strain occurs and should be used in

lieu of the usual yield strength specification for optical components. A large PEL is desirable to achieve mirror stability with time; 5000 psi was used for VISSR.

A low stress modified Kanigen electroless nickel plating was developed for Hughes Aircraft Company by General American Transportation. The specification of the phosphorous content and the post-baking temperature is among the factors that affects the final stress level.

To achieve low surface scatter, Kanigen plating as opposed to bare beryllium is essential. Off-axis (diffuse) scattering from the telescope optics would result in spreading of the image to a larger encircling radius for the same fractional energy containment. This leads to a reduced MTF and an increase in optical crosstalk between neighboring detectors. Flux from neighboring regions of a planetary disk thus would be mixed with that from the nominal IFOV. The consequence of these effects is a reduction in the effective resolution of the imager.

It has been found on the VISSR program that polished bare beryllium shows a hemispherical scattering coefficient of 2 to 3.5% and a near-field (within 7° of the specular direction) coefficient ranging to 1%. These values were measured by Dr. H. Bennett, NOTS, China Lake, on 2-inch flats. Larger figured mirrors will, of course, have larger scattering coefficients. By comparison, the hemispherical coefficient for polished Kanigen plating is $\leq 1\%$ and glass mirrors show $\leq 0.05\%$. As an example of the influence of mirror scattering on the radiometric fidelity (contrast), consider a uniform irradiation of each telescope mirror by a planet through a solid angle of 7° half-angle subtense. The optical system will have an effective scattering coefficient which is determined by the individual mirrors and by vignetting and baffling. Denoting this effective scattering coefficient by R_S and assuming that this integrated scattering coefficient over the solid angle subtended by

the planet is approximately equal to the hemispherical value, the signal S measured will be proportional to the planet albedo p_I in the IFOV, plus the surrounding planetary albedo p_p scattered into the IFOV and minus that scattered out of the IFOV. For the assumed conditions, then

$$S = K [p_I + R_S(p_p - p_I)] \quad (5-43)$$

where K is a responsivity constant. Thus, the ratio F of the albedo p_I measured by a "perfect" instrument to that measured with an instrument with an effective scattering coefficient R_S is given by

$$F = \frac{K p_I}{K [p_I + R_S(p_p - p_I)]} = \frac{p_I}{p_I + R_S(p_p - p_I)} \quad (5-44)$$

For Jupiter or Saturn at 600 nm, $p_p \approx 0.45$. Figure 5-15 shows the influence of telescope scattering on F as a function of planetary albedo for the IFOV region sampled. For Jupiter and Saturn these contrast ratios cover the range from near terminator to bright clouds. It is apparent from the figure that 4% scatter could give up to 15% uncertainty in the radiometry and imaging near the terminator and for the regions of greatest interest. Polished Kanigen, however, would produce less than 5% error.

5.4.5 Selection of Radiation-Resistant Optical Materials

An extensive program was undertaken at SBRC to identify optical materials for the Pioneer 10 and 11 Imaging Photopolarimeter and Infrared Radiometer. These instruments will encounter the high-energy trapped radiation zones near Jupiter. The program included samples of filter glasses, silicone elastomer bonding agents, optical glasses, optical fibers, thin film coatings, miniature incandescent lamps, and crystals. They were irradiated with the Hughes Aircraft linear accelerator which gave electron energies averaging 10 MeV, or ^{60}Co sources of 1-MeV gamma radiation. Transmission and reflection

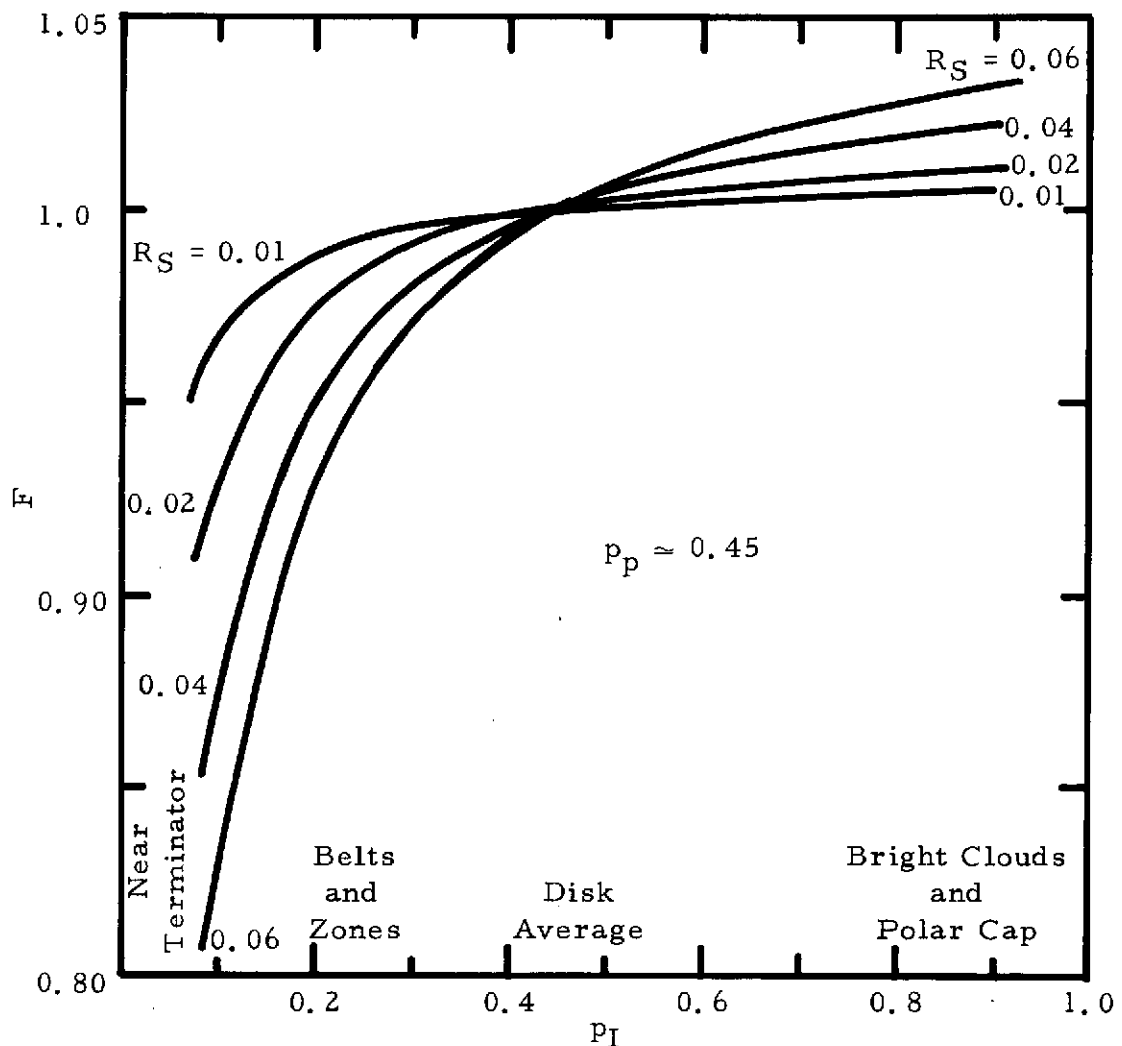


Figure 5-15. Effect of Mirror Scatter on Radiometric Measurements

losses were measured as a function of accumulated dose and dose rate. In some cases, the recovery was observed as a function of time at room temperature.

Table 5-2 presents a condensation of some of the results pertinent to the OPM Imager for 10-MeV electron irradiation except where noted. The dosages are referred to silicon.

A later study involving higher energies was undertaken and included a high-energy proton (142 and 80 MeV) fluence of 5×10^{10} p/cm², at 6% duty cycle, and neutrons of similar fluences. Items so irradiated include six Hoya and six Schott color filter glasses covering a spectral range of 300 to 900 nm, germanium and silicon materials, MgF₂ and calcite crystals, Suprasil and Corning 7940 fused silicas, and a Polacoat 105 UV polarizer. Various silicone resins were also evaluated. Table 5-3 presents the results of the proton irradiation study for unshielded materials.

Proton and neutron bombardment caused, in general, less darkening than the equivalent fluence of either 10-MeV electrons or 1-MeV gamma rays. This is most likely because the stopping ranges were about 20 g/cm² compared with 5 g/cm² for 10-MeV electrons. It should be noted that the introduction of actual hardware housings will, in turn, induce shower and bremsstrahlung radiation of smaller stopping ranges. Thus, damage in a finished instrument should be greater than indicated by these rudimentary tests of separate elements.

The active effects of high-energy interaction with transparent materials have not been studied. It is known, however, that fluorescence and phosphorescence do occur with all transmissive materials. Some materials, such as high-purity fused silica, emit less than others. For this reason, it is desirable to minimize the optical path through these materials as much as possible. The resultant effect of

Table 5-2. Radiation Induced Degradation of Selected Optical Components

	DOSAGE (rads)	λ (nm)		
		433	466	633
<u>FIBER OPTICS</u>				
OPTICS TECHNOLOGY UV 155/7056, GLASS	3.6×10^3	16	16	16
CORNING 5013, GLASS	6×10^2	7.5	7	4
FIBER PHOTICS LUMA CORD, GLASS	3.8×10^2	8	8.6	5
ELECTRO FIBER OPTICS, GLASS	1.4×10^3	15	12	5.6
AMERICAN OPTICAL UK50/EN1, GLASS	2×10^3	9	8	5
DUPONT CROFON, PLASTIC	1.27×10^5	2	1	1
FIBER PHOTICS, PLASTIC	3.2×10^4	3	2	2
UNITED OPTICAL, PLASTIC	2.2×10^4	1?	6	6
SCHOTT SUPRASIL FIBERS, CLAD	1.7×10^3	10	9	4
HITRI SUPRASIL, UNCLAD	10^6	0	0	0
<u>MINIATURE LAMPS (~300 mw)</u>				
L.A. MINIATURE PRODUCTS, TYPE II	1.2×10^5	8	6	0
L.A. MINIATURE, TYPE 14	1.5×10^5	20	9	4
CHICAGO MINIATURE, TYPE 713	2×10^5	13	10	4
<u>OPTICAL GLASSES</u>				
SCHOTT BaK1G	2×10^6	36	35	23
SCHOTT GG375G	2×10^6	7	10	5
SCHOTT GG385G	1.2×10^6	2	2	2
SCHOTT LF5G	1.5×10^6	16	12	4
DYNASIL FUSED SILICA	2×10^6	0	0	0
SUPRASIL I FUSED SILICA	2×10^6	0	0	0
CORNING 7940 FUSED SILICA	2×10^6	0	0	0
GE 124 FUSED SILICA	2×10^6	20	20	15
CORNING BOROSILICATE C7056, 2 mm	1×10^6 (^{60}Co)	60	45	17
CORNING BOROSILICATE C7052, 2 mm	1×10^6 (^{60}Co)	60	45	12
<u>COLOR FILTER GLASSES</u>				
SCHOTT OG-3, RED PASS, 3 mm	1.3×10^5	20 (630)	17 (660)	12 (700)
CORNING 2-63, RED PASS, 3.7 mm	4×10^5	12 (630)	10 (660)	8 (700)
SCHOTT BG-23, BLUE PASS, 2 mm	4×10^5	10 (400)	4 (500)	1 (600)
SCHOTT BG-38, BLUE PASS, 2 mm	4×10^5	10 (400)	4 (500)	1 (600)
<u>SILICONE ELASTOMER BONDING AGENTS</u>				
[SEE S.F. PELLICORI, APPL. OPT. 9, 2581 (1970)]				
<u>THIN FILM COATINGS – REFLECTIVE AND ANTIREFLECTIVE</u>				
IN GENERAL, IMMEASURABLE CHANGES.				

Table 5-3. Transmission Loss Due to 142-MeV and 80-MeV
Proton Irradiation

<u>COLOR FILTER GLASSES</u>	HOYA	U330	30% LOSS $\lambda < 450$ nm
		LB130	<2% LOSS
		LB200	<1% LOSS
		R-62	<2% LOSS
	SCHOTT	BG-23	<10% LOSS
		BG-24	16% LOSS $\lambda < 450$ nm
		WG-345	6% LOSS $\lambda < 550$ nm
		BG-12	10% LOSS $\lambda < 450$ nm
		RG-715	NO CHANGE
<u>CRYSTALS</u>	MgF_2		<5%
	CALCITE		YELLOW TINT
<u>POLACOAT</u>	105 UV POLARIZER		NO CHANGES
<u>FUZED SILICA</u>	CORNING C7940		<10% LOSS UV
	SUPRASIL		<10% LOSS UV
<u>SILICONE RESINS</u>			<5% LOSS UV
<u>THIN FILM COATINGS</u>			NO MEASURABLE CHANGES

fluorescence is to decrease the contrast, because a constant background is added to the signal. This may cause a severe compression of the dynamic range according to the fluorescence efficiency and signal level.

5.5 ELECTRONICS

The important considerations (especially radiation susceptibility) which affect electronic component selection for the outer planets missions imagers are discussed in this subsection. The recommended approaches for the packaging of the electronics also are discussed.

5.5.1 Component Selection

Electronic component selection is based on the need for component reliability, low weight and power, and minimum instrument change over the anticipated operating conditions. For most space programs, this phase is relatively straightforward. However, for the OPM Imager, possible operation in a severe radiation environment must be considered and has a dominant effect on component selection and circuit design.

Radiation can affect the electronic circuitry operation in two ways: 1) by introducing rate effects such as channel offsets which can alter the dynamic range of the imaging device; and, 2) by causing permanent damage to the semiconductor devices. The electronic design must then consider both problems.

Radiation-induced offsets are most pronounced in the low-level circuitry, where they may produce signals as large as the desired electrical signal. The offset signals must then be removed after amplification of the signals to a high level. This can be accomplished by sample, hold, and subtraction circuits. The channel offset can be sampled when no imaging signal is present, and the offset value can then be subtracted during the data taking period of the spacecraft roll. This technique is used on the Pioneer IPP instruments for the imaging

mode because of the radiation problem and has been used in many space programs for reducing offsets produced by temperature changes and component drift with lifetime.

Permanent semiconductor damage cannot be prevented, so allowances for component parameter changes must be made in the initial circuit designs. This is not too difficult because considerable radiation exposure data are available on most semiconductor types and logic elements (including CMOS). Component selection from slower degrading devices is also required. A rather complete line of radiation hardened, linear integrated circuits of the dielectric isolated type is presently available in high reliability configurations (HA2-2700 amplifiers are of this type). Field effect transistors have been used in low-level sections of space systems where radiation tolerance was required. These devices significantly reduced the rate effect offsets and showed little or no permanent damage effects. In large-signal or slow-speed applications, large geometry transistors should be selected because the rate of degradation is much slower than small-geometry devices. If new devices are required in the circuit design, extensive testing in radiation environments should be performed prior to their approval.

5.5.2 Electronic Packaging

Because of the variations in circuit types required for low-level amplification, high-speed digitization, power switching for motors, and power conversion circuitry, extremely good isolation between the various circuit types is required. An electronics housing to make this isolation possible must contain several compartments, each containing circuitry of the appropriate power or speed level, with feed-through capacitors between compartments. A logical division is grouping the power converter and the drive motor circuitry for the calibration source and telescope drive in one compartment, thus isolating all of the highest noise generating electronics. The digital processing

circuitry and logic devices should be contained in a separate compartment to ensure that radiation damage of the fast logic transitions is minimized. Two compartments are recommended for analog electronics, one for preamplification and the other for high-level analog signals.

Packaging of individual circuits can be accomplished with conventional techniques, except for two areas: 1) preamplifiers must be packaged with special consideration given to stray capacitance if extreme gain bandwidth is required; and 2) processing sections must be designed to effectively transfer heat out of the processor to the instrument housing (or space). Many techniques have been used successfully in handling the high voltages required for Digicon or photo-multiplier tubes, most involving encapsulation or potting of the high-voltage components. Considerable weight savings can be obtained by use of glass micro-balloons in the potting material at no loss of physical or dielectric strength. Additional weight savings can be realized by use of flat printed circuit cables in place of conventional wiring. This technique has advantages in vibration as well because of the reduced mass of the wiring.

Section 6

SYSTEM MODELING

The primary factors of importance in imager design are abstracted from the preceding section and summarized below. These provide a series of performance constraints which the instrument must satisfy. The interaction of these constraints may be accomplished conveniently and rapidly by means of parametric tradeoff figures. The use of these figures is demonstrated for photoemissive detectors and silicon array detectors. The results of these tradeoff analyses are preliminary specifications for the imager point designs. The final imager designs must consider hardware capabilities and weight restrictions, and these may dictate alternative imager specifications. In this case, the effects of such revisions are apparent from the tradeoff figures. This section considers only the preliminary tradeoffs for a Jupiter orbiter mission, and for flyby missions to Uranus and Saturn. The subsequent process of optimization for minimum weight of detailed hardware designs applicable to the Jupiter orbiter mission is accomplished in Section 7.

6.1 PARAMETRIC ANALYSIS

In this subsection, the interaction of a number of the major constraints is summarized. The functional dependence of these constraints is discussed, and parametric modeling figures (nomographs) are presented to illustrate the interactions involved.

6.1.1 Summary of Constraints

To design an outer planets mission Imager, it is necessary to select values for several pertinent parameters: the instantaneous field of view, α ; the spacecraft spin rate, Ω ; the number of detectors per spectral channel, n ; the number of spectral channels, n_s ; the aperture diameter, D ; and the number of pixels per line, L . These

parameters must be selected in such a manner as to satisfy the major scientific and spacecraft constraints discussed above: signal-to-noise ratio (SNR), resolution, overlap, coverage, and data rate. These constraints are summarized in the following.

For photoemissive detectors, to obtain a specified level of SNR, the IFOV must satisfy the following condition:

$$\alpha \geq \left(\frac{\Omega}{k_N} \right)^{1/3} \left(\frac{\text{SNR } (\nu = 0)}{KD} \right)^{2/3} \quad (6-1)$$

where SNR ($\nu = 0$) is the SNR at zero spatial frequency, k_N is a scaling factor which relates the signal in the spectral interval of interest to that in the 400- to 900-nm spectral band at the subsolar point, and K is a constant. Both k_N and K are dependent on the nominal scene and instrument characteristics, and they are given by equations (5-7) and (5-8). An explicit expression for α for silicon array detectors would require that simplifying assumptions be made.

Since the imager resolution is primarily determined by the instantaneous field of view, α , within the limits of subsection 3.1.1, the desired surface resolution of dimension, ℓ_c , can be related to the range to the planet, R (measured to the center of the planet)

$$\alpha \leq \frac{\ell_c}{R - r_p} \quad (6-2)$$

where r_p is the radius of the planet.

The requirement that there be no gaps between image segments generated on successive rolls (i. e., no underlap) can be expressed as

$$\frac{d\phi}{dt} \leq (A + 1)W\Omega \quad (6-3)$$

where A is the number of look angle steps per roll, and W is the effective width of the n-detector image segments generated each roll

$$W = n\alpha \quad (6-4)$$

with $1/2 \leq f \leq 1$. Here f is the ratio of the spacing of "adjacent" detectors to the cross-scan detector width. From equation (3-19), the maximum value of $d\phi/dt$ is

$$\frac{d\phi}{dt} = \frac{C - R\omega_p r_p}{R(R - r_p)} \quad (6-5)$$

where C is given by either equation (3-16) or equation (3-18), depending on the type of trajectory, and ω_p is the angular velocity of rotation of the planet.

The requirement that the effective bit rate, B , at which data are collected be no greater than the effective spacecraft telemetry rate, $B_{s/c}$, can be expressed as

$$B_{s/c} \geq L n n_s b k_s \Omega = B \quad (6-6)$$

where b is the number of bits per sample, and k_s is the number of samples along the scan per pixel. For this equation to be valid, one of two conditions must be satisfied: either 1) the time to image the scene is negligible compared to the roll period, or 2) read-in to the spacecraft memory can be accommodated while a portion of the memory is read out. If the condition expressed in equation (6-6) is not satisfied, large on-board storage would be required, and one of the advantages of spin-scan imaging would thereby be sacrificed.

For full-disk coverage of the planet at some resolution, ℓ_{fd} , the line length must satisfy

$$L \geq 2r_p/\ell_{fd} \quad (6-7)$$

The bit-rate limitation for this case is then given by equation (6-6).

6.1.2 Modeling Nomographs

Nomographs have been developed to facilitate the use of the constraint equations summarized in the previous subsection. Their format and examples of their use are presented below.

Figure 6-1 shows an example of the first type of nomograph, which summarizes the constraints given in equations (6-1) through (6-5). This nomograph can be built up most simply from SNR calculations such as those shown in Table 6-1. These provide single points on the nomograph for each spectral band at the specified planet. The nomograph construction is completed either from a knowledge of the SNR dependence produced by changes of imager parameters (see Section 5) or by the calculation of a sufficient number of points to define the dependence.

In Figure 6-1, the functional dependence for signal-shot-noise-limited detectors indicated in equation (6-1) can be seen from portions B, C, and D of the figure. In the example shown, an SNR ($\nu = 0$) of 30 combined with an optical system with an aperture diameter of 10 cm defines, for extended-red Digicon detectors, a value for the magnitude of the intermediate quantity, $(D/SNR)^{2/3}$. If the 500-600 nm band is of interest, then section C of Figure 6-1 determines the corresponding value for the magnitude of the second intermediate quantity, $\alpha/\Omega^{1/3}$. If a spacecraft roll rate of 5 rpm is specified, then the minimum required IFOV, α , is given, from section B, as ~ 0.08 mr. It is interesting to note at this point that: section D is related only to the detection system and is, in fact, generated from Table 6-1; section C is related, through equations (5-7) and (5-8), to the spectral dependence of scene radiance, optical transmittance, and detector responsivity; and section B is related to characteristics of the spacecraft. Section A of Figure 6-1 relates the IFOV to the spacecraft trajectory through the constraints represented by equations (6-2) and (6-3) through (6-5).

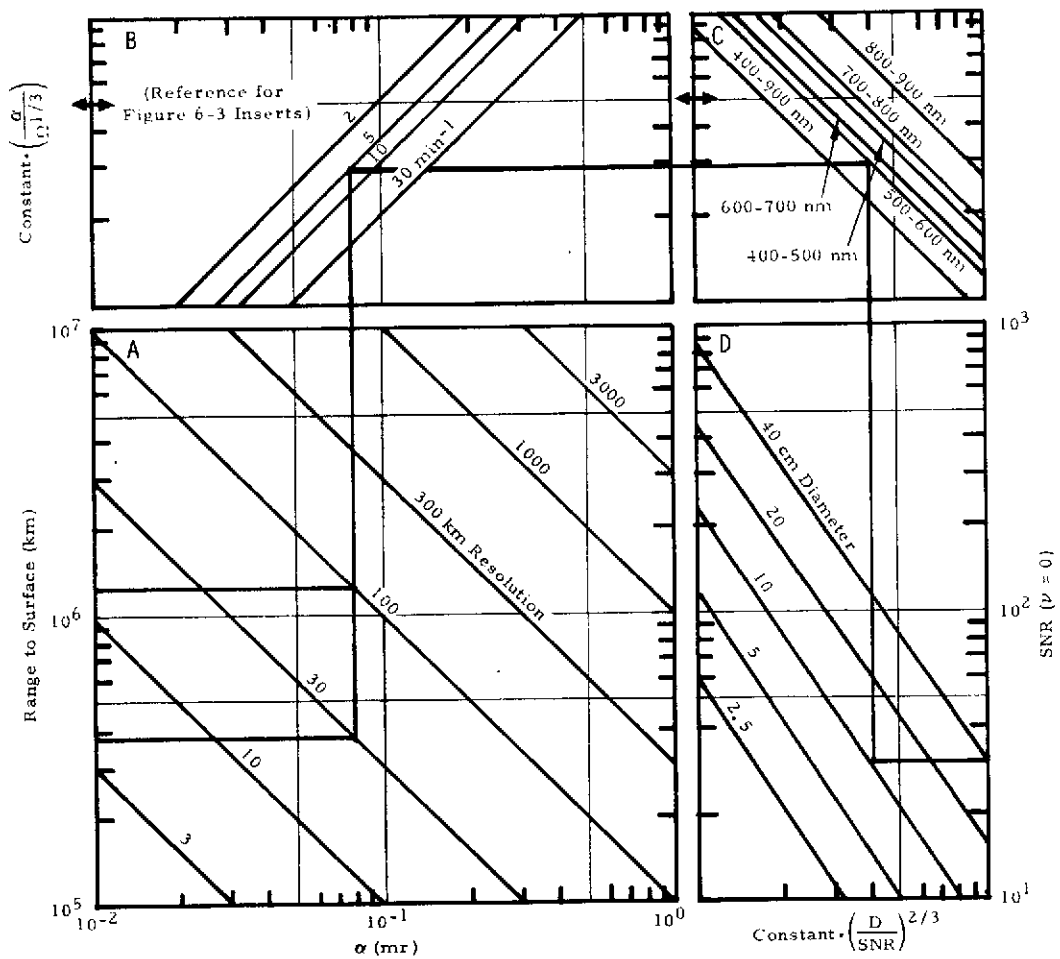


Figure 6-1. Imager Modeling Nomograph

Table 6-1. OPM Imager Point Design 1 (Extended-Red, Digicon-Type Detector)
Signal-to-Noise Calculations

OPM IM/GER DESIGN 1 WITH EXTENDED RED, DIGICON-TYPE DETECTORS										
IMAGER PERFORMANCE FOR JUPITER (D= 5.2 A.U.) WITH IFOV =0.100 MR AND ROLL RATE =10.0 RPM										
WAVELENGTH (NM)	DELTA WVL (NM)	DET. RESP. (A/W)	ALBEDO	OPTICAL TRANS. (W/(CM ² -SR-NM))	SPECTRAL RAD. (A)	ICATHODE COUNT RATE (C/S)	S/N RATIO	RSS OF S/N RATIOS		
450.	100.	0.020	1.00	0.45	0.90	0.998E-06	0.479E-11	0.299E 08	0.378E 02	0.378E 02
550.	100.	0.042	1.00	0.53	0.90	0.114E-05	0.115E-10	0.722E 08	0.587E 02	0.698E 02
650.	100.	0.036	1.00	0.53	0.90	0.903E-06	0.850E-11	0.531E 08	0.503E 02	0.861E 02
750.	100.	0.025	1.00	0.40	0.90	0.603E-06	0.362E-11	0.226E 08	0.328E 02	0.922E 02
850.	100.	0.013	1.00	0.21	0.90	0.371E-06	0.116E-11	0.725E 07	0.186E 02	0.940E 02
INTEGRATED OVER TOTAL WAVELENGTH INTERVAL:										0.296E-10 0.155E 09
IMAGER PERFORMANCE FOR SATURN (D= 9.5 A.U.) WITH IFOV =0.100 MR AND ROLL RATE =10.0 RPM										
WAVELENGTH (NM)	DELTA WVL (NM)	DET. RESP. (A/W)	ALBEDO	OPTICAL TRANS. (W/(CM ² -SR-NM))	SPECTRAL RAD. (A)	ICATHODE COUNT RATE (C/S)	S/N RATIO	RSS OF S/N RATIOS		
450.	100.	0.020	1.00	0.23	0.90	0.219E-06	0.105E-11	0.659E 07	0.177E 02	0.177E 02
550.	100.	0.042	1.00	0.47	0.90	0.304E-06	0.307E-11	0.191E 08	0.302E 02	0.350E 02
650.	100.	0.036	1.00	0.46	0.90	0.255E-06	0.221E-11	0.138E 08	0.256E 02	0.434E 02
750.	100.	0.025	1.00	0.36	0.90	0.162E-06	0.977E-12	0.610E 07	0.170E 02	0.467E 02
850.	100.	0.013	1.00	0.26	0.90	0.933E-07	0.291E-12	0.182E 07	0.932E 01	0.476E 02
INTEGRATED OVER TOTAL WAVELENGTH INTERVAL:										0.760E-11 0.475E 08
IMAGER PERFORMANCE FOR URANUS (D= 19.5 A.U.) WITH IFOV =0.100 MR AND ROLL RATE =10.0 RPM										
WAVELENGTH (NM)	DELTA WVL (NM)	DET. RESP. (A/W)	ALBEDO	OPTICAL TRANS. (W/(CM ² -SR-NM))	SPECTRAL RAD. (A)	ICATHODE COUNT RATE (C/S)	S/N RATIO	RSS OF S/N RATIOS		
450.	100.	0.020	1.00	0.55	0.90	0.867E-07	0.417E-12	0.260E 07	0.111E 02	0.111E 02
550.	100.	0.042	1.00	0.46	0.90	0.706E-07	0.713E-12	0.445E 07	0.145E 02	0.183E 02
650.	100.	0.036	1.00	0.20	0.90	0.263E-07	0.228E-12	0.142E 07	0.825E 01	0.201E 02
750.	100.	0.025	1.00	0.06	0.90	0.643E-08	0.386E-13	0.241E 06	0.339E 01	0.204E 02
850.	100.	0.013	1.00	0.03	0.90	0.255E-08	0.798E-14	0.499E 05	0.154E 01	0.204E 02
INTEGRATED OVER TOTAL WAVELENGTH INTERVAL:										0.140E-11 0.874E 07
IMAGER PERFORMANCE FOR NEPTUNE (D= 30.0 A.U.) WITH IFOV =0.100 MR AND ROLL RATE =10.0 RPM										
WAVELENGTH (NM)	DELTA WVL (NM)	DET. RESP. (A/W)	ALBEDO	OPTICAL TRANS. (W/(CM ² -SR-NM))	SPECTRAL RAD. (A)	ICATHODE COUNT RATE (C/S)	S/N RATIO	RSS OF S/N RATIOS		
450.	100.	0.020	1.00	0.63	0.90	0.419E-07	0.201E-12	0.126E 07	0.776E 01	0.776E 01
550.	100.	0.042	1.00	0.52	0.90	0.337E-07	0.340E-12	0.212E 07	0.100E 02	0.127E 02
650.	100.	0.036	1.00	0.32	0.90	0.178E-07	0.154E-12	0.964E 06	0.678E 01	0.144E 02
750.	100.	0.025	1.00	0.17	0.90	0.770E-08	0.462E-13	0.289E 06	0.371E 01	0.148E 02
850.	100.	0.013	1.00	0.08	0.90	0.287E-08	0.899E-14	0.562E 05	0.163E 01	0.149E 02
INTEGRATED OVER TOTAL WAVELENGTH INTERVAL:										0.752E-12 0.476E 07
IMAGER PERFORMANCE FOR PLUTO (D= 30.0 A.U.) WITH IFOV =0.100 MR AND ROLL RATE =10.0 RPM										
WAVELENGTH (NM)	DELTA WVL (NM)	DET. RESP. (A/W)	ALBEDO	OPTICAL TRANS. (W/(CM ² -SR-NM))	SPECTRAL RAD. (A)	ICATHODE COUNT RATE (C/S)	S/N RATIO	RSS OF S/N RATIOS		
450.	100.	0.020	1.00	0.11	0.90	0.733E-08	0.352E-13	0.220E 06	0.324E 01	0.324E 01
550.	100.	0.042	1.00	0.13	0.90	0.843E-08	0.851E-13	0.532E 06	0.504E 01	0.599E 01
650.	100.	0.036	1.00	0.15	0.90	0.836E-08	0.723E-13	0.452E 06	0.464E 01	0.758E 01
750.	100.	0.025	1.00	0.15	0.90	0.679E-08	0.408E-13	0.255E 06	0.349E 01	0.834E 01
850.	100.	0.013	1.00	0.15	0.90	0.539E-08	0.168E-13	0.108E 06	0.224E 01	0.864E 01
INTEGRATED OVER TOTAL WAVELENGTH INTERVAL:										0.250E-12 0.156E 07

TELESCOPE DIAMETER= 20.0 CM, OBSCURATION FACTOR= 0.15, AND NOISE BANDPASS=1,000/GWELL TIME= 0.104E 05HZ

Thus, the value of α in the example, 0.08 mr, can be seen to correspond to 100-km resolution at $\sim 1.23 \times 10^6$ km from the target and to 30-km resolution at $\sim 3.8 \times 10^5$ km from the target.

The number of detectors necessary to prevent underlap is trajectory dependent. From equation (6-5) or Figures 3-7 through 3-9 for the trajectory of interest, the rate of change of look angle may be obtained. From equations (6-3) and (6-4), may be obtained the parameter $fn\Omega$ and hence the number of detectors. For the parameters used in this example at 3.8×10^5 km ($5.3 R_J$),

$$n \geq \left| \frac{d\phi}{dt} \right| \left(\frac{1}{2\alpha f\Omega} \right) = 1 \quad (6-8)$$

with one FOV step per roll ($A = 1$). The parameter $fn\Omega$ may be superimposed on section A of Figure 6-1.

The data rate limitation is given by equation (6-6). A nomograph for the evaluation of this equation is shown in Figure 6-2; the indicated example illustrates its use. Thus, for $\Omega = 4$ rpm, $n = 1$, $n_s = 2$, $L = 500$, and $bk_s = 12$, the value $B = 8000$ bits/sec is obtained, which can be verified by direct substitution into equation (6-6).

In subsequent usage, these nomographs will be represented without the intermediate scales in order to avoid confusion. Scales C and D, which are detector and planet dependent, are provided in Figure 6-3 for Jupiter, Saturn, and Uranus and the three detectors of interest. This readily permits a consideration of alternative missions. For convenience, specific missions and detectors have been incorporated into complete tradeoff figures in the following subsection.

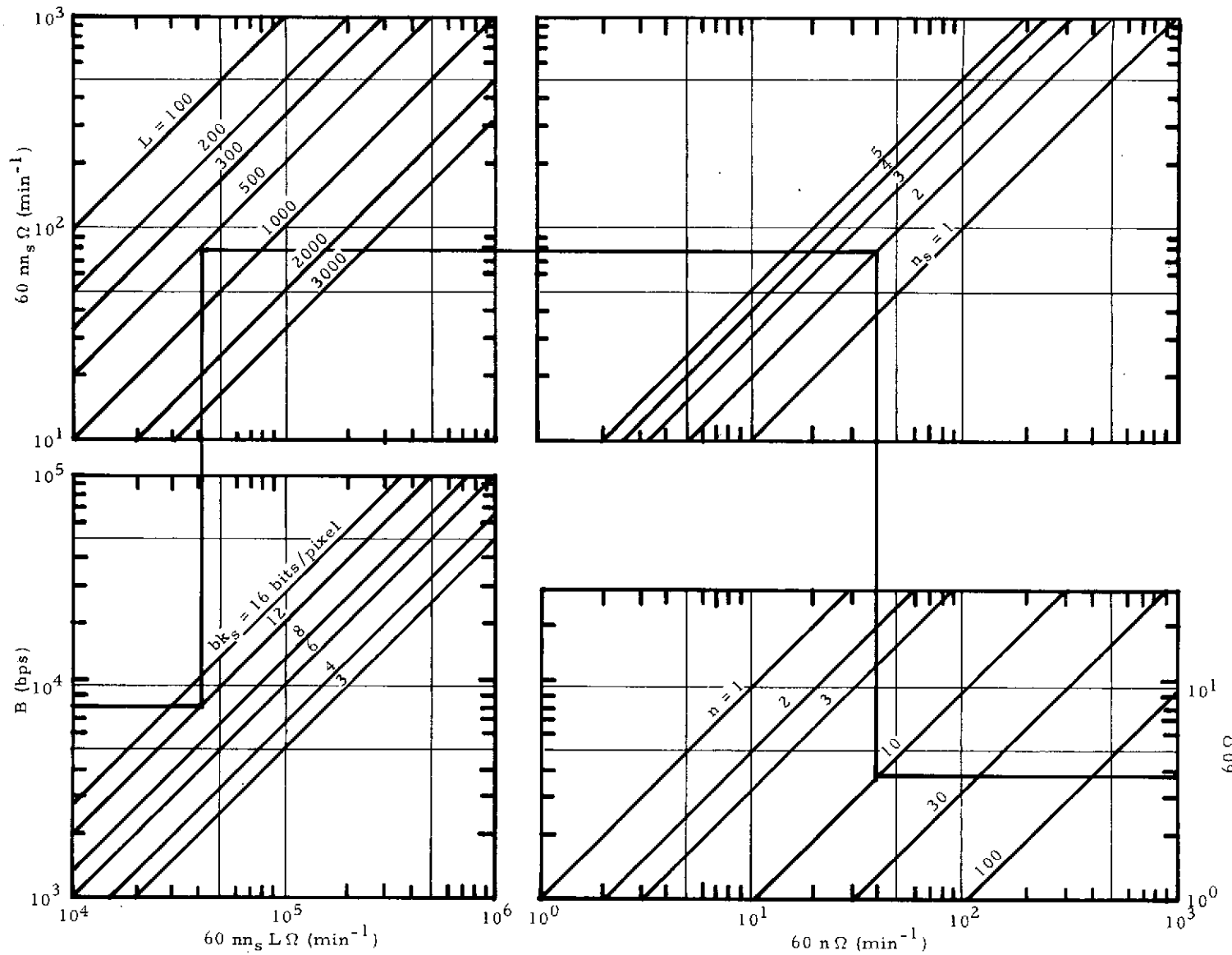


Figure 6-2. Data Rate Modeling Nomograph

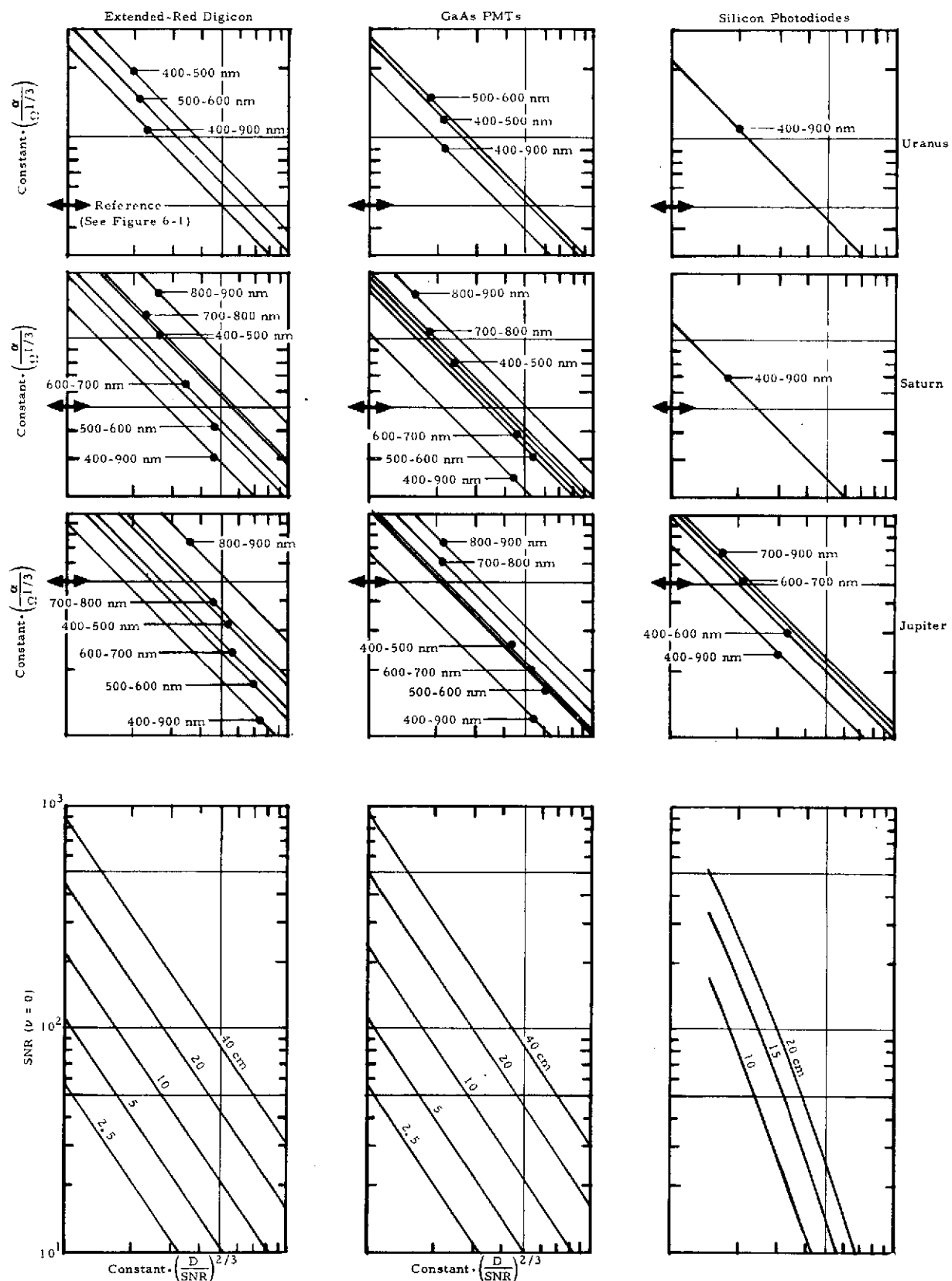


Figure 6-3. Nomograph Inserts

6.2 APPLICATION TO JUPITER

A Jupiter orbiter mission has been postulated which permits repeated encounters of the Jovian satellites.³⁸ This mission will be used for the Jupiter orbiter point design. The orbit is specified by the following parameters:

Date	2443905.5
Periapsis Radius	2.29 R _J
Apoapsis Radius	45.131 R _J
Inclination	0°
Ascending Node RA	-104.5°
Eccentricity	0.903
a	23.71 R _J
Period	14.228 days

System modeling figures have been constructed for this orbit for three detectors: a Digicon with extended-red sensitivity, an array of photomultiplier tubes, and a silicon photodiode array. These are shown in Figures 6-4, 6-5, and 6-6. In addition, the telemetry rate limitation for these imagers is provided in Figure 6-7.

Referring to Figure 6-4 for a Digicon detector for a SNR ($\nu = 0$) = 100, 20-cm optics and full-spectrum sensitivity (400- to 900-nm), one may obtain the feasible zone of operation. This is shown by the heavy lines to lie between an IFOV of 0.06 mr and an IFOV of 0.15 mr to ensure an adequate SNR over the range of spin rates between 2 and 30 rpm. To satisfy the requirement of 10-km surface resolution at periapsis (1.29 R_J from the surface sub-satellite point), it is necessary to choose an IFOV no larger than 0.1 mr. This limits the space-craft spin rate to be no greater than 10 rpm as indicated by the dashed line.

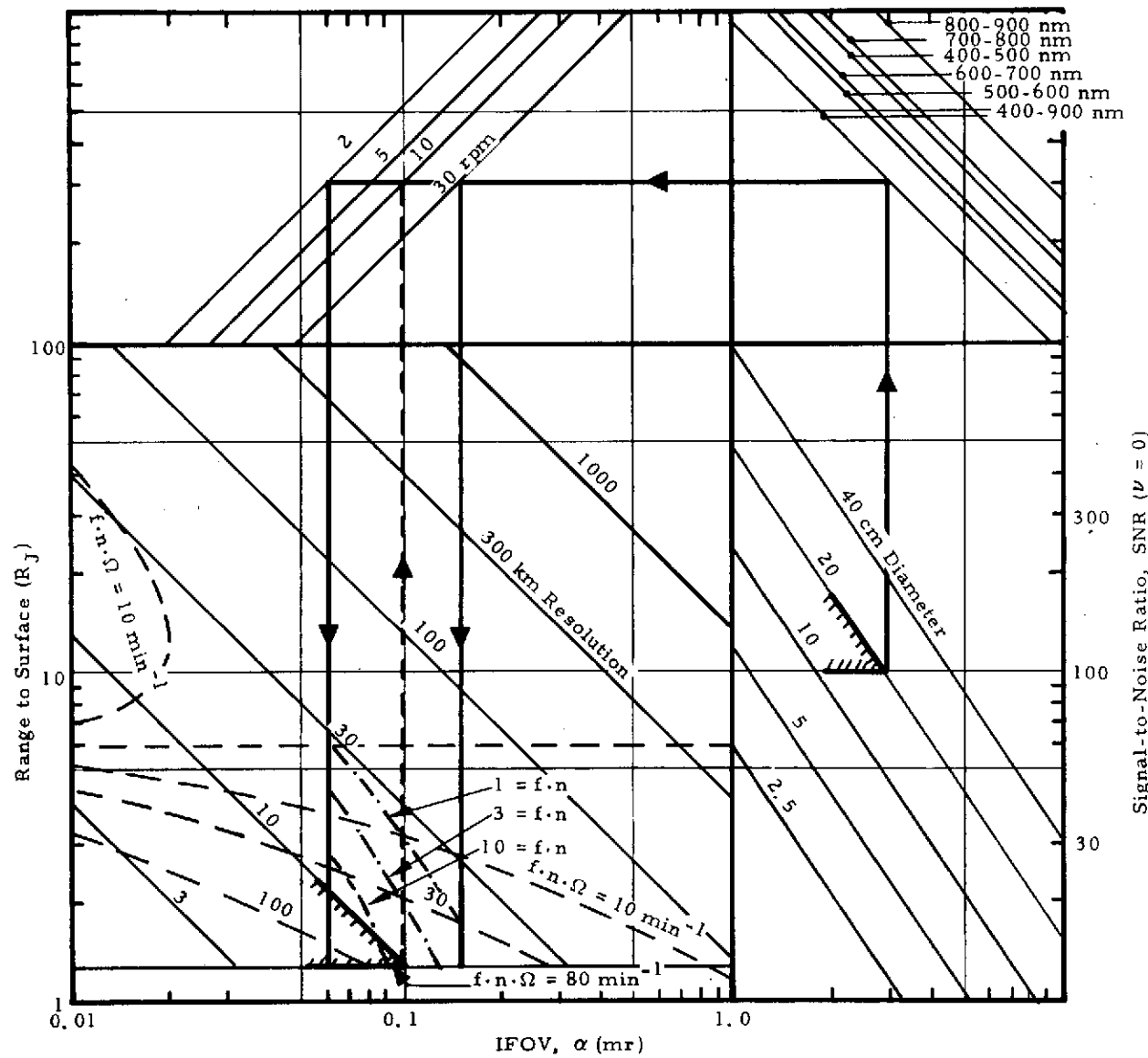


Figure 6-4. Parametric Modeling for OPM Imager Design 1
(Extended-Red, Digicon-Type Detector)
at Jupiter

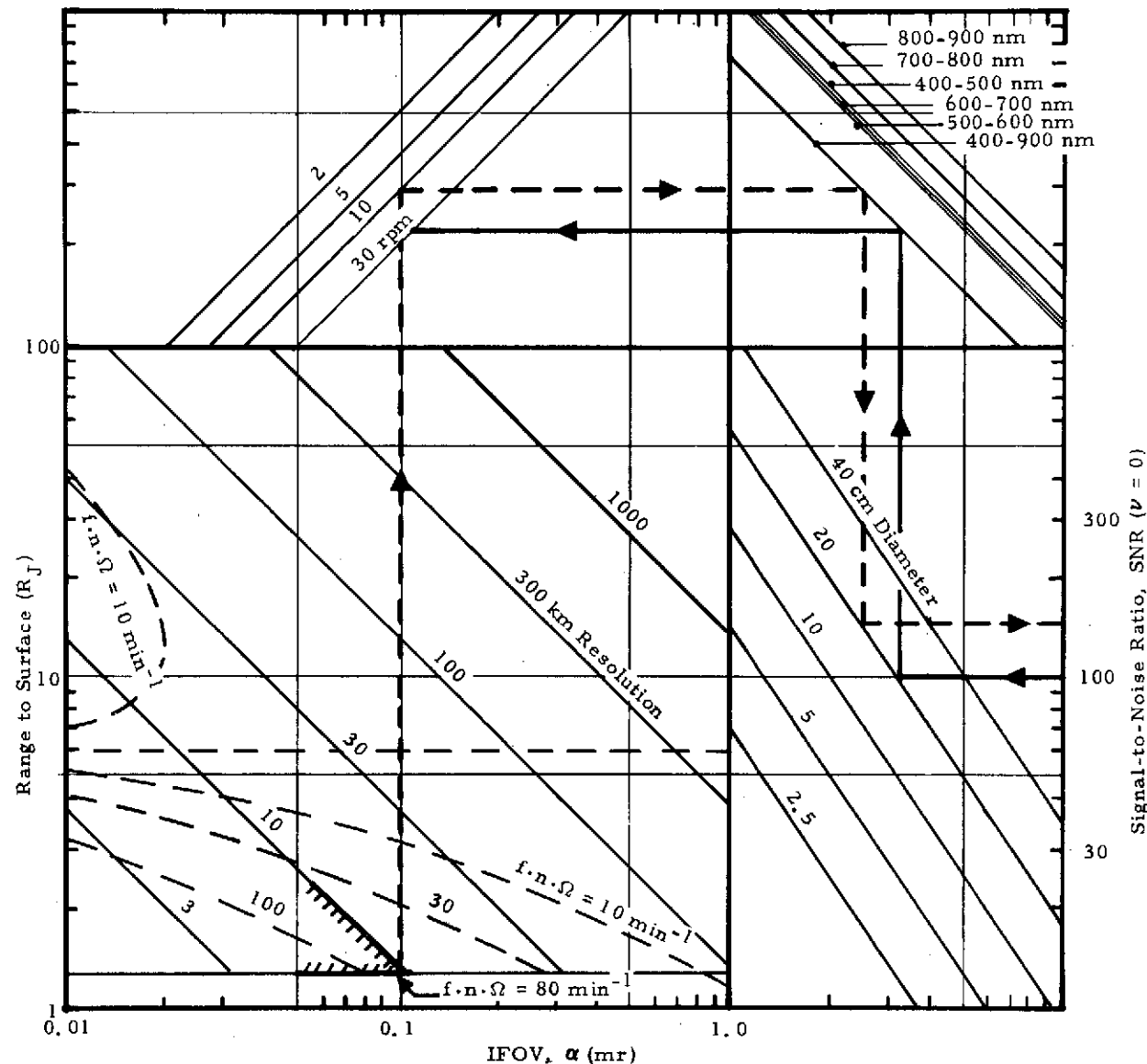


Figure 6-5. Parametric Modeling for OPM Imager Design 2
(GaAs PMT Detectors) at Jupiter

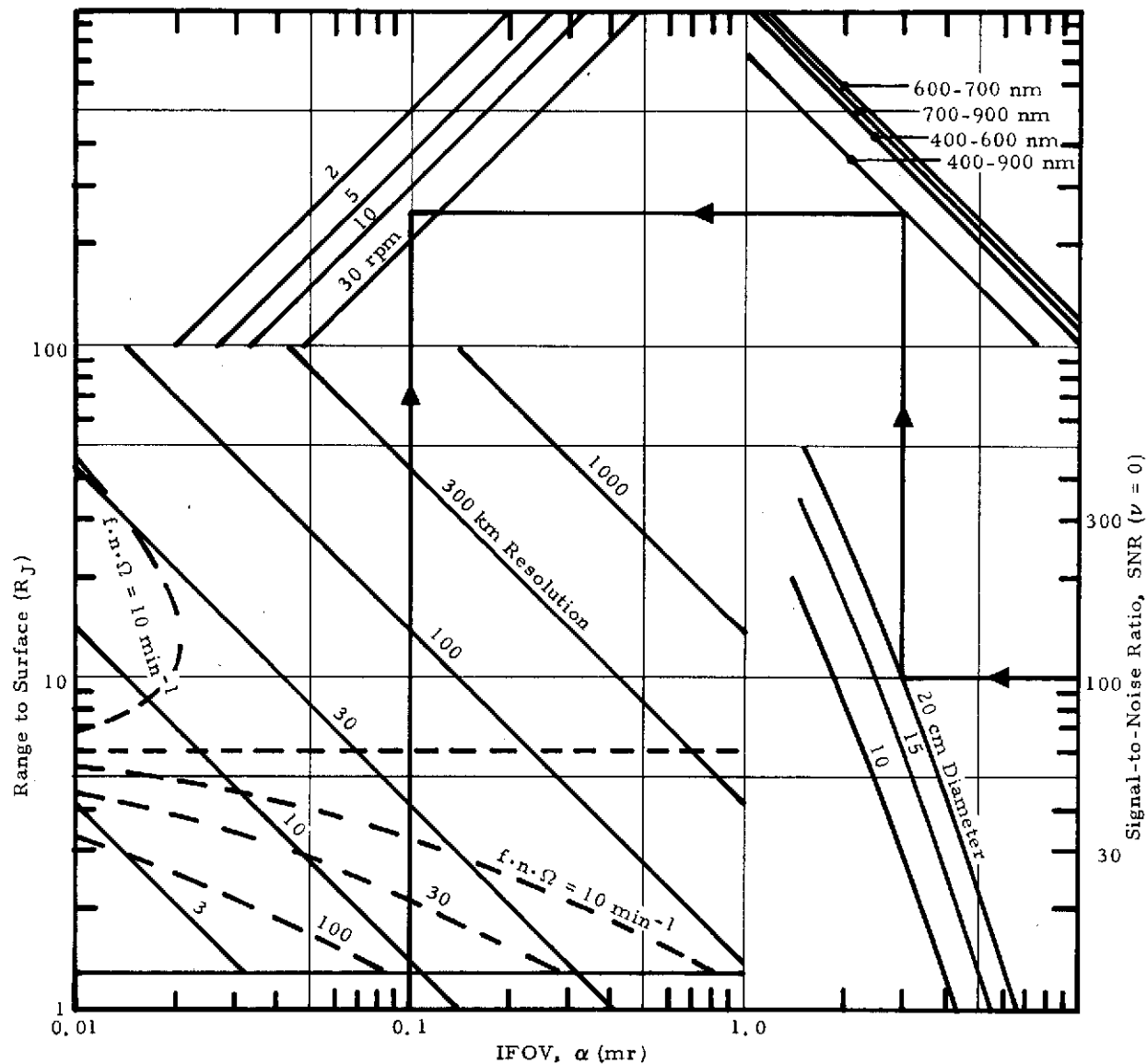


Figure 6-6. Parametric Modeling for OPM Imager Design 3
(Silicon Photodiode Detectors) at Jupiter

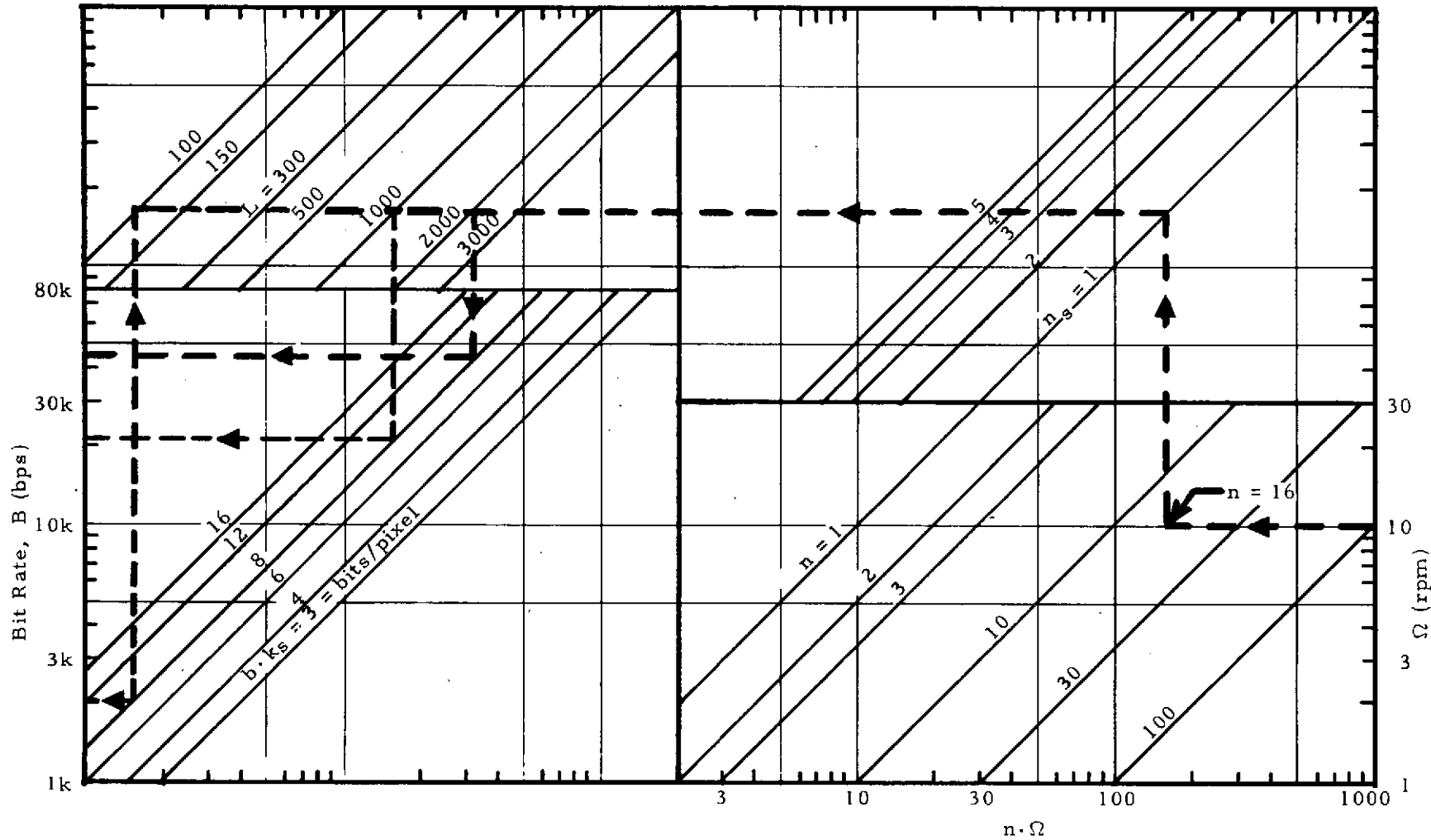


Figure 6-7. Telemetry Rate Modeling at Jupiter

A spin rate less than 10 rpm would allow an IFOV smaller than 0.1 mr to be used and would provide correspondingly improved resolution with the same SNR, but only by imposing other system penalties. For example, to provide the same coverage rate, the number of detectors would have to increase by the combined factor by which α and Ω decrease. The minimum coverage rate necessary to prevent underlap at periapsis could require n to be quite large. Another penalty would be a decrease in line length because the overlap condition requires n to increase more than Ω decreases. This would lead to decreased full-disk resolution.

However, if one were willing to take the highest resolution images (10 km per pixel) somewhat before periapsis and accept underlap inside of that range, one could spin slower, make the IFOV smaller, increase the line length, reduce coverage slightly, and improve full-disk resolution. Since this may preclude good imaging at periapsis when the spacecraft is likely to be over the terminator, it is not generally encouraged except as a compromise system for the Saturn/Uranus mission to be discussed in the next subsection.

Thus, one tradeoff to be analyzed is the relative advantage of a more narrow IFOV with consequent improved periapsis resolution, which is possible with a slower spin rate, versus the advantages of a higher spin rate. The latter are simply increased coverage, improved full-disk resolution, and fewer detectors. A reasonable preliminary choice would be to use the highest spin rate which permits adequate resolution.

As indicated, the highest spin rate for 0.1-mr IFOV would be 10 rpm. From Figure 6-4, to prevent gaps between image segments, $f\pi\Omega = 80 \text{ min}^{-1}$, so that at least 16 detectors must be used. This, then, is the specification for one Jupiter orbiter imager (Design 1) which will be further refined in the Point Design Study, Section 7.

To provide a full-disk resolution of 140 km, a scan length of 1000 pixels is necessary. By reference to Figure 6-7, a telemetry rate of at least 22 kbps is required for a postulated system with two samples per pixel ($k_s = 2$) and data compaction which allows effectively 4 bits/sample. As also shown, the resolution may be improved to 70 km by means of a 2000-pixel scan for a data rate of 44 kbps. Other compaction factors and telemetry limitations are readily obtained from this figure. It is apparent that the minimum telemetry system with 2 kbps would be inadequate since it would result in scans of only 100 pixels.

A second outer planet mission imager design under consideration uses an array of GaAs photomultiplier tubes. This is depicted in Figure 6-5. For the conditions previously described, a spin rate of approximately 22 rpm may be used or, at 10 rpm, an SNR ($\nu = 0$) = 150 results. While it is clear that an array of GaAs photomultipliers gives better performance for a given telescope size than the Digicon, it would also be significantly heavier. In Section 7, the performance weight tradeoffs among the three primary point designs will be detailed.

The third imager design under consideration uses a silicon photodiode solid-state array, shown in Figure 6-6. For this detector, the rms noise currents i_n were calculated with equation (5-9) for the following detector and preamplifier characteristics: photodiode dark current $i_{dark} = 50 \text{ pA}$; preamplifier $\bar{i}_n = 1 \times 10^{-15} \text{ A Hz}^{-1/2}$ and \bar{e}_n given by equation (5-11) where $e_o = 3 \times 10^{-9} \text{ V Hz}^{-1/2}$, and $f_o = 10 \text{ Hz}$; total correlation between preamplifier noise components [equation (5-12)]; input capacitance seen by preamplifier $C_{in} = 10 \text{ pF}$; capacitance associated with feedback resistor $C_f = 0.1 \text{ pF}$; and temperature $T = 300^\circ\text{K}$. Since no one component of the noise current dominates over the entire range of parameters indicated in Figure 6-6, the lines representing each telescope diameter are not quite straight as was the case for Point Designs 1 and 2. However, the methods for using the figure are analogous to those discussed for the point designs with photoemissive detectors.

6.3 APPLICATION TO OTHER OUTER PLANET MISSIONS

To evaluate the applicability of the baseline Jupiter orbiter imaging system to planets beyond Jupiter, a 1980 Saturn/Uranus flyby mission was postulated. The imaging instrument designed for Jupiter was to be used (Point Design 1 with extended-red Digicon) with no change in telescope, drive, or pointing mechanisms. The Digicon detector package, however, is relatively easily modified. Thus, the number of detectors and their FOVs were specified as required for each application. The planetary coverage (line length) is commanded at encounter as specified by the mission planner. The spacecraft roll rate may likewise be adjusted within limits (2 to 30 rpm). The only spacecraft modification considered was an increase in telemetry capability above that available for a Jupiter orbiter mission. This can impose severe weight penalties, however. To provide adequate coverage of these far outer planets, and due to the short duration of the encounter, it was necessary to assume that the highest pioneer class telemetry capability would be available for these missions: 83.2 kbps from Jupiter. This is reduced to about 19.5 kbps at Saturn and 4.1 kbps at Uranus.

The parameters of a Saturn/Uranus imager could be optimized for either encounter. Some compromise between these values could be chosen, but only the extreme values are investigated here. Certain trajectory parameters are of importance:

	<u>Saturn</u>	<u>Uranus</u>
Date	2445704.7	2447109
ϵ	1.486	2.542
Periapsis Radius	2.70 R_S	2.0 R_U
Periapsis RA	151.5°	8.65°
Periapsis Decl.	14.95°	-1.92°
Sub-sun RA	41.9°	-141.7°
Sub-sun Decl.	18.45°	77.4°
V_∞	10.63 km/sec	13.79 km/sec
Inclination	29.685°	83.36°
Ascending Node RA	-0.57°	-171.574°

6.3.1 Saturn/Uranus Mission: Uranus Encounter

The Uranus mission consists of a near-polar hyperbolic flyby which passes within one Uranus radius of the surface of the planet. Tradeoff figures have been constructed for the mission (see Figures 6-8 and 6-9). The conditions of an SNR ($\nu = 0$) of 100, a 20-cm optics diameter, and the 400- to 900-nm band are shown in Figure 6-8. It is apparent that the IFOV used for the Jupiter orbiter design (0.1 mr) would not be adequate with the low light levels at Uranus; at the minimum spin rate of 2 rpm, α must be at least 0.17 mr.

On the basis of operating at the highest spin rate commensurate with the resolution requirements, the following preferred design specification results for Uranus:

Spectral Band = 400 to 900 nm

$\Omega = 23$ rpm

$n = 6$ detectors

$\alpha = 0.38$ mr

$\ell_c = 10$ km

$L = 222$ pixels

The wide IFOV compared to that specified for the Jupiter instrument is feasible due to the smaller periapsis radius, which improves the surface resolution. The scan length of 222 pixels would result in a surface resolution of

$$\ell_c = \frac{2 R_U}{222} = 225 \text{ km} \quad (6-9)$$

for full-disk images. This is approximately 30 times better than the best potential Earth-based resolution and is therefore satisfactory for full-disk pictures.

The Uranus encounter and the Saturn encounter, discussed in the next subsection, differ in certain respects. At Uranus, the large communication distance reduces the bit rate and therefore coverage and

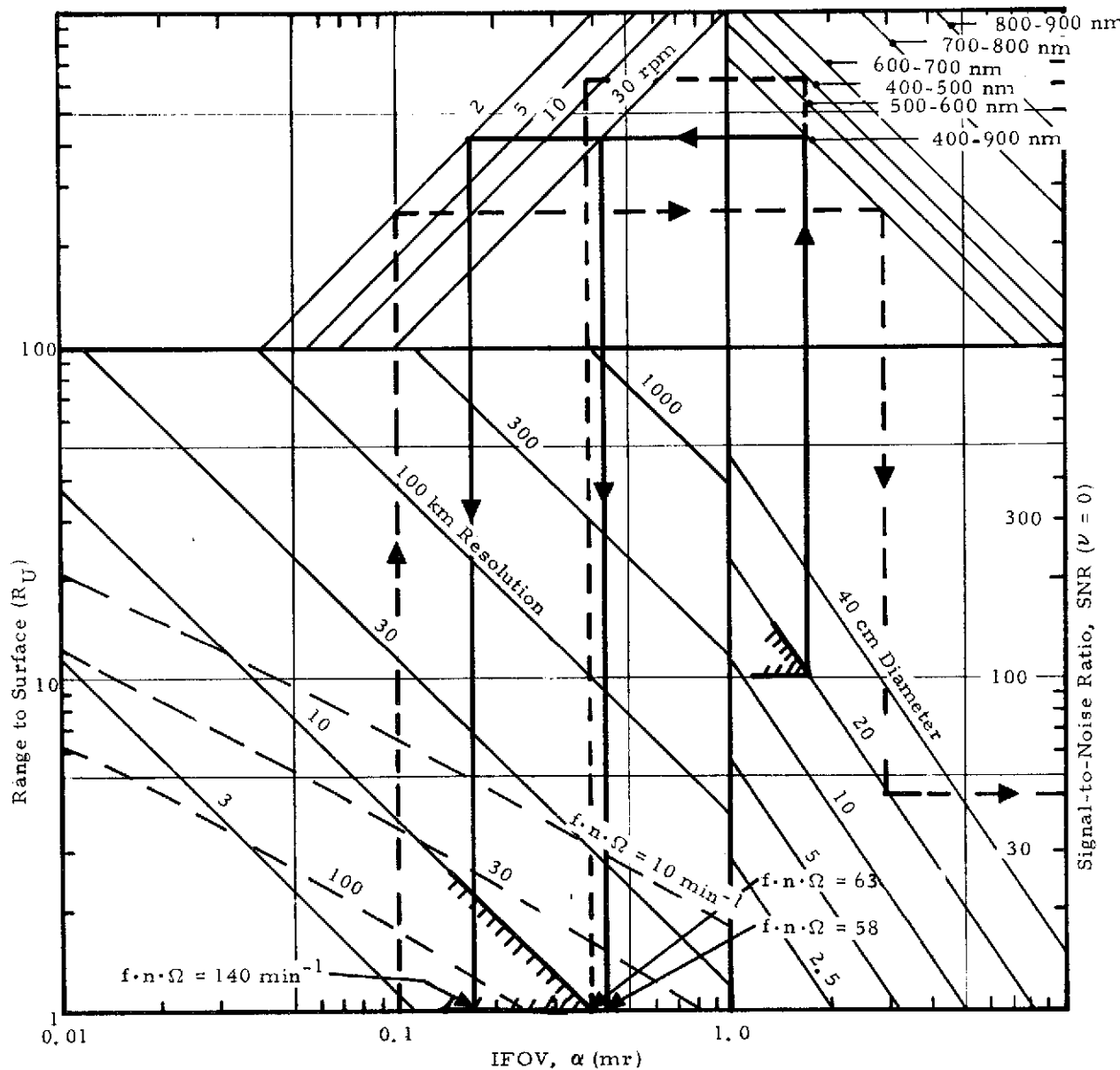


Figure 6-8. Parametric Modeling for OPM Imager Design 1
 (Extended-Red, Digicon-Type Detector)
 at Uranus

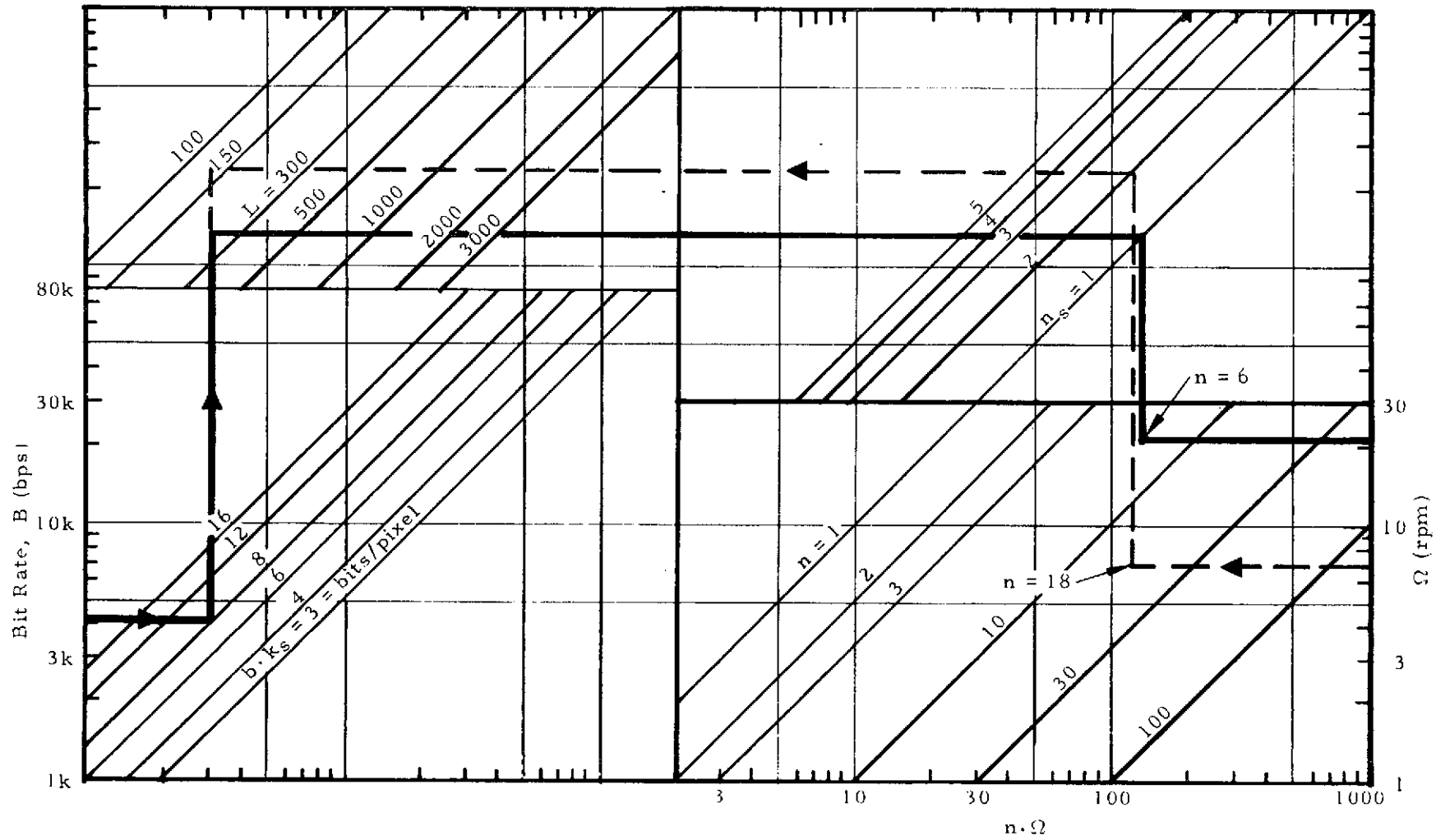


Figure 6-9. Telemetry Rate Modeling at Uranus

line length. At Saturn, this is not a problem since the data rate is nearly 5 times as great. At Uranus, the reflected light is approximately one-fourth that at Saturn due to the relative heliocentric distances and albedos. However, for the flybys under study, the distance to the surface at periapsis is one-fourth that at Saturn. As a result, for the same resolution requirement (10 km), the IFOV at Uranus may be four times as large and the light gathering capability may thus be sixteen times as large. This more than compensates for the reduced light due to distance and albedo. Therefore, one can expect better resolution and worse coverage at Uranus than at Saturn. One could even consider the possibility of two spectral channels at Uranus. The following paragraphs examine this possibility.

Figure 6-8 also illustrates the impact of including a second spectral region: 400 to 500 nm. The inclusion of this band results in the following specifications:

Spectral Band = 400 to 500 nm

Ω = 7 rpm

n = 18 detectors

α = 0.38 mr

ℓ_c = 10 km

SNR ($\nu = 0$) = 100

The spin rate is therefore reduced to compensate for the signal loss in the narrower spectral band. The original specification must also be modified to operate at this lower spin rate, but the SNR ($\nu = 0$) is improved:

Spectral Band = 400 to 900 nm

Ω = 7 rpm

n = 18 detectors

α = 0.38 mr

ℓ_c = 10 km

SNR ($\nu = 0$) = 200

A more narrow IFOV could have been used with this spectral band instead, but this could complicate the alignment of the scans (registration) from the two bands. With the above two-wavelength system, the scan length would be reduced to 123 pixels. As a result, two frames of imagery would be necessary to obtain full-disk coverage at 225 km resolution (versus 30,000 km resolution for one arc sec seeing from Earth). The coverage would be reduced throughout the balance of the encounter as well.

Some flexibility does exist, however. For example, the degree of detector overlap, f , to prevent aliasing of high-frequency signal components, could be reduced. Again, a scientific judgment beyond the scope of this report would be necessary to balance the value of a system with a single spectral band with no aliasing and with an acceptable scan length versus another system with two spectral bands but reduced coverage and/or a higher degree of aliasing. For this study, the primary system with a single spectral band will be assumed.

Another alternative which would result in increased line length would be to obtain the best resolution images without underlap at a range greater than the minimum range of the trajectory. For example, for a system with one spectral channel, images with 10-km resolution and SNR ($\nu = 0$) = 100 could be obtained at $2 R_U$ if $\Omega = 2$ rpm and $\alpha = 0.18$ mr. For no underlap at this range $fn\Omega$ would have to be 40 giving $n = 40$ with $f = 1/2$ and $\Omega = 2$ rpm. From Figure 6-9, it is seen that one spectral channel and $n\Omega = 80$ allows a line length of 384 pixels and a full-disk resolution of 130 km. This system could be summarized as follows:

Spectral Band = 400 to 900 nm

$\Omega = 2$ rpm

$n = 40$ detectors

$\alpha = 0.18$ mr

$$\begin{aligned}\ell_c &= 10 \text{ km (at } R = 2 R_U\text{)} \\ L &= 384 \text{ pixels} \\ \ell_{fd} &= 130 \text{ km} \\ \text{SNR } (\nu = 0) &= 100\end{aligned}$$

This system will be of particular interest when Saturn imaging is also desired.

6.3.2 Saturn/Uranus Mission: Saturn Encounter

An examination of Figure 6-10 shows that the Jupiter orbiter design previously discussed would function at Saturn with only minor modifications; specifically, an increase in the number of detectors and a reduction in spin rate. However, the construction of an imager for both Saturn and Uranus necessitates either optimizing for one planet and accepting the consequent degraded performance at the other, or selecting one of the many compromise specifications between these extremes. This latter approach is followed in this subsection, with the result that the previously postulated design for a system optimized for Uranus must be amended. This subsection then illustrates the sacrifices in performance which are the result of a compromise design.

As can be seen from Figure 6-10 with an SNR ($\nu = 0$) of 100, the IFOV at Saturn is restricted to be greater than 0.1 mr. Since at Uranus, a value of 0.18 mr was the smallest considered, it will be considered for the compromise design.

As a result of a first application of the tradeoff figures, the following specification is obtained for a Saturn/Uranus imager:

	<u>Saturn</u>	<u>Uranus</u>
Spectral Band	400 to 900 nm	400 to 900 nm
SNR ($\nu = 0$)	100	100
Ω	13 rpm	2 rpm
α	0.18 mr	0.18 mr
ℓ_c	18 km	10 km (at $2 R_U$)
n	3 detectors	40 detectors
L	(see below)	384 pixels

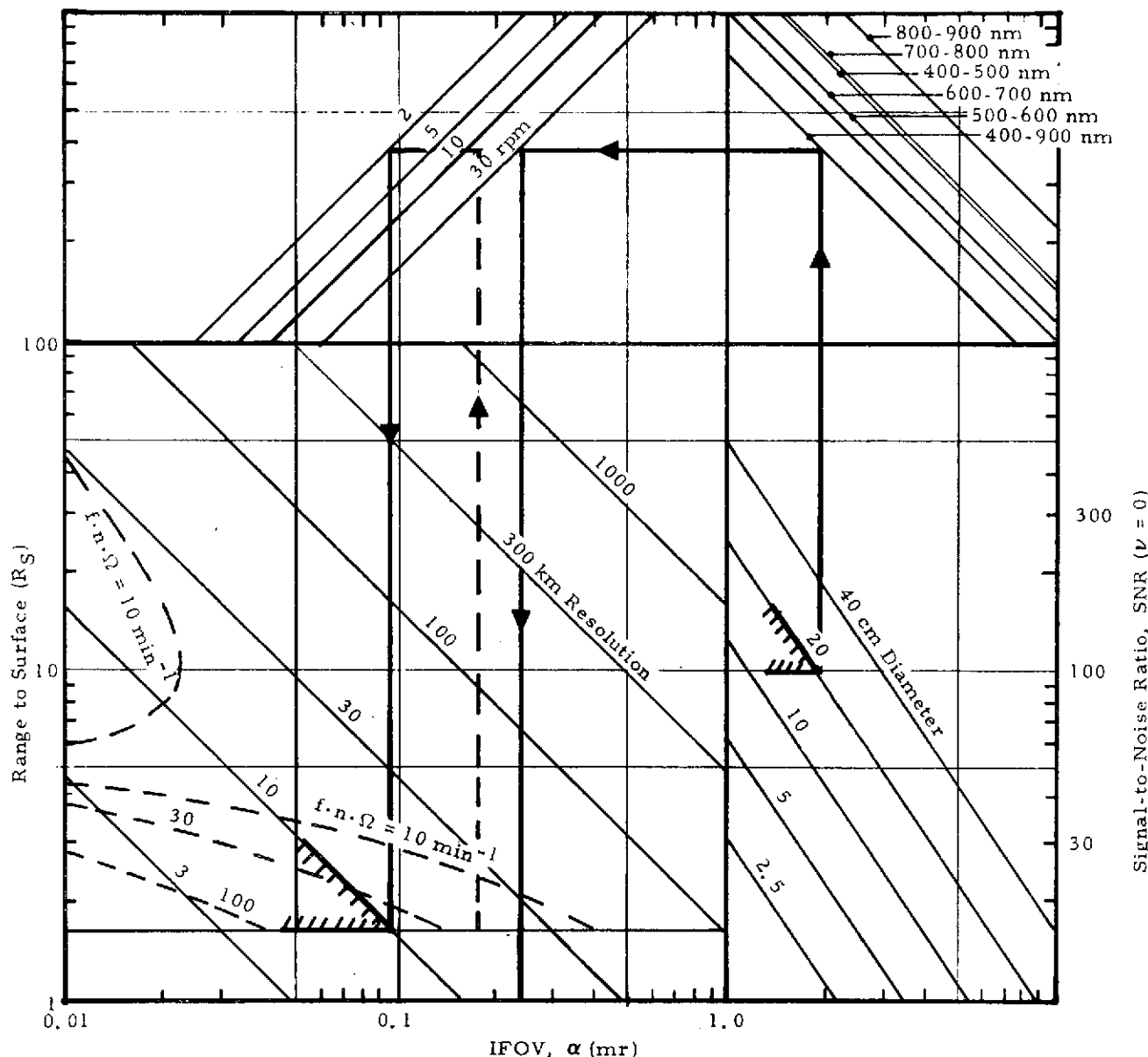


Figure 6-10. Parametric Modeling for OPM Imager Design 1
(Extended-Red, Digicon-Type Detector)
at Saturn

At Uranus, 40 detectors must be used to prevent underlap. With the restricted telemetry rate, this results in a scan length of 384 pixels. This would permit a resolution of 130 km at Uranus for far-encounter pictures.

At Saturn, 3 detectors only would suffice. However, the full 40-detector array could be used if it were available. In this case, it would be possible to use many rolls of the spacecraft to transmit the 40 scans of imagery rather than a single roll, which would permit complete flexibility in choosing the scan-line length at Saturn. The near-encounter resolution, however, can never be better than 18 km with this system, as indicated.

Some improvement in resolution at Saturn could be obtained by accepting a degraded SNR at Uranus. This permits a more narrow IFOV; hence, better resolution. This effect is illustrated in Figure 6-8. The resulting system may be postulated:

	<u>Saturn</u>	<u>Uranus</u>
Spectral Band	400 to 900 nm	400 to 900 nm
SNR ($\nu = 0$)	100	40
Ω	2 rpm	2 rpm
α	0.10 mr	0.10 mr
ℓ_c	10 km	10 km (at $3.5 R_U$)
n	40 detectors	30 detectors
L	2000 pixels	512 pixels

For this increase in surface resolution, from 18 to 10 km at Saturn, the SNR at Uranus must be decreased from 100 to 40, although the line length at Uranus can be increased from 384 to 512 pixels.

The modifications to increase resolution at Saturn act to decrease the SNR at Uranus, although such a compromise is probably acceptable. This discussion serves to illustrate the types of tradeoffs available to the designer of spin-scan imaging systems.

Section 7

POINT DESIGN FOR JUPITER ORBITER

7.1 SYSTEM DESIGN

The system modeling described in Section 6 formed the basis for the preliminary OPM Imager Point Designs. In this section, the important imager subassemblies are detailed along with the rationale behind the various design choices. In the final subsection, each of the three primary Point Designs is optimized for minimum weight with each providing the same reasonable performance characteristics.

7.1.1 Imager Point Design Assumptions

The spacecraft parameters assumed for the OPM Imager Point Designs are listed in Table 7-1. Some of the basic electrical inputs assumed to be supplied from the spacecraft (e.g., the sector pulses) could be generated within the instrument. However, those inputs listed or their equivalents presumably would be required of other scientific instruments and overall economy of mission hardware should thereby result. The roll index pulse repeatability and wobble angle requirement are probably more severe than would be imposed by other scientific instruments. However, based on the Pioneer 10 and 11 experience, these requirements should be within potential capability.

The assumption of four independent spacecraft memory processors is made to avoid the large power increase required in the spacecraft and OPM Imager for a relatively modest increase in read-in rate. There is also an advantage with this approach from the reliability point of view since the OPM Imager could function with only modest degradation should a portion of the imager or spacecraft processing capability be lost. The detailed reasoning which led to this multiprocessor approach is discussed further in subsection 7.2.5.

Table 7-1. Spacecraft Characteristics Assumed for Spin-Scan
Imager Point Design Analysis

TIMING SIGNALS:	1-MHz CLOCK, ROLL INDEX PULSE, AND SECTOR PULSE (512 OR 1024) [DESIRABLE]
TIMING SIGNAL REPEATABILITY:	ROLL INDEX AND SECTOR PULSES BETTER THAN ~20 μ s (AT 10 RPM) [NECESSARY]
WOBBLE ANGLE:	LESS THAN ~15 μ r DURING IMAGING [NECESSARY]
MEMORY STORAGE:	MINIMUM STORAGE ~250 K BITS [DESIRABLE]
MEMORY PROCESSOR(S):	FOUR INDEPENDENT PROCESSORS, EACH WITH 1 MBPS READ-IN RATE [DESIRABLE]
MEMORY PROCESSOR SIGNALS:	DATA STORE GATE AND END-OF-MEMORY PULSES [NECESSARY]
TELEMETRY RATE:	~50 KBPS AT JUPITER [DESIRABLE], TRADE-OFF HERE AFFECTS SCAN LINE LENGTH
COMMANDS:	ALLOCATION OF 15 COMMANDS (OR 16 WITH TWO SPECTRAL BANDS) PLUS POWER ON/OFF [DESIRABLE]
COMMAND STORAGE:	MINIMUM OF 10 STORABLE COMMANDS [DESIRABLE]
THERMAL ENVIRONMENT:	MAINTAINED BETWEEN 0° AND 45°C [DESIRABLE]
ROLL RATE RANGE:	2 TO 30 RPM [DESIRABLE]

The telemetry rate available to the OPM Imager basically determines the length of the image swath swept out each roll. To simplify the command activity that provides the image sequencing, it has been assumed that the maximum step size should be equal to the array width. For a given imaging geometry (as discussed in Sections 3 and 6), the $f n \Omega$ product required is related to the telescope step rate (angular step per roll). The above parameters plus a specification of the number of grey levels, samples per dwell time, and the effective data-compaction factor define the line length for a given pixel. The OPM Imager Point Designs that are described in this section will yield full-disk images at $10 R_J$ for the baseline Jupiter orbit with the assumed spacecraft characteristics.

The memory storage for the OPM Imager designs serves to buffer the data so that they may be more efficiently telemetered. The storage requirement is based on the assumption that only one roll of data need be stored. A memory storage on the order of 250 k to 1000 k bits should be consistent with the OPM Imager Point Designs and the probable telemetry rates for an advanced Pioneer-type spacecraft.

A total of about 15 commands seems appropriate to provide desired flexibility for image sequencing. In addition, it is highly desirable that provision be made to store a minimum of ten commands for flexible imaging.

In Table 7-2 are shown the basic characteristics of the preliminary OPM Imager Point Designs. Included are the three primary Point Designs and an alternate design which could be considered to enhance reliability and spectral coverage. These assumed properties formed the basis for the detailed analyses described in later portions of this section. The effect of changing various instrument parameters was evaluated with particular emphasis on the consequent weight change.

Table 7-2. Characteristics of Preliminary OPM Point Designs

	POINT DESIGN 1	ALTERNATE POINT DESIGN 1	POINT DESIGN 2	POINT DESIGN 3
DETECTORS	ONE DIGICON-TYPE (EXTENDED RED)	TWO DIGICON-TYPE (EXTENDED RED)	16 PHOTOMULTIPLIERS (GaAs)	SILICON PHOTO-DIODE ARRAY (INDIVIDUAL PREAMPLIFIERS)
LINEAR ARRAY INSTANTANEOUS FIELD OF VIEW	16 STAGGERED INDIVIDUAL IFOVs ~0.1 mr (RECTANGULAR SHAPE)	SIMILAR TO POINT DESIGN 1 EXCEPT f~1 WITH TWO SPECTRAL BANDS	SIMILAR TO POINT DESIGN 1 (IFOVs APPROXIMATELY SQUARE)	SAME AS POINT DESIGN 1
TELESCOPE	f/3, 20 CM DIAMETER CASSEGRAIN; IFOV ARRAY ON PHYSICAL TELESCOPE AXIS	SIMILAR TO POINT DESIGN 1 EXCEPT SECOND FOLDED BEAM PROVIDED WITH BEAM-SPLITTER	SIMILAR TO POINT DESIGN 1 EXCEPT BEAM FOLDED PERPENDICULAR TO PHYSICAL TELESCOPE AXIS	SAME AS POINT DESIGN 1
SPECTRAL COVERAGE	ONE OR TWO SPECTRAL BANDS; TOTAL SPECTRAL RANGE ~400-900 nm	TWO SPECTRAL BANDS; SPECTRAL RANGE SAME AS POINT DESIGN 1	SIMILAR TO POINT DESIGN 1	ONE OR TWO SPECTRAL BANDS; TOTAL SPECTRAL RANGE ~400-1000 nm
GRAY SCALE	256 LEVELS (8 BITS / SAMPLE)	SAME AS POINT DESIGN 1	SAME AS POINT DESIGN 1	SAME AS POINT DESIGN 1
DYNAMIC RANGE	GREATER THAN 3000:1 WITH COMMANDABLE GAIN CHANGES	SAME AS POINT DESIGN 1	SAME AS POINT DESIGN 1	SAME AS POINT DESIGN 1
DATA COMPACTION	3-BIT DPCM WITH AUTOMATIC AND PERIODIC UPDATES	SAME AS POINT DESIGN 1	SAME AS POINT DESIGN 1	SAME AS POINT DESIGN 1
INFILIGHT RADIO-METRIC CALIBRATION	S/C MOUNTED SOLAR DIFFUSER PLUS INTERNAL SOURCE PROVIDING SIX LEVELS	SAME AS POINT DESIGN 1	SAME AS POINT DESIGN 1	SAME AS POINT DESIGN 1
TELESCOPE CROSS-SCAN DRIVE	MECHANICAL DRIVE PLUS 'TRIM' DEFLECTION WITHIN DIGICON	SAME AS POINT DESIGN 1	SIMILAR TO POINT DESIGN 1 EXCEPT SERVO DRIVE USED FOR 'TRIM'	SAME AS POINT DESIGN 2
ANGULAR RANGE AND STEP SIZE OF TELESCOPE CROSS-SCAN DRIVE	ANGULAR RANGE -120° WITH SELECTABLE STEP SIZE AND DIRECTION	SAME AS POINT DESIGN 1	SAME AS POINT DESIGN 1	SAME AS POINT DESIGN 1
USABLE SCAN (ROLL) ANGLE	ESSENTIALLY 360°	SAME AS POINT DESIGN 1	SAME AS POINT DESIGN 1	SAME AS POINT DESIGN 1

7.1.2 Functional Operation

The basic concept of spin-scan imaging was described in subsection 2.2. The functional operation of the OPM Imager Point Designs follows the general approach used with the Pioneer 10 and 11 Imaging Photopolarimeter but with the functions not associated with imaging deleted. However, to increase flexibility (and thereby increase the utilization of available imaging opportunities) a small increase in the number of commands was deemed appropriate.

It is convenient to discuss the functional operation of the OPM Imager by referring to the command list given in Table 7-3. In addition to listing the 15 commands (16 with two spectral bands), a brief functional description is also provided.

With power ON, the imager is configured to a "nominal" data-taking state. The spoke (roll position), starting look angle, telescope step direction and step size, and channel gain resistors of the imager are set to preselected values and the data output is initiated. The SIMS command turns on the high voltage (if PMT detectors are used) and starts the telescope slewing to a starting look angle prior to initiating the automatic sequencing. The STBY command puts the instrument into a standby condition (high voltage off if PMT detectors are used). The RESET command resets various registers to preselected states.

The telescope step direction is changed to forward or reverse stepping (in place of the power ON condition of inhibited stepping) by means of the FORST and REVST commands, respectively. The step size is changed by incrementing a step size register with the TSINC command. Preselected look angles called Starting Look Angles (SLAs) serve as angles to which the telescope can rapidly be slewed. The SLA register can be incremented or decremented with the LAINC and LADEC commands, or reset to one of two "prime" SLAs with the power ON (to SLAPR1) or RESET command (to SLAPR2).

Table 7-3. OPM Imager Command List

COMMAND NAME	ABBREVIATION	FUNCTIONAL DESCRIPTION
POWER ON/OFF	ON/OFF	TURNS "ON" INSTRUMENT POWER; SETS THE FOLLOWING REGISTERS: SPOKE - RP = RPPR1, STARTING LOOK ANGLE - SLA = SLAPR1, TELESCOPE STEP DIRECTION AND SIZE - TELDIR = 0 (INHIBIT) AND TELSIZ = 0 (ZERO STEP SIZE); ACTIVATES DATA COMPACTION; TURNS HIGH VOLTAGE 'ON'; STARTS SIX ROLL CALIBRATION SEQUENCE FOLLOWED BY NORMAL DATA TAKING OPERATION.
START IMAGING SEQUENCE	SIMS	TURNS "ON" HIGH VOLTAGE; RESETS DATA COMPACTION INHIBIT 'OFF'; STARTS TELESCOPE SLEWING TO SLA IN REGISTER; STARTS SIX ROLL CALIBRATION SEQUENCE FOLLOWED BY NORMAL DATA TAKING OPERATION.
STANDBY	STBY	PUTS INSTRUMENT INTO A STANDBY CONDITION; TURNS "OFF" HIGH VOLTAGE, INSTRUMENT DATA OUTPUT IS <u>NOT</u> DISABLED.
RESET	RESET	RESETS THE FOLLOWING REGISTERS: SPOKE - RP = RPPR2, STARTING LOOK ANGLE - SLA = SLAPR2, TELESCOPE STEP DIRECTION AND SIZE - TELDIR = 0 AND TELSIZ = 0.
SPOKE ADVANCE FINE	SPAF	INCREMENTS SPOKE REGISTER BY AMOUNT EQUAL TO 1/256th OF A ROLL.
SPOKE ADVANCE COARSE	SPAC	INCREMENTS SPOKE REGISTER BY AMOUNT EQUAL TO 1/64th OF A ROLL.
SPOKE REVERSE COARSE	SPREC	DECREMENTS SPOKE REGISTER BY AMOUNT EQUAL TO 1/16th OF A ROLL.
START DATA AT THRESHOLD	SDAT	CAUSES DATA TO START AT ROLL POSITION NEAR WHERE SPECIFIED CHANNEL SIGNAL EXCEEDS PRESET THRESHOLD LEVEL.
FORWARD STEPPING	FORST	PROGRAMS TELESCOPE STEP DIRECTION TO "FORWARD," AND INSERTS SIX ROLL CALIBRATION SEQUENCE.
REVERSE STEPPING	REVST	PROGRAMS TELESCOPE STEP DIRECTION TO "BACKWARD," AND INSERTS SIX ROLL CALIBRATION SEQUENCE.
TELESCOPE STEP SIZE INCREMENT	TSINC	INCREMENTS TELESCOPE STEP SIZE REGISTER: 0 STEP SIZE (NO STEP), 1 STEP, 2 STEPS, OR 4 STEPS, THEN 0 STEP, ETC.
GAIN INCREMENT BAND 1	GINC1	INCREMENTS GAIN REGISTER FOR SPECTRAL BAND 1 BY ONE STEP (6 TOTAL STEPS) REPEATING STEP 0 AFTER STEP 6.
GAIN INCREMENT BAND 2*	GINC2	INCREMENTS GAIN REGISTER FOR SPECTRAL BAND 2 BY ONE STEP (6 TOTAL STEPS) REPEATING STEP 0 AFTER STEP 6.
LOW SAMPLE RATE INHIBIT	LOSIN	INHIBITS AUTOMATIC KEYING OF SAMPLE RATE TO LOOK ANGLE; SAMPLE RATE REMAINS AT NOMINAL VALUE REGARDLESS OF LOOK ANGLE.
DATA COMPACTION INHIBIT	DCOIN	INHIBITS NORMAL M-BIT DPCM DATA COMPACTION FUNCTION; ALL DATA SAMPLES DIGITIZED IN ABSOLUTE NUMBERS (N-BIT PCM).
LOOK ANGLE INCREMENT	LAINC	INCREMENTS LOOK ANGLE REGISTER IN CYCLIC FASHION (RESETTING TO LOWEST VALUE AFTER HIGHEST VALUE).
LOOK ANGLE DECREMENT	LADEC	DECREMENTS LOOK ANGLE REGISTER IN CYCLIC FASHION (RESETTING TO HIGHEST VALUE AFTER LOWEST VALUE).

*NOT USED IN SINGLE-COLOR INSTRUMENTS

The 360° of roll angle has a number of equally spaced "spokes" (512 for Pioneer 10 and 11) referred to a space-fixed direction by means of a star pipper. In "normal" operation, the start of each swath of data would begin at the spoke number stored in a register. The stored spoke can be changed by ground command with the SPAF, SPAC, or SPREC commands and set or reset to one of two "prime" spokes (roll positions) with the power ON or RESET commands as noted above. The Start Data at Threshold command (SDAT) causes the data start to begin at a spoke located near where the signal(s) first exceeded a preset threshold level. As discussed in subsection 8.3.1, an automatic sequencing function could provide a marked increase in time spent on object and/or decrease of command activity. It would be appropriate to control this function by the SIMS (or possibly SDAT) command.

The effective gain in each spectral band can be adjusted with the GINC1 and GINC2 commands. The second command would not be required for a single-color instrument.

It is appropriate to key the sampling rate to the look angle since the effective overlap of successive samples increases as $[\sin(\text{look angle})]^{-1}$. The sampling rate is automatically changed at preselected look angles. The LOSIN command would allow this automatic function to be overridden if desired. The DCOIN command allows the data compaction function of the OPM Imager to be overridden.

Coding of the commands was not done but may be appropriate if the command list is appreciably expanded, for example, to achieve redundancy. Obviously, some of the commands included could be deleted at the cost of a greater number of commands to "set up" the instrument for a given imaging sequence. There is some redundancy built into the selection of commands although the primary aim was operation flexibility.

7.2 ELECTRONIC DESIGN

In this subsection, the preamplifiers, high-voltage supplies, analog and digital signal processing, and signal information rates for the various imager configurations are discussed. Estimates of power, weight, and size are included to allow for direct comparison between the primary Point Designs.

7.2.1 Preamplifiers

Preamplifiers for photodiode signals are typically mechanized using current-mode, low-noise amplifiers with large feedback resistors. This approach has proven to give the best SNRs because signal output increases directly with the feedback resistance value, while noise contributed by the feedback resistor (the dominant amplifier noise source) increases as the square root of the resistance value. It is easily seen then that making the feedback resistor as large as possible improves the SNR (assuming the system is preamplifier noise limited).

Practical limits for the feedback resistor size are reached when the phase shift introduced by the feedback resistor/stray or circuit capacitance affects the amplifier stability in the required signal passband. The required signal passband is a direct function of spin rate. For example, with a spacecraft roll rate of 5 rpm and a 0.1-mr FOV, a preamplifier bandwidth of approximately 5 kHz is required. This high-frequency response requirement limits the feedback resistance to approximately 180 megohms with the assumptions discussed in subsection 5.1.5. The resulting equivalent input current noise contributed by the preamplifier would be $1 \times 10^{-14} \text{ A Hz}^{-1/2}$ including the thermal noise of the feedback resistor. Some additional reduction of this noise figure might be possible by use of special packaging techniques and trim capacitors to neutralize stray circuit capacitance. However, individual channel adjustment would be required at system test level (with detectors installed) which may be unattractive in a system with a large

number of channels. Approximately eight components and 15 mw are required per preamplifier for the first type and eleven components and 25 mw for the second.

Preamplification of PMT or Digicon signals can be performed by means of a simple current mode amplifier because system noise is predominately shot noise of the photoelectrons rather than preamplifier noise. For this reason, a discussion of circuitry is not necessary. Approximately eight components and 15 mw per channel are required to mechanize these preamplifiers.

7.2.2 High-Voltage Supply

Voltages on the order of 1 to 2 Kv are required to power the photomultiplier tubes used in Design 2. Two dynode biasing methods are possible, using a resistor voltage divider or directly driving dynodes from various points along the high-voltage multiplier chain. The most efficient method is use of the multiplier chain; however, individual multipliers are required for each tube, or many interconnecting high-voltage cables must be used. Direct sensing and regulation of the high voltage is probably necessary to ensure constant gain from the photomultiplier tubes.

This can be mechanized by use of a high-resistance voltage divider feeding a FET input sensing amplifier which controls the ac signal to the multiplier by one of several methods. If a tube anode current of 0.1 to 0.5 μ a is assumed, and individual multipliers are used for each tube, approximately 1 watt, 200 components, and 0.92 pound will be required for powering each eight tubes.

Dynode biasing with a resistive divider is not recommended because of the inherent high power consumption. The tube output linearity is a function of the tube anode current and the dynode impedances. For anode currents of 0.1 μ a, 5.0 to 10.0 μ a should flow through the dynode divider. With this mechanization, a power increase of 1 watt per eight tubes could be expected, over the dynode approach.

For the Digicon-type detector, approximately 20 Kv at less than 1 μ A is required. Detector sensitivity is not a strong function of high voltage and regulation can be performed using a feedback winding from the high-voltage step-up transformer rather than a divider feedback from the high-voltage output. This is very significant in the design because a 1-G Ω resistor, which is close to the state of the art in stable resistors, dissipates 0.4 watt at 20 Kv, and would result in a very high voltage supply. One successful mechanization of an efficient high-voltage supply involves the use of a Hartley oscillator composed of a transistor and high-voltage transformer. In this configuration, the transformer parasitic capacitance, which usually limits the efficiency of high-voltage converters driven by square waves, can be used as the tuning capacitance of the oscillator. The resulting high Q tuned circuit is extremely efficient and required very few components.

Digicon mechanizations requiring relatively large cross-scan steps (0.5 mr or larger) can incorporate a fine position scanning servo using the deflection plates within the tube, thus removing the requirement for extremely precise mechanical scanning components. An additional dc voltage of approximately 100 volts at less than 1 μ A is required. Encoder feedback from the scanning mechanism can be used to control the deflection voltage source. A high-voltage supply with deflection circuitry can be mechanized with approximately 80 components, consuming 500 mw and weighing 0.23 kg (0.5 pound).

7.2.3 Analog Channel Electronics

The OPM Imager electronic block diagram is shown in Figure 7-1. The electronic filtering and amplification of the analog signals is identical for photodiode, PMT, and Digicon detectors. A six-level attenuation, controlled by an incrementing ground command (see Command List given in Table 7-3), is required for each spectral channel. The six levels can correspond to binary gain increments or have individually adjustable step sizes through the use of select resistors. Since no

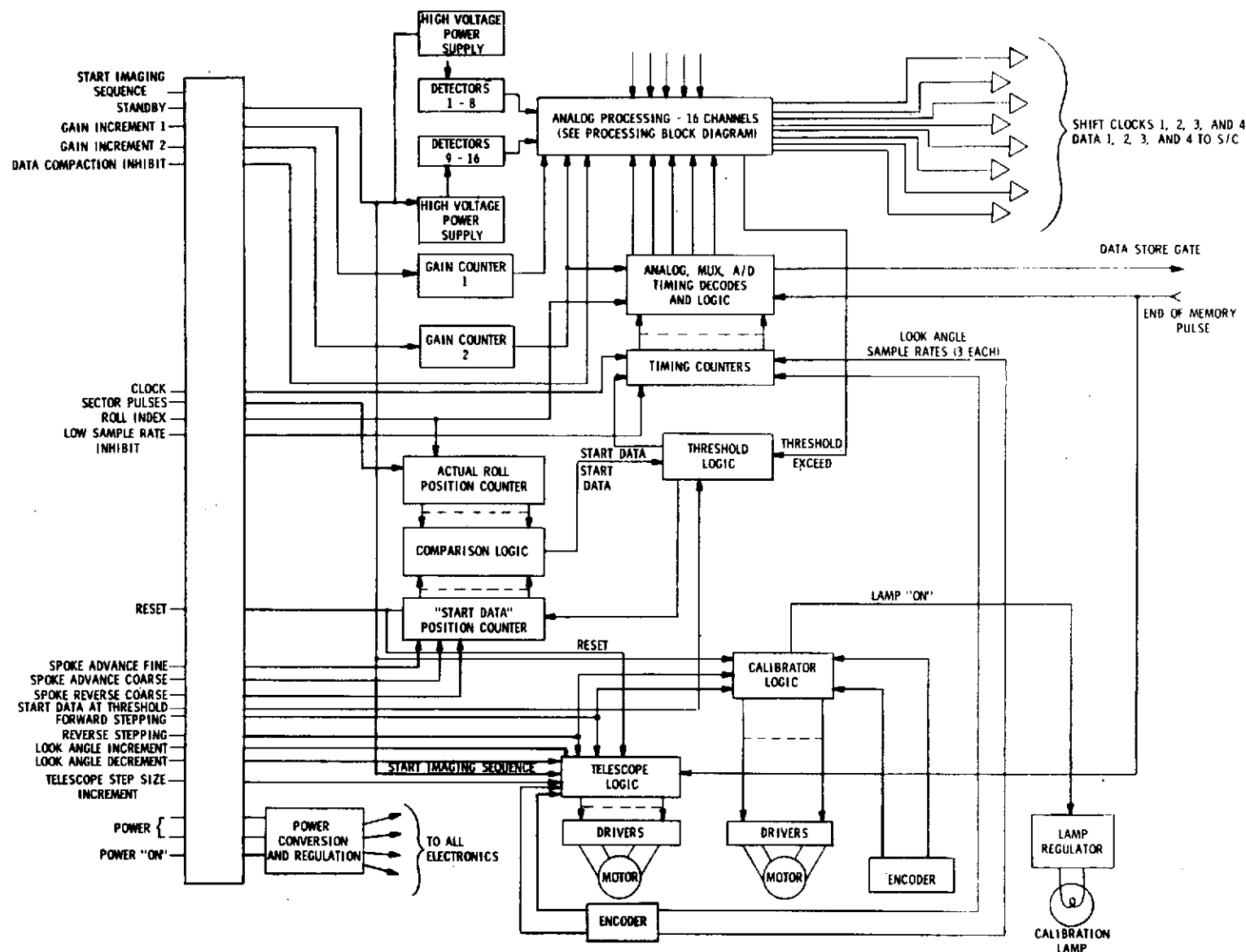


Figure 7-1. Electronic Block Diagram of OPM Imager

overload protection is required for the electronics or detectors, a command to decrement the gain counters is not necessary, i.e., incrementing through the highest gain to reach the lowest is acceptable.

Mechanization of the attenuator by use of integrated circuit switching FETs, six to a package, ensures a low component count. Counter state decoding can be performed by use of gating diodes in series with the FET control leads, thereby reducing component count for level conversion circuitry. This is an important reliability improvement because it minimizes the circuitry which is common to all channels, thereby reducing the probability of a failure of all channels of a given spectral band. Parts count for mechanization of this design is approximately 25/channel consuming no power and 12 counts/spectral channel consuming a total of 125 mw.

Signal filtering to simplify data processing should be of the linear phase type. In system with fewer than about 20 channels where component count is not prohibitive, four-pole filters could be considered. Another approach to signal filtering is signal integration with a resetting integrator. This technique would yield the lowest component count per channel (approximately seven components). The self-scanned and CCD silicon arrays are particularly suited for use in the photon integration mode. For these arrays, the need for such components would be eliminated entirely.

The use of two-pole filters as a compromise has been assumed for simplicity in assessing weight and power. With an assumed bandwidth of 10 kHz, filter mechanization with small sized capacitors is allowed which ensures high component density as well as relative ease of packaging. Mechanization of the two-pole filter would require approximately nine components and 30 mw/channel.

7.2.4 Analog Processing

The Sample and Hold, Differential Pulse Code Modulation Subtraction, and DC Restoration functions (Figure 7-2) can be performed by a single functional block circuit consisting of approximately 30 components per channel. The accuracies required for 8-bit digitization allow the use of small 0.05- μ f "hold" and "subtraction hold" capacitors. These and the other components of the analog processor are physically small and easily packaged. Radiation-hardened low-power amplifiers can be used at the proposed 10-kHz band limit, which will result in a power dissipation of 0.1 watt per channel.

The analog subtraction method of implementing the Differential Pulse Code Modulation (DPCM) method with both automatic and periodic updating incorporates an additional "hold" circuit in each data channel. This is mechanized (see Figure 7-2) to store the last data value of that channel while it is being multiplexed into the digitizer. This data value is stored and subtracted via a difference amplifier from the following data sample, at which time the "difference stored sample" is updated. Upon command from the sequencing logic, the "difference stored sample" may be set to zero, yielding an absolute sample to be digitized (and telemetered) to full 8-bit precision. Circuitry which can detect all "ones" or "zeros" in the digitized samples of the DPCM can be incorporated to trigger the "memory zero" function. These overload signals can be detected in the data stream, and can be used as a flag to indicate that a full 8-bit sample will follow.

Another mechanization of DPCM data compaction involves the use of digital logic elements to successively subtract the digitized value of a previous data sample from the present data sample. The method could result in a slight system weight savings but was rejected because severe inaccuracies could result. This may be avoided by digitizing data samples to a higher resolution than required with

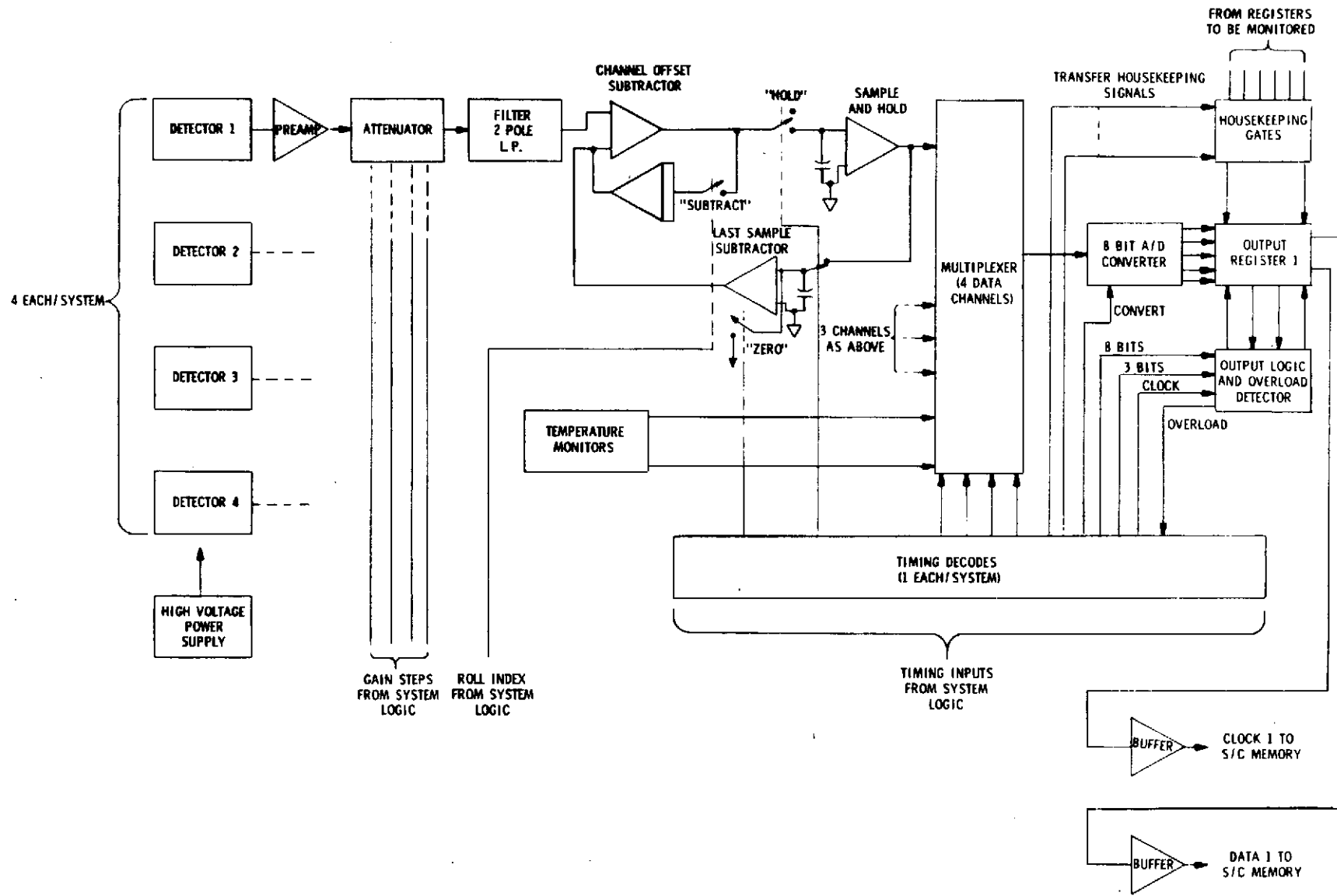


Figure 7-2. Analog Processing for OPM Imager Designs

round-off or truncation of the data samples to be telemetered. This results in very high conversion bit rates, however, with correspondingly high power consumption. This approach is not recommended.

7.2.5 Data Handling

If a spacecraft roll rate of 10 rpm and a 0.1-mr FOV are assumed, a 50- μ sec sample interval is required so that two data samples will be taken per dwell period. Using DPCM, 16 data channels (digitized to 3-bit resolution) will generate 3×16 or 48 data bits to be telemetered each 50 μ sec. Once each 64 sample intervals, all channels must be digitized to the full 8-bit resolution generating 16×8 or 128 data bits. The average number of bits per sample interval is then 49.25 bits per 50 μ sec. It is apparent then that with a single A/D converter, conversion and data shift rates to the instrument memory must be on the order of 0.25 μ sec per bit or an interface frequency of 4 Mbps. Conversion at this rate is possible but power consuming (5 to 10 watts estimated). Interfacing with the memory is an additional problem. Noise generated by conventional voltage type drivers (and interface currents due to stray capacitance) would be quite high as well as the power consumed by low-impedance cable drivers. Full differential current mode drivers and receivers would probably be required. Note that integrity of the data processing/interfacing is particularly important when DPCM is used because of the ambiguities which can result from words of non-uniform length. Data dropouts could make data reconstruction difficult.

An alternate to the high data rate mechanization mentioned above is possible by division of the instrument processor and spacecraft memory into four independent processors (four A/D converters, four output registers, four multiplexers, etc.), each accommodating four data channels (see Figure 7-2). This mechanization while increasing the system component count has the effect of lowering the interface and conversion frequency by a factor of 4, to 1 Mbps, and offers a

corresponding power savings. A factor of 10 in processor logic power can result because low-power logic can be used at 1 Mbps whereas high-power elements must be used at 4 Mbps.

The greatest advantage is the increase in reliability of the instrument and spacecraft having four independent processors. Selection of alternate colors processed by each section would be advisable to make full use of the redundant characteristics. This four-processor mechanization is assumed in the following circuit descriptions and power/weight estimates.

Multiplexing of the four groups of data channels can be performed by low capacitance switching devices (probably MOS), so that a total settling time of less than 2 μ sec is possible for both the sample and hold and multiplexer. Two clock periods of the instrument 1 MHz clock can be allocated for settling time. The A/D conversion circuitry requires approximately 60 components and 1.0 watt (four per system) and the multiplex circuitry, 20 components and 25 watts (four per system).

Data from the instrument will be transmitted to the spacecraft memory in 1-Mbps bursts, 3 bits or 8 bits per burst on 50- μ sec intervals. In the lower sample rate modes (commandable low sample rate operation), the interval between bursts of data will change, but data presentation will remain at the 1-Mbps rate. Spacecraft storage of 246 k bits will be required to store 15° of DPCM data at a spacecraft roll rate of 10 rpm (assuming no overload conditions). The resulting readout rate from the memory to the telemetry system is then 42.8 kbps to transmit all data samples. In the lower sample rate modes (1/2 and 1/4 the nominal rate), the readout rate will increase because the time required to fill the spacecraft memory will be longer. In the 1/4 sample rate mode, a maximum telemetry rate of 49.2 kbps is required.

Interfacing with the memory can be accomplished by conventional voltage type drivers of discrete or integrated circuit configuration. One method which may be considered is the use of parallel logic element drivers, driving shielded twisted pair lines (twisted pairs having a higher characteristic impedance than coax and hence a better match to the drivers). Current mode drivers could also be considered. Approximate power required (per driver) is 100 mw, and eight drivers are required.

7.2.6 Logic Design

Analog timing functions can be performed by a central timing counter, decoded into various timing signals to control "sample and hold," "multiplex," "convert," and "data transfer" signals. Using one counter for all these signals ensures that signals can be forced into synchronization with a single counter "clear" signal issued at the start of each line of data. Component count for the analog timing counter and decoder is expected to be 15 flat-pack integrated circuits dissipating a total of 100 mw.

Signals from the A/D register must be transferred into a shift-out register so that conversion of the next data sample can continue (see sample timing sequence). This output register can be mechanized with MSI components such as the 54L95 register, in conjunction with gates to multiplex housekeeping data and a shift clock counter. A total component count of 22 integrated circuits and power of 150 mw can be expected. These low-power elements can be used only because of the four-processor approach and must be replaced with higher power devices if additional speed is required.

Threshold positions can be detected by storing the value of the spacecraft roll position (spoke counter contents) at the time when the analog "threshold exceed" signal is present. This stored value can be compared to the actual roll position on the next roll, and data can proceed from the time the comparison is made. The addition of a

"decrement" function to the stored spoke value has the effect of allowing the subsequent roll of data to proceed prior to the actual threshold position by an integral number of spokes. This feature is very useful because it allows the threshold to be set at a level which is always above the peak noise, but does not exclude the imaging of faint edges of planets. It is imperative that the spacecraft roll position counter have enough resolution (512 or 1024 states) so that large amounts of data will not be wasted prior to the leading edge of the planet. A ground commanded "back-up" feature could be incorporated to control how many spokes the threshold circuitry should decrement. Component count for threshold mechanization is expected to be 18 integrated circuits, dissipating a total of 100 mw.

Circuitry for command buffers and the gain counters can be mechanized with approximately 10 digital integrated circuits and dissipating a total power of 50 mw. Commands are assumed to be of the pulse type and storage within the instrument is assumed.

7.2.7 Telescope Control Electronics

Telescope control must be performed by digital electronics (to interface with the command buffers), and analog electronics to servo the fine telescope position in the case of PMT or photodiode array mechanizations. No fine telescope positioning is required in the Digicon-type detector mechanization because beam deflection is performed in the detector by the high-voltage power supply. However, digital processing and analog control signals from the fine position encoder are identical in all mechanizations.

Telescope operation (see Figure 7-3) is via one of two modes, "Slew" mode or "Step" mode. The slew function is incorporated to send the telescope at a rapid rate to the approximate angle that the image is expected. An incrementing register accessed by the look angle Increment, Decrement, and Reset ground commands stores the binary value of the desired look angle. When the Slew mode is entered

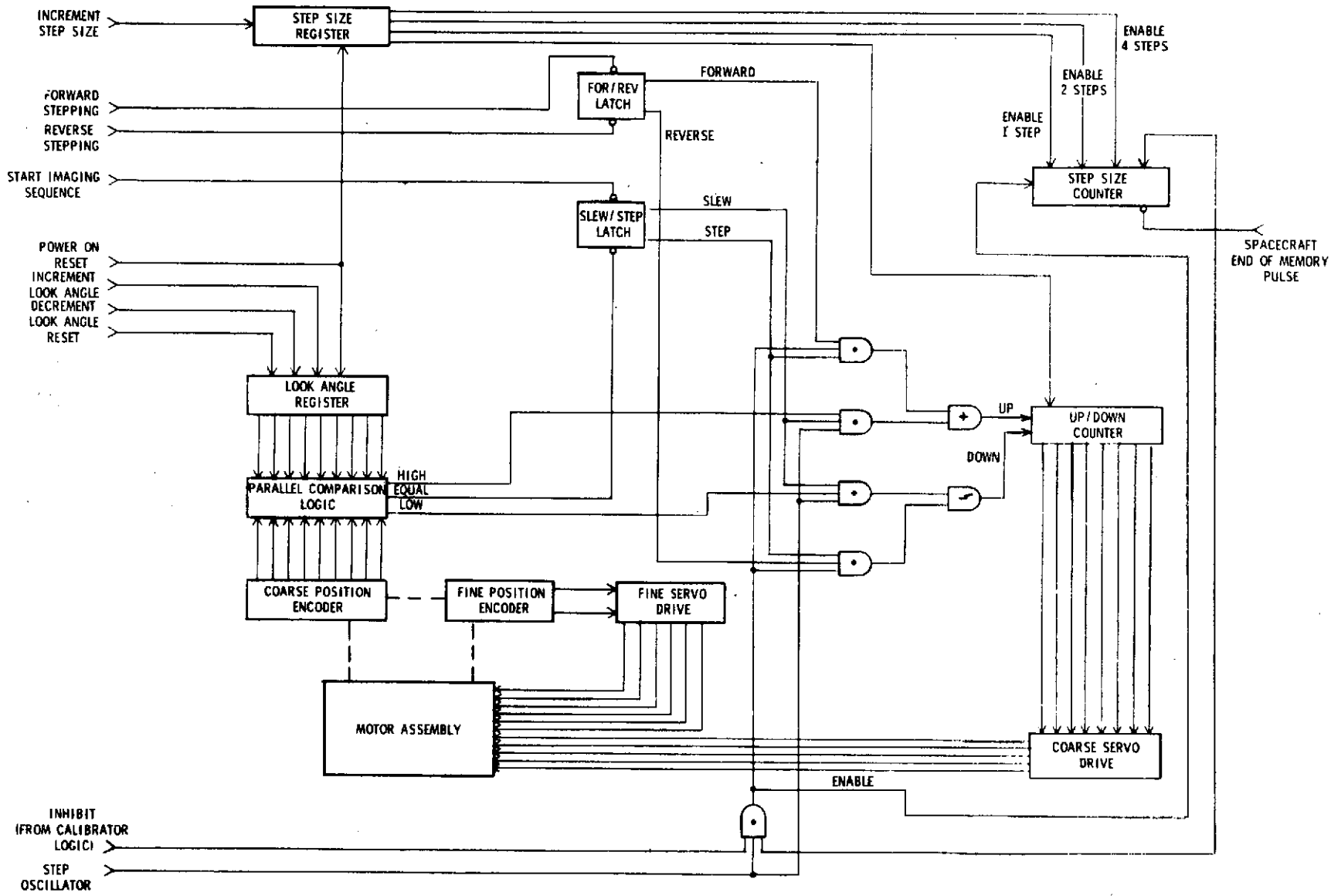


Figure 7-3. Telescope Control Logic for OPM Imager

by the "Start Imaging Sequence" command, a parallel comparison can be made between the register contents and the actual telescope position, and a direction signal can be formed to begin rapid telescope motion in the proper direction. Once a comparison of actual and desired position has been made, the Slew mode is reset (disabled) and Step mode can proceed.

In the case of a stepper motor coarse telescope drive, the "Up" and "Down" signals can be used to control a bidirectional counter which can generate motor drive signals via decoding gates and power drivers. If a servo-type motor is preferred, continuous parallel comparison of the position encoder output and desired step position will be required to control a bang-bang type servo (as well as the fine position analog signal). Fine telescope position can be detected by the encoder and represented as a voltage ramp (bi-polar) with zero crossing denoting the center of a given step. This signal can be used, then, to control fine position drivers to center each telescope step. When the desired step position is reached, servo voltage can be removed, thereby greatly reducing the power dissipation.

The telescope control logic can be mechanized with 25 integrated circuits and the coarse telescope drive with approximately 30 components. The fine telescope position detection and drive requires approximately 40 components and 0.4 watt.

7.2.8 Calibration Circuitry

The calibration circuitry (see Figure 7-4) consists of a calibration lamp and driver, stepper motor drivers, and control logic which form a means by which a six-level optical signal can be fed to the detectors. Six spacecraft roll periods are required for a complete sequence. The motor step phases can be generated by a counter which, when enabled (see Command List given in Table 7-3), is triggered by each spacecraft "end of memory" pulse, each of the first six counter

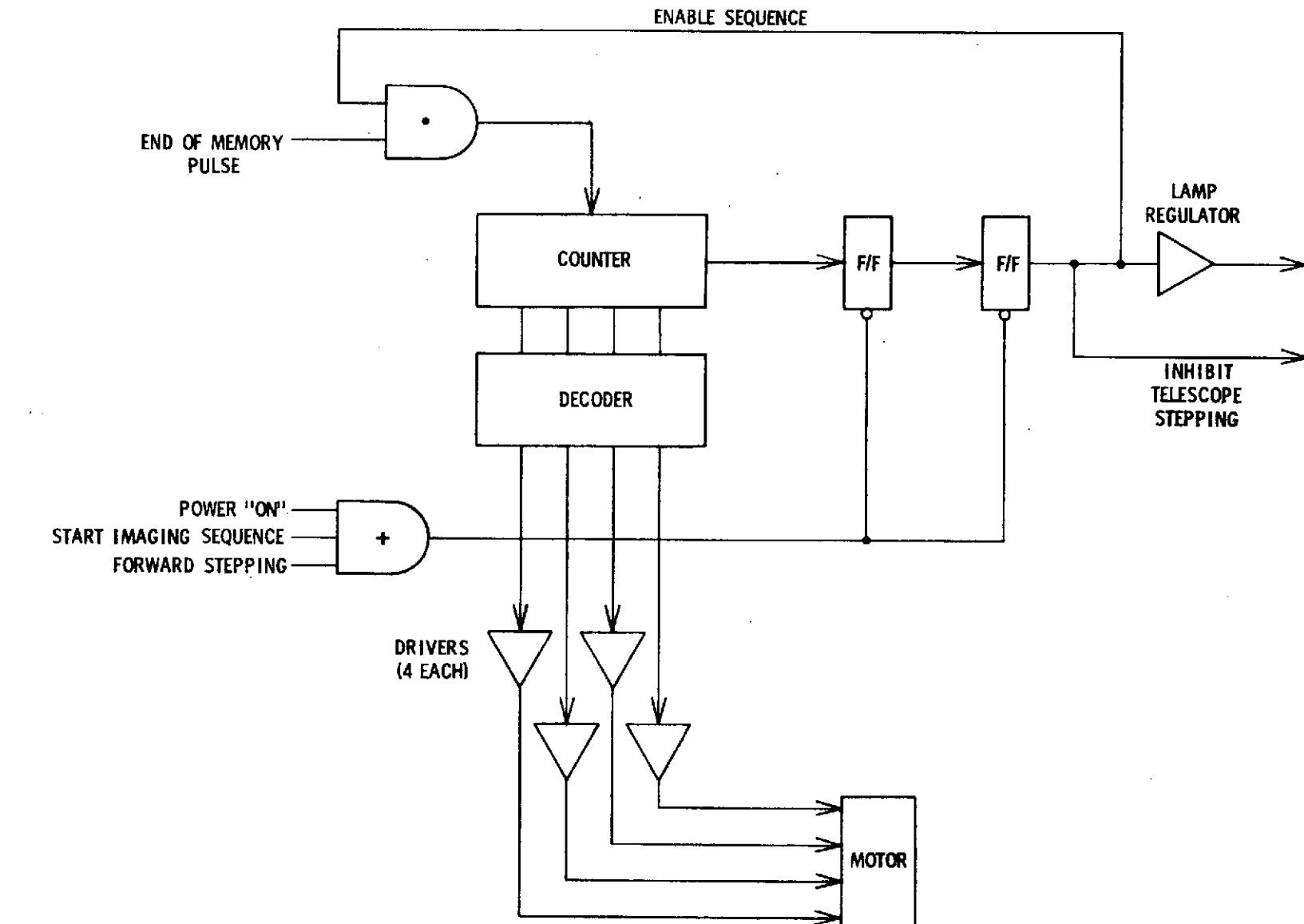


Figure 7-4. Calibrator Sequence Logic for OPM Imager

states corresponding to a calibration level. When the counter is incremented into the seventh state, the "lamp on" signal is removed, and the motor phases are de-energized, completing the calibration sequence.

Expected component count for calibration logic is five integrated circuits, dissipating a total of 50 mw. Approximately 4.5 watts of peak power are required to operate the stepper motor drivers and the stepper motor. The duration of this peak power is quite short, perhaps 25 msec, occurring once per roll or less than 0.5% duty cycle. Approximately 30 components are required to mechanize the drivers. Calibration lamp power of 0.5 watt can be expected; however, the duty cycle again can be quite low (~ 0.25 sec/roll) resulting in a low average power.

7.2.9 Electronics Weight

In Table 7-4 the weights, power consumption, and size of individual functional subassemblies of the electronics are tabulated. These quantities are tabulated for each of the four Point Designs analyzed in detail. A total of 16 detectors was assumed for each design, and this is reflected in the tabulated totals. Since each subassembly is separately listed, a change in the electronics weight resulting, for example, from a change in the number of detectors can be readily calculated.

7.3 TELESCOPE OPTICAL DESIGNS

Two Cassegrainian configurations were found which satisfy the spacecraft and optical constraints. The particular configuration to be used for actual hardware is dictated by the detector choice. In Figure 7-5 is shown the minimum weight configuration (Designs 1 and 3). The focal plane detector array, consisting of either a Digicon-type sensor or a solid-state array, is integrated with the gimballed telescope. Another configuration which makes maximum use of space qualified hardware (although with some weight penalty) uses an optical fiber

Table 7-4. OPM Imager Electronics, Power/Weight/Size Comparison

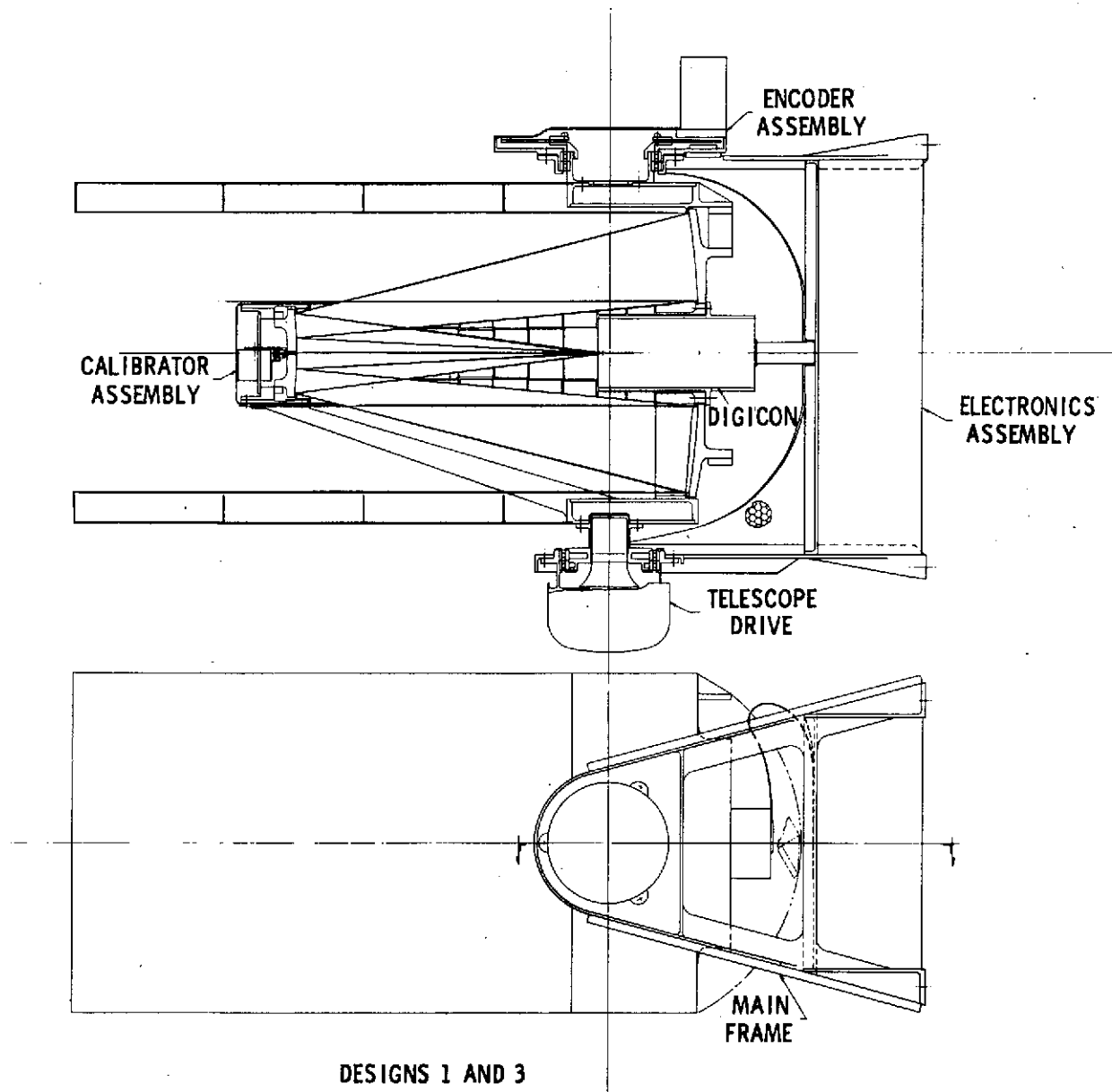


Figure 7-5. Design Layouts for OPM Imager Point Designs 1 and 3

array which terminates at a bank of multiplier phototubes. In this case, the beam from the telescope is folded and exists along the telescope scan axis through the gimbal bearing to the stationary framework. This configuration is shown in Figure 7-6 (Design 2).

7.3.1 Point Designs 1 and 3

Three telescope configurations were considered in detail. The particular variation is dictated by the number or type of detector. The first Cassegrainian telescope shown in Figure 7-5 has the characteristics shown in Table 7-5. This is the most compact system and is used for Designs 1 and 3. Bandpass filters are located on the face of the modified Digicon (Design 1) or in front of the silicon detector array (Design 3).

The geometrical image quality for this design is shown in Figure 7-7 (spot diagram). Figure 7-8 shows a ray trace in the vicinity of the nominal focus.

An error budget distributed among typical geometrical aberrations, manufacturing tolerance, diffraction, decentration, and defocus for the design is given in Table 7-6. The importance of critical focus is evident. For a system constructed entirely of beryllium having the same linear thermal coefficient (no anisotropy) under isothermal conditions, the defocusing due to temperature changes will be zero. In practice, thermal gradients will exist and the beryllium parts will differ in their thermal coefficient along the optic axis direction. Thus, some thermal defocusing will occur. To complicate matters even further, beryllium would not be suitable for the secondary supports because of inadequate precision elastic limit. Instead a support composed of titanium and aluminum was devised to reproduce the change in length of beryllium to give zero focal shift with temperature change. This is discussed in subsection 7.4.

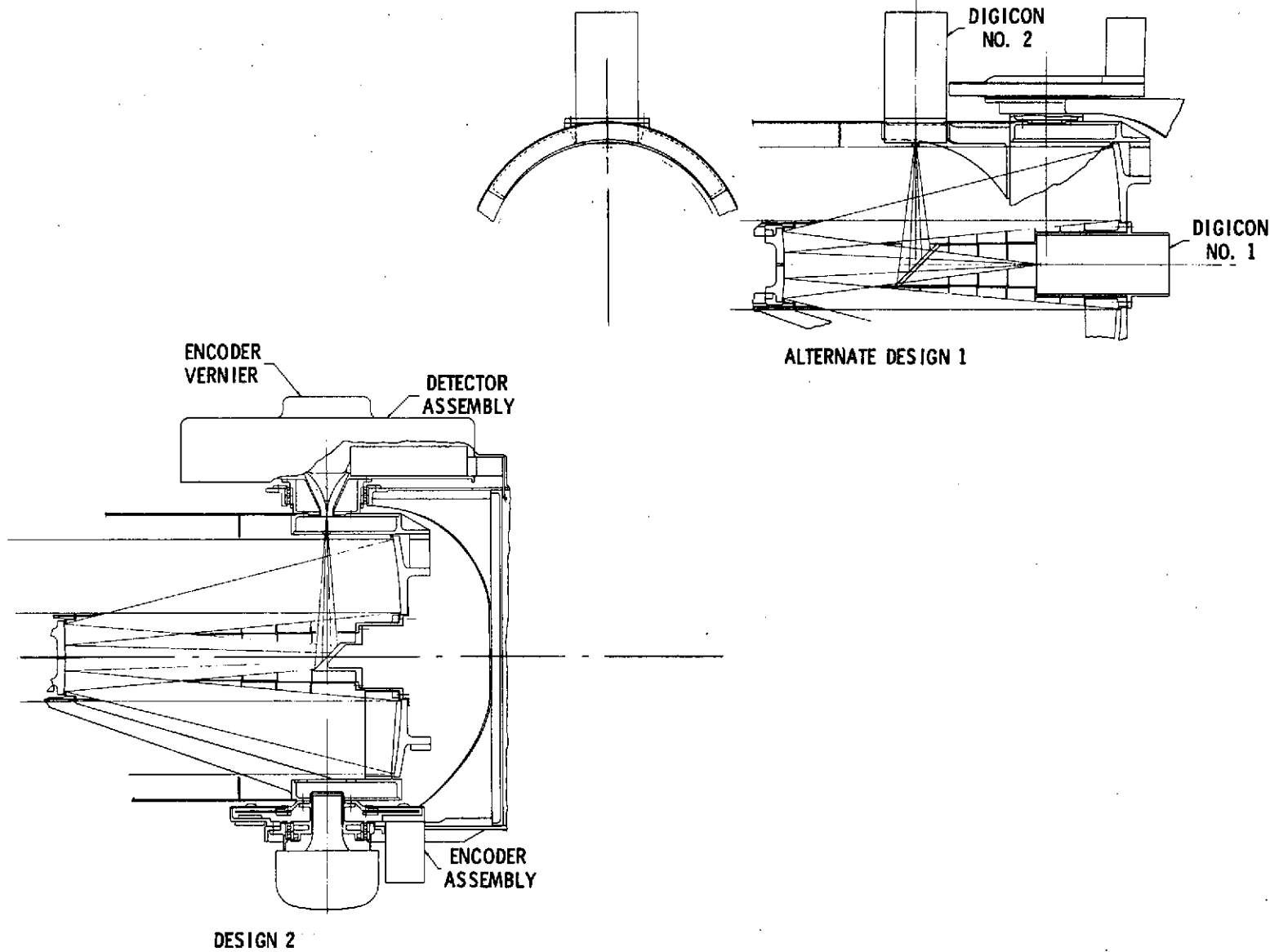
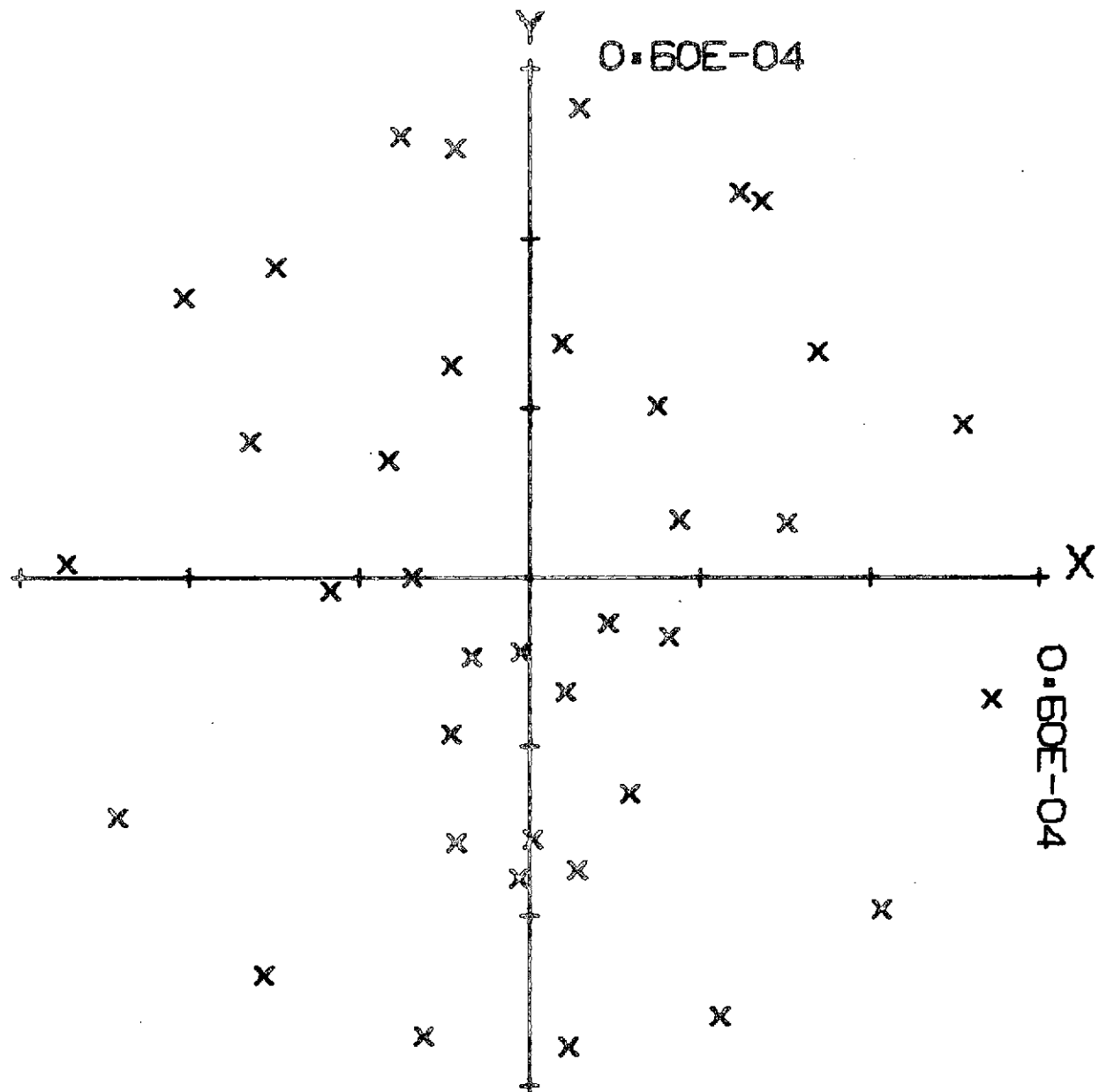


Figure 7-6. Design Layouts for OPM Imager Point Design 2 and Alternate Design 1



X, Y OF CENTER -0.44913E-06, 0.12030E-01

Figure 7-7. Spot Diagram of Telescope Design for OPM Imager Designs 1 and 3

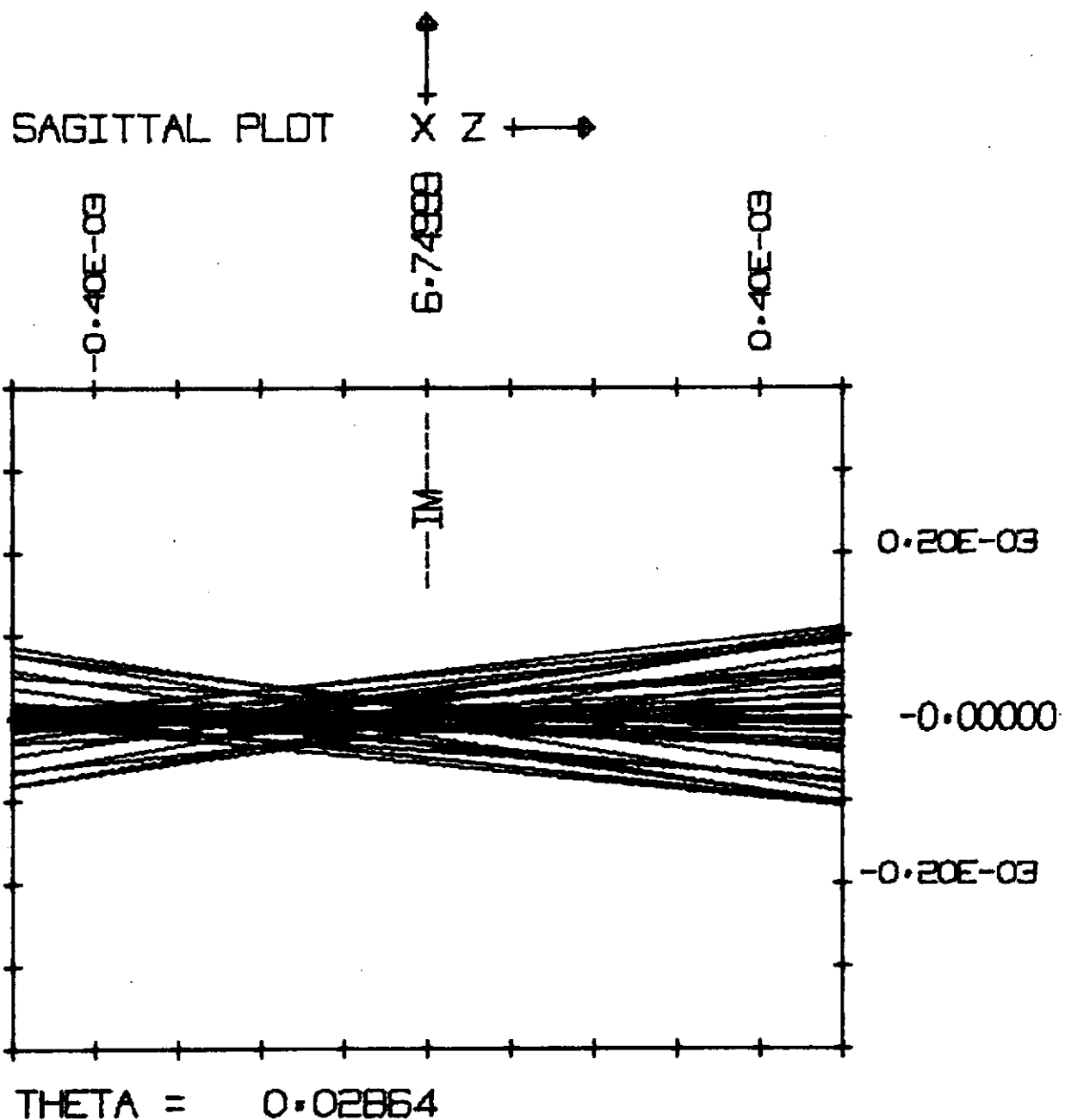


Figure 7-8. Ray Trace of Telescope Design for OPM Imager
Designs 1 and 3

Table 7-5. Telescope Design for OPM Imager Designs 1 and 3

ELEMENT	RADIUS (INCHES)	SPACING (INCHES)	CONIC CONSTANT
PRIMARY	-32.00	11.500	-1.259
SECONDARY	-27.00	-6.750	-50.50
APERTURE DIAMETER:			8.000 INCHES
BACK FOCAL LENGTH:			6.750 INCHES
EFFECTIVE FOCAL LENGTH:			24.000 INCHES
BALANCED ABERRATION			
BLUR CIRCLE RADIUS:			2.5 μ RAD
PETZVAL SURFACE RADIUS:			-86 INCHES

Table 7-6. Optical System Error Budget for 90% Energy Containment

	<u>DIAMETER (μRAD)</u>
GEOMETRICAL ABERRATIONS (POINT SOURCE)	5
DECENTERED SECONDARY (0.002 INCH)	9
DIFFRACTION ($\epsilon = 0.4$)	5
MANUFACTURING ERROR (0.25 λ rms)	~6
DEFOCUS (0.001 INCH)	<u>20</u>
ROOT-SUM-SQUARE	~24

7.3.2 Alternate Point Design 1

Alternate Design 1 (see Figure 7-6) uses two Digicon-type devices, each optimized by choice of photocathode spectral responsivity. For example, the folded beam might contain wavelengths $< 0.6 \mu\text{m}$, the transmitted beam $\lambda > 0.6 \mu\text{m}$. This scheme alleviates the demands on the spectral purity of the bandpass filters, and provides a measure of backup should either Digicon fail. The Pioneer 10 and 11 Imaging Photopolarimeter (IPP)³⁹ followed this design principle. For Alternate Design 1 where a folding dichromatic beamsplitter is introduced, the back focal distance is increased from that for Designs 1 and 3 to 8.75 inches. The secondary mirror radius would be decreased to compensate for this change. A boresighting requirement arises with this design for ensuring simultaneous spatial coverage. This, however, should be a relatively straightforward alignment task.

7.3.3 Point Design 2

The third basic arrangement (used for Design 2) folds the telescope beam so that the image plane occurs outside the telescope barrel co-axial with the telescope scan axis. At the image plane is an array of optical fibers; each fiber end defines the IFOV. The energy in each fiber is conducted to a photomultiplier tube (PMT). Based on the wide spectral coverage and high photocathode responsivity afforded by the opaque GaAs photocathode, such PMTs seem particularly suitable for the OPM Imager (see subsection 5.1). It has been assumed that such detectors would be used for Design 2.

Another approach would be to borrow from technology established on the Earth Resources Technology Satellite Multispectral Scanner (ERTS MSS) and the Synchronous Meteorological Spacecraft Visible Infrared Spin-Scan Radiometer (SMS VISSR). In these instruments, each fiber is terminated in an enhancing prism bonded to the window of an extended-red PMT. The prism couples the light into the window at such an angle that multiple bounces occur, thus ensuring more complete

absorption by the photocathode coating. For the extended-red type cathodes, average quantum efficiency gains due to enhancement for the PMTs used on the ERTS MSS were 1.33, 1.85 and 1.90 for the 0.5- to 0.6-, 0.6- to 0.7-, and 0.7- to 0.8- μm spectral bands, respectively.

The bandpass filters can be coupled to the enhancing prisms, should they be used, or to the end of the optical fibers. The telescope f/# for Design 2 is approximately f/3.6.

A major problem is obtaining optical fibers that have high transmission to at least 0.40 μm and that will not lose transmission in a hard radiation environment. The only choice available is a fiber of fused silica. While fused silica fibers are commercially available (Schott Optical Glass Company), the organic cladding material was found (on the IPP materials study) to be susceptible to radiation darkening. Few other choices of cladding material exist because the refractive index of silica is lower ($n = 1.46$) than nearly all other materials.

Experimental cladding using KEL-F and vacuum-deposited magnesium fluoride was accomplished by Illinois Institute of Technology Research Institute. SBRC has obtained samples of each type for evaluation. The KEL-F cladded fibers were found to require a large (>3-inch) minimum bend radius to prevent breakage. The MgF_2 cladded fibers are more flexible and offer promise for space flight.

Another approach is to use uncladded silica fibers. It is necessary for these to eliminate contact points with foreign objects such as dust or housing parts to prevent light leakage due to frustrated internal reflection at these contact points. A possible method for supporting a naked fiber at a minimum number of low-loss points is to make the supports from MgF_2 ($n = 1.38$) and contact the fiber to the support with a silicon resin ($n = 1.43$). The minimum number of supports required to safely suspend a fiber of a given length in a vibration environment of variable frequency will require analysis to determine the vibrational modes and amplitudes.

7.4 MECHANICAL DESIGN

In this subsection, the structural configurations for the specific OPM Imager Point Designs are described. Thermal effects and the cross-scan drive are discussed in detail because of their importance. Finally, the results of a detailed weight analysis of the Point Designs are included which form the basis for the Point Design optimization given in subsection 7.6.

7.4.1 Structural Configuration

The proposed structural configurations were shown in Figures 7-5 and 7-6. Each configuration serves to optimize the design for a specific candidate detector.

The basic structural configuration is the same for all three designs. A beryllium ring forms the primary structure for the telescope from which all telescope components are supported. The telescope assembly is then mounted through bearings on the ring to the main frame.

The primary mirror is mounted to the ring by tangent bars. This design (coupled with specially developed fabrication techniques) was used on SMS VISSR and ERTS MSS to produce a stress free mirror mounting unaffected by thermal changes and main frame stresses.

The secondary mirror and the calibration lamp assembly is supported in front of the primary mirror by titanium struts which mount to the structural ring. Titanium is used in lieu of beryllium because of its higher PEL. The struts are sized so that under 1 g conditions, the secondary mirror will not sag more than 0.005 cm relative to the primary and so that the PEL of the material will not be exceeded when exposed to a vibrational environment of 10 g from 5 to 2000 Hz. If the PEL were exceeded during test or launch, a permanent shift in the position of the secondary could result.

In Design 1 and Alternate Design 1, the detector assembly is supported not by the primary mirror or primary mirror structure but by struts located in front of the primary mirror and mounted to the structural ring. These struts are aligned to the struts supporting the secondary mirror so that no additional optical obscuration results. This technique minimizes the loads induced into the primary mirror structure by separating the load producing structures and stiffening the structural ring.

Alternate Design 1 has a second modified Digicon detector mounted at right angles to the first. The long-wavelength flux is transmitted through the dichromatic mirror to one detector and the short-wavelength radiation is reflected to the other detector. The second detector is mounted to the structural ring by its own support and moves with the telescope when scanning.

Design 2 is structurally the same as Design 1 and Alternate Design 1 except that the encoder assembly is packaged around the telescope drive, and the Digicon-type detectors are replaced by a mirror that folds the optical rays onto the telescope axis of rotation. The optical image is then transferred by minimum length optical fibers to a group of PMTs. The entire detector assembly is fixed to the telescope and rotates with the telescope assembly. This allows the optical axis to be noncoincident with the rotational axis without the orientation of the cross-scan track as projected onto the planet during rotation.

The main frame structure consists of an upper and lower beryllium A-frame spaced apart by a beryllium panel that also serves as the electronics assembly base. Readily available titanium honeycomb fitted with structural end caps is used for side panels to give the structure the required rigidity and strength while minimizing the weight.

The telescope gimbal bearings are internal to the telescope drive on one side and internal to the encoder on the other. This allows for independent development and test of the individual components prior to integration with the telescope. The bearings would be specially fabricated of nonmagnetic materials and then cleaned, assembled, and dry lubed with moly-disulfide. This technique was used successfully on the Pioneer IPP in an almost identical application.

Maintaining the cleanliness of the optics is of primary concern prior to, during, and after launch. Various methods of protecting the optics are possible. The Pioneer IPP instrument uses a "mousetrap" design which is mounted to the side of the spacecraft adjacent to the instrument. The telescope is covered during and after launch by the mousetrap. At the desired time, the telescope is stepped away from the mousetrap cover. When the telescope is clear, the mousetrap snaps away leaving the instrument ready for operation.

The exact concept to be used is dependent on the spacecraft configuration. A self-contained design could be developed for a particular instrument, although the resultant weight might be considerably greater than if mounted onto the spacecraft. The final decision on the type and method should be reserved until the spacecraft configuration is known.

7.4.2 Thermal Effects

As discussed earlier, the use of titanium to support the secondary mirror, even though its expansion coefficient is close to that of beryllium, will cause a defocusing as a result of temperature change unless compensated for. An active focus drive to refocus would solve the problem but results in a significant weight increase and decrease in system reliability. The approach proposed and shown in Figures 7-5 and 7-6 does not require an active focus but rather adds another material in series with the titanium to produce an overall expansion equivalent to that of beryllium.

If aluminum is the intermediate material, then

$$\left. \begin{aligned} L_B \alpha_B &= L_T \alpha_T + L_A \alpha_A \text{ and} \\ L_B &= L_T + L_A \end{aligned} \right\} \quad (7-1)$$

where

L_B = length of equivalent beryllium

L_T = length of titanium

L_A = length of aluminum

α_B = thermal expansion of beryllium

α_A = thermal expansion of aluminum

α_T = thermal expansion of titanium

It follows then that

$$L_A = L_B \frac{(\alpha_B - \alpha_T)}{(\alpha_A - \alpha_T)} \quad (7-2)$$

with $L_B = 23$ cm, $\alpha_B = 11.3 \times 10^{-6}$ per $^{\circ}\text{C}$, $\alpha_T = 8.8 \times 10^{-6}$ per $^{\circ}\text{C}$, and $\alpha_A = 23.1 \times 10^{-6}$ per $^{\circ}\text{C}$, then $L_A = 4.0$ cm and $L_T = 19$ cm. Therefore, 19 cm of titanium in series with 4 cm of aluminum will produce the same thermal expansion as 23 cm of beryllium over a specific temperature range.

A related question is how to join the aluminum to the beryllium and titanium without having excessive stresses or sloppy fits as a result of the large differences in thermal expansion. This would be accomplished by sandwiching a split ring of aluminum between a ring of titanium which is part of the strut structure and a ring of beryllium which is part of the secondary mirror assembly. The aluminum would then follow the beryllium and titanium as the parts expanded. The expansion mismatch between the beryllium and titanium for a ΔT of 90°F would only amount to a change in fit of 0.0008 cm and would have a negligible effect.

Titanium as a material has a very low thermal conductivity, and depending on the design configuration, may present a problem with regard to a thermal gradient between the secondary and primary mirrors. A detailed thermal analysis is necessary to determine the magnitude of any gradients. This analysis was not performed as part of this study but would form an important part of the detailed engineering prior to construction of an actual imager. Should titanium prove to be too much of an insulator as a result of such an analysis, strips of copper could be plated or bonded to the sides of the titanium struts to increase the thermal conductivity.

The symmetrical design of the main frame and the central location of the electronics assembly ensure a balanced heat distribution and minimum thermal gradients. Heat sources can be distributed in the electronics assembly to balance the heat input to both sides of the telescope.

7.4.3 Telescope Cross-Scan Drive Systems

Method C as depicted in Figure 5-7 is recommended as the basic scan approach for the OPM Imager. Point Design 1 and Alternate Design 1, which use the modified Digicon detectors, also use electrostatic deflection to achieve the "pointing" accuracy required for the imager. Point Designs 2 and 3 do not possess this built-in capability and require the use of a servo-type telescope drive to achieve the required pointing accuracy.

The cross-scan drive system for the OPM Imager was assumed to require a scan range of $\sim 120^\circ$ in steps as small as 0.4 mr (0.8 mr nominal) and with an accuracy of ± 0.02 mr. Various drive systems were considered to meet these requirements. In this subsection, two promising systems are described, each having its own implications on overall system design and weight. In addition, drive systems which were rejected are also discussed.

The drive system proposed for Design 1 and Alternate Design 1, as shown in Figures 7-5 and 7-6, consists of a coarse telescope drive, a high-resolution drive, and a position indicator. The coarse telescope drive takes advantage of the experience and technology developed on the Pioneer IPP Program by utilization of the same basic drive but modified to increase the load carrying capacity and torque. This drive contains a stepper motor specially designed to minimize the stray magnetic field and magnetic susceptibility. These magnetic effects will increase somewhat as a result of the increased torque.

Gear reduction is obtained through a conventional gear pass and harmonic drive. The final motion is transmitted through the harmonic drive; the motor, gears, and bearings are all hermetically sealed with all lubrication completely contained. This drive provides coarse telescope positioning in steps of 0.4 ± 0.1 mr.

Position indication is provided by an optical encoder attached to the telescope shaft (similar to the encoder used on SMS VISSR for scan mirror positioning). This encoder provides a natural binary word denoting the angular position of the telescope within 0.1 mr, and an analog output providing a zero voltage crossover at the center of each binary word within 0.02 mr.

The high-resolution drive utilizes deflection plates in the modified Digicon-type detector to electrostatically translate the optical image on the photocathode. This is equivalent to scanning the array across the telescope field. A deflection voltage proportional to the analog output of the encoder thus provides the "trim" capability for the imager.

When the three units are used together, the coarse telescope drive steps the telescope in 0.4-mr steps within 0.1 mr. The position indicator senses the actual error and the appropriate signal is fed to the high-resolution drive which shifts the image on the photocathode

and reduces the telescope position error to within ± 0.02 mr. The amount of the high-resolution motion is not sensed by the optical encoder since the high-resolution drive moves the image and not the telescope. To verify that the proper amount of image motion does occur, a light emitting diode is installed at a fixed physical offset on the face of the detector. A known change in the deflection voltage will periodically be applied to verify the required image offset. When proper image translation occurs, one channel will sense diode output and verify proper stepping.

Designs 2 and 3 do not use the Digicon-type detectors. Therefore, a different drive concept is required to obtain the necessary high resolution. The proposed design uses the same proven hermetically sealed design discussed for coarse stepping of Design 1 and Alternate Design 1, except that the stepper motor is replaced by a servo motor.

Precise angular position information is provided by a coarse optical encoder used in conjunction with a finite vernier encoder. The system function is identical to a typical servo system in that when the motor is commanded to move to a particular position, the motor will drive until that position is indicated by the position indicating system. The accuracy of each step should again be within ± 0.02 mr. This system is not suggested for Design 1 and Alternate Design 1 since increased power and electronics are required for the servo system.

In addition to the two drive systems previously described, other drive systems were considered and rejected. These included piezoelectric and direct-drive systems and will be described here for completeness.

A piezoelectric device was considered as an alternative to the electrostatic deflection method described above. This would be used in conjunction with the coarse telescope drive and position indicator to improve the step accuracy from ± 0.1 mr to ± 0.02 mr. The piezoelectric device would be installed between the moving telescope and the

fixed support and would require an amount of travel equal to the step size of 0.4 mr. At a radius of 2.5 cm (1 inch), this amounts to approximately 0.001-cm travel. With the present state-of-the-art techniques, this would require an active length on the order of 5 cm. While this approach is feasible, the selected method using electrostatic deflection is simpler and thus preferred.

A direct-drive, brushless, dc motor in conjunction with a servo system and optical encoder was considered and rejected because of the large weight, power, and size. Lead screw type drives (such as were used on the ATS 1 and 3 Cloud Cameras) also were considered and rejected for similar reasons.

The drive system used for Design 1 and Alternate Design 1 is well understood and minimal future developmental effort would be required. The drive system for Designs 2 and 3 seems quite feasible; however, it should be empirically verified. It is conceivable that stiction could prove to be a significant problem, and for this reason experimental tests on an actual device are strongly recommended. Refinement of the vernier encoder to reduce weight and electronic complexity is feasible and also should be pursued to optimize the OPM Imager system.

7.4.4 Weight

Weight estimates were generated for the four Point Designs. In Table 7-7, the weights are given for each design along with those for the individual component assemblies. The telescope assembly was based on comparison to the ERTS MSS telescope which was of similar configuration although made from different materials. All other weights were based on actual weights of similar components from past programs when applicable.

Table 7-7. Weight Summary for Preliminary OPM Imager Point Designs
 (20-cm Diameter Telescopes; 16 Detectors)

	OPM IMAGER DESIGN 1 (DIGICON-TYPE DETECTOR) (KG)	OPM IMAGER ALTERNATE DESIGN 1 (TWO DIGICON-TYPE DETECTORS) (KG)	OPM IMAGER DESIGN 2 (GaAs PMT DETECTORS) (KG)	OPM IMAGER DESIGN 3 (SILICON ARRAY DETECTORS) (KG)
TELESCOPE ASSEMBLY	2.91	2.91	2.91	2.91
DETECTOR ASSEMBLY	0.32	0.73	2.59	0.14
ENCODER ASSEMBLY	0.95	0.95	1.18	1.41
CALIBRATOR ASSEMBLY	0.09	0.09	0.09	0.09
SUN SHADE	0.27	0.27	0.27	0.27
MAIN FRAME/TELESCOPE DRIVE	2.45	2.45	2.55	2.45
ELECTRONICS ASSEMBLY	1.82	2.05	2.64	1.64
SOLAR DIFFUSER	0.05	0.05	0.05	0.05
TOTAL SYSTEM	8.9	9.5	12.3	9.0

Figures 7-9 through 7-12 shows weight versus aperture diameter for the four Point Designs. The curves were calculated using the weights for 20-cm (8-inch) aperture systems as references and adjusting for larger and smaller diameters. The total system weight and system weight excluding the electronics assembly are given in each figure. The accuracy of the weight estimates for the proposed designs is felt to be within 10% over the range shown.

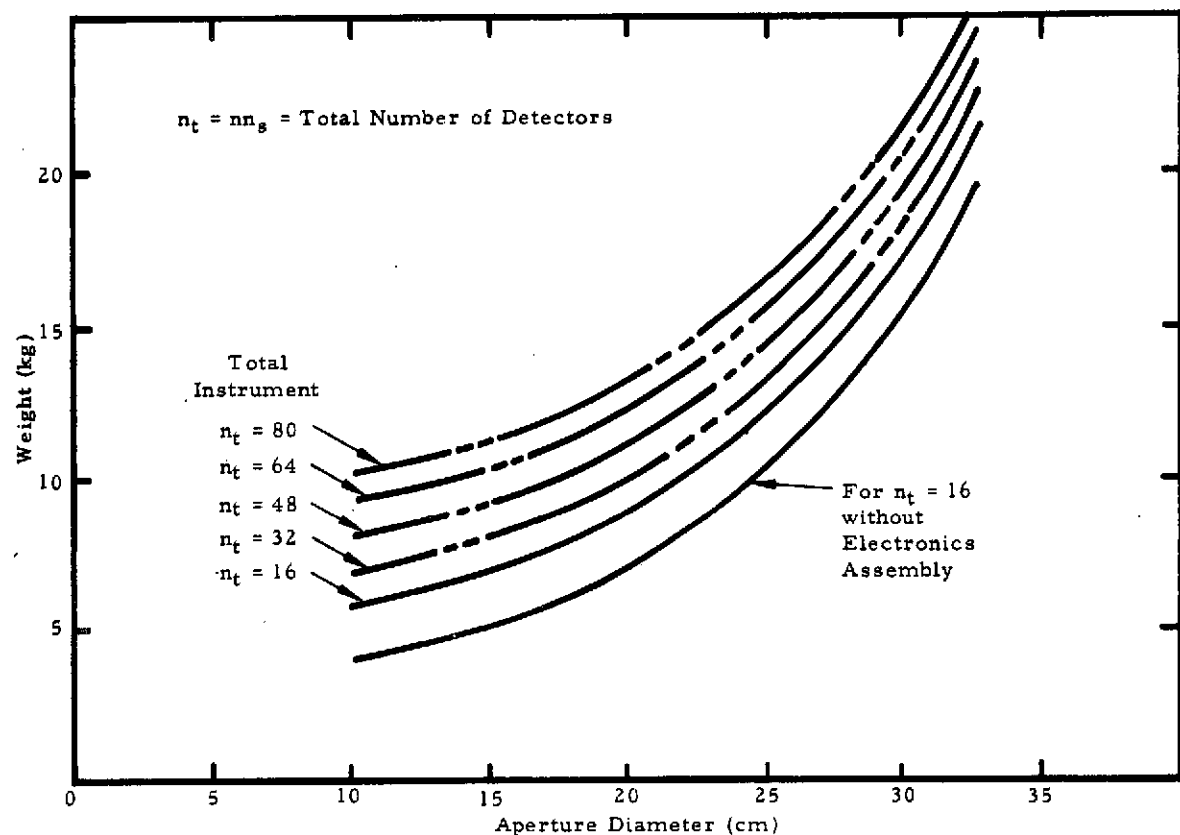


Figure 7-9. Weight Versus Aperture Diameter for OPM Imager Design 1

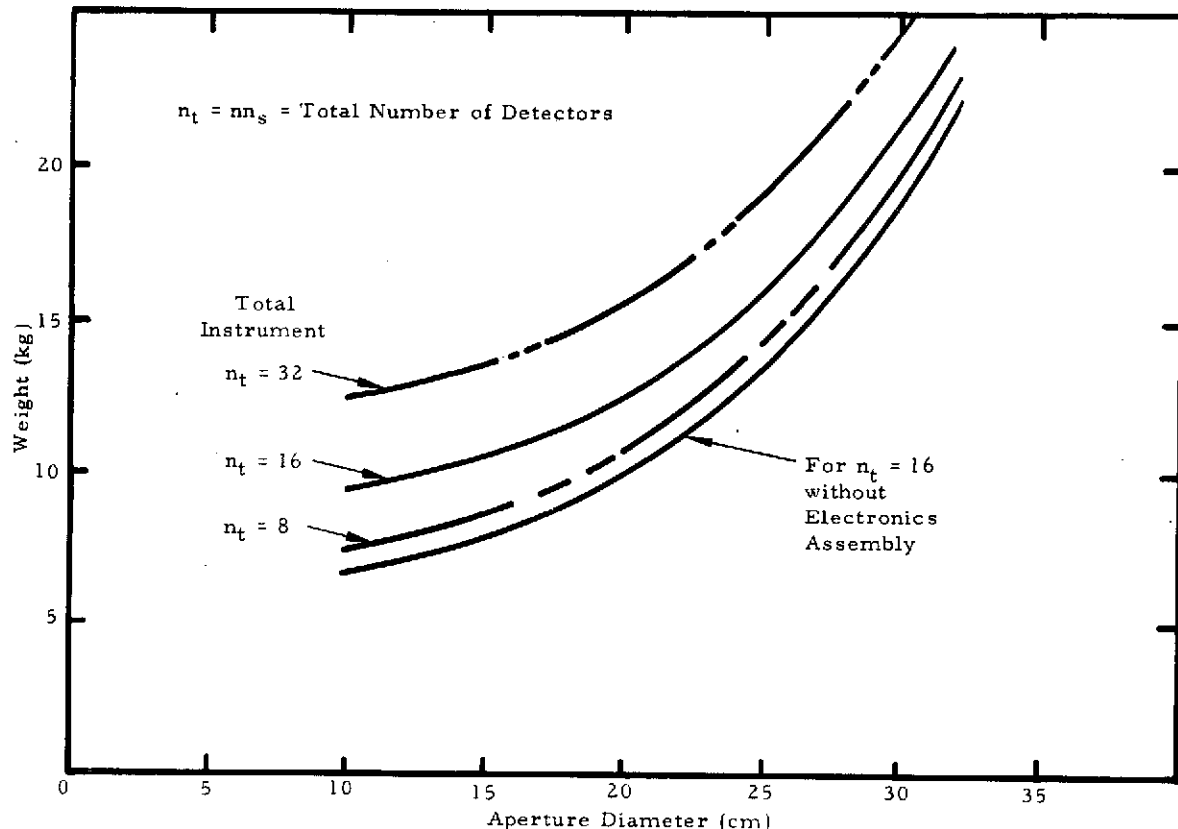


Figure 7-10. Weight Versus Aperture Diameter for OPM Imager Design 2

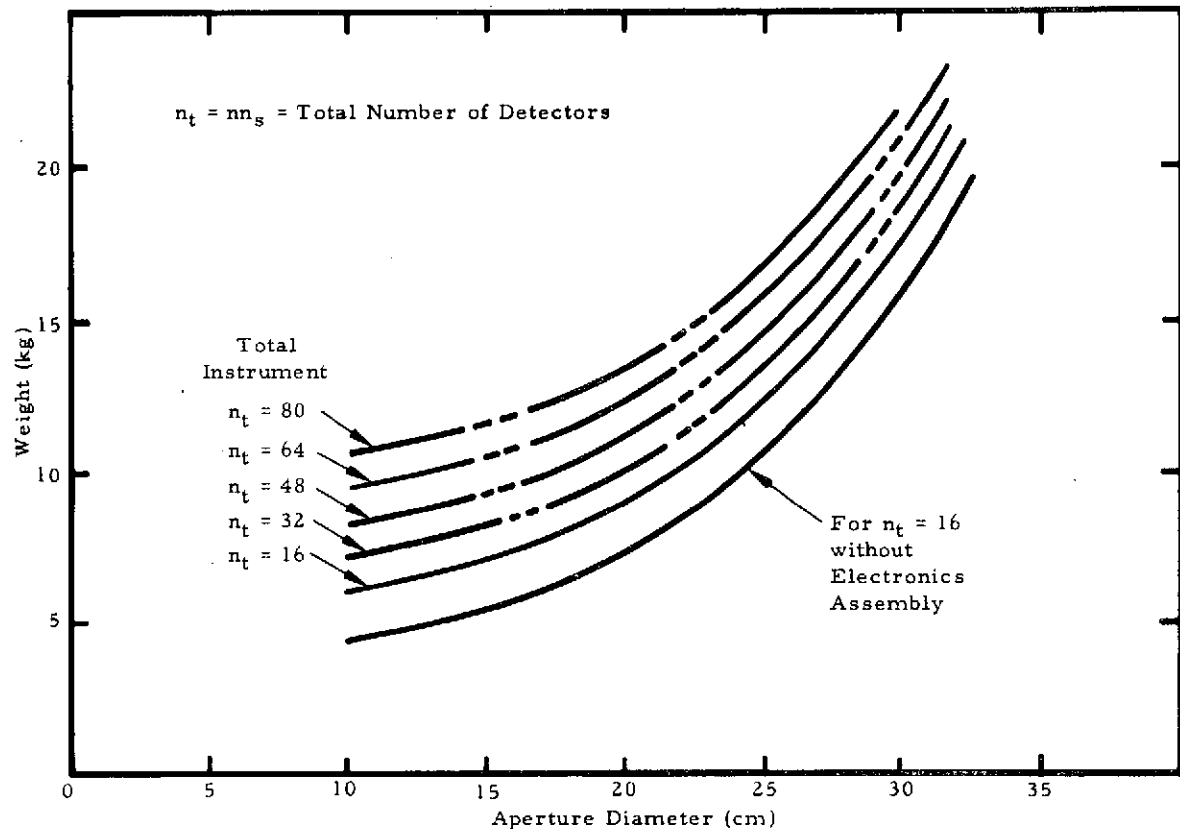


Figure 7-11. Weight Versus Aperture Diameter for OPM Imager Design 3

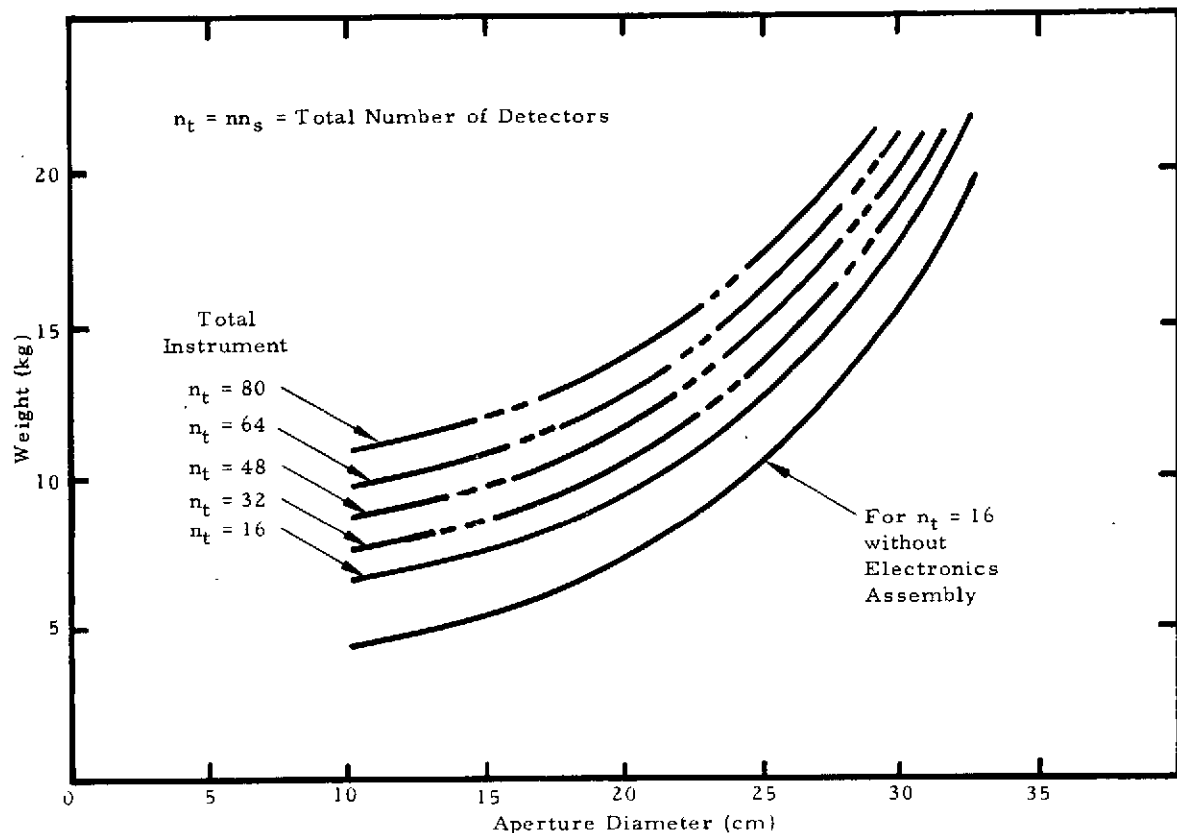


Figure 7-12. Weight Versus Aperture Diameter for OPM Imager Alternate Design 1

7.5 CALIBRATION

During the flight, it will be necessary to monitor any changes that may occur in the system radiometric responsivity of the imager channels. Such changes may occur in individual components as a result of thermal influence, aging, accumulation of condensed volatiles, photon or particulate radiation, etc. Knowledge of the radiometric responsivity on an absolute basis is essential for the determination of planetary albedos and energy budgets.

Before launch, it will be necessary to determine accurately the system spatial and spectral as well as radiometric characteristics. These are measured by specialized laboratory equipment and are monitored by the ground support test equipment under simulated space environmental conditions.

7.5.1 Inflight Radiometric Calibration

The prime radiometric calibration will be an absolute one, based on knowledge of the solar irradiance attenuated a precisely known amount by a solar diffuser attenuator. The diffuser probably would be located in the high-gain antenna dish. This calibration scheme is successfully used for the Pioneer Imaging Photopolarimeter (IPP) experiment. For the IPP, it was necessary that the diffuser be larger than the telescope aperture since the telescope entrance aperture was imaged on the detectors. For the OPM Imager under discussion, illumination of the FOV (detector) matrix is sufficient, and the diffuser can be smaller than the telescope entrance aperture since field imaging is used.

The IPP diffuser attenuator was constructed of a spaced stack of fused silica disks whose surfaces are roughened. Attenuation to a radiance level comparable to that expected from a planet ($\sim 10^{-7}$ times the solar radiance for Jupiter) is produced by scattering and by a neutral metal film coating. The materials and component preparations

were chosen to provide long term invariant properties in the presence of uv and charged particle irradiation and micrometeorites. For the OPM Imager, the attenuation factor can be less by the ratio of the diffuser area to the clear aperture area. This should allow improved absolute radiometric accuracy to be achieved. Note that since the solar irradiance of the diffuser decreases as the square of the heliocentric distance, apart from albedo differences, the desired inverse-square variation relative to the objects of interest is maintained.

For purposes of short-term relative responsivity and linearity monitoring during preflight testing and inflight operation, an internal tungsten lamp source can be used to illuminate the detectors. The lamp would be color corrected to the solar spectral distribution over the wavelength bands of interest, and a set of discrete radiance levels would be provided by means of a small stepper motor with attached neutral density filters. These levels are used to simulate the expected brightness levels over a range of anticipated objects of interest and lighting conditions (solar phase and sun-zenith angles) and to provide a linearity monitor. The IPP uses a single radiance level from its lamp. The six-position aperture actuator of the IPP could be used directly in this imager because of its small size and mass. Position encoding is not necessary, nor is detent accuracy or perfect cyclic operation.

This actuator and the lamp and filters would be located in the secondary mirror mounting, and the radiant output would be through a central 2-mm hole in the secondary mirror. This arrangement does not affect the optical performance of the telescope, and any failures do not reduce the imaging capabilities of the system. The lamp would be energized only as often as required (perhaps once per complete image) to monitor the system responsivity. Again, the IPP experience has provided a knowledge of materials which exhibit the greatest stability to hard-radiation (see subsection 5.4.5). The lamp and filters would

be the same or similar to that used in IPP for spectral range 0.40 to 0.75 μm . Extension of the calibration limit to longer wavelengths as may be required for the OPM Imager can also be accomplished within the range of the selected radiation-resistant materials available.

While the solar diffuser/attenuator calibrates and monitors the entire optical system, the internal source excludes the telescope. Since mirror coatings of the type used here have been shown not to change in a hard-radiation environment (in the visible), this is not a significant disadvantage.

Contamination of the telescope mirrors following launch could pose a problem with respect to the absolute radiometric calibration of the OPM Imager. Actual measurements of the effects of contamination of optical surfaces from Surveyor 3 indicate the importance of this consideration.⁴⁰ Obviously, a "clean" spacecraft, both as regards to outgassing materials and propellents, will reduce this problem. However, it is still highly desirable, if not essential, that a deployable cover be incorporated in the design to protect the telescope during the critical post launch phase of the mission. The design of such a cover is discussed in subsection 7.4.1.

7.5.2 Preflight Calibration

Three basic descriptors must be known for each discrete, image-space FOV of the OPM Imager. These, along with their associated characteristics, are listed below, viz:

Spectral responsivity

In-band relative spectral responsivity

Out-of-band relative spectral responsivity

FOV dimensions

Line spread function

Adjacent IFOV crosstalk

Modulation transfer function (MTF)

Radiometric response

- Dynamic range
- Linearity
- IFOV-to-IFOV uniformity
- Absolute radiometric responsivity

Alternate Design 1, which has a dichromatic beamsplitter, would require, in addition, boresight alignment.

With proper design, it is expected that these descriptors would have low sensitivity to temperature over the range predicted during flight. The most critical characteristic is MTF since it is most sensitive to focus. Some change of radiometric responsivity is to be expected due to detector changes with temperature. A check of MTF behavior and radiometric response at intervals over the predicted flight thermal range should be undertaken. For such tests, it is advisable that predicted inflight thermal gradients be simulated as nearly as is practical during thermal-vacuum testing.

Verification of the stability of these two parameters over the vibration and shock ranges anticipated during launch would also be essential. Alternate Design 1 would potentially have greater sensitivity to vibration than the other designs because of the boresight alignment requirements.

Ground support equipment for the OPM Imager would be required to simulate the spacecraft input functions and record the outputs during calibration and test. Since the multiple channels will produce large volumes of data, a magnetic tape and/or direct computer interface for automatic recording probably would be the most economical configuration along with some supplementary direct data readout capability. Appropriate test equipment such as radiometric reference sources, suitable collimators, MTF test equipment, spectrometers, thermal-vacuum test chambers, etc., are required to provide preflight instrument calibration.

7.6 MINIMUM WEIGHT OPM IMAGER DESIGNS

The effect of roll rate on weight is shown in Figures 7-13 through 7-15 for the three primary Point Designs under consideration. These were generated by using each system modeling figure (Figures 6-4 through 6-6) to determine the required telescope diameter at each roll rate, subject to the assumed requirements. Specification of the nominal requirements for the SNR ($\nu = 0$) (radiometric precision), IFOV size (resolution), and wavelength interval (spectral selectivity) leaves the roll rate and telescope diameter as the primary unspecified variables in a given scene. The roll rate can therefore be traded off versus telescope diameter, with the number of detectors determined in each case by the underlap constraint.

The dependence of weight on telescope diameter and number of detectors was presented in Figures 7-9 through 7-12 for the primary Point Designs and one Alternate Design. These then permit a determination of the effect on weight of the design specification. As can be seen, Designs 2 and 3 have a broad minimum and so are relatively insensitive to the choice of operating point, specified by the optics diameter and the corresponding maximum roll rate. Design 1, however, is more sensitive to this selection. As shown, a roll rate under about 10 rpm is preferable, with 5 rpm and a 15-cm optics producing the minimum weight design configuration. Table 7-8 compares these optimum designs for the three primary Point Designs under consideration.

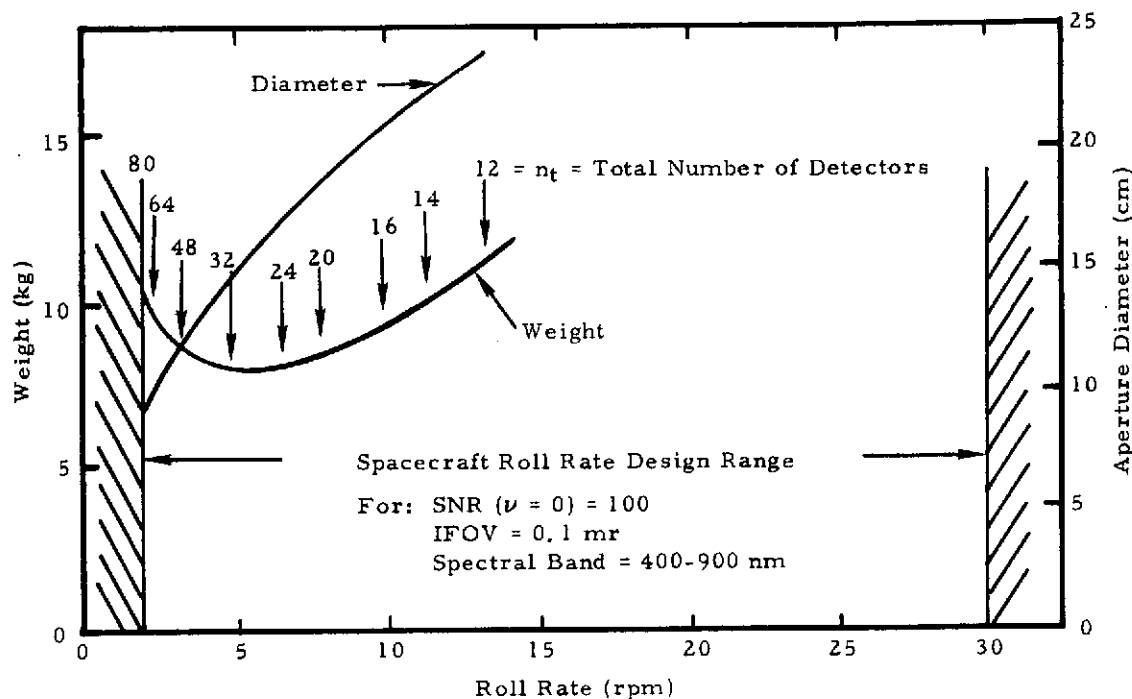


Figure 7-13. Weight Versus Roll Rate for OPM Imager Design 1
(Extended-Red, Digicon-Type Detector)

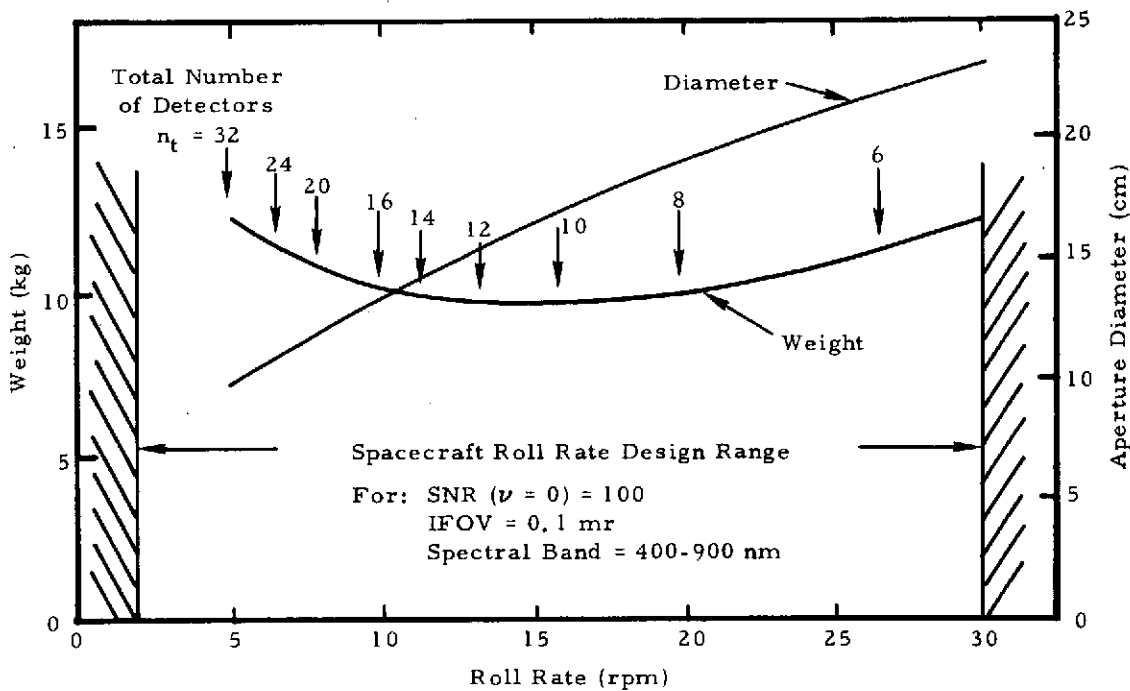


Figure 7-14. Weight Versus Roll rate for OPM Imager Design 2
(GaAs PMT Detectors)

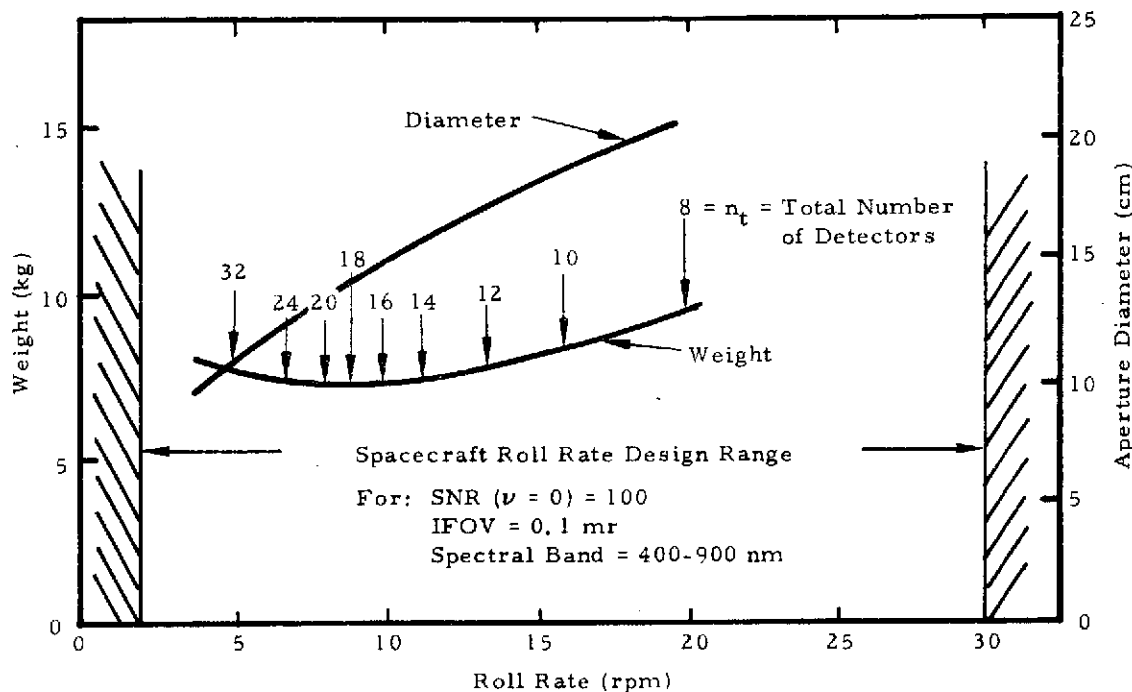


Figure 7-15. Weight Versus Roll Rate for OPM Imager Design 3 (Silicon Array Detectors).

Table 7-8. Comparison of OPM Imager Point Designs Optimized for Minimum Weight

POINT DESIGN	TELESCOPE DIAMETER (cm)	NUMBER OF DETECTORS	ROLL RATE (rpm)	WEIGHT (kg)
DESIGN 1 (DIGICON-TYPE DETECTOR)	15	32	5	8.2
DESIGN 2 (InGaAs PHOTO-MULTIPLIERS)	16	12	13	9.5
DESIGN 3 (SILICON PHOTODIODE ARRAY)	14	18	9	7.3

(WEIGHT MINIMIZED FOR SNR ($\nu = 0$) = 100
AND IFOV = 0.1 mr)

THESE POINT DESIGNS PROVIDE:

1. 10 km RESOLUTION AT JUPITER
2. RADIOMETRIC QUALITY IMAGERY
3. FULL DISK IMAGES AT 10R_J (<50 kbps)
4. INSTRUMENT WEIGHT ~ 9 kg

Section 8

IMAGE SEQUENCE PLAN FOR JUPITER ORBITER MISSION

8.1 INTRODUCTION TO ORBIT GEOMETRY

The Jovian orbits for which an image sequence plan has been outlined are described in Reference 38. In this document, the possibility of initial insertion into a $2.29 \times 100 R_J$ orbit (see Figure 8-1) followed by transfer to a $2.29 \times 45.13 R_J$ orbit allows repeated near encounters with the Jovian satellites Io, Europa, and Ganymede on several successive orbits. While imaging opportunities certainly exist on the initial $2.29 \times 100 R_J$ transfer orbit, planning has been limited to the smaller orbit. A copy of the computer program used to generate these orbits has been kindly provided by Ames Research Center. This program, which for simplicity assumes Jupiter's equator, the plane of the satellite orbits and the plane of the spacecraft orbit coincide, has been used to generate a tape of spacecraft coordinates relative to the Earth, the Sun, Jupiter, and the satellites Io, Europa, and Ganymede for six consecutive orbits. Figure 8-2 shows the first of these six orbits when viewed from above Jupiter's north pole. For the close satellite encounters on this orbit, the position of the satellite is connected to the position of the spacecraft at the time of closest approach and at two-hour intervals before closest approach.

The main difference for subsequent orbits is the geometry of the satellite encounters. Figures 8-3, 8-4, and 8-5 show the geometry of all six encounters of Ganymede, Io, and Europa, respectively, in a frame of reference fixed to these bodies; that is, they show the path of the spacecraft past the satellite as seen when viewed from above the satellite's north pole. The direction to the sun is indicated, and the numbers along the trajectories indicate the time in hours from closest

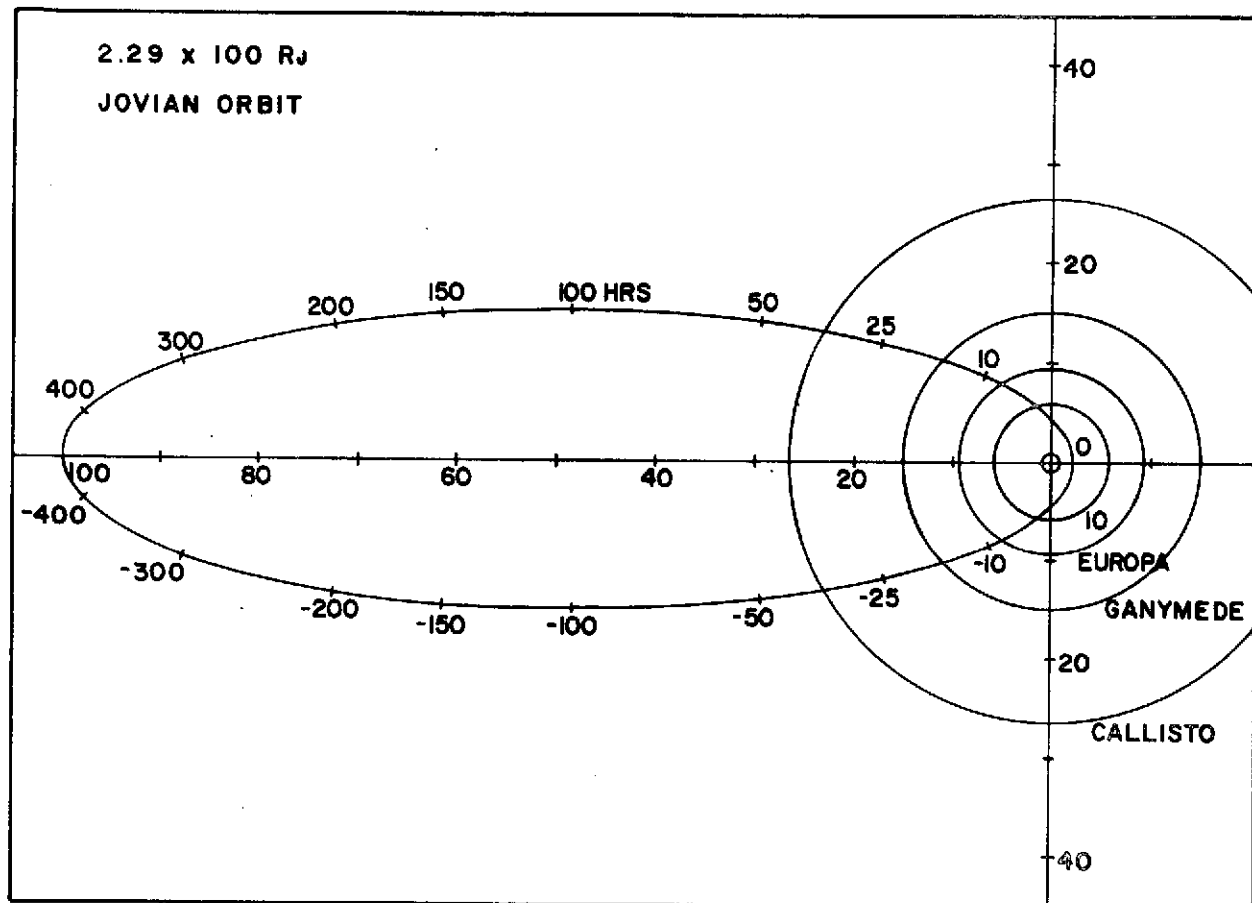


Figure 8-1. Possible Initial Insertion Orbit for Jupiter Orbiter Mission

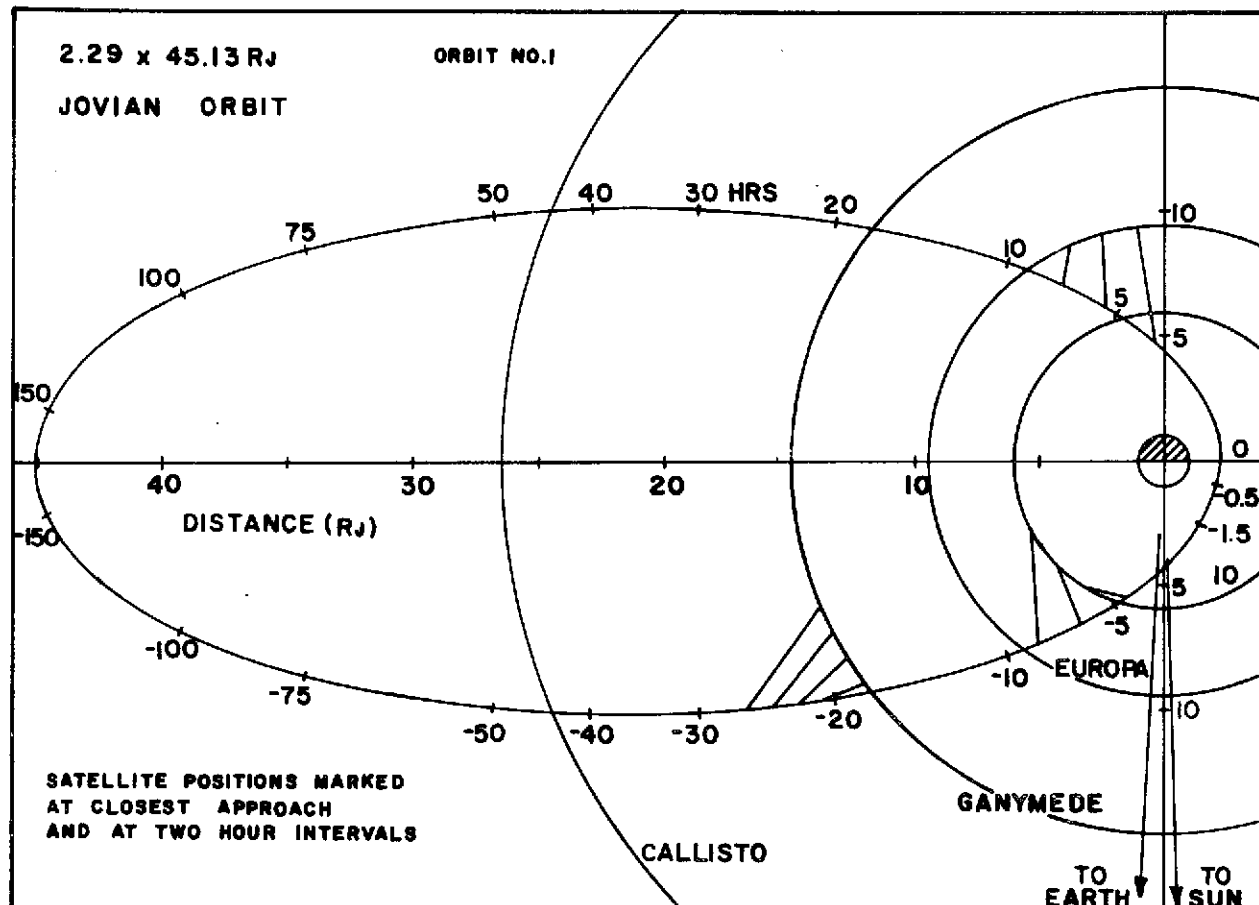


Figure 8-2. Geometry of One Possible Orbit during Jupiter Mission

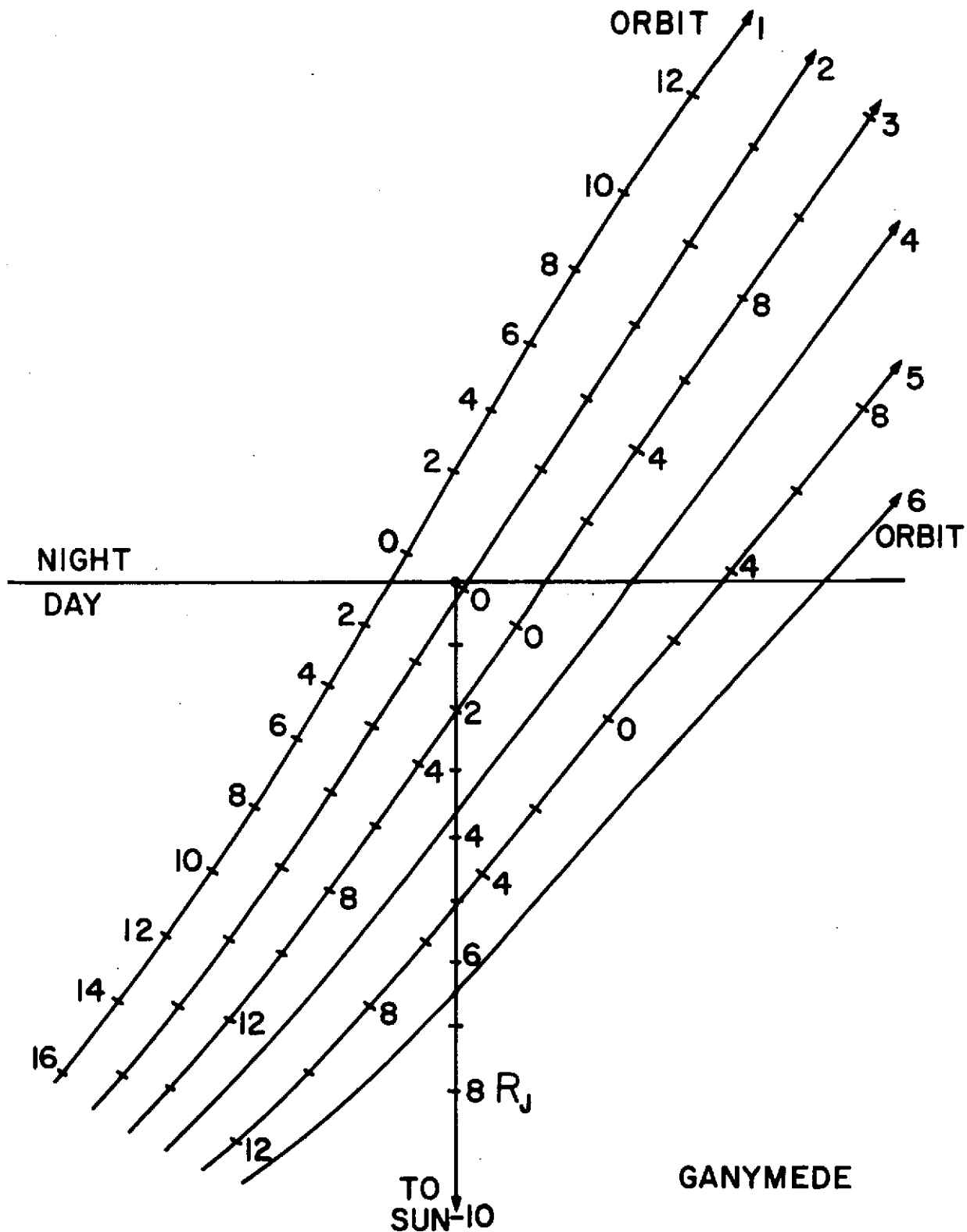


Figure 8-3. Geometry of Encounters with Ganymede during Six Successive Orbits

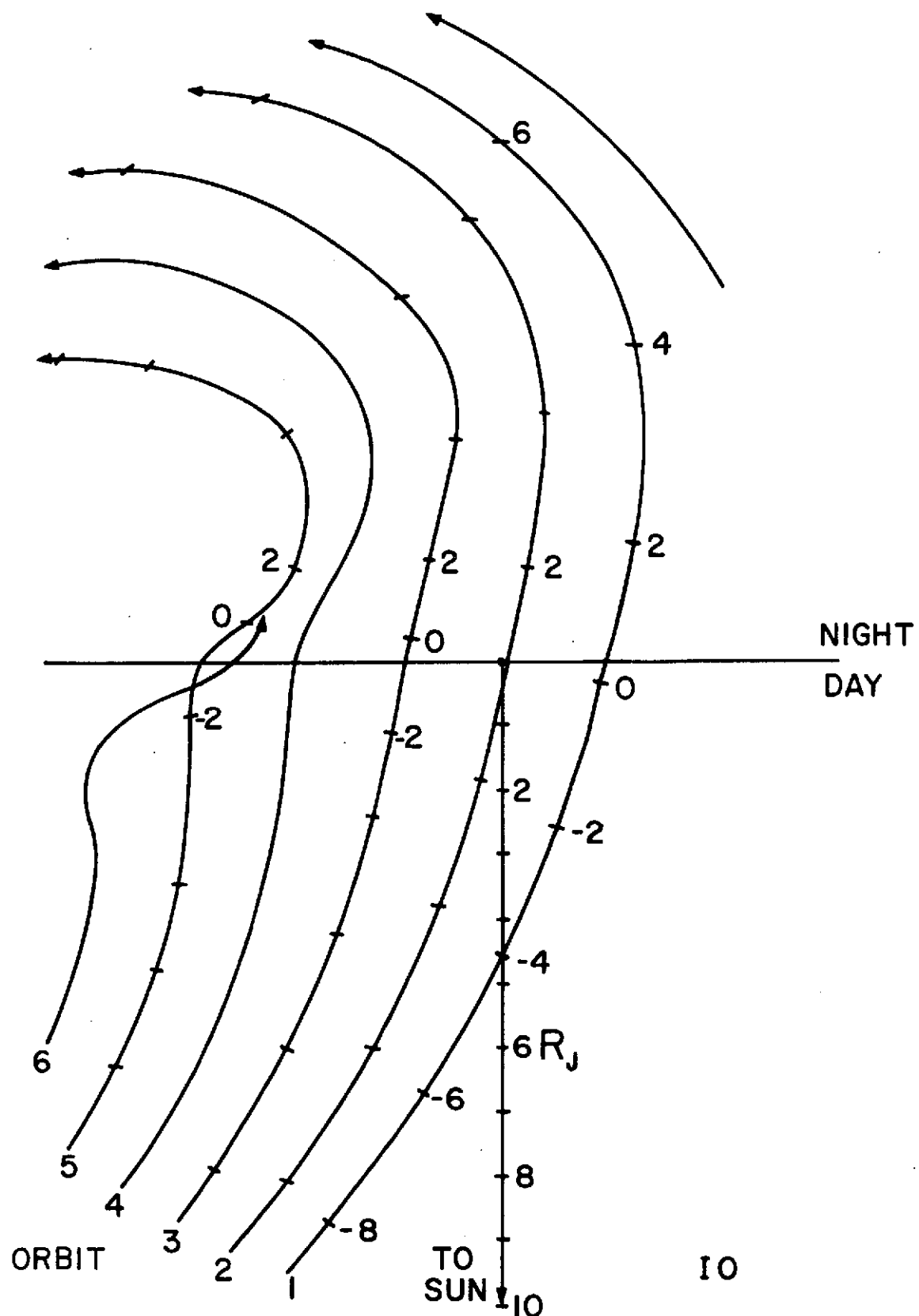


Figure 8-4. Geometry of Encounters with Jupiter during Six Successive Orbits

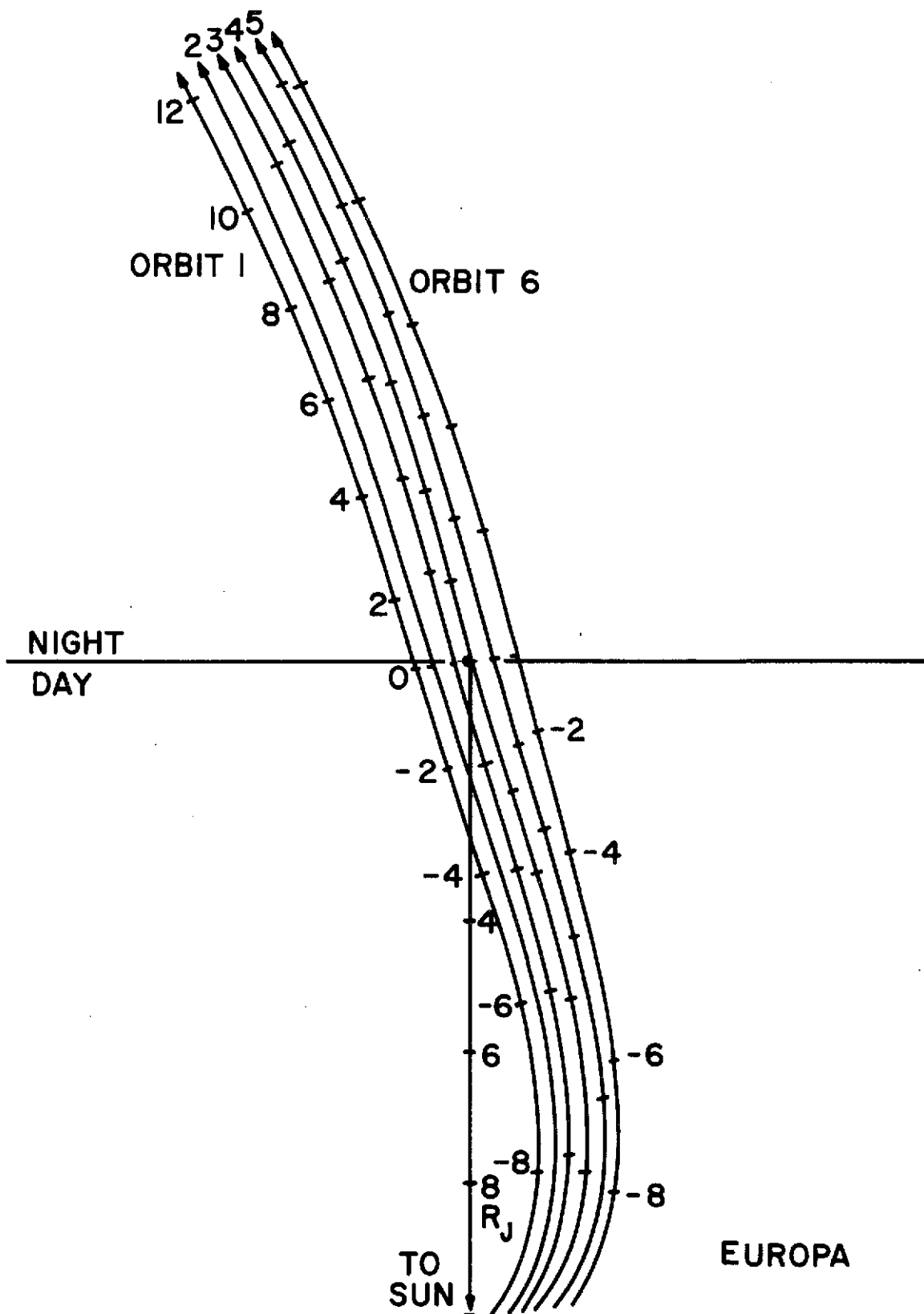


Figure 8-5. Geometry of Encounters with Europa during Six Successive Orbits

approach to the satellite. Except for the last three Io encounters, the relative trajectories are rather straight lines with various miss distances typically of the order of a Jupiter radius although some of the encounters are quite close.

After a short discussion of how the imaging step rates depend on orbit geometry in subsection 8.2, a plan for the Jovian and satellite imaging for the first $2.29 \times 45.13 R_J$ orbit is discussed in subsection 8.3. The overview of the imaging opportunities for the six orbits is summarized in subsection 8.4.

8.2 STEP RATE SELECTION

It is convenient to define the unit stepping rate to be one array width per spacecraft rotation. For reasons to be detailed here, it is appropriate to require a "half-stepping" rate both in increasing and decreasing look angle for the OPM Imager.

Consider Figure 8-6. A "scene rate" of zero means that a scene appears stationary to an observer moving with the spacecraft. In that case, the unit stepping rate of the imager moves the scan line across the scene at a "frame rate" of ± 1 . The sign of the frame rate has the following convention here. Allow the spacecraft to increase speed away from the Earth. At some point, the scene rate becomes equal to the unit stepping rate of the scanner "backwards" (toward the Earth). At that point, Full-Step-Back (FSB) continues to scan the same line in the scene indefinitely and the frame rate vanishes. Allowing the spacecraft speed to increase further until the scene rate is two units, then the scene moves past the scanner in FSB mode in just the manner that it would if both scene and spacecraft were stationary, and the imager were in Full-Step-Forward (FSF) mode. The frame rate in either case is taken to be $+1$.

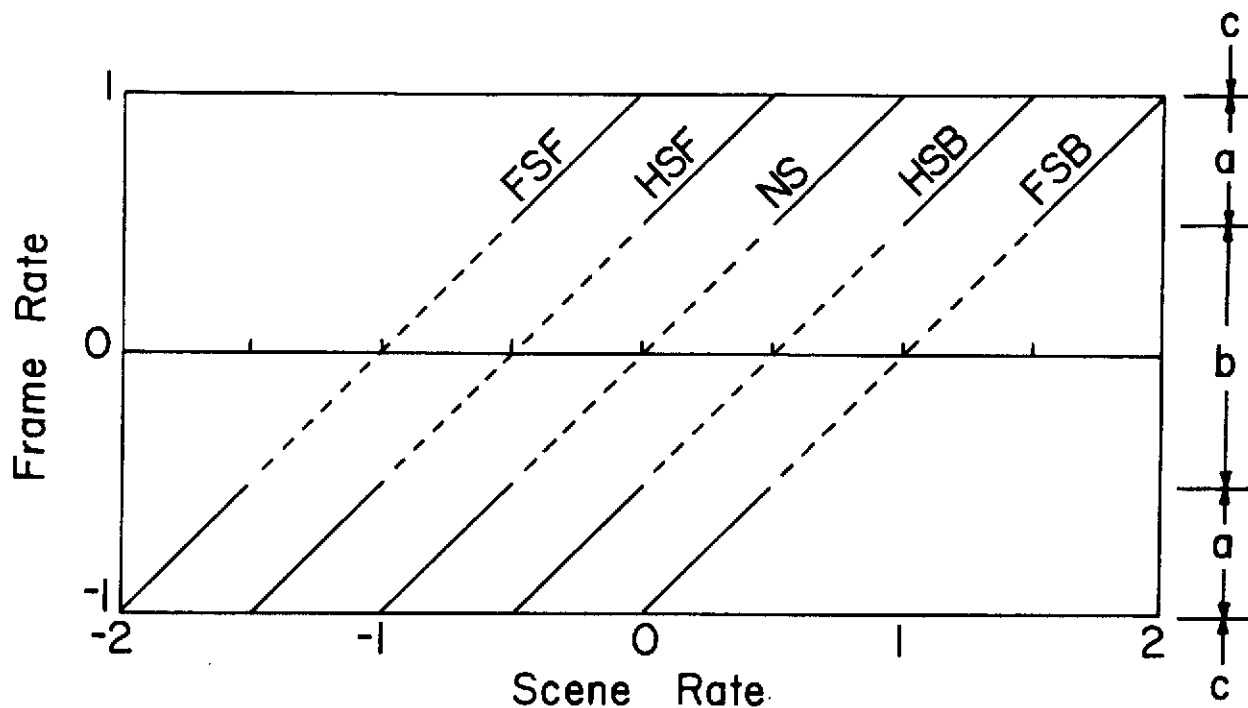


Figure 8-6. Stepping Rate Selection Chart for Imager

Note that a frame rate of ± 1 corresponds to scanned strips that are exactly adjacent — no overlap or underlap. The above example showed that a frame rate of zero corresponds to indefinitely large overlap, i.e., the overlap is reciprocal to the frame rate. Overlap up to a factor of 2 might be used to enhance resolution or to improve the accuracy of relative placement of scans on a map. Larger overlap tends to be wasteful of data-taking time. Figure 8-6 shows that for unit scene rate and FSB, the frame rate vanishes. It also shows that Non-Step (NS) would give a frame rate ± 1 and Half-Step-Back (HSB) would give a frame rate $\pm 1/2$. Suppose HSB did not exist and the scene rate were just greater than 1. Then the wasteful use of FSB would be necessary because NS would give a frame rate of more than 1. But, the reciprocal of the frame rate using NS would be less than 1. An overlap factor of less than 1 is "underlap," which is totally unacceptable.

Thus, it is desirable to require that an advanced spin-scan imager have half-stepping rates so that for scene rates from -2 to +2, a frame rate from 1/2 to 1 or -1/2 to -1 can always be selected.

8.3 PLAN FOR ORBIT 1

The foregoing principles will be applied in a detailed study of orbit 1 and checked by computing rectified scan maps. The detailed study illustrates the operations that might be necessary to obtain image sequences and points to the importance of on-board recognition of the end of an image and automatic reversal of the scanning. The number of images available by line scanning will be presented with emphasis on the coverage as a function of resolution.

Consider Figure 8-7, in which the angles from the spacecraft spin axis to Jupiter, Io, Europa, and Ganymede (called "look angles") are plotted for times throughout orbit 1 and the beginning of orbit 2. When the range of an object passes through a minimum, the look angle changes rapidly. Figure 8-8 shows that the roll angle also changes rapidly then.

In Figure 8-9, the time scale is expanded to show more detail as the orbiter passes close to Jupiter and the satellites Ganymede, Io, and Europa. A possible division of observing time between Jupiter and its satellites is indicated, which will be detailed below. The orbit parameters of this study result in six orbits which nearly repeat the pattern of Figure 8-9, so some orbits might emphasize Jupiter more or less than shown, depending on scientific needs.

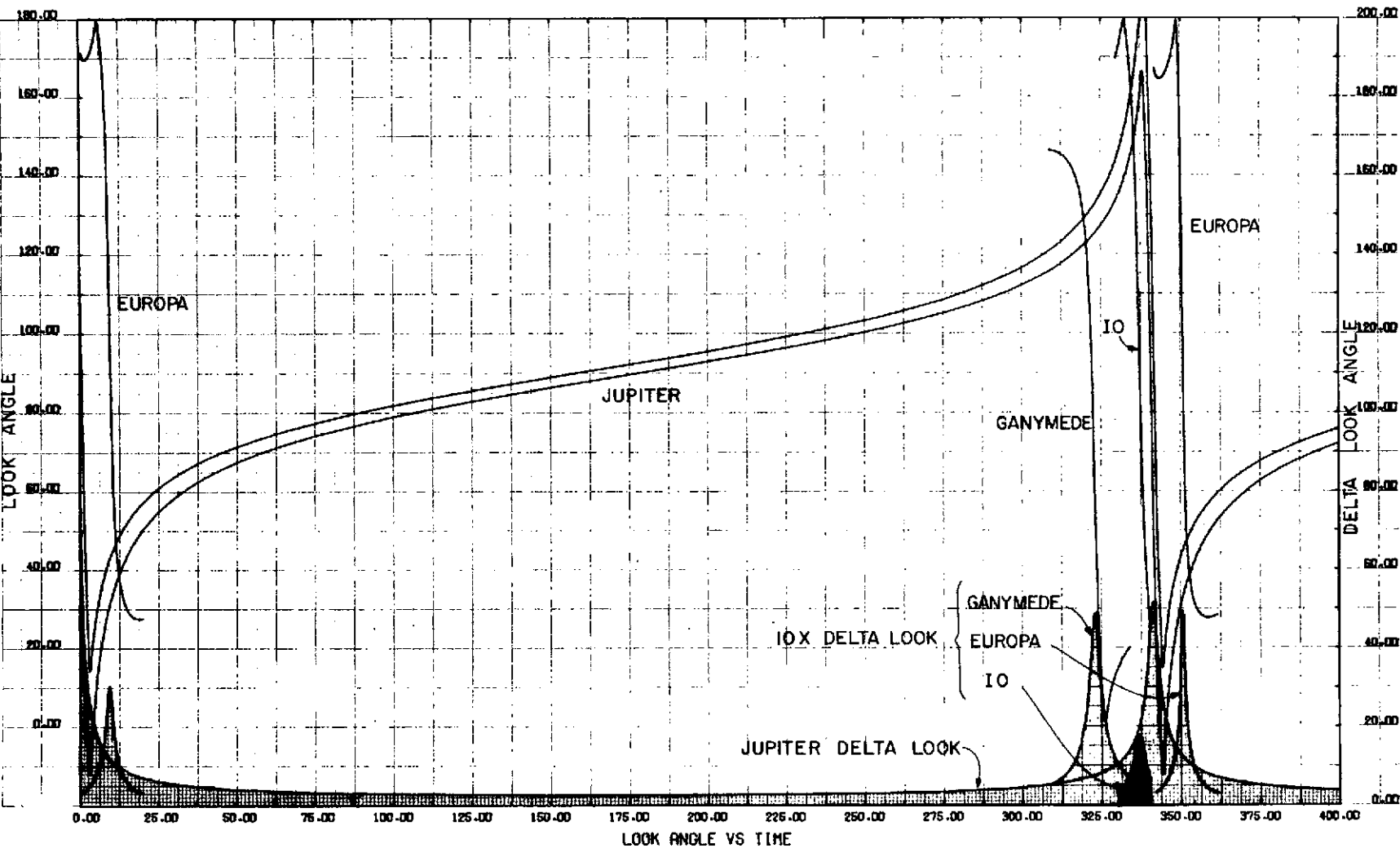


Figure 8-7. Look Angle (Degrees) Versus Time (Hours) for Orbit 1 and Part of Orbit 2

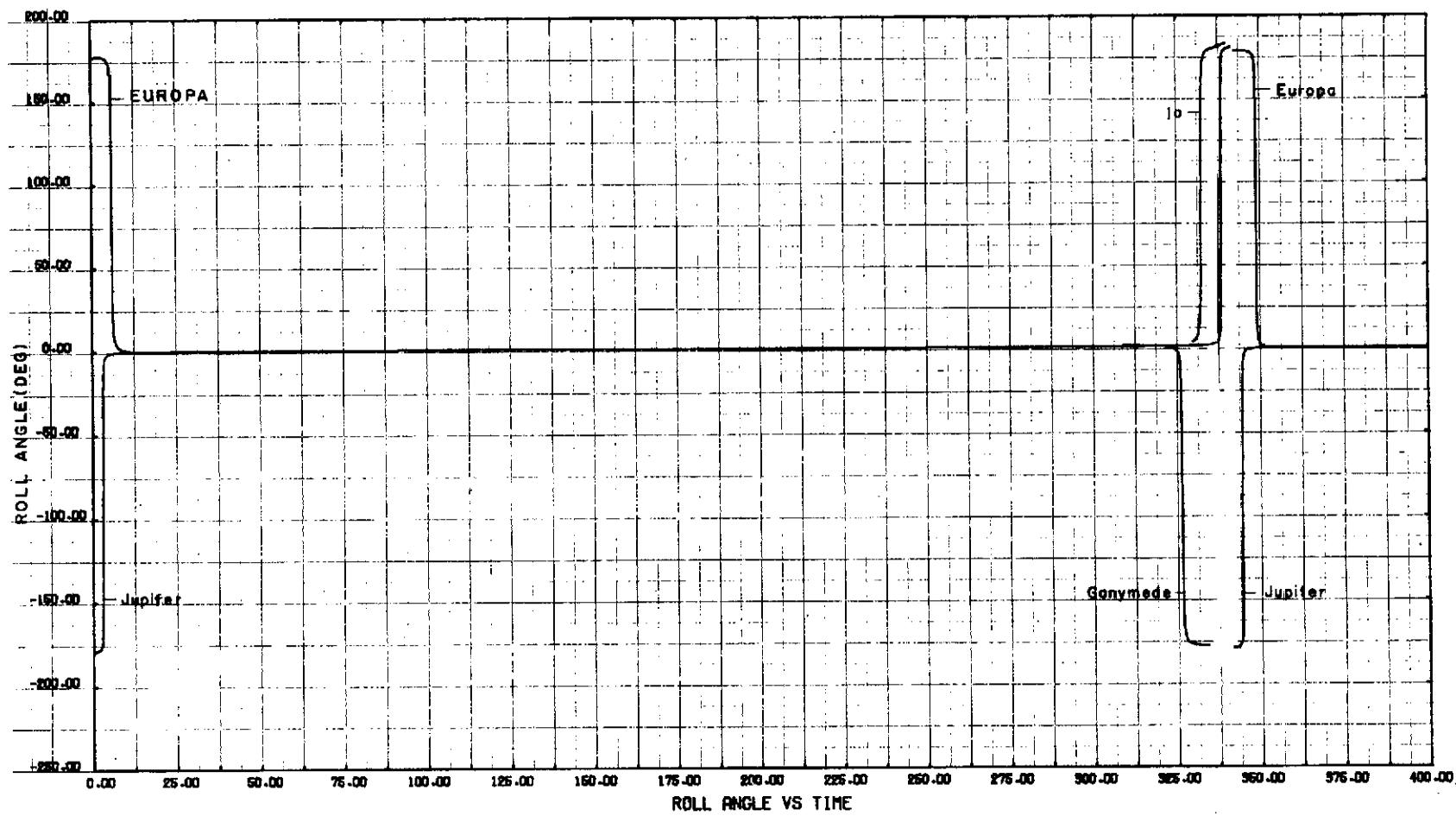


Figure 8-8. Roll Angle (Degrees) Versus Time (Hours) for Orbit 1 and Part of Orbit 2

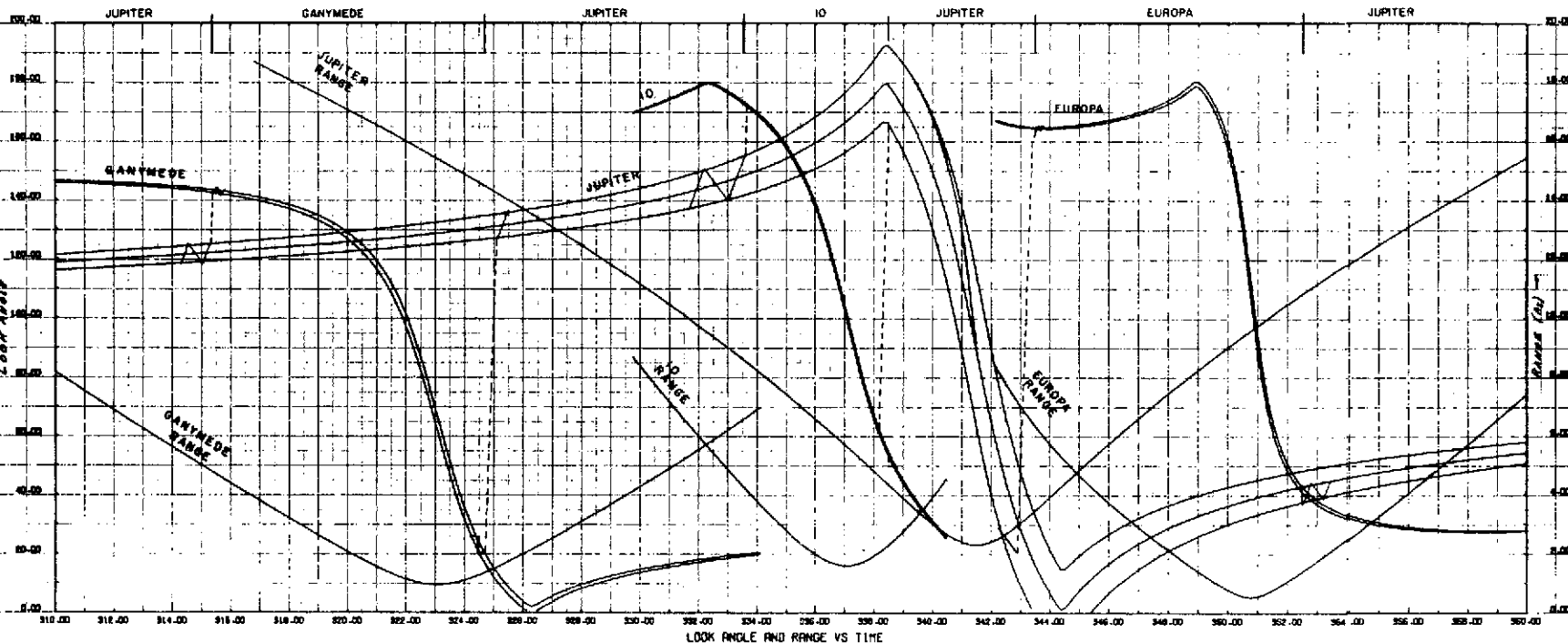


Figure 8-9. Look Angle Versus Time on Expanded Scale Near Encounter

8.3.1 Jupiter Imaging

In Figure 8-10, the time scale is further expanded in a presentation of look angle and range near Jupiter periapsis. The Io passage will be discussed later. The maximum rate of change of look angle for Jupiter is -55° per hour. Following the discussion of subsection 8.2, this is taken to be a scene rate of +2 units. Then the stepping rate FSB is -27.5° per hour in look angle.

As noted in subsection 3.1, the surface velocity of Jupiter is appreciable. The scene rate is variable along one scan line from pole to pole. In particular, at periapsis the equatorial velocity decreases the scene rate below 2 units. However, the desire to image polar regions requires that the maximum stepping rate be obtained from the time derivative of look angle. Thus, Figure 8-10 shows the times at which the derivative in look angle is half-integral multiples of the stepping rate.

As a first approximation, the surface velocity of Jupiter can be ignored and then the rate of change of look angle becomes the scene rate. From Figure 8-6, the prescription for stepping rate can be read off: FSB, HSB, NS, HSF, FSF. A slew rate of 300° per hour is assumed. Images A, B, C, and D were selected on this basis and slight variants shown in Figure 8-10. In the 4.5 hours from full phase viewing to a crescent view, there is time for basically three large detailed pictures separated by two slew periods.

In Figures 8-11a through 8-11g are shown scan maps of Jupiter. The distant view of Figure 8-11a can be obtained ten times per hour for much of the two-week orbit, i.e., about 3000 such pictures. Pixel surface subtense would be ~ 320 km on the images obtained at maximum range and proportionately better at closer range. Time coverage would permit detailed meteorological studies. Figure 8-11b is the last

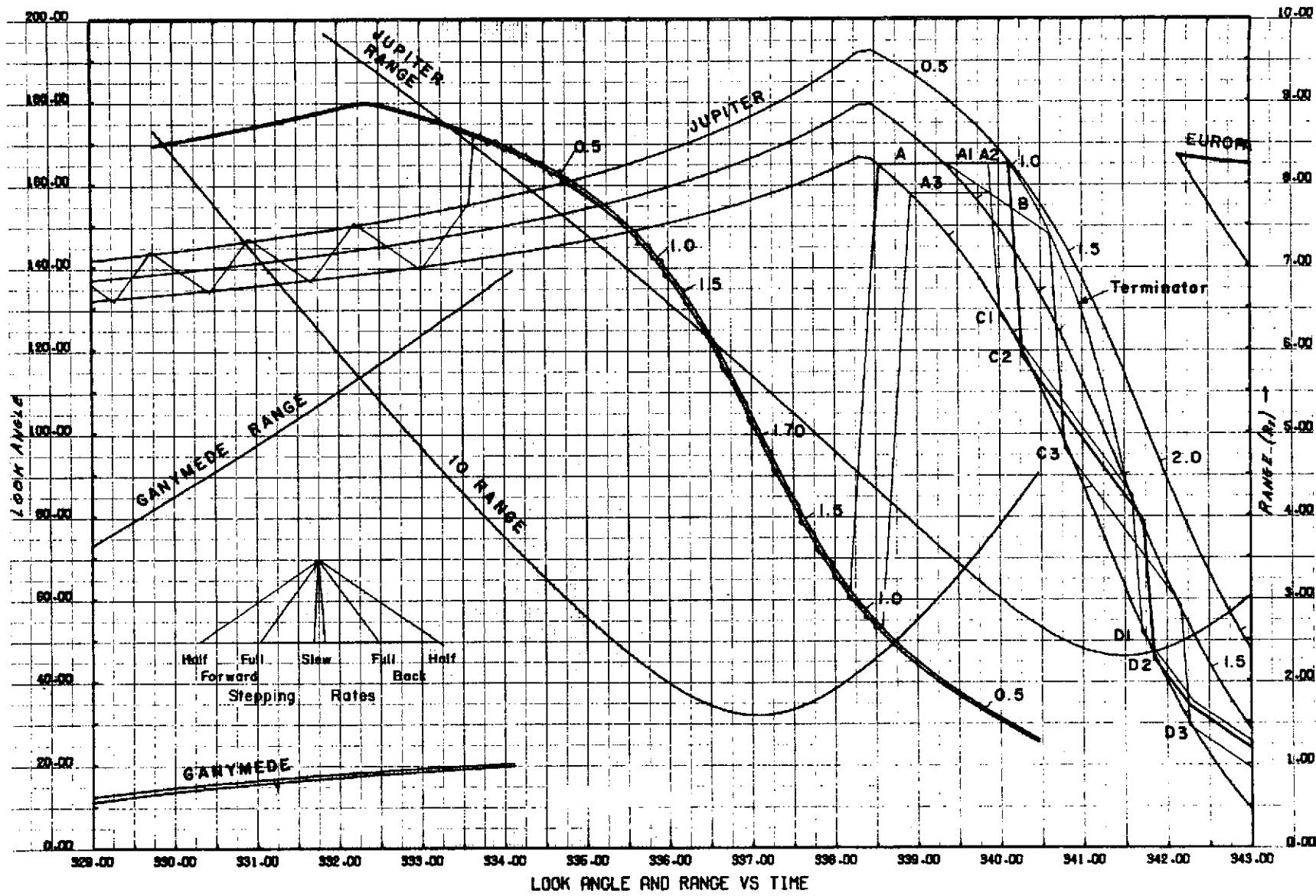
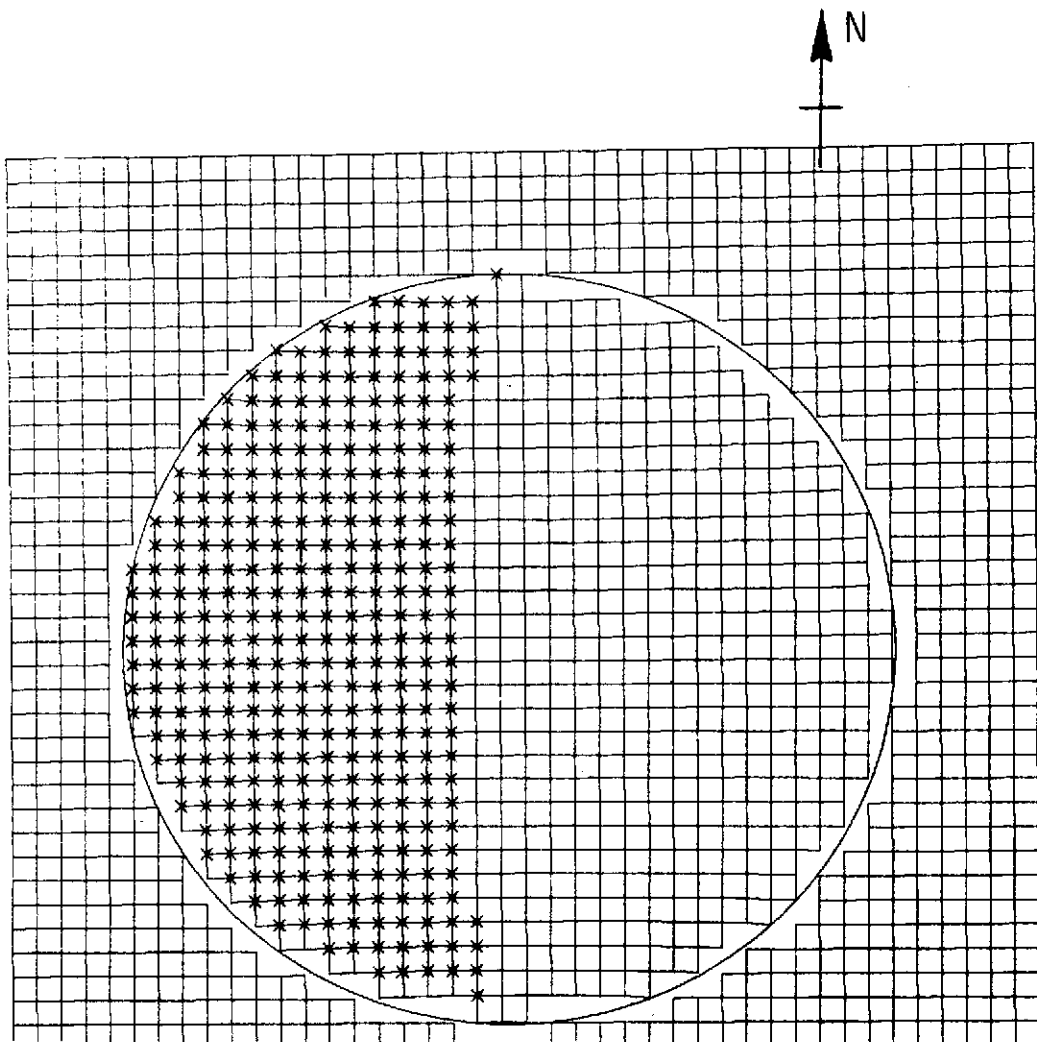
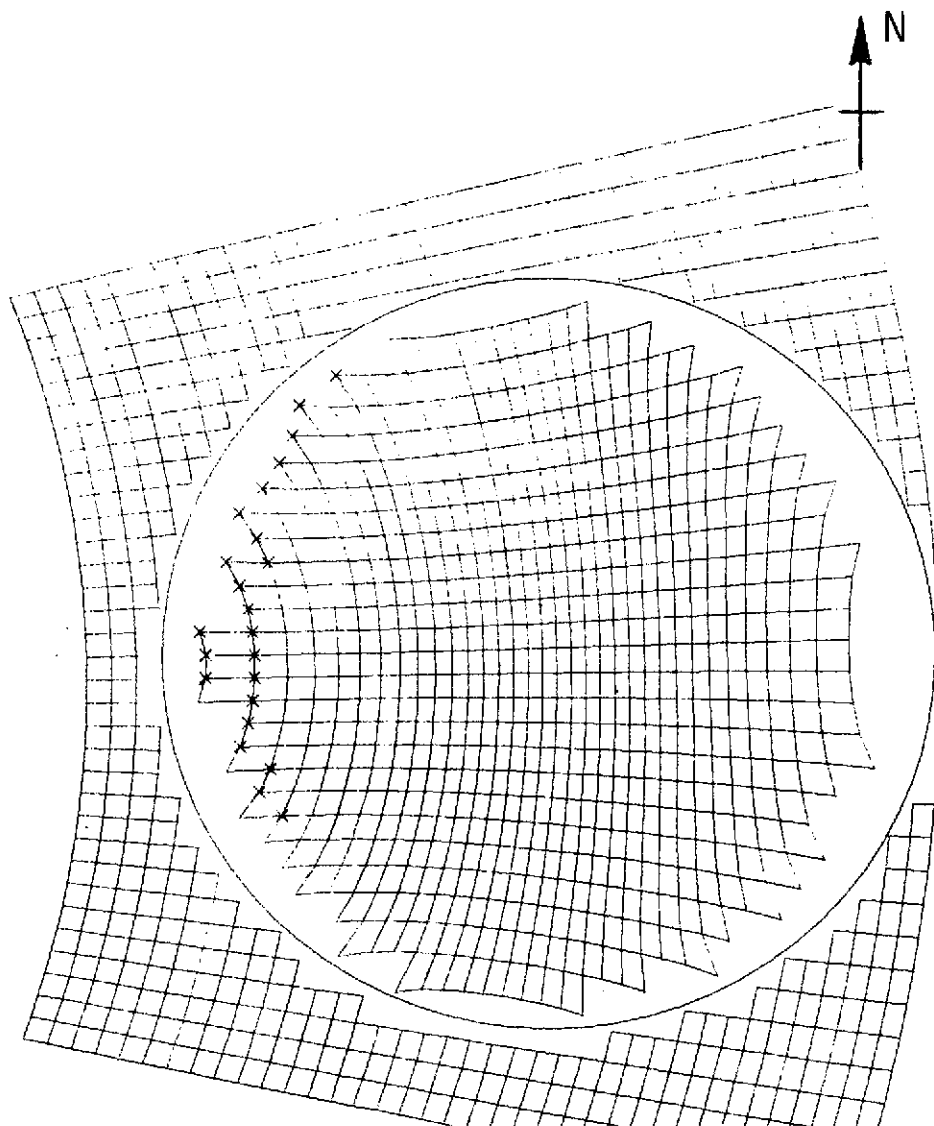


Figure 8-10. Look Angle Versus Time on Further Expanded Scale Near Periapsis



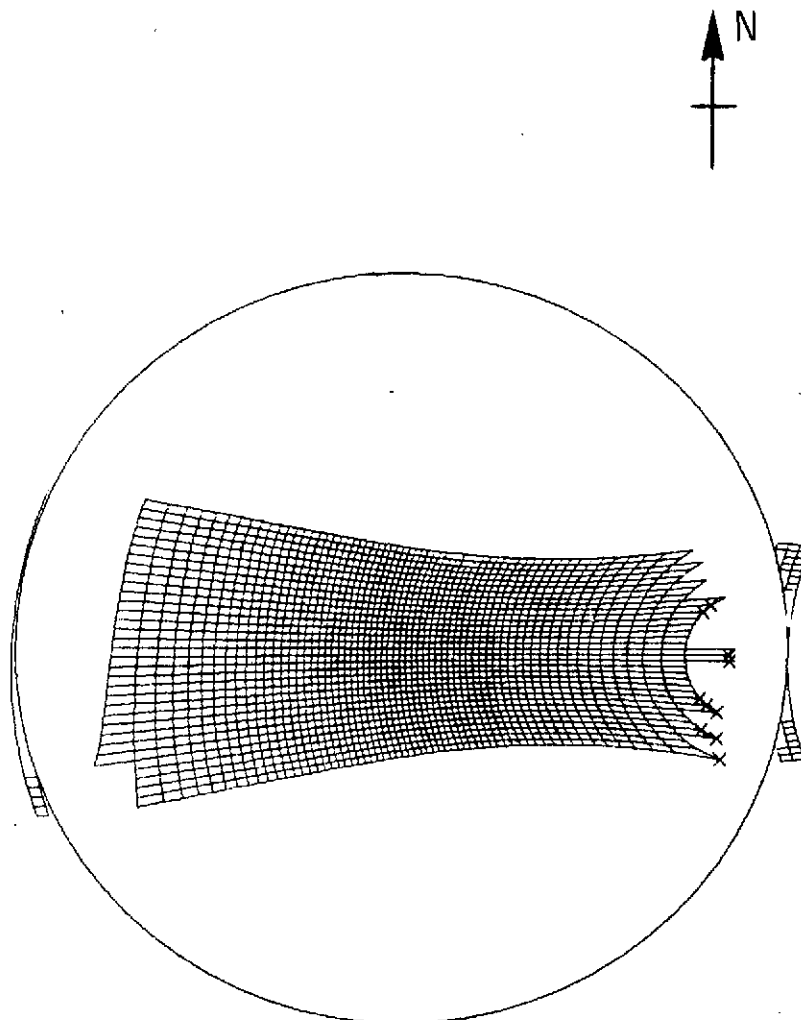
JUPITER ORBIT NO. 1 START TIME 244.15 END TIME 244.29 HRS.
CLOSEST APPROACH 39.50 RJ SAMPLE RATE 1 FORWARD STEPPING
S/C ROTATION 10.00 RPM EVERY 2TH LOOK AND 16TH ROLL POINT SHOWN
STARTING LOOK ANGLE 98.50 DEG STARTING ROLL ANGLE -1.40 DEG
NO. DETECTORS PER CHANNEL 8 NO. POINTS PER ROLL 600
IMAGE FIELD OF VIEW IN THE ROLL 0.10 AND LOOK DIRECTION 0.10 MRAD

Figure 8-11a. Scan Map of Jupiter for Conditions Indicated



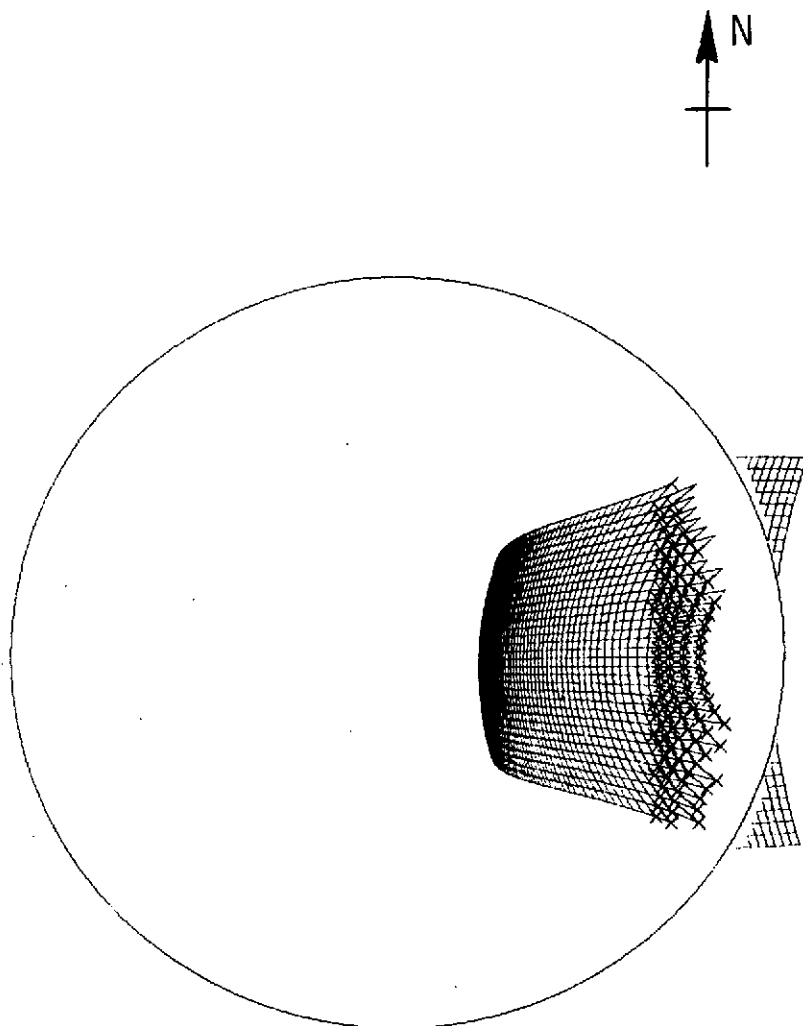
JUPITER ORBIT NO. 1 START TIME 334.70 END TIME 335.65 HRS.
CLOSEST APPROACH 6.85 RJ SAMPLE RATE 2 BACK STEPPING
S/C ROTATION 10.00 RPM EVERY 15TH LOOK AND 120TH ROLL POINT SHOWN
STARTING LOOK ANGLE 161.40 DEG STARTING ROLL ANGLE -21.60 DEG
NO. DETECTORS PER CHANNEL 4 NO. POINTS PER ROLL 4000
IMAGE FIELD OF VIEW IN THE ROLL 0.10 AND LOOK DIRECTION 0.10 MRAD

Figure 8-11b. Scan Map of Jupiter for Conditions Indicated



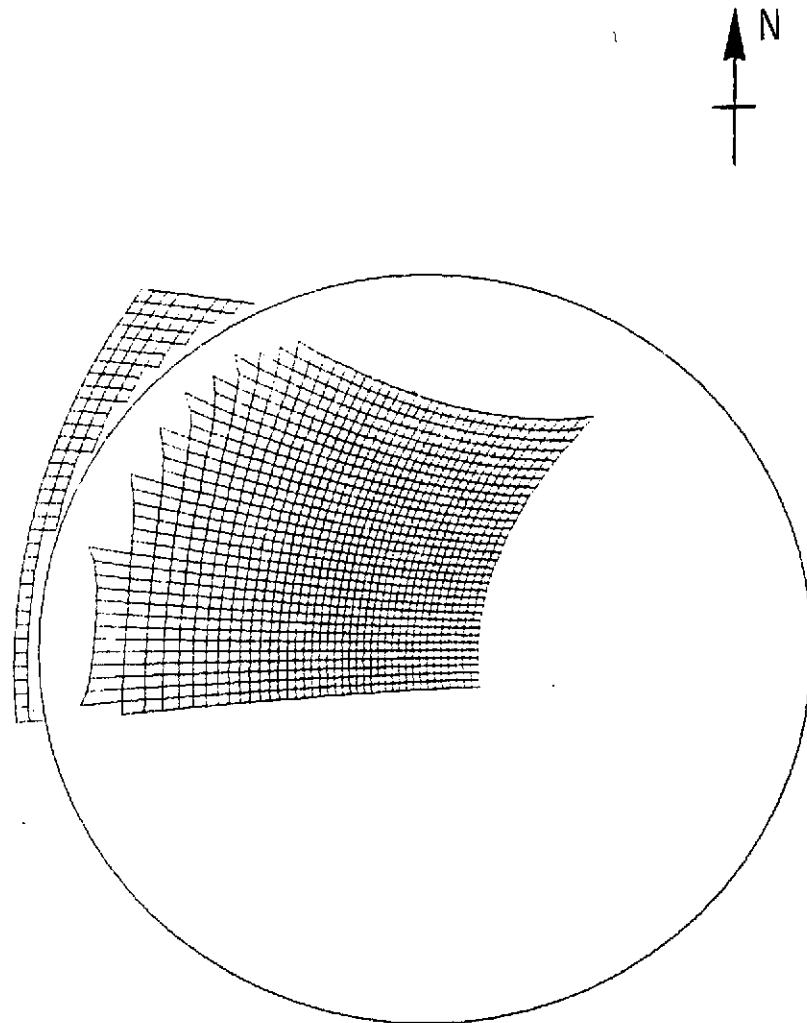
JUPITER ORBIT NO. 1 START TIME 338.50 END TIME 340.15 HRS.
CLOSEST APPROACH 2.85 RJ SAMPLE RATE 2 STEP INHIBIT
S/C ROTATION 10.00 RPM EVERY 15TH LOOK AND 120TH ROLL POINT SHOWN
STARTING LOOK ANGLE 165.00 DEG STARTING ROLL ANGLE 155.50 DEG
NO. DETECTORS PER CHANNEL 8 NO. POINTS PER ROLL 4000
IMAGE FIELD OF VIEW IN THE ROLL 0.10 AND LOOK DIRECTION 0.10 MRAD

Figure 8-11c. Scan Map of Jupiter for Conditions Indicated



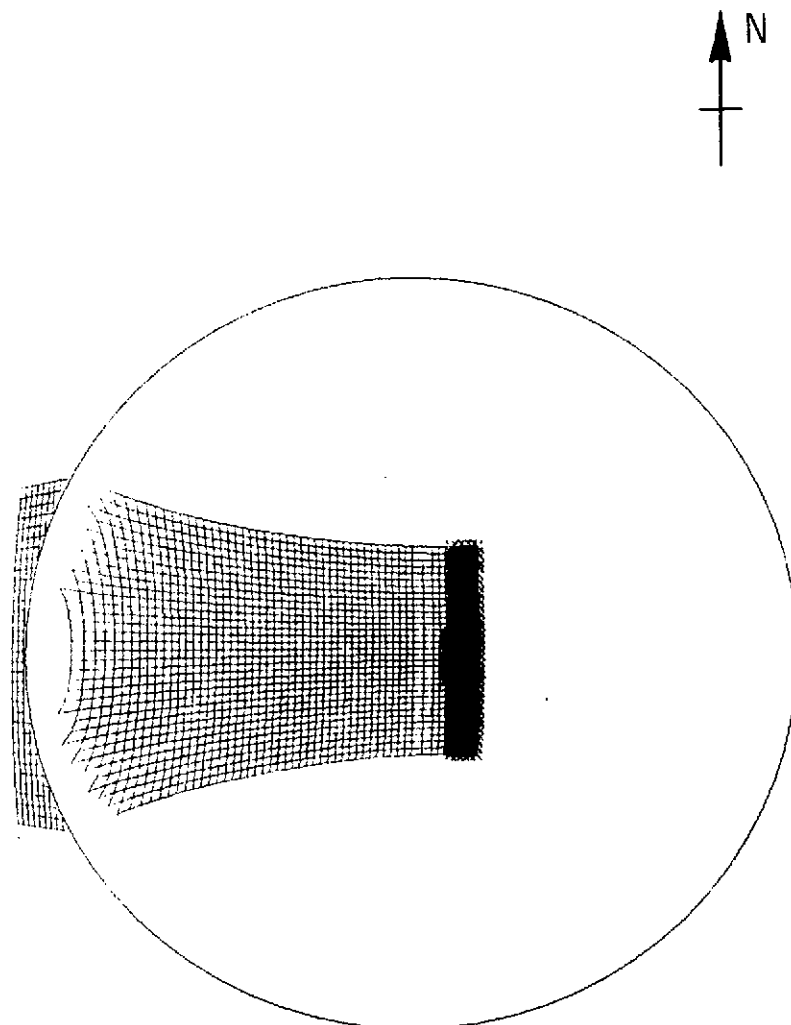
JUPITER ORBIT NO. 1 START TIME 339.40 END TIME 340.70 HRS.
CLOSEST APPROACH 2.50 RJ SAMPLE RATE 2 BACK STEPPING
S/C ROTATION 10.00 RPM EVERY 15TH LOOK AND 120TH ROLL POINT SHOWN
STARTING LOOK ANGLE 165.00 DEG STARTING ROLL ANGLE 156.20 DEG
NO. DETECTORS PER CHANNEL 4 NO. POINTS PER ROLL 4000
IMAGE FIELD OF VIEW IN THE ROLL 0.10 AND LOOK DIRECTION 0.10 MRAD

Figure 8-11d. Scan Map of Jupiter for Conditions Indicated



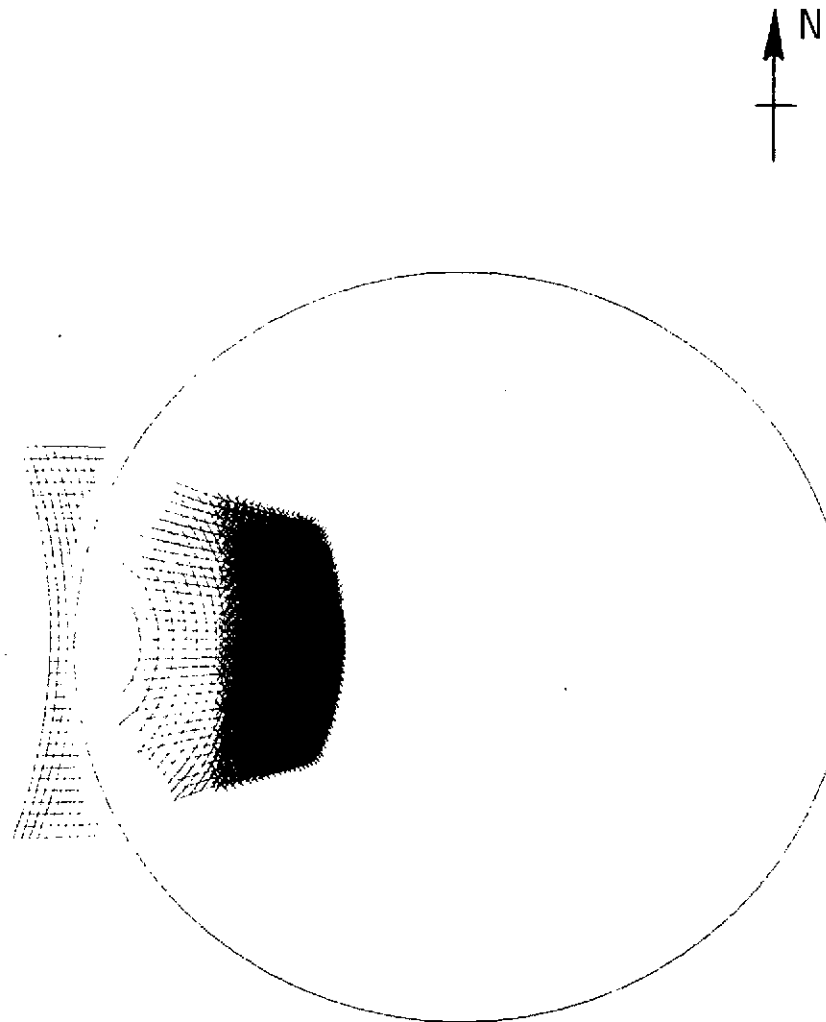
JUPITER ORBIT NO. 1 START TIME 338.85 END TIME 339.92 HRS.
CLOSEST APPROACH 2.80 RJ SAMPLE RATE 2 STEP INHIBIT
S/C ROTATION 10.00 RPM EVERY 15TH LOOK AND 120TH ROLL POINT SHOWN
STARTING LOOK ANGLE 158.00 DEG STARTING ROLL ANGLE 140.00 DEG
NO. DETECTORS PER CHANNEL 8 NO. POINTS PER ROLL 4000
IMAGE FIELD OF VIEW IN THE ROLL 0.10 AND LOOK DIRECTION 0.10 MRAD

Figure 8-11e. Scan Map of Jupiter for Conditions Indicated



JUPITER ORBIT NO. 1 START TIME 340.28 END TIME 341.72 HRS.
CLOSEST APPROACH 2.29 RJ SAMPLE RATE 1 BACK STEPPING
S/C ROTATION 10.00 RPM EVERY 15TH LOOK AND 120TH ROLL POINT SHOWN
STARTING LOOK ANGLE 118.50 DEG STARTING ROLL ANGLE 168.34 DEG
NO. DETECTORS PER CHANNEL 8 NO. POINTS PER ROLL 4000
IMAGE FIELD OF VIEW IN THE ROLL 0.10 AND LOOK DIRECTION 0.10 MRAD

Figure 8-11f. Scan Map of Jupiter for Conditions Indicated



JUPITER ORBIT NO. 1 START TIME 342.17 END TIME 343.00 HRS.
CLOSEST APPROACH 2.50 RJ SAMPLE RATE 2 BACK STEPPING
S/C ROTATION 10.00 RPM EVERY 15TH LOOK AND 120TH ROLL POINT SHOWN
STARTING LOOK ANGLE 32.00 DEG STARTING ROLL ANGLE 157.80 DEG
NO. DETECTORS PER CHANNEL 4 NO. POINTS PER ROLL 4000
IMAGE FIELD OF VIEW IN THE ROLL 0.10 AND LOOK DIRECTION 0.10 MRAD

Figure 8-11g. Scan Map of Jupiter for Conditions Indicated

image showing the whole planet at 4000 points per line. It shows the distortion due to variable scene rate from equator to poles in its most severe form.

Figures 8-11c, 8-11d, and 8-11e illustrate variable scene rates in the vicinity of 0.8 unit. The tighter spacing of lines from left to right in the center of Figure 8-11c is the result of the scene rate decreasing to nearly 0.5 unit at the equator. Note from Figure 8-10 that image B starts from the midtime of image A-A₁-A₂ (Figure 8-11c). In Figure 8-6, it is seen that a change from NS to HSB at scene rate 0.5 would give very high overlap. Thus, in Figure 8-11d, the scan lines are highly compressed at the left. They are spread out at the right by the increasing speed of the spacecraft. Figure 8-11c illustrates the first image in an alternate sequence that begins at the middle of the scans of Figure 8-11d. This sequence would permit three more images of Io, as shown in Figure 8-10. Image A₃ has less overlap than the comparable image A. For study of an equatorial region, image B at step rate HSB should be started later than shown and image A₃ prolonged. The choice shown is appropriate for high-latitude coverage.

Note that low sample rate was used in Figures 8-11b, 8-11c, 8-11d, and 8-11e (twice the normal interval between samples along the roll). Consider a time increment such that the spacecraft rolls one FOV. At look angle L, the apparent motion of the imager FOV is shorter by a factor sin (L).

If $\sin (L) \leq 0.5$, it is advantageous to decrease the sampling rate by a factor of 2 and double the length of the scanned line. These regions are $0^\circ \leq L \leq 30^\circ$ and $150^\circ \leq L \leq 180^\circ$. The former region is represented by Figure 8-11g.

The center of one of the three large pictures is represented by Figure 8-11f. It is image C2 of Figure 8-10. Variants C1 and C3 change the look angle at which a given feature on Jupiter would be imaged by only 10° . The final large view of a crescent Jupiter is shown in Figure 8-11g. It is intermediate between D2 and D3 of Figure 8-10 so that low sample rate could be used for the whole image.

The period of 4.5 hours just discussed could be handled quite differently. Suppose, rather, that some longitude of Jupiter were of special interest or that closer coverage in time were desired at some longitude. Then a much larger number of images than three could be obtained by following that region during the flyby. This emphasizes that the "number of images" is not a proper basis for comparison of imaging devices. A much better basis is the number of scan lines produced at given resolution or better.

The length of a scan line depends on the data link. It was shown above that a length of $(1-4) \times 10^3$ pixels is apt to be feasible for the parameters of Figures 8-11a through 8-11g. At 10 rpm, the scanner yields 9,600 lines/hour. The trajectory data give time from periapsis and radial distance. All scans at a smaller radial distance than some given distance are of equal or better resolution. Apart from a rate factor, a plot of "time from periapsis versus radial distance" is a plot of the "number of scans of given resolution or better." Figures 8-12 and 8-13 give the results for half of each orbit of Jupiter. Since at $45 R_J$ Jupiter still covers 880 pixels (440 non-aliased line pairs), the images can be compared to full TV screen images. Figure 8-12 shows up to 16000 such images per half orbit. More realistically, Figure 8-13 shows the higher resolution possibilities. No correction for time spent on satellites was made.

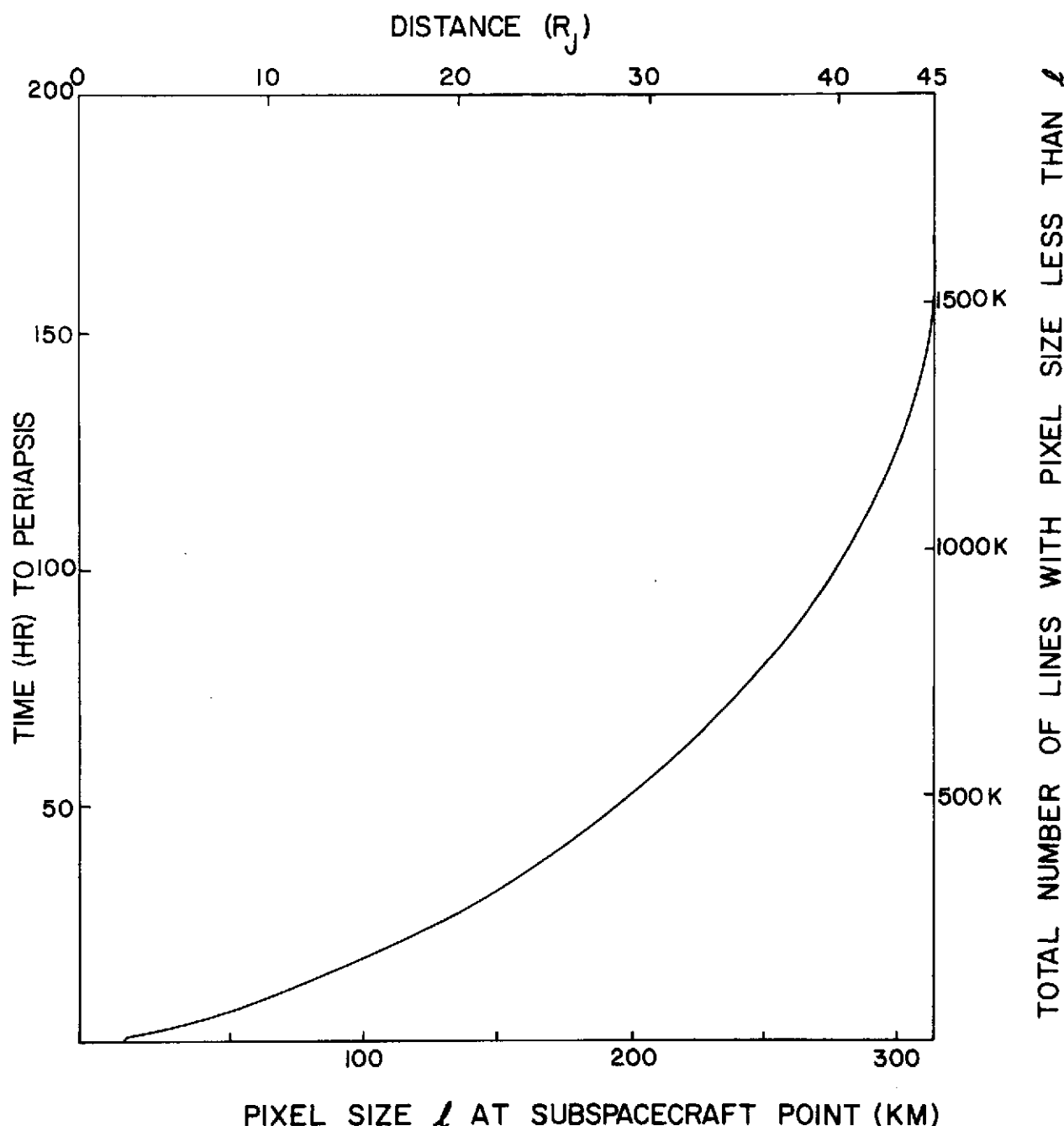


Figure 8-12. Number of Scans at Given Resolution or Better

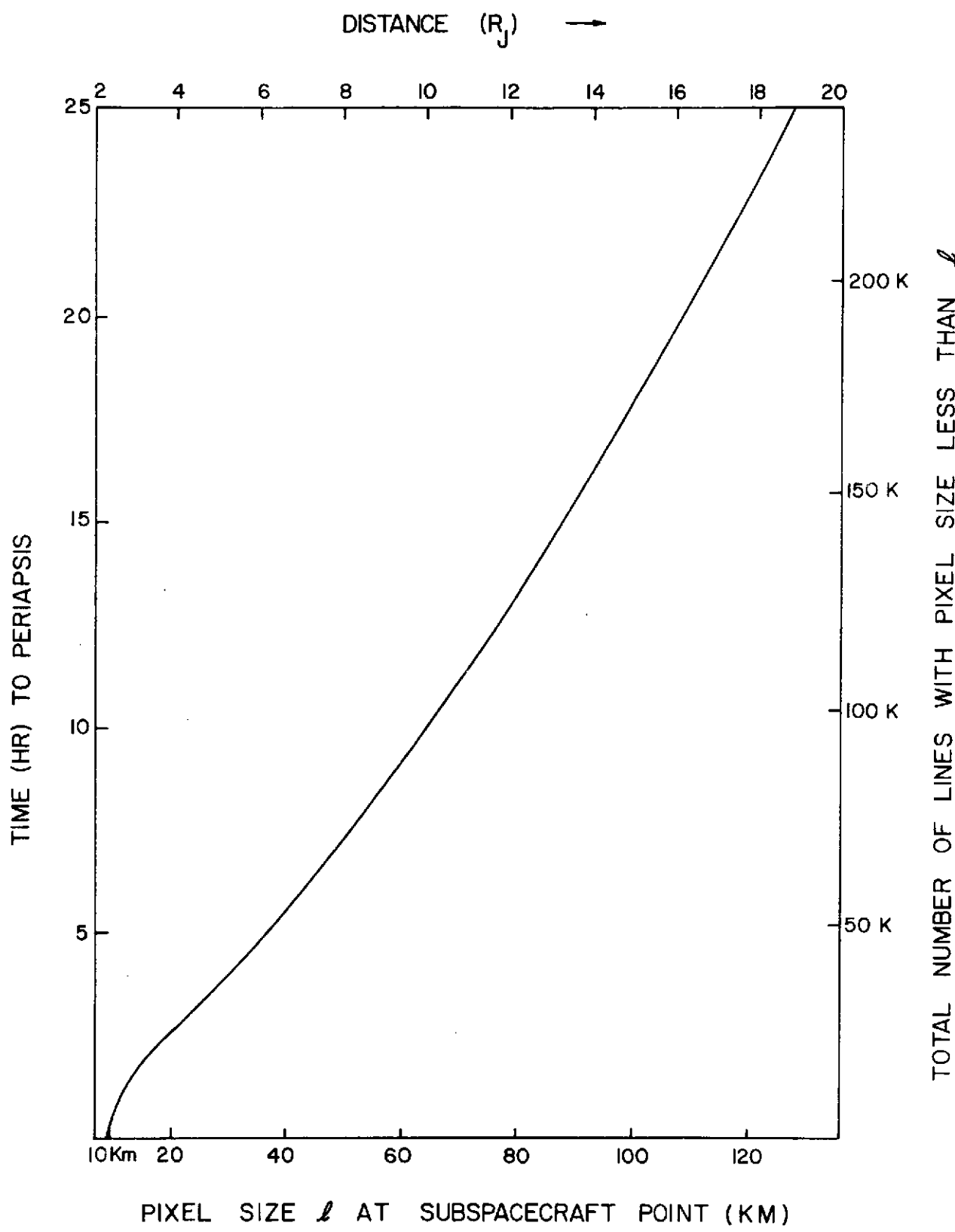


Figure 8-13. Number of Scans at Given Resolution or Better
(Expanded Scale)

No correction has been made for time spent off Jupiter. Consider the operations problems when Jupiter subtends 2.5° so that 11 images per hour are obtainable. Suppose commands are needed to reverse the stepping direction. A round trip light time of 1.5 hours means that for full utilization of observing time, commands for 16 images must be sent before any error in procedure can be learned. In practice, liberal boundaries outside Jupiter would be set to avoid long sequences of time-critical commands.

An automatic sequencer in the imager would markedly increase the fraction of time spent on the object and would sharply decrease command activity. Suppose a commandable threshold of intensity, corresponding to the desire to recognize acquisition of an object and stepping beyond the object. Acquiring an object is a more general problem and includes acquiring objects smaller than the swath of sky covered by the multiple detectors. For acquisition, it is desirable to require that at least one of the detectors sees a light increase above threshold. For a large object, it is desirable to add that after acquisition of the object, stepping will continue according to one commandable rate (HSB, NS, etc.) until none of the detectors sees light above threshold. This corresponds to passing the object, so stepping for the next roll should be changed to the second commandable rate (FSF, slew, etc.) and acquisition sought again. The commandable thresholds might be important if radiation belt noise were a problem or if a detector malfunctioned and gave a continuous full scale reading. The sum of all detectors is to be compared with threshold.

Refer to Figure 8-10 to consider use of the automatic sequence. The closing sequence on Io alternates between NS and slew back (SB). At some convenient time, SB is changed to slew forward (SF) in the appropriate register by command. When an Io image is finished, the scanner will slew up to Jupiter. During an image A, the same register is changed again to SB. The alternate register can be set to FSB.

When the terminator is reached, the scanner slews down to begin an image C. The rates SB and SF would not be appropriate to small objects; in the 10 or so steps per spacecraft rotation, the object might be stepped over. But for Jupiter and the program satellites, this is no limitation. To change from an image A to B without reaching an edge, it would be easy to arrange so that register 1 were set to HSB and have a command "Respond to step rate in register 1." Then register 1 can be set to FSB for the upcoming image C. Some consideration of Figure 8-10 shows that the interval between commands falls to 0.5 hour for recovery of most of the desired science when using automatic sequencing. Without it, the interval is about 0.05 hour, and the amount of time spent on satellite images near periapsis would also decrease.

8.3.2 Satellite Imaging

In Figure 8-10, a detailed imaging plan for Io is presented. The number of images is more than 20. The stepping allowed excessive time off Io as drawn if automatic sequencing were used. On the other hand, the time off Io would undoubtedly be larger than shown for a first orbit of Jupiter if automatic sequencing were not used. The figure illustrates the intervention of imaging that will be necessary when the satellite passes in front of Jupiter. Figures 8-14 and 8-15 give the analogous plans for Ganymede and Europa, respectively. A number of images of Ganymede are given in Figures 8-16a through 8-16e to illustrate the phase coverage. Images of Io and Europa are given in Figures 8-16f through 8-16h. Note that Europa has scene rates in excess of 2 units in the passage studied. Thus, underlap in a few images cannot be avoided. The drawn plan indicates images anyway, because the strips of data give imaging of scientific interest even if the coverage is incomplete, since each feature is imaged many times in complete maps.

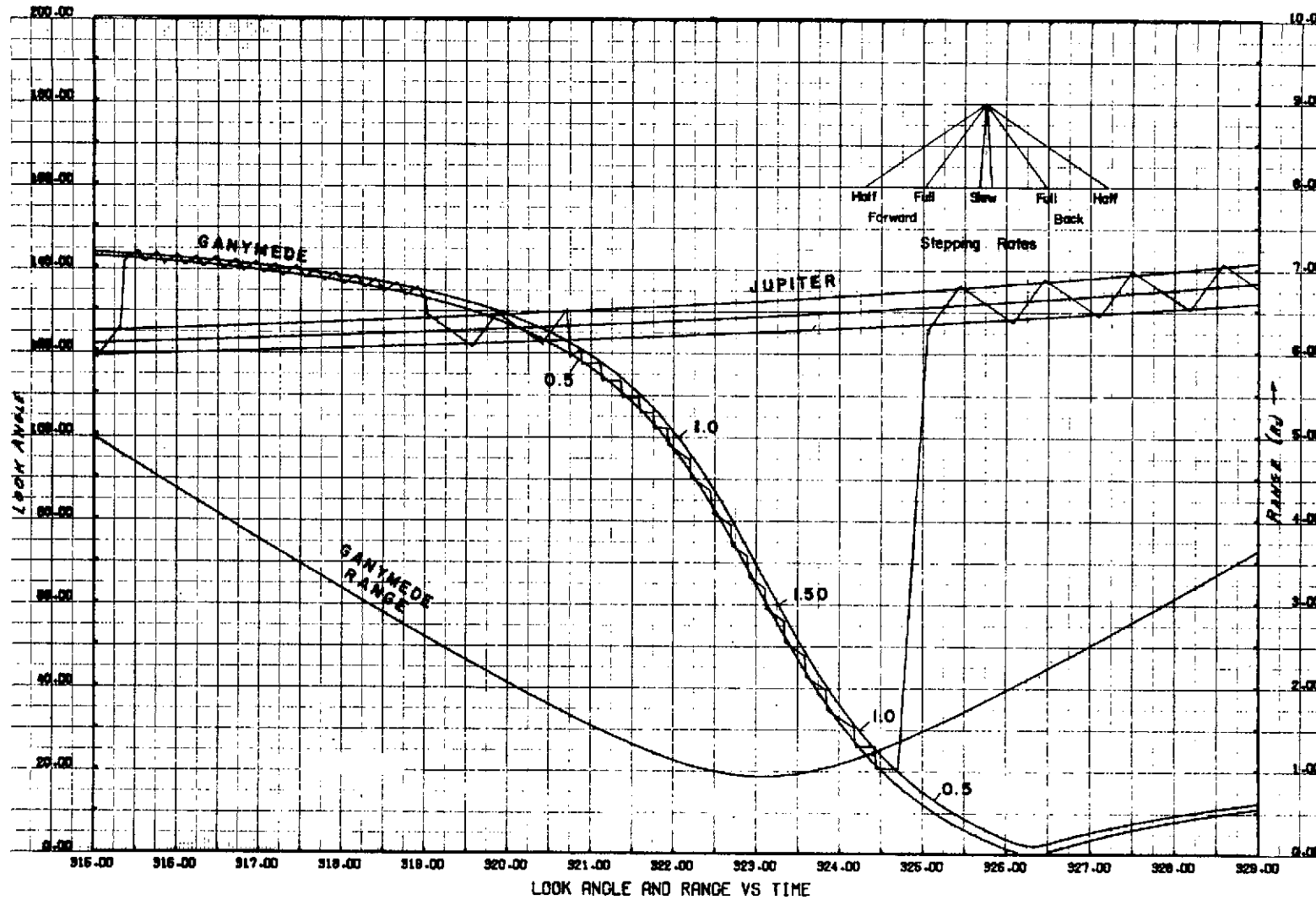


Figure 8-14. Imaging Sequence Plan for Ganymede

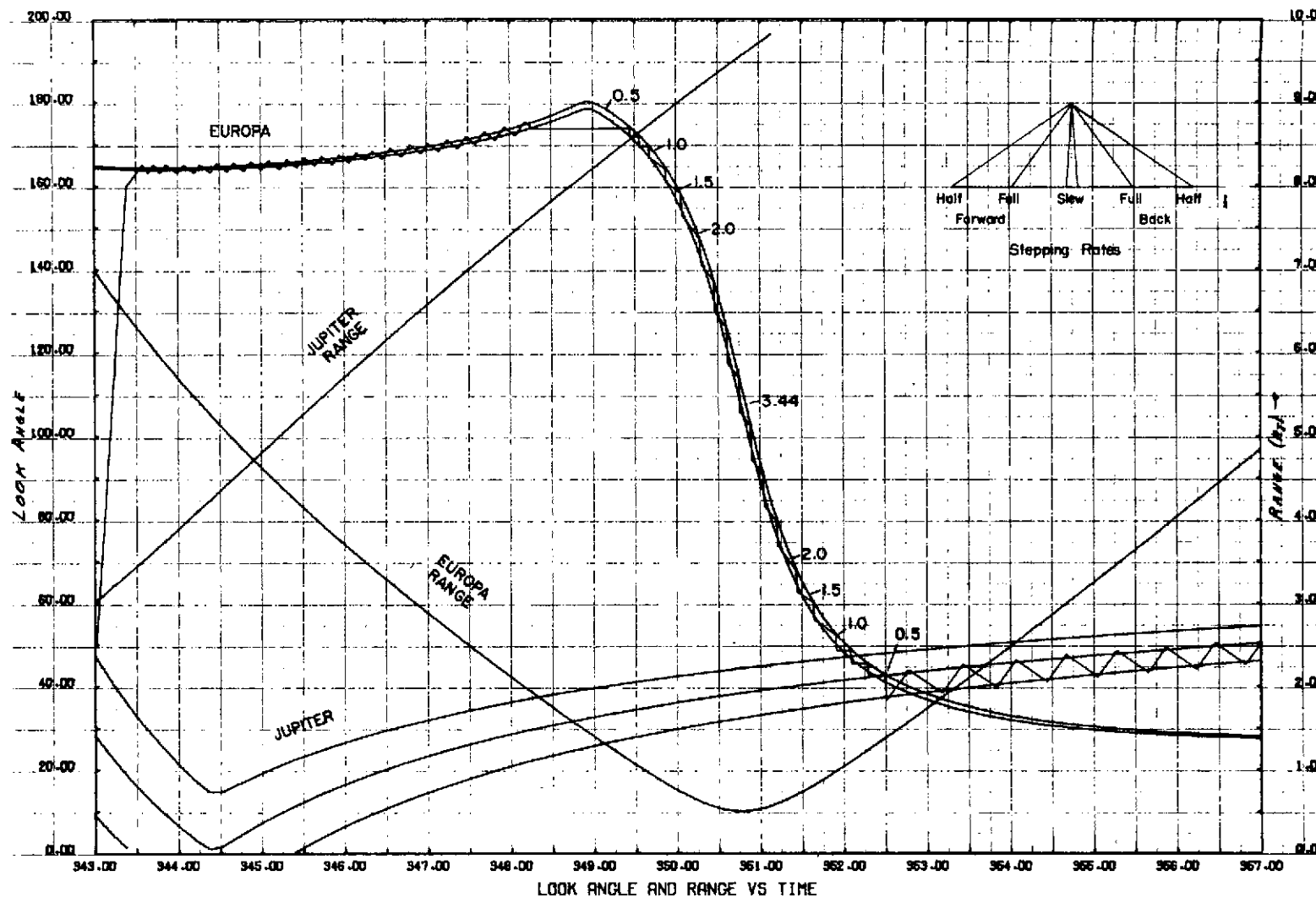
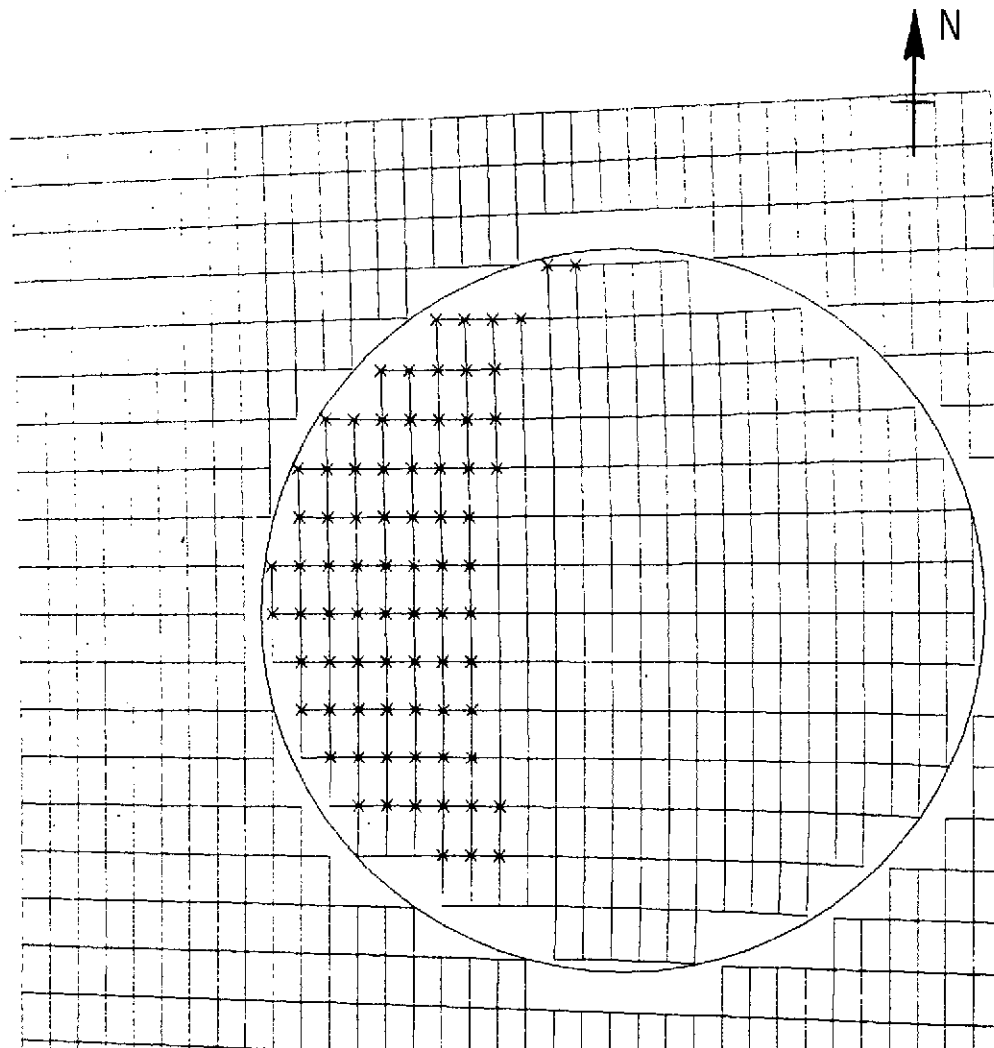
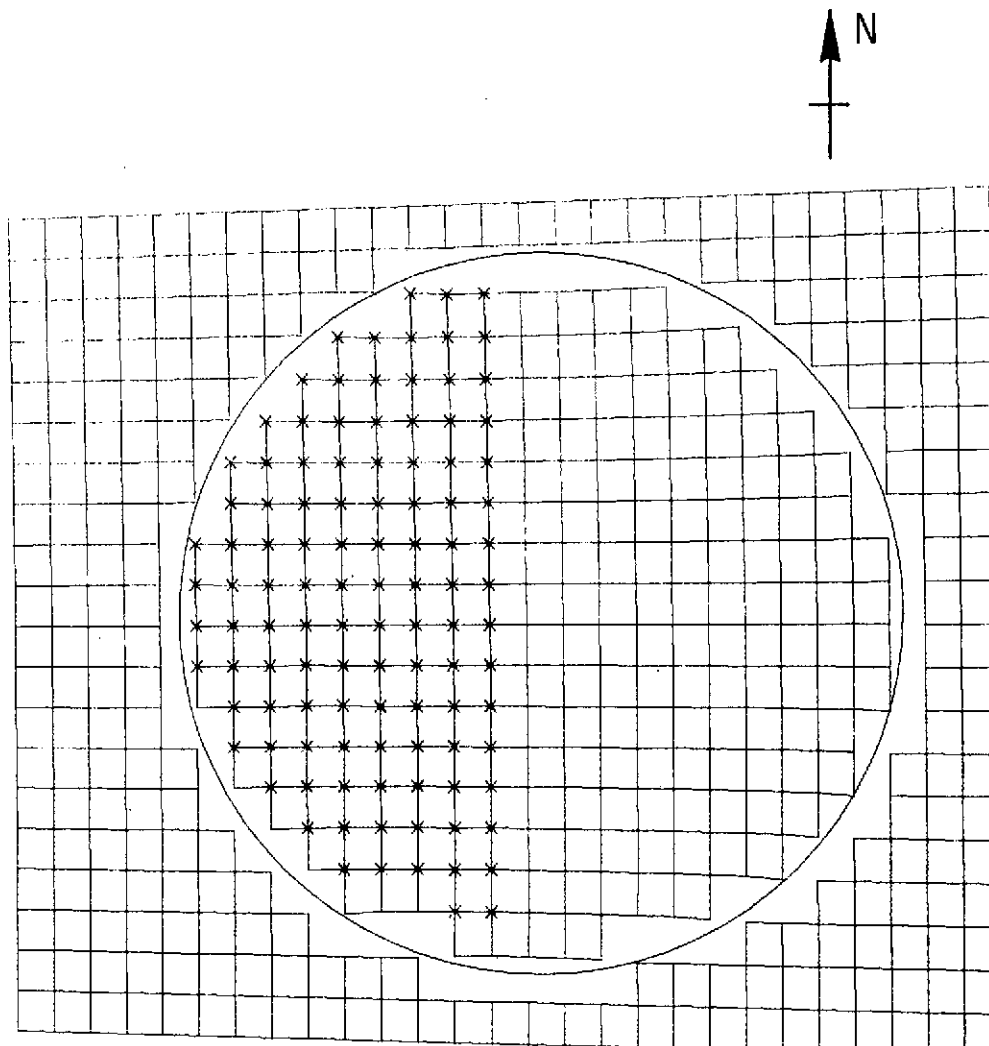


Figure 8-15. Imaging Sequence Plan for Europa



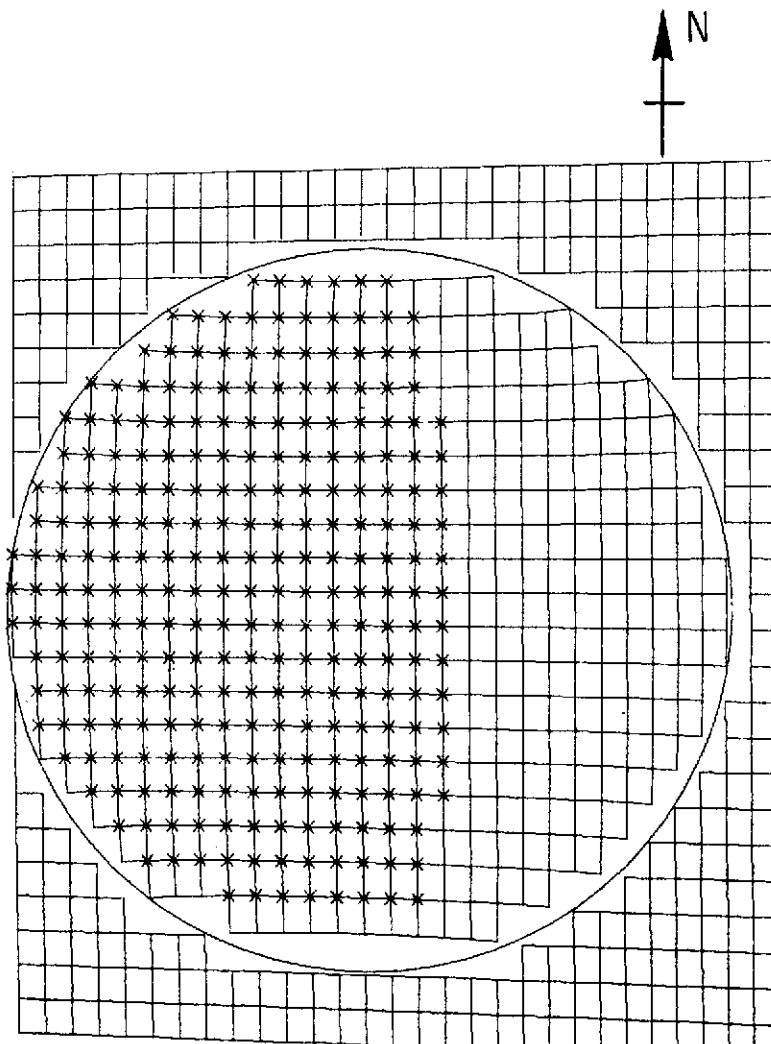
GANYMEDE ORBIT NO. 1 START TIME 320.92 END TIME 321.22 HRS.
CLOSEST APPROACH 1.42 RJ SAMPLE RATE 1 STEP INHIBIT
S/C ROTATION 10.00 RPM EVERY 5TH LOOK AND 40TH ROLL POINT SHOWN
STARTING LOOK ANGLE 117.00 DEG STARTING ROLL ANGLE -1.99 DEG
NO. DETECTORS PER CHANNEL 8 NO. POINTS PER ROLL 800
IMAGE FIELD OF VIEW IN THE ROLL 0.10 AND LOOK DIRECTION 0.10 MRAD

Figure 8-16a. Scan Map of Ganymede for Conditions Indicated



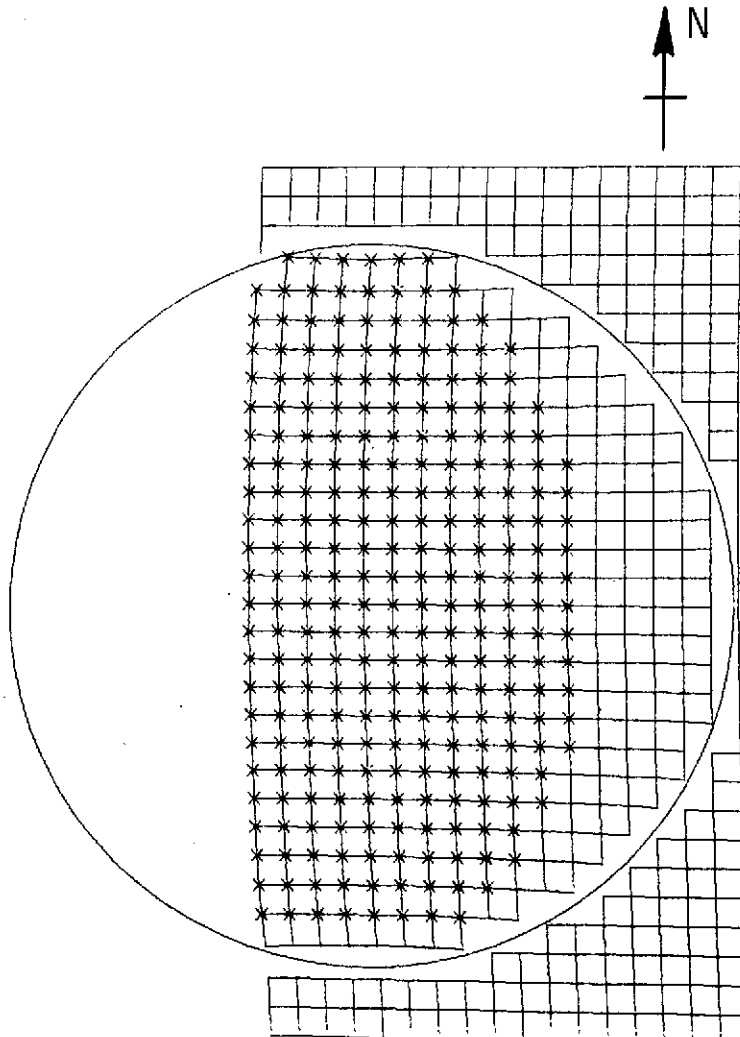
GANYMED ORBIT NO. 1 START TIME 321.76 END TIME 321.99 HRS.
CLOSEST APPROACH 1.13 RJ SAMPLE RATE 1 STEP INHIBIT
S/C ROTATION 10.00 RPM EVERY 5TH LOOK AND 40TH ROLL POINT SHOWN
STARTING LOOK ANGLE 102.00 DEG STARTING ROLL ANGLE -2.22 DEG
NO. DETECTORS PER CHANNEL 8 NO. POINTS PER ROLL 800
IMAGE FIELD OF VIEW IN THE ROLL 0.10 AND LOOK DIRECTION 0.10 MRAD

Figure 8-16b. Scan Map of Ganymede for Conditions Indicated



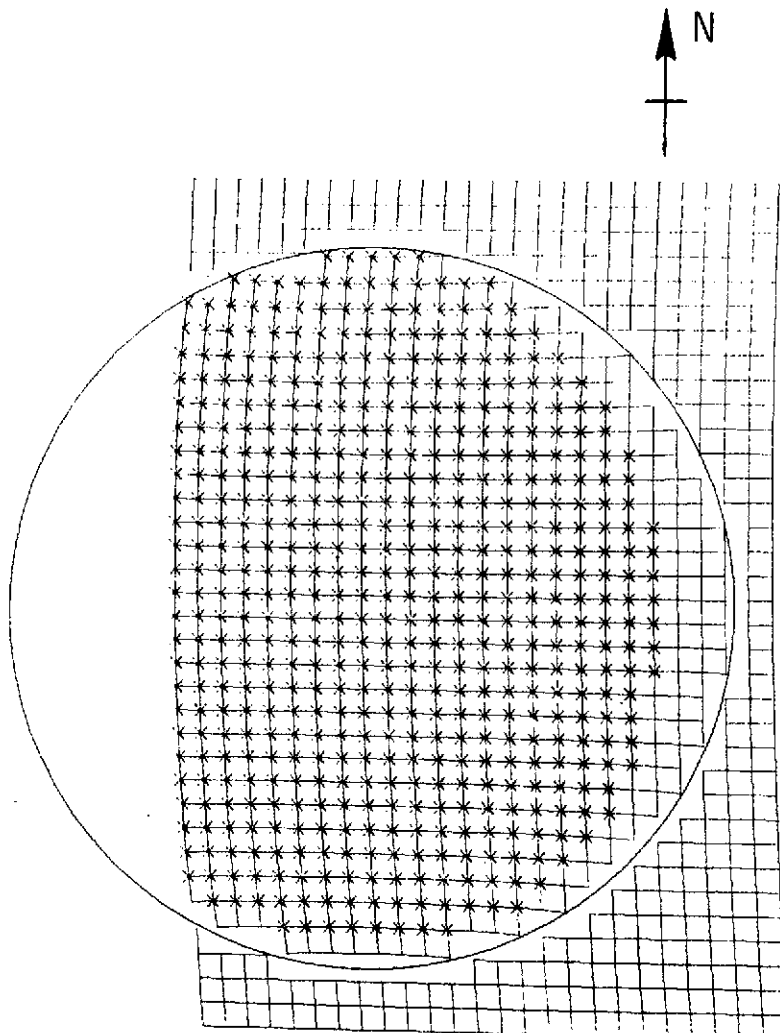
GANYMEDE ORBIT NO. 1 START TIME 322.49 END TIME 322.74 HRS.
CLOSEST APPROACH 0.95 RJ SAMPLE RATE 1 BACK STEPPING
S/C ROTATION 10.00 RPM EVERY 5TH LOOK AND 40TH ROLL POINT SHOWN
STARTING LOOK ANGLE 82.00 DEG STARTING ROLL ANGLE -2.95 DEG
NO. DETECTORS PER CHANNEL 4 NO. POINTS PER ROLL 1000
IMAGE FIELD OF VIEW IN THE ROLL 0.10 AND LOOK DIRECTION 0.10 MRAD

Figure 8-16c. Scan Map of Ganymede for Conditions Indicated



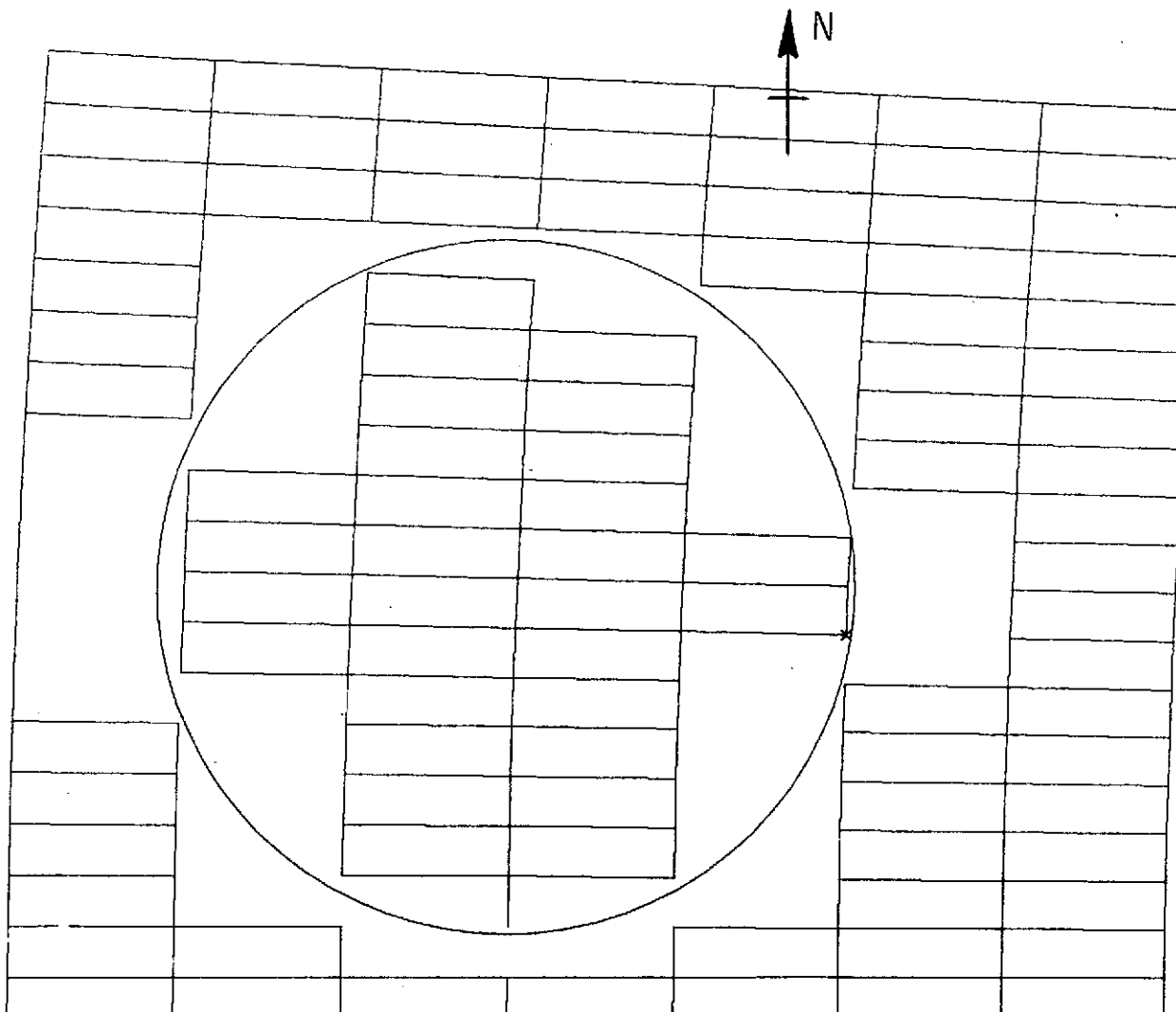
GANYMEDE ORBIT NO. 1 START TIME 323.15 END TIME 323.30 HRS.
CLOSEST APPROACH 0.91 RJ SAMPLE RATE 1 BACK STEPPING
S/C ROTATION 10.00 RPM EVERY 5TH LOOK AND 40TH ROLL POINT SHOWN
STARTING LOOK ANGLE 58.70 DEG STARTING ROLL ANGLE -3.80 DEG
NO. DETECTORS PER CHANNEL 4 NO. POINTS PER ROLL 1200
IMAGE FIELD OF VIEW IN THE ROLL 0.10 AND LOOK DIRECTION 0.10 MRAD

Figure 8-16d. Scan Map of Ganymede for Conditions Indicated



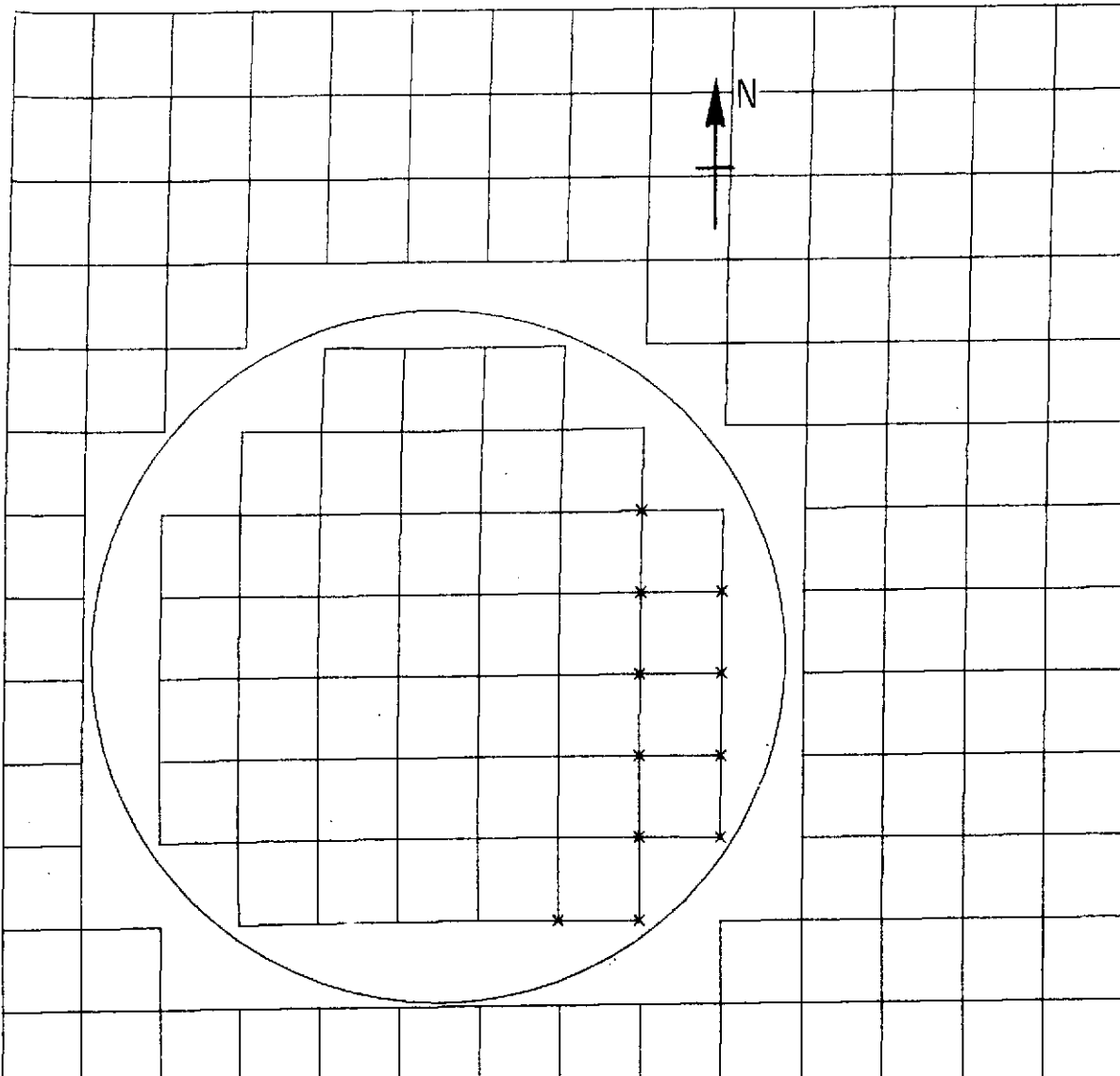
GANYMEDE ORBIT NO. 1 START TIME 323.61 END TIME 323.82 HRS.
CLOSEST APPROACH 1.00 RJ SAMPLE RATE 1 BACK STEPPING
S/C ROTATION 10.00 RPM EVERY 5TH LOOK AND 40TH ROLL POINT SHOWN
STARTING LOOK ANGLE 42.50 DEG STARTING ROLL ANGLE -4.69 DEG
NO. DETECTORS PER CHANNEL 4 NO. POINTS PER ROLL 1400
IMAGE FIELD OF VIEW IN THE ROLL 0.10 AND LOOK DIRECTION 0.10 MRAD

Figure 8-16e. Scan Map of Ganymede for Conditions Indicated



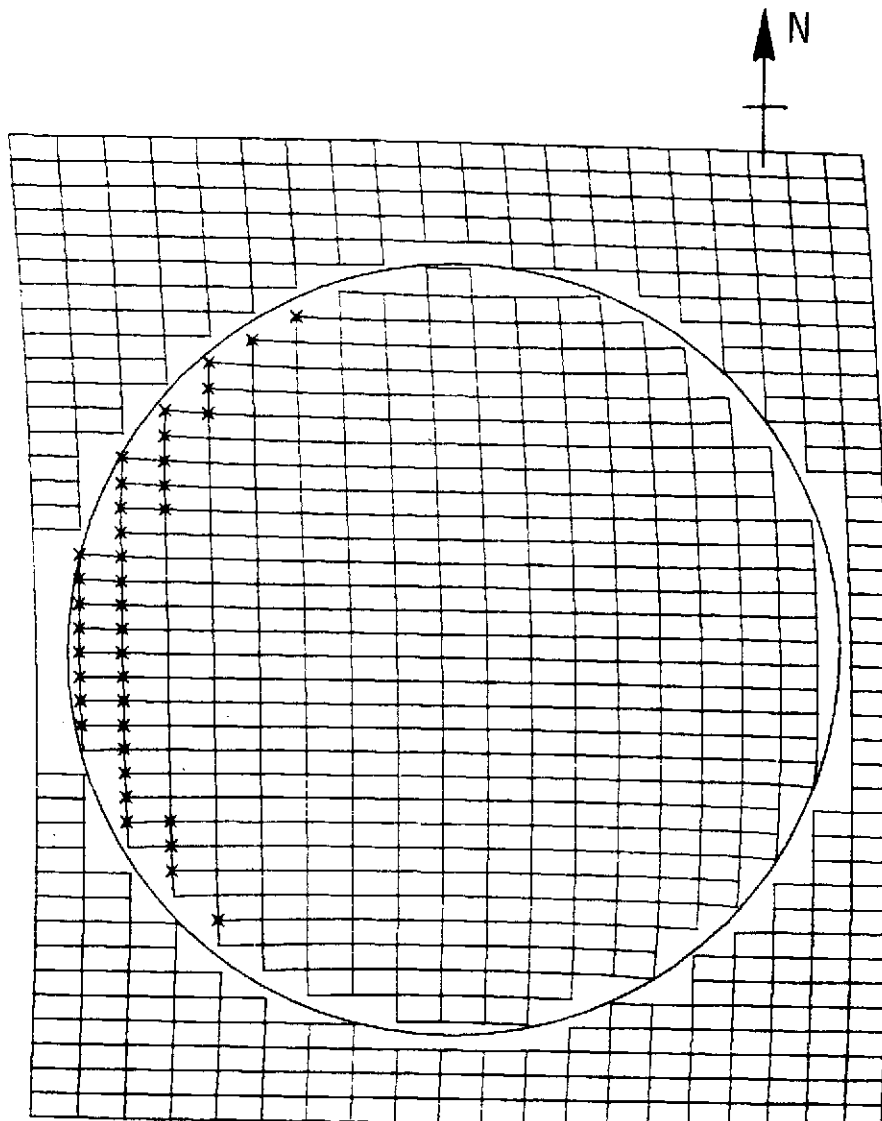
IO ORBIT NO. 1 START TIME 334.45 END TIME 334.52 HRS.
CLOSEST APPROACH 3.25 RJ SAMPLE RATE 1 FORWARD STEPPING
S/C ROTATION 10.00 RPM EVERY 5TH LOOK AND 40TH ROLL POINT SHOWN
STARTING LOOK ANGLE 164.00 DEG STARTING ROLL ANGLE 175.50 DEG
NO. DETECTORS PER CHANNEL 4 NO. POINTS PER ROLL 800
IMAGE FIELD OF VIEW IN THE ROLL 0.10 AND LOOK DIRECTION 0.10 MRAD

Figure 8-16f. Scan Map of Io for Conditions Indicated



IO ORBIT NO. 1 START TIME 336.58 END TIME 336.71 HRS.
CLOSEST APPROACH 1.63 RJ SAMPLE RATE 1 BACK STEPPING
S/C ROTATION 10.00 RPM EVERY 5TH LOOK AND 40TH ROLL POINT SHOWN
STARTING LOOK ANGLE 118.50 DEG STARTING ROLL ANGLE 177.90 DEG
NO. DETECTORS PER CHANNEL 4 NO. POINTS PER ROLL 600
IMAGE FIELD OF VIEW IN THE ROLL 0.10 AND LOOK DIRECTION 0.10 MRAD

Figure 8-16g. Scan Map of Io for Conditions Indicated



EUROPA ORBIT NO. 2 START TIME 350.16 END TIME 350.33 HRS.
CLOSEST APPROACH 0.60 RJ SAMPLE RATE 1 BACK STEPPING
S/C ROTATION 10.00 RPM EVERY 5TH LOOK AND 40TH ROLL POINT SHOWN
STARTING LOOK ANGLE 149.20 DEG STARTING ROLL ANGLE -3.50 DEG
NO. DETECTORS PER CHANNEL 8 NO. POINTS PER ROLL 1600
IMAGE FIELD OF VIEW IN THE ROLL 0.10 AND LOOK DIRECTION 0.10 MRAD

Figure 8-16h. Scan Map of Europa for Conditions Indicated

The planned images are analyzed statistically in Figure 8-17. In the curve for each satellite, the interruption by Jupiter gives a short horizontal section of the curve followed by a diagonal line of intermediate slope. At the best resolution, the steep slope results from data on both sides of closest passage. At the poorest resolution, the details of a histogram would depend on assumptions about the efficiency of time usage, so a diagonal line was drawn showing only the first pair of images as one step. The diagonal lines are corrected for the efficiency of an automatic sequencer. Clearly, this imager would give a substantial body of scientific imaging on the Jovian satellites.

8.4 OVERVIEW FOR SIX ORBITS AND SUMMARY

This study was selected to be synchronous with three of the Jovian satellites. Thus, the encounters of Figure 8-9 tend to be repeated in the later encounters of Figures 8-18 through 8-21. This has the advantage that "quick look" can be used to emphasize some special topics two weeks later at next close passage. Notable omissions in the present study are Callisto (JIV) and JV. Even at $10 R_J$, this imager resolves 70-km features. From Figure 8-2, it is clear that a passage this close to Callisto is quite possible. The orbit of JV is inside that of Io, so close passage is possible during the close passages by Jupiter. The diameter of JV may be about 70 km, so the imager would give of the order of ten resolution elements on its surface. Similar remarks hold for the numerous other small satellites of Jupiter, which could be studied in the week spent far from Jupiter. Indeed, the sky could be scanned in a search mode for additional satellites of Jupiter in 6-hour scans.

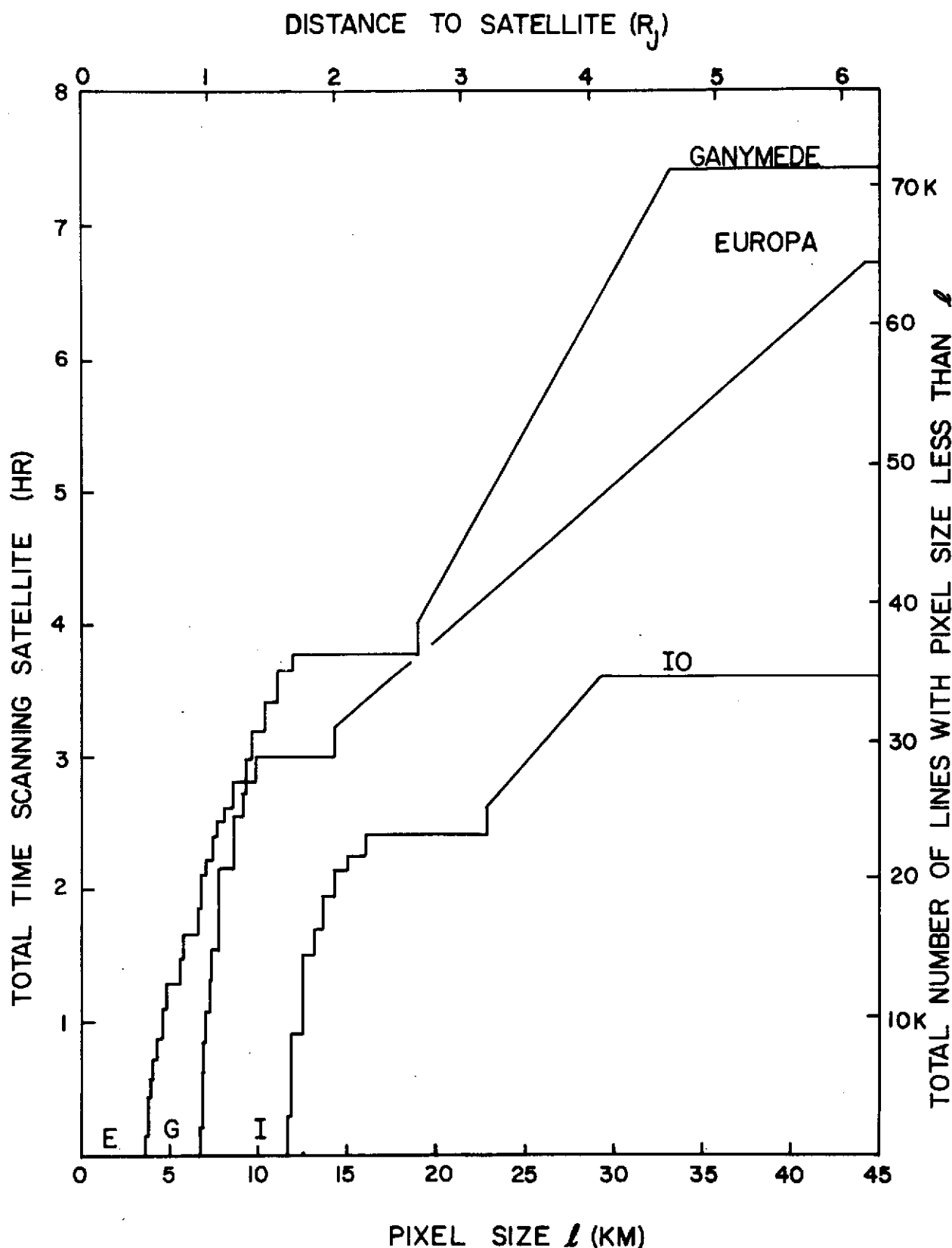


Figure 8-17. Statistical Analysis of Planned Images

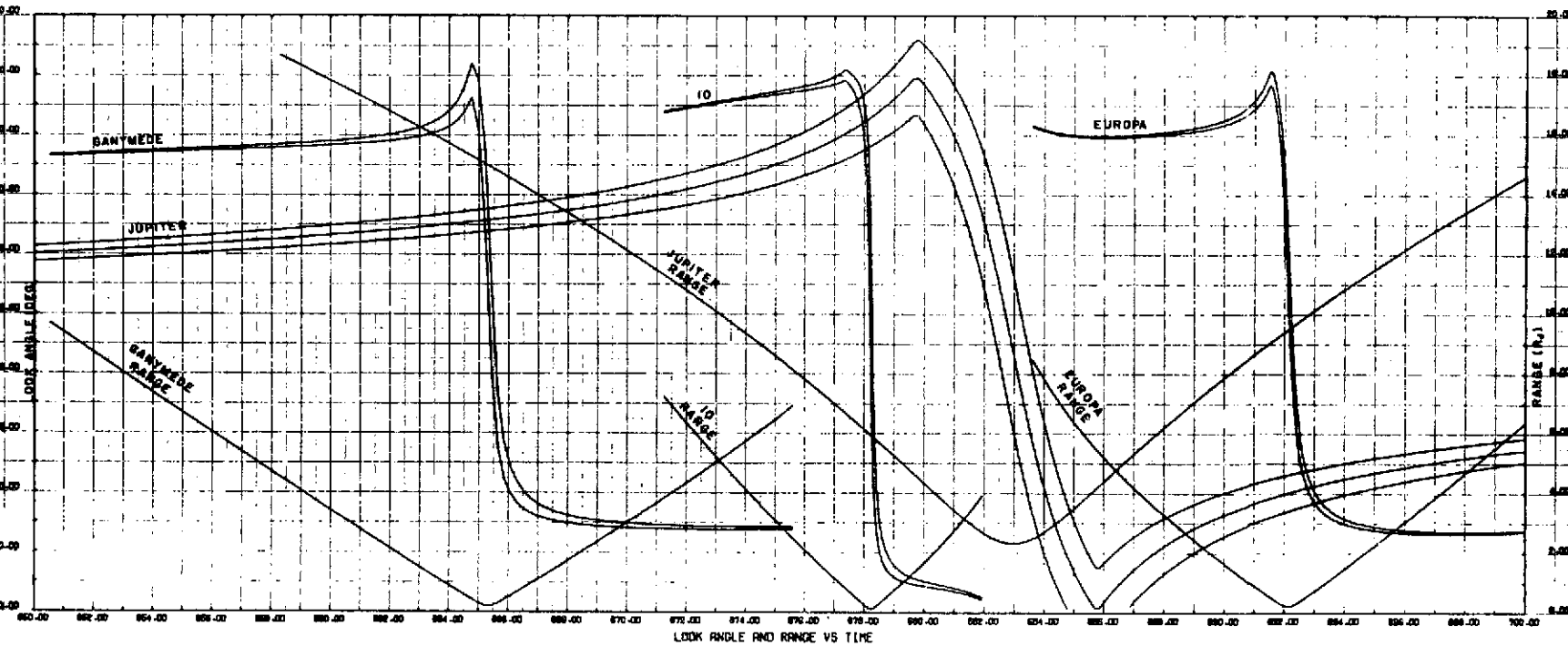


Figure 8-18. Look Angle Versus Time for Orbits 2 and 3

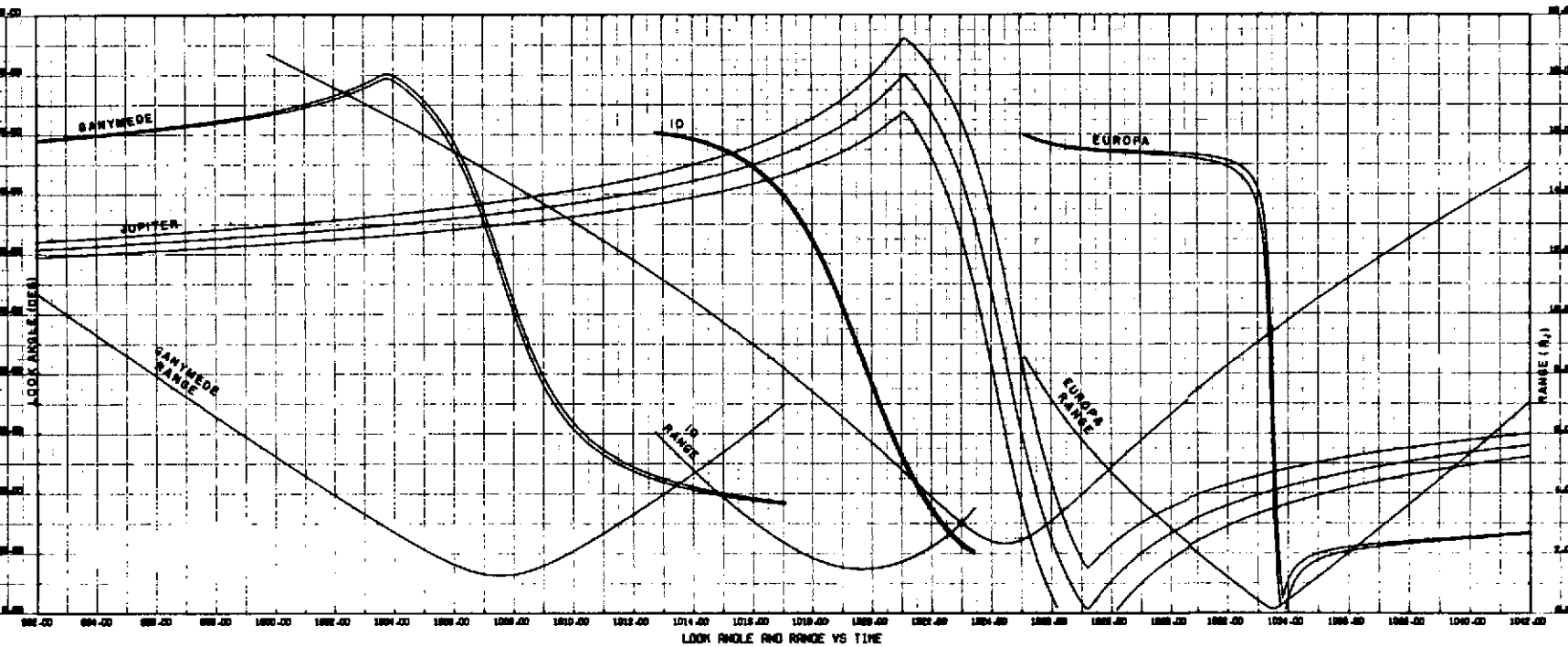


Figure 8-19. Look Angle Versus Time for Orbits 3 and 4

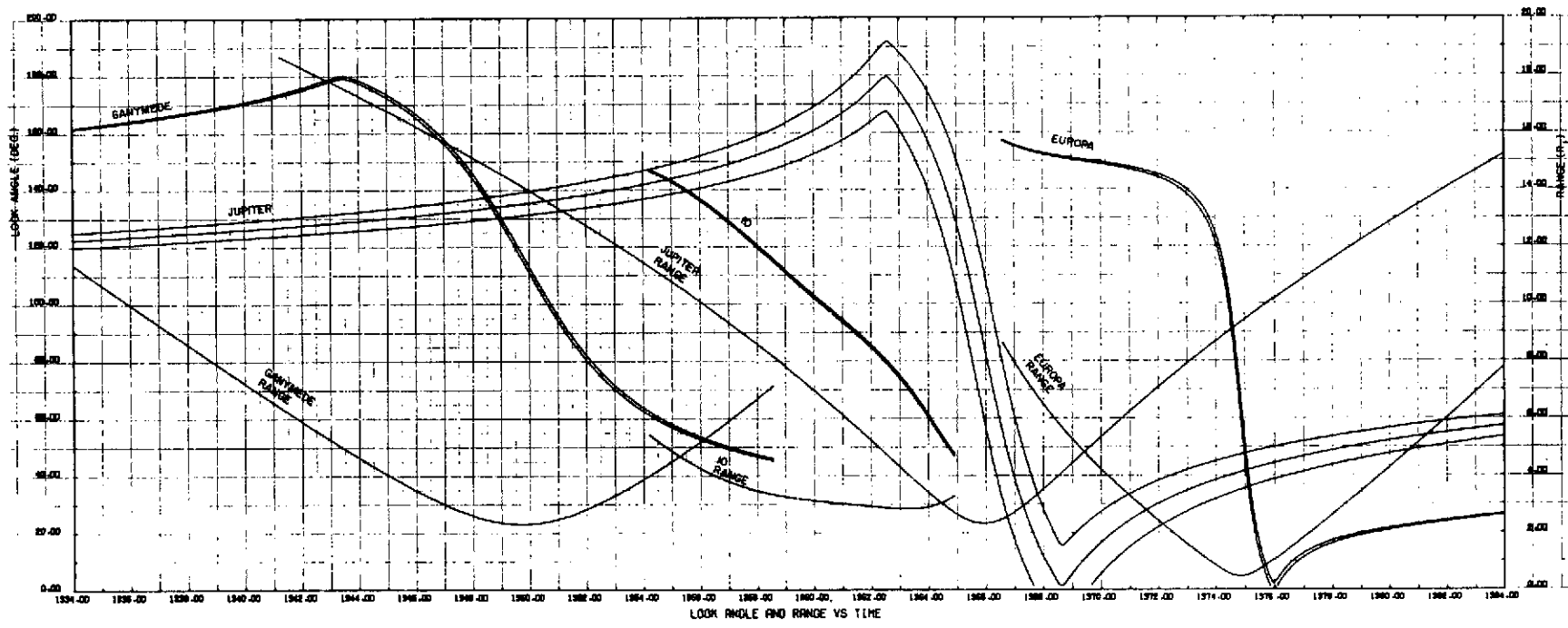


Figure 8-20. Look Angle Versus Time for Orbits 4 and 5

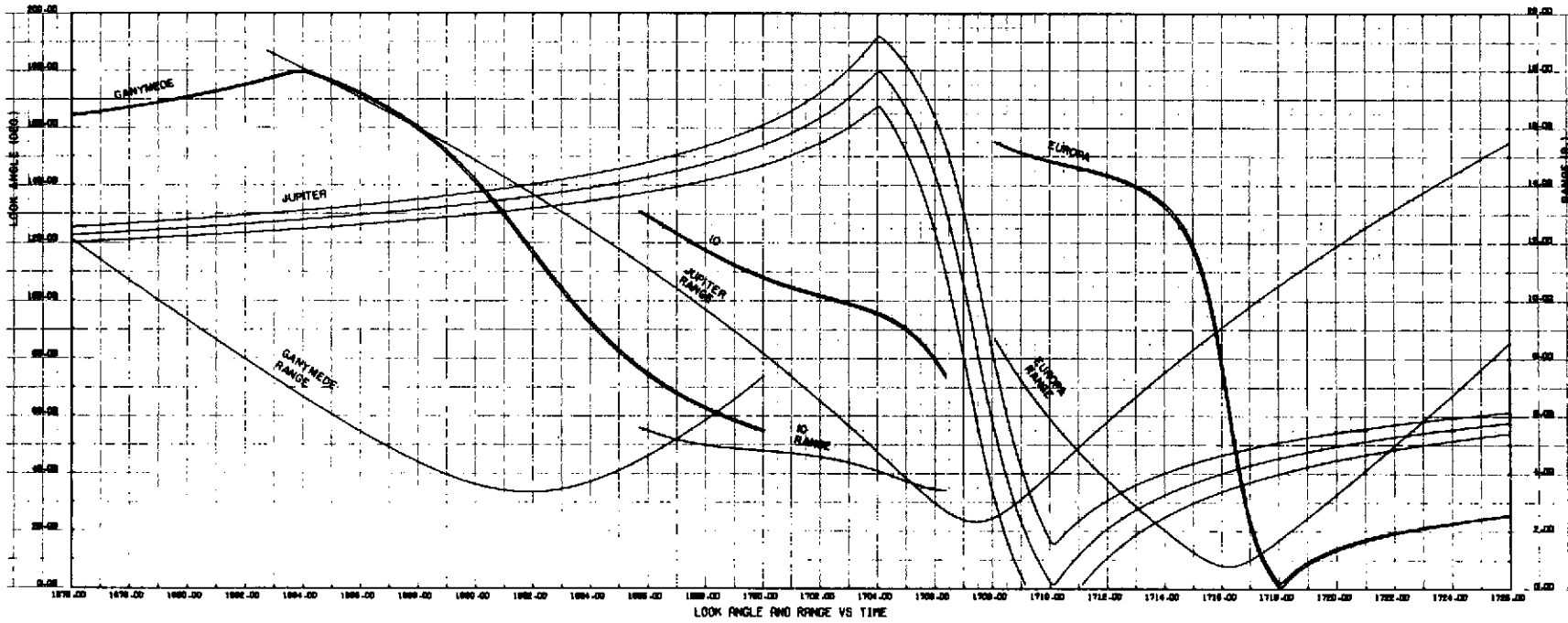


Figure 8-21. Look Angle Versus Time for Orbits 5 and 6

In summary, it is noted that of the order of ten complete images having pixel surface subtenses of about 10 km are attained during each of the three close satellite encounters on each orbit. Near maximum range (about 150 hours before periapsis), complete Jupiter images are obtained at a rate of about 10 images per hour, each image having a pixel surface subtense of about 320 km. A few hours before periapsis, complete disk images are obtained at a rate of about one per hour down to images with pixel surface subtenses of the order of 60 km. The pixel surface subtense of the highest resolution Jupiter images is 10 km, and about 25,000 lines of Jupiter imaging are obtained at pixel surface subtense of less than 20 km. There is great flexibility in how these 25,000 lines are divided into images. In short, there is sufficient time for the system to acquire an enormous amount of imaging data on Jupiter and its satellites over a variety of spatial scales down to 10 km for photometric and meteorological analysis.

Section 9

R E F E R E N C E S

1. O. H. Schade, Jour. SMPTE 73, 81 (1964).
2. R. L. Sendall, Proc. IRIS Specialty Group of Infrared Imaging, p. 59, held 7-8 January 1971.
3. S. J. Katzberg, F. O. Huck, and S. D. Wall, Appl. Opt. 12, 1054 (1973).
4. Albedo data shown are a composite from following sources:
D. L. Harris, Planets and Satellites
J. F. Appleby and W. M. Irvin, Astron. J. 76, 617 (1971)
W. M. Irvine, et al., Astron. J. 73, 251 (1969)
A. C. Binder and D. W. McCarthy, Jr., Astrophys. J. 171:L1-L3 (1972)
5. W. D. Gunter, Jr., G. R. Grant, and S. A. Shaw, Appl. Opt. 9, 251 (1970).
6. S. F. Pellicori, E. E. Russell, and L. A. Watts, Critical Components Study by SBRC for NASA Outer Planets Grand Tour Missions Photometry/Polarimetry Experiment Team.
7. Name registered by Bendix Corporation.
8. A. Egidi, R. Marconero, G. Pizzella, and F. Sperli, Rev. Sci. Inst. 40, 88 (1969).
9. L. A. Frank, N. K. Henderson, and R. L. Swisher, Rev. Sci. Inst. 40, 685 (1969).
10. Private communication, L. A. Watts (SBRC).
11. Paper presented by C. E. Catchpole and C. B. Johnson at Advanced Electronic Systems for Astronomy Conference, University of California at Santa Cruz, 1 September 1971.
12. E. A. Beaver and C. E. McIlwain, Rev. Sci. Inst. 42, No. 9 (1971).
13. J. P. Choisser and W. Wysoczanski, Proc. SPIE 28, 223 (1972).
14. Private communication, J. Choisser, Electronic Vision Corporation.
15. RCA technical literature for Image Tube C33105.
16. C. B. Johnson and K. L. Hallam, Proc. SPIE 32, 53 (1972).
17. Private communication, L. L. Thompson, Goddard Space Flight Center.
18. Private communication, N. P. Laverty, TRW Systems Group.
19. See, for example, M. F. Tomsett, J. Vac. Sci. Technol. 9, 1166 (1972).

20. The model given in "Proceedings of the Jupiter Radiation Belt Workshop," edited by Andrew J. Beck, Pasadena, California, NASA TM 33-543, July 1, 1972 is probably the best present model of these belts.
21. See, for example, W. B. Fowler, E. I. Reed, and J. E. Blamont, Goddard Space Flight Center Report X-613-68-486, December 1968.
22. A. J. Young, Rev. Sci. Inst. 37, 1472 (1966).
23. E. I. Reed, W. B. Fowler, C. W. Aitken, and J. F. Brun, Goddard Space Flight Center Report X-613-67-132, March 1967.
24. W. C. Way, "SPAC Star Sensor Radiation Effects," Hughes Aircraft Report IDC 2781.2/17, 28 June 1968.
25. C. Wolff, Appl. Opt. 5, 1838 (1966).
26. G. W. Goodrich, C. C. Matle, and L. A. Watts, J. Opt. Soc. Am. 61, 691A (1971).
27. Space Materials Handbook, Third Edition, NASA SP-3051, p. 407 (1969).
28. Measurements performed by Hughes Aircraft Company personnel.
29. D. E. Martz and I. R. Neilsen, Final Report on the Effects of Ionizing Radiation on Photodetectors (AD 423373), February 1963.
30. Private communication, N. P. Laverty, TRW Systems Group.
31. Richard H. Parker, IEEE Transaction on Nuclear Science 19, 156 (1972).
32. R. E. Simon and B. F. Williams, IEEE Transaction on Nuclear Science NS 15, 167 (1968).
33. R. E. Simon, A. H. Sommer, J. J. Tietjen, and B. F. Williams, Appl. Phys. Letters, No. 15, 1968.
34. M. Born and E. Wolf, Principles of Optics, Pergamon Press (1963).
35. A. Wissinger, et al., Three-Meter Telescope Study Final Report, NASA Contract NAS 5-21540, August 1971.
36. Large Space Telescope Final Report, Itek Corporation NASW-2174, 3 September 1971.
37. W. B. Wetherell and M. P. Rummer, Appl. Opt. 11, 2817 (1972).
38. Byron L. Swenson, et al., Preliminary Mission Designs for Jupiter Orbiter Missions, NASA TM X-2565, May 1972.
39. S. F. Pellicori, E. E. Russell, and L. A. Watts, Appl. Opt. 12, 1246 (1973).
40. NASA Report SP-284, "Analysis of Surveyor 3 Material and Photographs Returned by Apollo 12," p. 76-89 (1972).